# Waveform optimization for 6G communication systems in the sub-THz bands

Yaya Bello

THÈSE

Pour obtenir le grade de

**DOCTEUR DE L'UNIVERSITÉ GRENOBLE ALPES**

École doctorale : EEATS - Electronique, Electrotechnique, Automatique, Traitement du Signal (EEATS)
Spécialité : Signal Image Parole Télécoms
Unité de recherche : Laboratoire d'Electronique et de Technologie de l'Information (LETI)

# Optimisation des formes d'ondes pour les systèmes de communication 6G dans les bandes sub-THz

# Waveform optimization for 6G communication systems in the sub-THz bands

Présentée par :


## Yaya BELLO


Direction de thèse :

| | |
|---|---|
| **José Luis GONZALEZ JIMENEZ**<br>CEA | Directeur de thèse |
| **David DEMMER**<br>CEA | Co-encadrant de thèse |
| **Jean-Baptiste DORE**<br>Docteur Ingénieur, CEA | Co-encadrant de thèse |

Rapporteurs :

**Didier LE RUYET**
PROFESSEUR DES UNIVERSITES, CNAM PARIS
**Matthieu CRUSSIERE**
PROFESSEUR DES UNIVERSITES, INSA RENNES

Thèse soutenue publiquement le **14 décembre 2023**, devant le jury composé de :

| | |
|---|---|
| **Inbar FIJALKOW,**<br>PROFESSEURE DES UNIVERSITES, ECOLE NAT SUP ELECTRONIQUE APPLIS | Présidente |
| **José Luis GONZALEZ JIMENEZ,**<br>DIRECTEUR DE RECHERCHE, CEA CENTRE DE GRENOBLE | Directeur de thèse |
| **Didier LE RUYET,**<br>PROFESSEUR DES UNIVERSITES, CNAM PARIS | Rapporteur |
| **Matthieu CRUSSIERE,**<br>PROFESSEUR DES UNIVERSITES, INSA RENNES | Rapporteur |
| **Laurent ROS,**<br>PROFESSEUR DES UNIVERSITES, GRENOBLE INP | Examinateur |
| **Jean-Christophe SIBEL,**<br>INGENIEUR DOCTEUR, Mitsubishi Electrique R&D Centre Europe | Examinateur |

Invités :

**Jean-Baptiste DORE**
INGENIEUR DOCTEUR, CEA-LETI
**David DEMMER**
INGENIEUR DOCTEUR, CEA-LETI

À la mémoire de mon grand-père
**Yaya Djalo**,
*Puisses-tu être fier de ton petit-fils.*

## Abstract

The deployment of cellular technologies with broader bandwidths at higher frequencies presents an attractive solution for augmenting the capacities of wireless communication systems, particularly in terms of enhancing throughput. Fortunately, the sub-THz spectrum, spanning from 100 to 300 GHz, has been recognized as a promising contender for the next generation of wireless technology, known as 6G. This is primarily due to the substantial bandwidth it offers. However, transmitting signals in the sub-THz frequencies introduces several challenges. These include the significant attenuation of electromagnetic waves by the propagation environment, the demand for high sampling rates for analog-to-digital conversion, and the adverse impact of phase noise mainly generated by oscillators. Consequently, the direct transposition of existing wireless technologies is not straighforward. On one hand, the IEEE 802.15.3d specification standardizes a single-carrier waveform with carrier aggregation. On the other hand, ongoing research aims to adapt 5G New Radio multi-carrier waveforms like Orthogonal Frequency Division Multiplexing (OFDM) and Discrete Fourier Transform-Spread-OFDM (DFT-s-OFDM) to suit the characteristics of sub-THz frequencies. In this thesis, our objective is to investigate the performance of multi-carrier waveform systems that are affected by the harmful effects of high-frequency oscillator phase noise.

The genesis of phase noise can be traced back to sudden, brief and random fluctuations in the phase of an oscillator's components. This issue becomes increasingly severe as the carrier frequency rises, posing a substantial challenge to system performance, especially when operating in sub-THz frequency bands. As a result, the primary focus of this thesis centers on the development of signal-processing algorithms aimed at mitigating phase noise. To achieve this goal, two core aspects are explored within this research: the formulation of efficient techniques for phase noise reduction and their practical implementation for realistic radio-frequency transmissions. To provide a fair performance evaluation, we consider statistical phase noise models such as: (i) correlated phase noise as proposed by the 3GPP and direct measurements obtained from a D-Band CMOS transceiver designed at CEA-Leti; as well as (ii) purely uncorrelated Gaussian phase noise. Leveraging these models, we have proposed a phase noise compensation algorithm characterized by a low pilot density, particularly effective when dealing with correlated phase noise in both OFDM and DFT-s-OFDM systems. This algorithm relies on the knowledge of stochastic properties of various noise sources induced by phase noise. We assess the performance for a-priori knowledge, *i.e* genie-aided, and estimated knowledge, *i.e.* practical scenario of these stochastic properties. In the case of uncorrelated phase noise where its tracking is no longer possible, we introduce an optimal detector particularly suited for DFT-s-OFDM systems, operating under strong uncorrelated phase noise conditions. The performance of this detector is contingent upon the statistical properties of the noises introduced by phase noise. Throughout these contributions, we maintain a focus on achieving low implementation complexity and high spectral efficiency, with an underlying assumption of coherent communication systems.

**Keywords** – *5G and beyond Networks, Wireless Networks, 5G-NR Multi-carrier waveforms, sub-THz bands, Phase Noise, CMOS transceivers, 3GPP, 6G.*

## Résumé

Le déploiement de technologies cellulaires dans des bandes de fréquences plus larges à des fréquences plus élevées constitue une solution attrayante pour accroître les capacités des systèmes de communication sans fil, notamment en termes d'amélioration du débit. Le spectre sub-THz, qui s'étend de 100 à 300 GHz, a été retenu comme un candidat prometteur pour la prochaine génération de technologie sans fil (connue sous le nom de 6G) dû à la largeur de bande substantielle qu'il offre. Cependant, la transmission de signaux dans les fréquences sub-THz pose plusieurs problèmes. En particulier, on peut citer l'atténuation significative des ondes électromagnétiques par le canal de propagation, la fréquence d'échantillonnage élevée pour la conversion analogique-numérique et inversement; et l'impact du bruit de phase généré par les oscillateurs. Par conséquent, la transposition directe des technologies sans fil existantes n'est pas triviale. Cependant, la spécification IEEE 802.15.3d normalise une forme d'onde à porteuse unique avec agrégation de porteuses. De plus, des recherches en cours visent à adapter les formes d'ondes multi-porteuses telles que l'OFDM et la DFT-s-OFDM pour répondre aux caractéristiques des fréquences sub-THz. Dans cette thèse, notre objectif est d'améliorer les performances des systèmes utilisant des formes d'ondes multi-porteuses et qui sont affectés par les effets du bruit de phase introduits par l'oscillateur à haute fréquence.

L'origine du bruit de phase peut être attribuée à des fluctuations soudaines, brèves et aléatoires de la phase des composants d'un oscillateur. Ce problème devient de plus en plus grave à mesure que la fréquence de la porteuse augmente, ce qui constitue un défi pour les systèmes de communication envisagés pour des bandes de fréquences du spectre sub-THz. Par conséquent, cette thèse se concentre principalement sur le développement d'algorithmes de traitement du signal visant à atténuer les effets du bruit de phase. Pour atteindre cet objectif, deux aspects essentiels sont explorés dans cette recherche : la formulation de techniques efficaces pour la réduction des effets du bruit de phase et leurs mises en oeuvre pratique pour des transmissions radiofréquence réelles. Pour ce faire, des modèles précis de bruit de phase sont utilisés dans cette étude, notamment le modèle de bruit de phase proposé par le standard 3GPP, le modèle de bruit de phase Gaussien et des mesures réelles de bruit de phase obtenues à partir d'émetteurs-récepteurs CMOS en bande D conçus au CEA-Leti. En nous appuyant sur ces modèles, nous avons proposé des algorithmes de compensation du bruit de phase caractérisés par une faible densité de pilotes, particulièrement efficaces pour traiter le bruit de phase de nature corrélé dans les systèmes OFDM et DFT-s-OFDM. Ces algorithmes reposent sur la connaissance et/ou l'estimation des propriétés stochastiques des différentes sources de bruit induites par le bruit de phase. En outre, nous présentons un détecteur optimal, particulièrement adapté aux systèmes DFT-s-OFDM fonctionnant dans des conditions de bruit de phase fort et non corrélé. La performance de ce détecteur dépend des propriétés statistiques des bruits introduits par le bruit de phase. Tout au long de ces contributions, nous nous sommes concentrés sur l'obtention d'une faible complexité de mise en oeuvre et d'une efficacité spectrale élevée, avec l'hypothèse sous-jacente de systèmes de communication cohérents.

**Mots-clés –** *Réseaux sans fil, Formes d'onde multi-porteuses 5G-NR, Spectre sub-THz, Bruit de phase, Emetteur-récepteur CMOS, 3GPP, 6G.*

## Acknowledgments

Avant d'attaquer le contenu de ce manuscrit, je tiens à remercier les personnes qui ont contribué à ce que ce travail soit mené à bon port.

Je tiens à remercier en premier lieu, Jean-Baptiste Doré et David Demmer pour l'encadrement qu'ils m'ont apporté au cours de ces trois années de thèse au sein du CEA-Léti. Merci pour vos conseils, vos retours, vos expertises, vos explications, vos corrections, vos suggestions et pour la patience que vous avez affichée tout au long de mon encadrement. Vous avez toujours trouvé les mots pour me motiver à chaque fois que j'avais une contribution refusée à une conférence. Un merci également à José Luis Gonzalez-Jimenez, qui a su diriger cette thèse et qui y a contribué à sa manière de façon technique et avec ses différentes relectures de mon travail.

Je tiens aussi à remercier mon jury de thèse, la présidente Inbar Fijalkow, les rapporteurs Didier le Ruyet et Matthieu Crussière; et les examinateurs Laurent Ros et Jean-Christophe Sibel, qui m'ont fait l'honneur d'examiner mon travail et qui ont tous su proposer des discussions et axes de reflexion très intéressants.

Merci également à l'ensemble de l'équipe LS2PR du STSF au CEA-Léti, qui m'a accueillie durant toute cette aventure. Merci à Benoit M., Rafik, Benoit D., Nicolas C., Valentin, Valerian, Patrick, Luc, Johan, Khaled, David M., François, Lionel, Hugo, Marc, Josua, Mattia et Mohamed. Merci également aux thesards Tomas, Joachim, Antoine, Ala-Eddine, Oscar, Jules, et tous ceux que j'oublie.

Un grand merci à mes parents pour leurs bénédictions et soutiens sans faille dans toutes les décisions que j'ai eues à prendre concernant mes études et également au reste de ma famille pour leur soutien.

# PUBLICATIONS

## INTERNATIONAL JOURNAL COMMUNICATIONS

[J1] **Y. Bello**, J-B. Doré and David Demmer, *"Analysis of Gaussian Phase Noise Effects in DFT-s-OFDM systems for sub-THz Transmissions,"* **submitted**, 2023.

[J2] **Y. Bello**, J-B. Doré and David Demmer, *"Low Complexity Time Domain Filtering of Phase Noise in OFDM Systems,"* **submitted**, 2023.

## INTERNATIONAL CONFERENCE COMMUNICATIONS

[C1] **Y. Bello**, S. Barnola, D. Demmer and J-B. Doré , *"OTFS Waveform with Phase Noise in sub-THz,"* In Proc. IEEE Vehicular Technology Conference (VTC2022-Fall), London, United Kingdom, pages 1–5, 2022.

[C2] **Y. Bello**, J-B. Doré and D. Demmer, *"DFT-s-OFDM for sub-THz Transmission – Tracking and Compensation of Phase Noise,"* In Proc. IEEE Consumer Communications & Networking Conference (CCNC), Nevada, United States of America, pages 297–300, 2023.

[C3] **Y. Bello**, D. Demmer, A. Hamani, A. Siligaris, C. Dehos, N. Cassiau, J-B. Doré and J.L. González-Jiménez, *"Performance Assessment of a 5GNR D-Band Transceiver with Phase Noise Impairments,"* In Proc. Joint European Conference on Networks and Communications & 6G SUMMIT (EuCNC/6G SUMMIT), Goteborg, Sweden, pages 246-251, 2023.

[C4] **Y. Bello**, J-B. Doré and D. Demmer, *"Wiener Interpolation Filter for Phase Noise Estimation in Sub-THz Transmission,"* In Proc. IEEE Vehicular Technology Conference (VTC2023-Spring), Florence, Italy, pages 1-5, 2023.

[C5] **Y. Bello**, J-B. Doré and D. Demmer, *"Time Domain Phase Noise Mitigation in OFDM Systems for sub-THz Bands,"* In Proc. IEEE Global Communications Conference (GLOBECOM), Kuala Lumpur, Malaysia, 2023.

## FRENCH CONFERENCE COMMUNICATIONS

[C6] **Y. Bello**, D. Demmer and J-B. Doré, *"Compensation du bruit de phase et évaluation des performances d'un émetteur-récepteur CMOS à 140 GHz,"* Colloque Gretsi, Grenoble, France, 2023.

[C7] **Y. Bello**, D. Demmer and J-B. Doré, *"Analyse des effets du bruit de phase Gaussien sur un signal DFT-s-OFDM,"* Colloque Gretsi, Grenoble, France, 2023.

# Contents

# List of Figures

# List of Tables

# List of Acronyms

| | |
|---|---|
| **3GPP** | 3rd Generation Partnership Project |
| **4G** | Fourth Generation |
| **5G** | Fifth Generation |
| **5G-NR** | 5G-New Radio |
| **6G** | Sixth Generation |
| **AWGN** | Additive White Gaussian Noise |
| **ADC** | Analog-to-Digital Converter |
| **AI** | Artificial Intelligence |
| **BS** | Base Station |
| **BER** | Bit Error Rate |
| **CFO** | Carrier Frequency Offset |
| **CEQ** | Channel Equalization |
| **CSI** | Channel State Information |
| **CR** | Coding Rate |
| **CPE** | Common Phase Error |
| **CMOS** | Complementary Metal-Oxide-Semiconductor |
| **CI** | Constant Interpolation |
| **CPEE** | CPE Estimation |
| **CDF** | Cumulative Distribution Function |
| **CP** | Cyclic Prefix |
| **DL** | Deep Learning |
| **DD** | Delay-Doppler |
| **DT** | Delay-Time |
| **DFT-s-OFDM** | Discrete Fourier Transform spread OFDM |
| **DFT** | Discrete Fourier Transform |

| | |
|---|---|
| **DCT** | Discrete Cosine Transform |
| **EE** | Energy Efficiency |
| **FFT** | Fast Fourier Transform |
| **FIR** | Finite Impulse Response |
| **FMCW** | Frequency Modulated Continuous Wave |
| **FT** | Frequency-Time |
| **GaAs** | Gallium Arsenide |
| **GPN** | Gaussian Phase Noise |
| **HSNR** | high SNR |
| **ILO** | Injection locked oscillator |
| **IEEE** | Institute of Electrical and Electronics Engineers |
| **IQ** | In-phase and Quadrature |
| **ICS** | Inter-Carrier Spacing |
| **ICI** | Intercarrier Interference |
| **IF** | Intermediate Frequency |
| **ISI** | Inter-Symbol Interference |
| **IDFT** | Inverse Discrete Fourier Transform |
| **IFFT** | Inverse Fast Fourier Transform |
| **ISFFT** | Inverse Symplectic Finite Fourier Transform |
| **LS** | Least Squared |
| **LoS** | Line-of-Sight |
| **LI** | Linear Interpolation |
| **LO** | Local Oscillator |
| **LLR** | Log-Likelihood Ratio |
| **LDPC** | Low Density Parity Check |
| **LNA** | Low Noise Amplifier |
| **ML** | Maximum Likelihood |
| **MSE** | Mean Squared Error |
| **mmWave** | millimeter-Wave |
| **MC** | Multi-Carrier |
| **MIMO** | Multiple-Input Multiple-Output |

| | |
|---|---|
| **NMSE** | Normalized Mean Squared Error |
| **NLoS** | Non Line-of-Sight |
| **OFDMA** | OFDM Access |
| **OFDM** | Orthogonal Frequency Division Multiplexing |
| **OTFS** | Orthogonal Time Frequency Space |
| **OOB** | Out-of-Band |
| **PAPR** | Peak-to-Average Power Ratio |
| **PROT** | Periodically Repeated Oscillations Train |
| **PLL** | Phase Locked Loop |
| **PN** | Phase Noise |
| **PT-RS** | Phase Tracking Reference Signals |
| **PHY** | Physical |
| **PQAM** | Polar QAM |
| **PA** | Power Amplifier |
| **PSD** | Power Spectral Density |
| **PDF** | Probability Density Function |
| **QAM** | Quadrature Amplitude Modulation |
| **RF** | Radio Frequency |
| **RB** | Resource block |
| **RRC** | Root Raise Cosine |
| **SNR** | Signal-to-Noise Ratio |
| **SC** | Single-Carrier |
| **SE** | Spectral Efficiency |
| **SPE** | Subcarrier Phase Error |
| **SEP** | Symbol Error Probability |
| **SFFT** | Symplectic Finite Fourier Transform |
| **TDF** | Time Domain Filter |
| **TBLER** | Transport Block Error Rate |
| **UE** | User Equipment |
| **VCO** | Voltage-Controlled Oscillator |
| **WIF** | Wiener Interpolation Filter |
| **ZF** | Zero Forcing |

# List of Symbols

## System parameters

| | |
|---|---|
| $N_{OFDM}$ | Number of OFDM symbols |
| $N_{FFT}$ | Number of FFT points for discrete-time PN generation |
| $N_f$ | Size of FFT for OFDM modulation |
| $N_{CP}$ | Size of cyclic prefix for OFDM |
| $N'$ | Size of the OFDM symbol after adding the cyclic prefix |
| $N_a$ | Number of active subcarriers |
| $N_s$ | Size of the spreading block for DFT-s-OFDM |
| $N$ | Size of the Delay axis for OTFS |
| $M$ | Size of the Doppler axis for OTFS |
| $\Delta_f$ | Subcarrier spacing frequency |
| $\mu$ | Numerology |
| $F_c$ | Carrier frequency |
| $F_s$ | Sampling frequency |
| $T_s$ | Sampling time |
| $M_s$ | Modulation Order |
| $B_W$ | System bandwidth |
| $C$ | Constellation |
| $K_0$ | Power spectral density of the white phase noise contribution |
| $K_2$ | Power spectral density of the Wiener phase noise contribution |

## Communication signals

| | |
|---|---|
| $\sigma_n^2$ | Thermal noise variance |
| $\sigma_\phi^2$ | Phase noise variance |
| $\hat{\cdot}_k$ | Estimated value of the argument $(\cdot)_k$ |
| $\tau$ | Discrete-time index |
| $t$ | Continuous-time index |
| $\phi(\tau)$ | Discrete-time phase noise |
| $\phi(t)$ | Continuous-time phase noise |

## Mathematical Notations

| | |
|---|---|
| $x$ | Lowercase symbol represents a scalar number |
| $\underline{\mathbf{x}}$ | Underlined bold symbol represents a vector |
| $\underline{\mathbf{x}}[k]$ or $x_k$ | $k^{th}$ element of the vector $\underline{\mathbf{x}}$ |
| $\underline{\mathbf{N}}_A$ | Column vector of size $A \times 1$ which contains the number $\mathbf{N}$ in all rows |
| $\mathbf{X}$ | Bold uppercase symbol represents a matrix |
| $\mathbf{diag}_k\{\mathbf{X}\}$ | $k^{th}$ element of the diagonal of the matrix $\mathbf{X}$ |
| $\mathbf{diag}\{\mathbf{X}\}$ | Diagonal of the matrix $\mathbf{X}$ |
| $\mathbf{X}^{(i,k)}$ | Element of the matrix $\mathbf{X}$ at the $i^{th}$ row and $k^{th}$ column |
| $\underline{\mathbf{X}}^{(k)}$ | Column vector which contains the $k^{th}$ column of the matrix $\mathbf{X}$ |
| $\mathbf{N}_A$ | Matrice of size $A \times A$ that fully contains the number $\mathbf{N}$ |
| $\mathbf{I}_A$ | Identity matrix of size $A \times A$ |
| $\mathbf{X}^R$ | Real part of matrix $\mathbf{X}$ |
| $\mathbf{X}^I$ | Imaginary part of matrix $\mathbf{X}$ |
| $\underline{\mathbf{x}}^R$ | Real part of the vector $\mathbf{x}$ |
| $\underline{\mathbf{x}}^I$ | Imaginary part of the vector $\mathbf{x}$ |
| $\mathbf{X}^\dagger$ | Moore-Penrose inverse of Matrix $\mathbf{X}$ |
| $\mathbf{X}^{-1}$ | Inverse of Matrix $\mathbf{X}$ |
| $\mathcal{N}(\mu, \sigma^2)$ | Normal distribution with mean $\mu$ and variance $\sigma^2$ |
| $\mathbb{C}\mathcal{N}(\mu, \sigma^2)$ | Complex normal distribution with mean $\mu$ and variance $\sigma^2$ |
| $\mathbb{E}[\cdot]$ | Expectation operator |
| $\lvert \cdot \rvert$ | Magnitude operator |
| $\arg(\cdot)$ | Argument or phase operator |
| $x_{k_\rho}$ | Magnitude valude of scalar $x_k$ |
| $x_{k_\theta}$ | Phase valude of scalar $x_k$ |
| $\underline{\mathbf{a}}_\rho$ | Column vector which contains magnitude values of vector $\underline{\mathbf{a}}$ |
| $\underline{\mathbf{a}}_\theta$ | Column vector which contains phase (argument) values of vector $\underline{\mathbf{a}}$ |
| $(\cdot)^*$ | Conjugate operator |
| $(\cdot)^T$ | Transpose operator |
| $(\cdot)^H$ | Transpose-conjugate |

## Mathematical Notations

| | |
|---|---|
| $\mathfrak{Re}\{\cdot\}$ | Real part |
| $\mathfrak{Im}\{\cdot\}$ | Imaginary part |
| $\max(\cdot)$ | Maximum value |
| $\min(\cdot)$ | Minimum value |
| $\mathbf{F}_A$ | Fourier matrix of size $A \times A$ |
| $\mathbf{R}_{\underline{\mathbf{a}}}=E[\underline{\mathbf{a}} \cdot \underline{\mathbf{a}}^H]$ | Correlation matrix of the vector $\underline{\mathbf{a}}$ |
| var $[\cdot]$ | Variance of the argument |
| $\mathbf{vec}(\cdot)$ | Operator which converts a matrix to a vector |
| $\log(\cdot)$ | logarithm value |
| $\odot$ | Hadamard product |
| $\|\cdot\|_2$ | Euclidean norm |
| $\cdot$ | Product operator |
| $e^{j\underline{\mathbf{x}}}$ | Column vector which contains the exponential of $1j \cdot \underline{\mathbf{x}}$ |
| $\otimes$ | Circular convolution |
| $p(r/s)$ | Channel likelihood function |
| $\underset{x \in C}{\operatorname{argmin}}(\cdot)$ | Value of $x \in C$ which minimizes the argument |

# Part I

# 6G Motivations and Challenges

CHAPTER 1

# Introduction

## Contents

## 1.1 Introduction to 6G visions

For many years now, communication technologies have been evolving at a rate of about one every decade. This evolution generally occurs to meet certain needs useful to mankind and/or sometimes for reasons of sovereignty. It is generally accompanied by an increase in performance, offering new services and applications. For this reason, a new communication technology named 6G is planned for 2030. This future communication technology is expected to provide better connections for people and things. Thereby, ongoing evolution of initiated scenarios in Fifth Generation (5G) such as AI and sensing are envisaged to be two new usage scenarios in 6G [2]. Different fundamental technology pillars will shape the 6G [1,3]:

- **native AI:** One of the main goals of 6G is to support AI in every aspect. It is planned for AI to be both a service and a fundamental part of the 6G communication systems. 6G will be like a smart system that blends communication, information and data technologies to support various AI applications like protecting sensitive information.
- **networked sensing:** In the future, 6G technology will have better sensing abilities in its network. 6G systems will both sense with wireless signals and communicate. This means the communication system can also work like a sensor, helping us understand the physical world by studying how radio waves travel and bounce. This will lead to new and useful services such as digital twin.
- **substainability:** The central demand and ultimate objective in the design of both network infrastructure and user devices in the context of 6G technology is to ensure its continued existence and sustainable growth. As we progress toward utilizing progressively higher frequency bands, addressing the significant challenge posed by diminished PA efficiency becomes a key concern.
- **extreme connectivity:** Fig. 1.1 illustrates the key performance indicators expected for 6G. It will offer super-fast wireless connections and will provide really high speeds, achieving a peak data rate of 1 Tbit/s with 10 to 100 Gbit/s on average. The latency is expected to be super short, and there will be more connections than 5G. In addition, it can locate things and will be very reliable. All these improvements will not only make amazing services for people but also helpful for industries to become more digital and productive.

Thus, 6G will require high data throughput. In line with the Shannon-Hartley theorem, channel capacity is characterized as the highest achievable information transmission rate while maintaining a low error rate. The Shannon-Hartley theorem [4] considering a channel impaired by Gaussian noise is given by

$$R < C = B_W \log\left(1 + \frac{P_r}{P_n}\right) = B_W \log\left(1 + \mathrm{SNR}\right), \tag{1.1}$$

where $R$ is the information rate in bit/s, $C$ the channel capacity in bit/s, $B_W$ the system bandwidth in Hz and $P_r$ the power of the received signal. The noise power is denoted by $P_n = N_0 B$, with $N_0$ representing the spectral density of the noise. One can notice the channel capacity is increasing linearly with the bandwidth and with the SNR (log). According to the latter equation, three approaches are possible to increase the data rate:

- Enhancing the data transmission rate of wireless systems $R$ to approach the channel capacity. This can be possible through the employment of capacity-achieving channel codes like Low Density Parity Check (LDPC) or polar codes, or through the utilization of

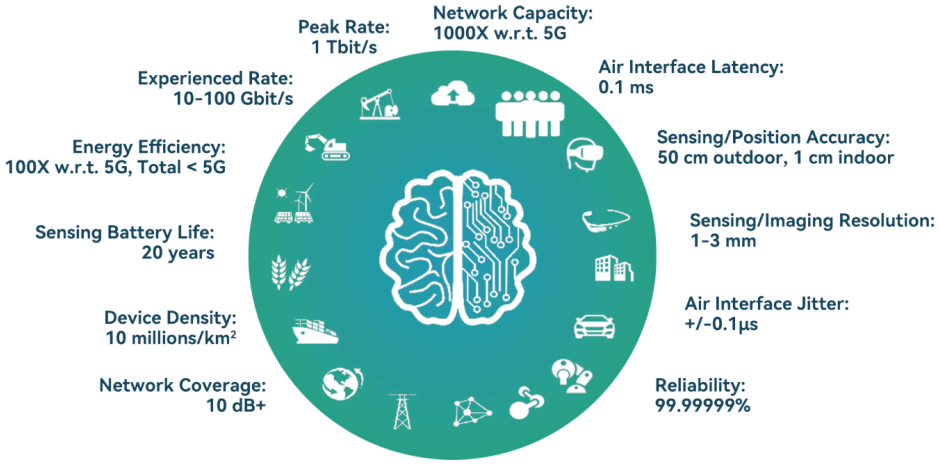


Figure 1.1: Key Performance Indicators for the future 6G technology [1].

higher order modulations. However, it's noteworthy that communication algorithms in the literature have already reached a level of performance remarkably proximate to the channel capacity.

- Increasing channel capacity via two principal approaches: boosting the SNR or utilizing a wider bandwidth $B_W$. Concerning SNR, it escalates with the amplification of transmitted signal power. Nonetheless, real-world systems impose restrictions and limitations on the increase of transmitted power. Hence, the most effective strategy for enhancing communication throughput involves the harness of broader frequency bands.
- Considering spatial multiplexing by using multi antenna systems such as MIMO and massive MIMO. However, this approach imposes constraints on complexity of the transceiver.

## 1.2 Sub-THz spectrum: A key solution for increasing the data throughput

As previously emphasized, exploiting wider frequency bands represents the most effective approach to enhance the data throughput. Indeed, the frequency bands of sub-6GHz spectrum are both costly and highly sought after for their excellent signal propagation characteristics [5]. Furthermore, in some cases, it is not possible to extend frequency bands due to the limitations of available bands in the sub-6GHz spectrum. Fortunately, advancements in semiconductor technologies now enable us to contemplate Radio Frequency (RF) communication systems operating at higher carrier frequencies, particularly in the millimeter-Wave (mmWave) range spanning from 30 to 52.6 GHz. Envisioning the expected peak data rate of 1 Tbit/s in 6G communication systems, the sub-THz bands, ranging from 100 to 300 GHz, emerge as a pivotal solution due to the extensive untapped frequency resources they offer as depicted in Fig. 1.2. However, transmitting in the sub-THz spectrum presents certain challenges, including the substantial attenuation of electromagnetic waves, analog-to-digital conversions, and PN generated by oscillators.

## 1.3 Sub-THz spectrum challenges

In spite of allowing large frequency bands availability, the sub-THz spectrum presents the following propagation and technological constraints.

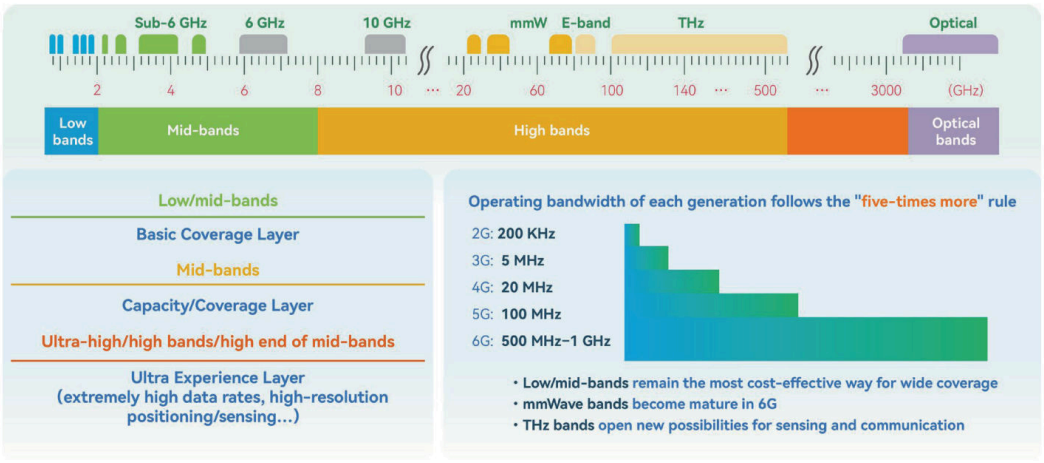


Figure 1.2: Spectrums and bandwidths per generation [1].

### 1.3.1 Transmission circumstances

As aforementioned, sub-THz communications suffer from severe propagation losses due to their high carrier frequencies. The expression of the received signal power $P_r$ is given by the Friis' formula as follows

$$P_r = \frac{G_A^{TX} \cdot G_A^{RX}}{L_p} P_t, \quad \text{s.t} \quad L_p = \left(\frac{4\pi F_c d}{c}\right)^2 \tag{1.2}$$

where $P_t$ is the power of the transmitted signal. The terms $G_A^{TX}$ and $G_A^{RX}$ denote the gains of the transmit and receive antennas; and $L_p$ the free-space path loss. In detail, $F_c$ is the carrier frequency, $d$ the propagation distance and $c$ the speed of light. In equation (1.2), it is clear that as the carrier frequency goes up, the free-space path loss ($L_p$) increases significantly. To tackle this issue, we need high-gain antennas that focus the signal. This means that using radio channels in sub-THz bands is quite different from what we are used to in the usual mmWave systems. The directional antenna limits the number of signal bounces, making the channel has just one primary path. High-frequency bands do not handle signal reflections, scattering, and penetration as well as lower frequencies, resulting in fewer and weaker signal bounces or "multi-path". Because of these factors, we often have what is called Line-of-Sight (LoS) channels, meaning the signal travels directly from the transmitter to the receiver without bouncing around a lot. Experiments [6–9] confirm that radio channels in sub-THz frequencies are mainly LoS channels. As a result, we can describe these channels as frequency flat and use a model with just one main signal path.

### 1.3.2 Analog-to-digital conversion and PA efficiency

The use of many gigahertz of frequency bands allows for high throughputs. However, this also creates a significant challenge for Analog-to-Digital Converter (ADC) to perform the conversion fastly. Even with the best current technology of ADC, it is difficult for smaller, embedded devices to handle such fast sampling rates [10]. Moreover, a recent examination of the energy usage of RF front-end transceivers has pinpointed the PA as the most energy-intensive element within the transmitter [11]. Consequently, there is a strong inclination to enable PAs to function at their peak efficiency *i.e.* with the smallest possible backoff.

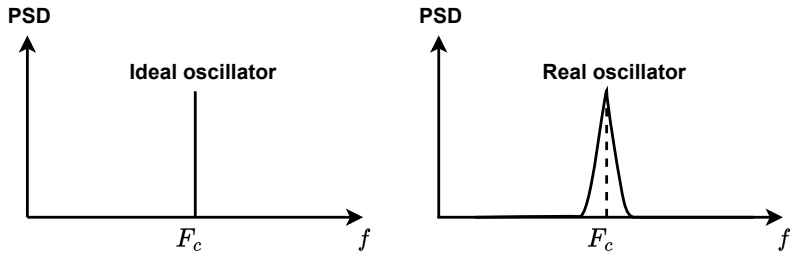


Figure 1.3: Power Spectral Density (PSD) of Ideal vs. Real oscillator response

### 1.3.3 PN impairments

One of the big challenges when it comes to setting up communication in sub-THz bands is dealing with a component called oscillators. They are responsible of the frequency translations between baseband and passband. The problem is, these RF oscillators present some phase instability when the carrier frequency rises to the high mmWave and sub-THz bands, specifically something called PN as highlighted in Fig. 1.3 by the real oscillator response. The higher the carrier frequency, the worse this PN problem gets. The complex output $v$ of an oscillator with carrier frequency $F_c$ is defined by

$$v(t) = (1 + \varepsilon(t))\, e^{j2\pi(F_c+\varsigma)t+j\phi(t)}, \tag{1.3}$$

where $\varepsilon$, $\varsigma$ and $\phi$ denote respectively the amplitude noise, the Carrier Frequency Offset (CFO) and the PN. For communications in the regular sub-6GHz bands, PN is not much of an issue because the oscillators are quite stable, and other issues are usually more significant. But when you are working with digital communication systems in sub-THz bands, the PN from the oscillators becomes one of the major problems [12, 13], and it can seriously limit how well the system works and how fast it can transfer the data with a high level of reliability [14].

As one can notice in (1.3), PN is not the only phase alteration generated by the oscillator. We also have the so-called CFO which is caused by the unsynchronization of the carrier frequency between the oscillator at the transmitter and the receiver one. Generally, reference signals are inserted to track and compensate the CFO in order to reduce its effects.

## 1.4 PHY Layer

To summarize, sub-THz bands appear as a potential solution for the increase of communication data throughput. But, technological constraints encountered in those bands do not allow to reutilize existing wireless communication systems. As an example, PN leads to performance degradation caused by detection errors in PHY layer. It is therefore necessary to develop techniques to improve the performance of wireless communication systems. Research in this area has already been presented for SC systems. [15, 16] propose few optimized modulation schemes and optimum detection criterion assuming the presence of an uncorrelated GPN.

Similarly, given that 5G systems use MC waveforms such as OFDM and DFT-s-OFDM, ongoing research aims to adapt them to suit the characteristics of sub-THz frequencies. OFDM is a widely used waveform standardized in Fourth Generation (4G) and 5G-NR for wireless systems [17]. 5G-NR introduced the concept of numerology [18] which consists in increasing the Inter-Carrier Spacing (ICS) to cope with the mobility and to take advantage of mmWave spectrums. The ICS is defined by

$$\Delta_f = 15 \times 2^{\mu}\ [\text{kHz}], \tag{1.4}$$

Table 1.1: Numerology scaling framework according to 5G-NR.

| | $\mu$ | Intercarrier Spacing [kHz] | $N_f$ | Sampling Frequency [MHz] | 80% of Bandwidth [MHz] |
|---|---|---|---|---|---|
| 5G-NR | 0 | 15 | 4096 | 61.44 | 49.15 |
| | 1 | 30 | 4096 | 122.88 | 98.30 |
| | 2 | 60 | 4096 | 245.76 | 196.61 |
| | 3 | 120 | 4096 | 491.52 | 393.22 |
| | 4 | 240 | 4096 | 983.04 | 786.43 |
| | 5 | 480 | 4096 | 1966.08 | 1572.86 |
| | 6 | 960 | 4096 | 3932.16 | 3145.73 |
| Option 1 | 7 | 1920 | 4096 | 7864.32 | 6291.46 |
| | 8 | 3840 | 4096 | 15728.64 | 12582.91 |
| | 9 | 7680 | 4096 | 31457.28 | 25165.82 |
| | 10 | 15360 | 4096 | 62914.56 | 50331.65 |
| Option 2 | 7 | 1920 | 2048 | 3932.16 | 3145.73 |
| | 8 | 3840 | 1024 | 3932.16 | 3145.73 |
| | 9 | 7680 | 512 | 3932.16 | 3145.73 |
| | 10 | 15360 | 256 | 3932.16 | 3145.73 |

where $\mu$ is the numerology. This technique maintains compatibility with the 3GPP framework in terms of channel coding, synchronization, channel estimation, physical channel assignment, etc. Despite the LoS propagation and the low frequency selectivity of the channel in the sub-THz bands (by considering high gain and highly directive antennas [6]), OFDM-based waveforms could be particularly interesting for dealing with frequency-dependent RF degradation (in-band attenuation), carrier-based digital beamforming in combination with a phased array and OFDM Access (OFDMA). Nevertheless, the Peak-to-Average Power Ratio (PAPR) of OFDM is high, which puts a lot of constraints on the PA [19].

As the efficiency of high frequency PAs is low, it seems essential to have a low PAPR waveform. If the advantages of OFDM have to be maintained, the use of DFT-s-OFDM seems to be a good compromise. As OFDM, the DFT-s-OFDM is standardized in 4G and 5G-NR in uplink transmissions. By performing a full band Fourier transform, the signal envelope of a DFT-s-OFDM waveform tends towards the behavior of a single-carrier waveform and thus, leads to a low PAPR compared to OFDM, while allowing OFDM compatible processing [20]. However, the penalty is an increase of complexity. To address the very wide frequency bands offered by sub-THz, several approaches can be considered. Firstly, by stretching the bandwidth, *i.e.* increasing the addressable spectrum by increasing the numerology [18]. As shown in Table 1.1, a numerology of 10 allows 50 GHz of spectrum to be addressed, while considering the 4096 Fast Fourier Transform (FFT) size defined in 5G-NR. However, this configuration seems difficult to

realize in practice as it requires fast conversion systems that are far beyond the current limits [10]. A second option is to address the entire bandwidth by carrier aggregation. In this case, the constraints on conversion are limited at the cost of duplicating the components. To make the waveforms robust to PN, it is necessary to have large ICS, and therefore a high numerology. When the PN-induced distortions become critical and limit the system performance, "Option 2" of Table 1.1, inspired from [21], could be interesting. This option consists in increasing the numerology by controlling the sampling frequency at the cost of reducing the number of addressable Resource block (RB).

## 1.5 Objective of this thesis

As a consequence, the main goal of this thesis is to evaluate how 5G-NR MC systems can be adapted to sub-THz frequencies in terms of PN impairments. To do so, we will consider two types of PN which are: correlated and uncorrelated PN. Then, we will **design PN cancellation algorithms for MC communication systems considering sub-THz frequencies**.

## 1.6 Thesis outline and Contributions

In this section, we present the structure of this thesis report and, at the same time, a brief summary of the contents of each chapter presented in this work. To help readers follow the work carried out during this thesis, this report is divided into several parts, each containing at least one chapter.

### Part II: System modeling

This part is devoted to presenting the system model that will be considered in this report. From the characterization of the PN model to the presentation of its impact on various communication systems.

### Chapter 2

In this chapter, we present the origin of PN and the different models currently used in the literature, namely the 3GPP model and the Gaussian model. In addition to these two models, we present a new PN model obtained from measurements collected on a CMOS-based transceiver operating in the D-band. We then derive received signal expressions for different communication systems impacted by PN.

### Part III: Optimization of Receivers based on 5G-NR Multicarrier waveforms - Correlated PN

We consider the impact of a correlated PN upon MC systems. PN estimation and compensation algorithms are proposed and those presented in the state-of-the-art are also described. A comparison between both proposed and literature algorithms is made to validate the effectiveness of the proposed algorithms.

### Chapter 3

In this chapter, we tackle the problem of PN on MC systems, in particular DFT-s-OFDM systems. To this end, we propose a PN estimation and compensation algorithm based on knowledge of the PN statistics. It is performed in the frequency-domain at the receiver. A comparative study with other PN estimation algorithms is carried out to highlight the efficiency of the proposed algorithm. For instance, the proposed algorithm achieves a high SE. The technical novelties highlighted in this chapter have been disseminated in the following contributions.

[C2] **Y. Bello**, J-B. Doré and D. Demmer, *"DFT-s-OFDM for sub-THz Transmission – Tracking and Compensation of Phase Noise,"* In Proc. IEEE Consumer Communications & Networking Conference (CCNC), Nevada, United States of America, pages 297–300, 2023.

[C3] **Y. Bello**, D. Demmer, A. Hamani, A. Siligaris, C. Dehos, N. Cassiau, J-B. Doré and J.L. González-Jiménez, *"Performance Assessment of a 5GNR D-Band Transceiver with Phase Noise Impairments,"* In Proc. Joint European Conference on Networks and Communications & 6G SUMMIT (EuCNC/6G SUMMIT), Goteborg, Sweden, pages 246-251, 2023.

[C4] **Y. Bello**, J-B. Doré and D. Demmer, *"Wiener Interpolation Filter for Phase Noise Estimation in sub-THz Transmission,"* In Proc. IEEE Vehicular Technology Conference (VTC2023-Spring), Florence, Italy, pages 1-5, 2023.

### Chapter 4

The proposed algorithm in the previous chapter for DFT-s-OFDM systems is not directly applicable to OFDM systems. The efficiency highlighted by this algorithm led us to consider an algorithm based on the same principle of using the PN statistics. In the framework of OFDM, we propose a new algorithm compensating the PN in time-domain. By doing so, it reduces the PN-induced effects in the frequency-domain. In addition, a frequency-selective channel is considered to model the propagation environment. The technical content presented in this chapter has been validated by the following contributions.

[C5] **Y. Bello**, J-B. Doré and D. Demmer, *"Time domain Phase Noise Mitigation in OFDM Systems for Sub-THz Bands,"* In Proc. IEEE Global Communications Conference (GLOBECOM), Kuala Lumpur, Malaysia, 2023.

[J2] **Y. Bello**, J-B. Doré and David Demmer, *"Low Complexity Time Domain Filtering of Phase Noise in OFDM Systems,"* **submitted before**, 2023.

## Part IV: Optimization of Receivers based on 5G-NR Multicarrier waveforms - Uncorrelated PN

This section deals with the case of uncorrelated PN on MC systems. Different Gaussian PN regimes are considered, and a specific behavior for the DFT-s-OFDM waveform is presented.

### Chapter 5

In the previous chapters, the PN considered has a correlated nature which allows it to be tracked and estimated. However, when the PN has an uncorrelated nature, it becomes impossible to track it. Consequently, new signal processing techniques are needed to improve the performance of MC systems. We have addressed this issue in this chapter by proposing an optimal detector adapted to the DFT-s-OFDM systems and for a strong Gaussian PN regime. The technical novelties presented in this chapter have been validated by the following contributions.

[C7] **Y. Bello**, D. Demmer and J-B. Doré, *"Analyse des effets du bruit de phase Gaussien sur un signal DFT-s-OFDM,"* Colloque Gretsi, Grenoble, France, 2023.

[J1] **Y. Bello**, J-B. Doré and David Demmer, *"Analysis of Gaussian Phase Noise Effects in DFT-s-OFDM systems for sub-THz Transmissions,"* **submitted**, 2023.

### Chapter 6

The final chapter concludes this thesis report by taking stock of the work that has been presented and proposing future perspectives.

# Part II

# System modeling

CHAPTER 2

# Phase Noise Models and Effects

## Contents

## 2.1 Introduction

In order to achieve data rates exceeding 1 Tbit/s, conventional coherent architectures are integrated with communication schemes that possess high SE. This integration imposes several limitations on the design of RF components, particularly at the oscillator level. The complex output $v$ of an oscillator with carrier frequency $F_c$ is defined by

$$v(t) = (1 + \varepsilon(t))\, e^{j2\pi(F_c+\varsigma)t + j\phi(t)}, \tag{2.1}$$

where $\varepsilon$, $\varsigma$ and $\phi$ denote respectively the amplitude noise, the CFO and the PN. The CFO often occurs when the Local Oscillator (LO) signal for down-conversion in the receiver does not synchronize with the carrier signal contained in the received signal. This phenomenon is caused by a frequency mismatch in the transmitter and the receiver oscillators. The application of an output limiter to the oscillator effectively reduces amplitude noise $\varepsilon$ and is assessed to have minimal significance, as indicated by [22]. Regarding the CFO, reference signals are inserted to ensure its compensation. In our study, we assume the transmitter and receiver are synchronized.

The use of high-frequency oscillators in sub-THz systems introduces significant challenges related to PN. In coherent systems, PN has a fundamental impact inducing a performance degradation caused by detection errors. Therefore, it is vital to address the choice of the PN model when designing accurate PN compensation algorithms. In this chapter, we propose to define the basis for modeling the system we are going to study. Three PN models will be considered: an uncorrelated GPN, a Wiener PN proposed by the 3GPP and a measured PN based on the D-Band CMOS transceiver designed at CEA-Leti. The PN effects and their characterization will also be analyzed. In addition, the waveforms considered in this thesis will be presented, to give readers the concepts and notations that will be used later.

## 2.2 Phase Noise Models

### 2.2.1 Gaussian Phase Noise

The PN generated by the oscillator is generally modeled by the sum of two processes as depicted in Fig. 2.1: a Wiener process ($1/f^2$) representing the PN correlated part and the Gaussian process representing the uncorrelated part. Research in [23] has demonstrated that the performance of wide-band systems are considerably more affected by the uncorrelated PN rather than the correlated one. This finding inspires authors in [24] to assess the effectiveness of an uncorrelated Gaussian PN model against the commonly utilized correlated model for mm-Wave systems, which combines Wiener PN and Gaussian PN. The Wiener PN may be modeled by

$$\phi[\tau] = \phi_W[\tau] + \phi_G[\tau] \tag{2.2}$$

where $\phi_G[\tau] \backsim \mathcal{N}(0, \sigma^2_{\phi_G})$ represents the GPN. The correlated part is defined by

$$\phi_W[\tau] = \phi_W[\tau - 1] + \delta\phi_W[\tau], \tag{2.3}$$

where $\delta\phi_W[\tau] \backsim \mathcal{N}(0, \sigma^2_{\phi_W})$. To define the different PN variances, the authors in [24] considers a simplified model of the PSD of PN generated by a 200 GHz oscillator [25] as depicted in Fig. 2.1a. According to the simplified model presented in Fig. 2.1b, the variances are given by

$$\sigma^2_{\phi_G} = K_0/T_s \qquad \text{and} \qquad \sigma^2_{\phi_W} = 4\pi^2 K_2 T_s, \tag{2.4}$$

where $K_0$ and $K_2$ denote respectively the spectrum density of the GPN and of the correlated PN. The term $T_s$ is the sampling period and $f_c$ represents the corner frequency defined by

$$f_c^2 = K_2/K_0. \tag{2.5}$$

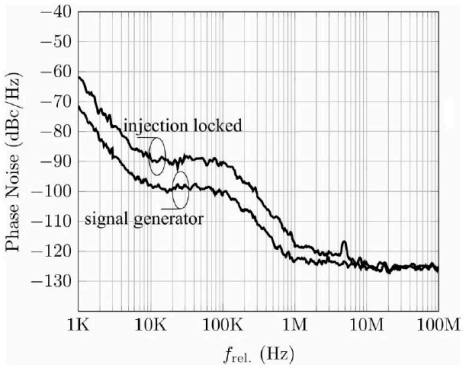


(a) PSD of the considered 200 GHz oscillator.

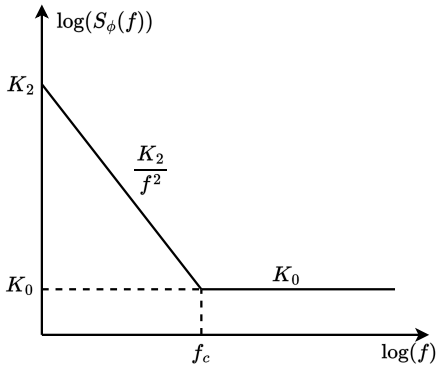


(b) PSD of the considered correlated PN model.

Figure 2.1: PSD Models

Then, by using the Pearson's $\chi^2$ goodness of fit test, [24] first confirms that the uncorrelated GPN model is accurate if the corner frequency remains small compared to the system bandwidth (*i.e.* $f_c \ll B_W$). This condition is likely to be validated in sub-THz and THz communications where it will be possible to increase the system bandwidth up to 10 GHz and even more. Additionally, they analytically express a PN model selection criterion by using the Log-Likelihood Ratio (LLR) of the models. They show that PN is accurately represented by an uncorrelated GPN if

$$N_b \cdot f_c^2 \cdot T_s^2 \leq \frac{\ln(2)}{2\pi^2} \tag{2.6}$$

where $N_b$ denotes the number of symbols within a frame. Consequently, according to the work in [24], an uncorrelated GPN model defined by

$$\phi[\tau] \backsim \mathcal{N}(0, \sigma_\phi^2), \tag{2.7}$$

may accurately model the oscillator PN for sub-THz and THz communications. GPN model is already exploited in [15, 16] for optimizing constellations in PN channels, in [26] for optimal demodulation, and in [27] to compare performance of digital modulations.

### 2.2.2 Wiener Phase Noise

It is suggested to model the PN as a Gaussian process for sub-THz and THz transmissions when condition (2.6) is satisfied. Further details are often discussed in the literature. However, several PN models have been introduced in the literature: Non-linear [28], Tikhonov [29] and Wiener [23]. The Wiener PN is generally a correlated PN with a partial uncorrelated contribution. In order to standardize a unique PN model which is more accurated with real measurements, the 3GPP proposed two different PN models [30] based:

- **upon measurements made on a prototype CMOS device with a larger PLL**: In this case, the 3GPP gives the expression of the PSD of PN based on a multi-pole/zero model as follows:

$$S(f) = PSD0 \frac{\prod_{b=1}^{B} 1 + \left(\frac{f}{f_{z,b}}\right)^{\alpha_{z,b}}}{\prod_{q=1}^{Q} 1 + \left(\frac{f}{f_{p,q}}\right)^{\alpha_{p,q}}}. \tag{2.8}$$

  The PSD of the suggested PN model is illustrated in Fig. 2.2 as "Model 1" and takes into account the parameters provided in Table 2.1 for a 29.55 GHz carrier frequency. To obtain

Table 2.1: Parameters for PLL PN model operating at 29.55 GHz valid from 100 Hz and upwards

| Model 1 | | | | |
|---|---|---|---|---|
| $PSD0$ | 1585 (32 dB) | | | |
| $b, q$ | $f_{z,b}$ | $\alpha_{z,b}$ | $f_{p,q}$ | $\alpha_{p,q}$ |
| 1 | $3 \cdot 10^3$ | 2.37 | 1 | 3.3 |
| 2 | $550 \cdot 10^3$ | 2.7 | $1.6 \cdot 10^6$ | 3.3 |
| 3 | $280 \cdot 10^6$ | 2.53 | $30 \cdot 10^6$ | 1 |

Table 2.2: Parameters for proposed PN models at UE and BS

| | Model 2, UE, Loop $B_W$ = 187 kHz | | | | Model 2, BS, Loop $B_W$ = 112 kHz | | | |
|---|---|---|---|---|---|---|---|---|
| | $Ref$ | $PLL$ | $VCO\_v2$ | $VCO\_v3$ | $Ref$ | $PLL$ | $VCO\_v2$ | $VCO\_v3$ |
| FOM | −215 | −240 | −175 | −130 | −240 | −245 | −187 | −130 |
| $f_z$ | $Inf$ | 1e4 | $50.3 \cdot 10^6$ | $Inf$ | $Inf$ | 1e4 | $8 \cdot 10^6$ | $Inf$ |
| $P$ (mW) | 10 | 20 | 20 | 20 | 10 | 20 | 50 | 50 |
| $k$ | 2 | 1 | 2 | 3 | 2 | 1 | 2 | 3 |

the PSD at a different carrier frequency $F_c$, we add the shift term to the expression (2.8) as follows

$$S_{F_c}(f) = S(f) + 20 \log_{10}\left(\frac{F_c}{29.55}\right). \tag{2.9}$$

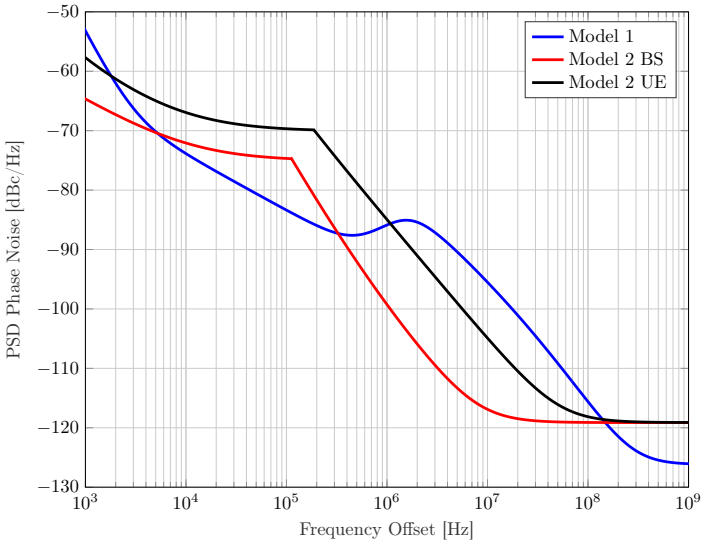


Figure 2.2: Proposed 3GPP PN Models for a 140 GHz carrier frequency

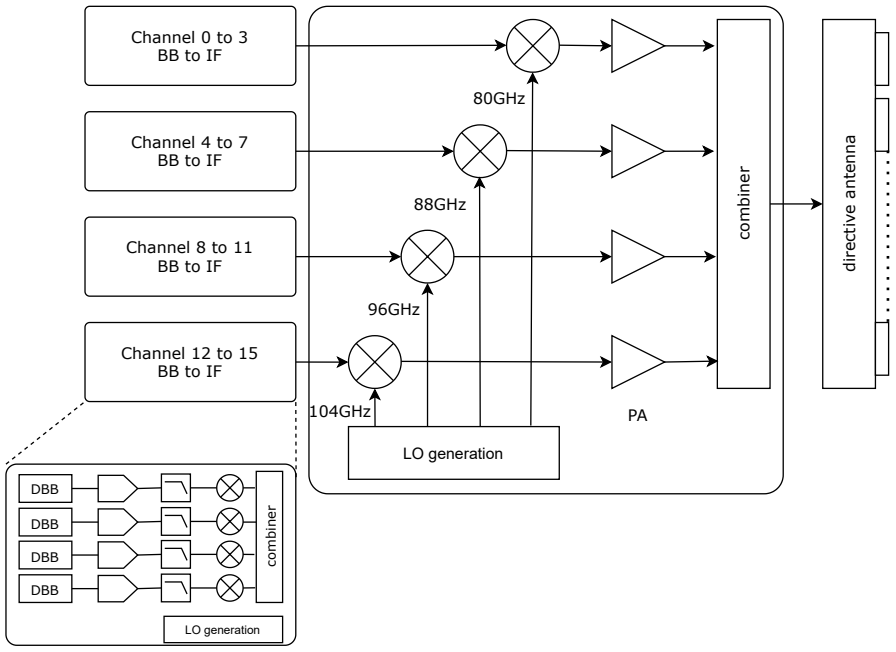


Figure 2.3: D-Band Transceiver architecture

- **on recent research which considers CMOS for the UE and Gallium Arsenide (GaAs) for the BS assuming a lower PLL bandwidth**: This case is considered as the appropriate PN for mmWave applications. The choice of the CMOS components at the UE relies on the cost and power constraint. The advantage of considering the GaAs is the lower PN level generation. However, it is expensive and power-consuming but, the performance gains may outweight the power consumption and cost ratio. The PSD of the PN is characterized by:

$$S_{PN}(f) = \begin{cases} S_{Ref}(f) + S_{PLL}(f), & \text{when } f \leq \text{ Loop } B_W \\ S_{VCO\_v2}(f) + S_{VCO\_v3}(f), & \text{when } f > \text{ Loop } B_W \end{cases} \tag{2.10}$$

where

$$\begin{cases} S_{Ref/PLL/VCO\_v2/VCO\_v3}(f) = PSD0 \cdot \left[\frac{1+(f/f_z)^k}{1+f^k}\right] \text{ (dB)} \\ PSD0 = \text{FOM} + 20\log(F_c) - 10\log\left(\frac{P}{1mW}\right) \text{ (dB)}\cdot \end{cases} \tag{2.11}$$

FOM represents the figure of merit, $F_c$ is the carrier frequency and $P$ is the consumed power. The PSD of the proposed PN models at both BS and UE are depicted in Fig. 2.2 as "Model 2" considering parameters in Table 2.2.

These presented PN models are intensely considered in the state-of-the-art especially the second one which is commonly extended to model the generated PN for sub-THz transmissions.

### 2.2.3 Measured Phase Noise

In this thesis, we also consider a correlated PN model based on real measurements upon a D-Band CMOS-based transceiver designed at CEA-Leti. Once the system illustrated in Fig. 2.3 is fabricated, PN measurements can be conducted using a spectrum analyzer. The LO generation process remains the same for both the transmitter and receiver. The Intermediate Frequency (IF)

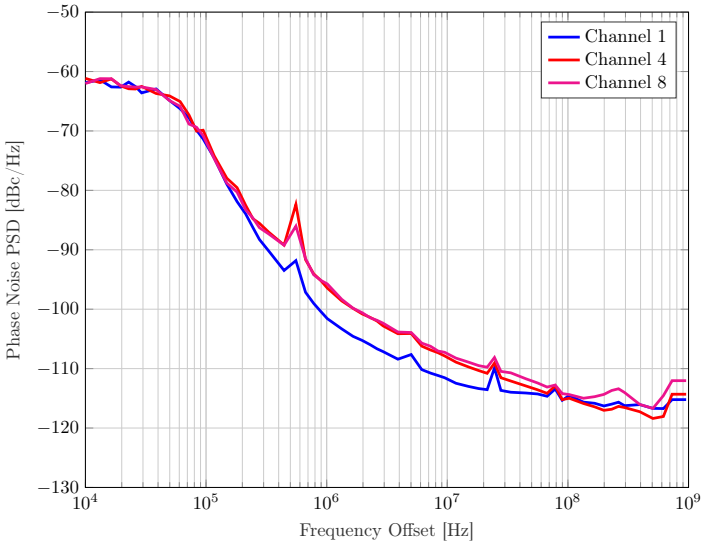


Figure 2.4: Measured PSD for channels 1, 4 and 8 for a 140 GHz carrier frequency.

LO generates a 2.16 GHz reference signal through a PLL. Additionally, a second LO produces a 4.32 GHz clock by doubling the original 2.16 GHz LO signal. The outcomes of these measurements are displayed in Fig. 2.4 for channels 1, 4, and 8. Fig. 2.5 depicts the measured PN for "channel 1" along with the generic model standardized by the 3GPP [30]. It is important to mention that in 3GPP context, the PN emitted by a BS differs from the UE one. Due to integration and cost constraints, UEs are designed with lower-quality and consequently noisier LOs. The attained performance is quite commendable, especially for a CMOS-based system. In the $1/f^2$ region, the PSD of the measured PN closely matches the 3GPP BS model (high-end). However, the noise floor is slightly higher with a measurement value of −115 dBc/Hz compared to the 3GPP BS value of −119 dBc/Hz. It is worth noting that the low-frequency (i.e. near-carrier)

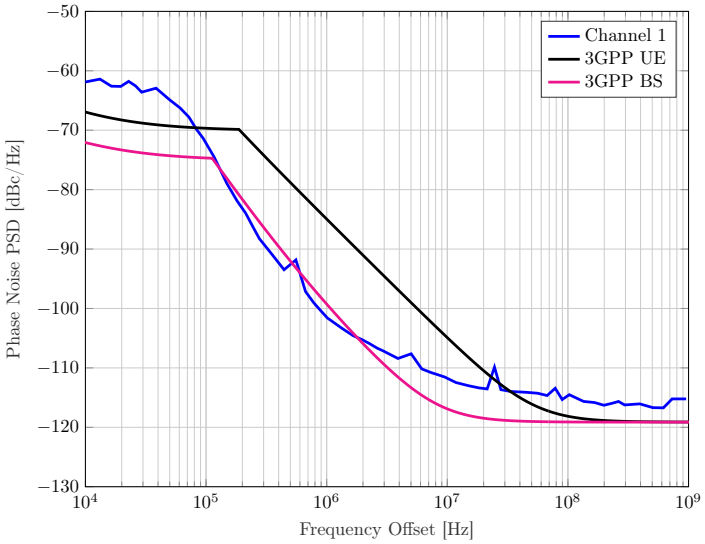


Figure 2.5: Measured PSD for channel 1 vs. 3GPP Models UE and BS for a 140 GHz carrier frequency.

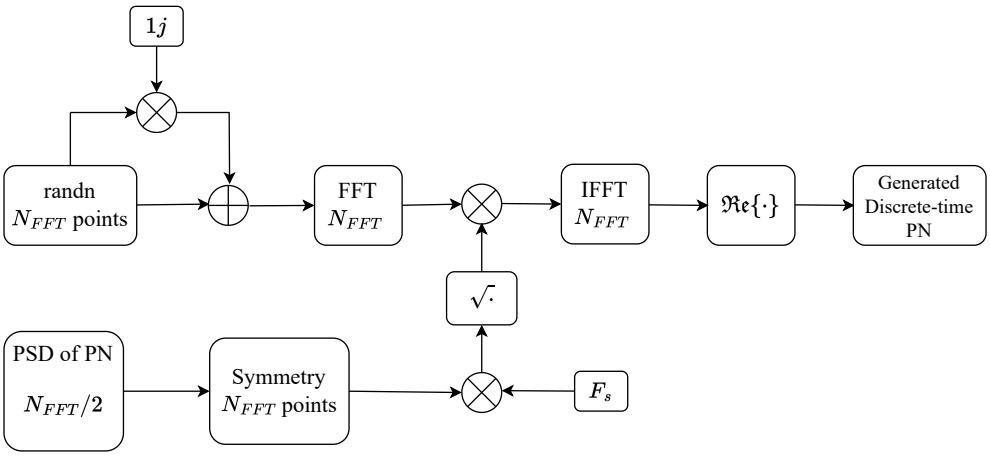


Figure 2.6: Discrete-time PN generation method.

contribution of the measured noise is higher than the expected value according to the 3GPP model.

The LO generation process involves a Voltage-Controlled Oscillator (VCO) that experiences periodic switching (on and off) influenced by the input signal, resulting in a Periodically Repeated Oscillations Train (PROT). This multi-harmonic signal is then fed into an Injection locked oscillator (ILO) that synchronizes with the desired harmonic, generating a continuous wave sinusoidal signal. The advantage of this programmable multiplication technique is the only requirement of a single fixed low-frequency reference to achieve LO generation for multiple channels simultaneously. As a result, this technique is exceptionally well suited for the concept of carrier aggregation. Furthermore, the notable aspect of the generated PN lies in the fact that it primarily originates from the low-frequency oscillator with only the multiplying impact:

$$\mathrm{PSD}_{LO} = \mathrm{PSD}_{in} + 20\log_{10}\left(\frac{f_{LO}}{f_{in}}\right), \tag{2.12}$$

where $\mathrm{PSD}_{LO}$ is the PSD of the PN at the output of the ILO at the carrier frequency $f_{LO}$. $\mathrm{PSD}_{in}$ is the PSD of the PN generated at the low frequency ocillator considering $f_{in}$. The PN resulting from the ILO operates in free-running mode, exhibiting a $1/f^2$ behavior and consequently leading to exceedingly low PN levels. This characteristic holds significant importance when dealing with upcoming sub-THz and THz frequency bands. For more in-depth information on the theoretical and implementation aspects, readers can find relevant details in references [31–33].

### 2.2.4 Phase Noise Generation Method

In order to propose advanced techniques for PN estimation and compensation, we need to generate properly the PN for numerical simulations. Thankfully, the GPN is easier to generate for performance assessment. In contrast for Wiener PN models, few generation methods are presented in the literature. On the one hand, the contributions [23] and [34] present techniques to approximate an analyical model of the discrete-time PN but, the accuracy of these methods depends on the shape of the PSD. On the other hand, [35] and [36] propose to generate directly PN by simple filtering of uncorrelated Gaussian noise with a filter representive of the PSD of PN. In this thesis, we generate the PN considering the method in [35] as depicted in Fig. 2.6. The generation steps are as follows:

- Generate linearly the PSD of PN up to half the sampling frequency ($F_s/2$) and using half of FFT points ($N_{FFT}/2$).

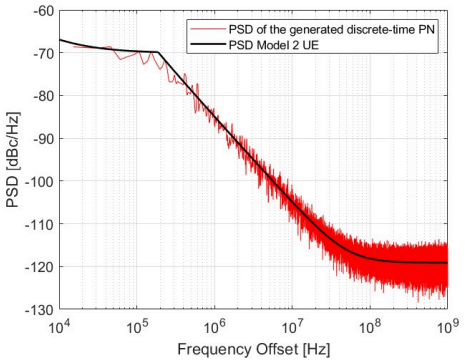


(a) PSD Model2 UE vs. PSD of the generated discrete-time PN.

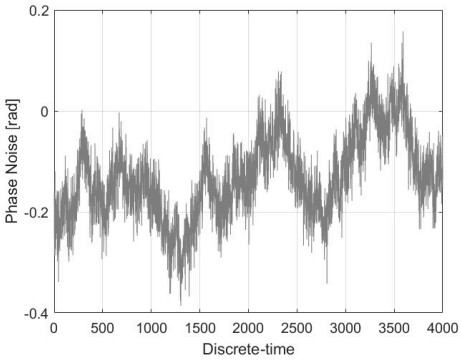


(b) Generated discrete-time PN.

Figure 2.7: Generation of the discrete-time PN at the carrier frequency of 140 GHz considering a sampling frequency $F_s = 2$ GHz.

- Symmetrize this PSD with respect to the frequency $F_s/2$ and obtain the PSD with $N_{FFT}$ length.
- Generate a complex Gaussian random process with a variance $\sigma^2 = 1$ with the same length as the PSD. Then, multiply it with the mask of the square root of the product between the PSD and the sampling frequency.
- Perform an Inverse Fast Fourier Transform (IFFT) of the latter and select the real part of the complex output.

Fig. 2.7b illustrates a discrete-time PN generated from the 3GPP Model 2 UE considering a carrier frequency of 140 GHz, a sampling frequency $F_s = 2$ GHz and using $N_{FFT} = 512000$ points. As shown in Fig. 2.7a, the generated discrete-time PN matches well with the measured PSD. This result allows us to validate the generated discrete-time PN for numerical analysis.

## 2.3 Phase Noise Effects on Waveforms

In this section, we will derive the expressions of the discrete-time received signal assuming SC and MC waveforms. For SC systems, we will consider the cases with and without pulse shaping filter. In order to explicitely highlight the effect of PN on these systems, we will consider the transmission of the signal through a frequency-flat channel (*i.e.* an Additive White Gaussian Noise (AWGN) channel). Moreover, we assume coherent communication systems impaired by PN with the receiver synchronized in time and frequency with the transmitter (*i.e.* without CFO). We denote $\mathbf{\Phi}_E$ as the diagonal matrix containing the $e^{j\underline{\phi}}$ on its diagonal where $\underline{\phi}$ is the sum of the applied PN at transmitter and receiver.

### 2.3.1 SC waveform

Considering a SC system transmitting through a frequency-flat channel with the presence of oscillator PN, the received signal without pulse shaping is expressed by

$$r[\tau] = s[\tau] \cdot e^{j\phi[\tau]} + n[\tau], \tag{2.13}$$

with $s[\tau] \in C$ is the transmitted signal, where $C$ denotes the constellation set of the chosen modulation scheme. The term $n[\tau] \backsim \mathbb{C}\mathcal{N}(0, \sigma_n^2)$ represents the thermal noise and $\phi[\tau]$ is the

PN. The term $\phi$ is the sum of the generated PN by the oscillators at the transmitter and receiver. The matrix form of the expression (2.13) is given by

$$\underline{\mathbf{r}} = \mathbf{\Phi}_E \underline{\mathbf{s}} + \underline{\mathbf{n}}. \tag{2.14}$$

For the case with presence of PN and pulse shaping filter, let us define $\underline{\mathbf{x}}$ as the signal after the pulse shaping filter at the transmitter. it is given by

$$\underline{\mathbf{x}} = \mathbf{G}_T \underline{\mathbf{s}}, \tag{2.15}$$

where $\underline{\mathbf{s}}$ and $\mathbf{G}_T$ denote respectively the information symbol frame and the pulse shaping matrix at the transmitter. The expression of the received signal after pulse shaping at receiver is given by

$$\begin{aligned} \underline{\mathbf{r}} &= \mathbf{G}_R \mathbf{\Phi}_E \underline{\mathbf{x}} + \mathbf{G}_R \underline{\mathbf{n}} \\ &= \mathbf{G}_R \mathbf{\Phi}_E \mathbf{G}_T \underline{\mathbf{s}} + \underline{\mathbf{w}}. \end{aligned} \tag{2.16}$$

The matrix $\mathbf{G}_R$ denotes the matching pulse shaping filter at receiver. If we assume a small angle approximation $e^{j\underline{\phi}} \simeq \underline{\mathbf{1}}_{N_b} + j\underline{\phi}$, the expression (2.16) becomes

$$\begin{aligned} \underline{\mathbf{r}} &= \mathbf{G}_R \mathbf{\Phi}_E \mathbf{G}_T \underline{\mathbf{s}} + \underline{\mathbf{w}}, \\ &\simeq \mathbf{G}_R \left( \mathbf{I}_{N_b} + j\mathbf{\Phi} \right) \mathbf{G}_T \underline{\mathbf{s}} + \underline{\mathbf{w}}, \\ &\simeq \mathbf{G}_R \mathbf{G}_T \underline{\mathbf{s}} + j\mathbf{G}_R \mathbf{\Phi} \mathbf{G}_T \underline{\mathbf{s}} + \underline{\mathbf{w}}, \end{aligned} \tag{2.17}$$

with $N_b$ the frame length and $\mathbf{\Phi}$ the diagonal matrix which contains the vector $\underline{\phi}$ on its diagonal. Considering $\mathbf{G}_R$ as the matching filter of the transmitter pulse shaping at the receiver side implies:

$$\mathbf{G}_R \mathbf{G}_T = \mathbf{I}_{N_b}. \tag{2.18}$$

Based on (2.18), the expression (2.17) becomes

$$\underline{\mathbf{r}} \simeq \underline{\mathbf{s}} + \underbrace{j\mathbf{G}_R \mathbf{\Phi} \mathbf{G}_T \underline{\mathbf{s}}}_{\text{ISI}} + \underline{\mathbf{w}}. \tag{2.19}$$

In (2.14), one can notice without the application of a pulse shaping, the presence of PN induces only the rotation of the transmitted signal. In contrast when a pulse shaping is considered, the PN causes Inter-Symbol Interference (ISI) as represented in (2.19) by the term $j\mathbf{G}_R \mathbf{\Phi} \mathbf{G}_T \underline{\mathbf{s}}$.

Regarding SC systems, [15] proposes few optimized modulation schemes such as spiral. Moreover, a modulation scheme named Polar QAM (PQAM) and an optimum detection criterion are proposed assuming the presence of an uncorrelated GPN [16].

### 2.3.2 OFDM waveform

OFDM is a MC waveform standardized in 4G and 5G-NR for wireless transmission. It consists in sending the signal simultaneously on many orthogonal subcarriers by using FFT [37]. It is suitable for frequency-selective channels and reduces the design complexity through equalizers in the frequency-domain [38] when the size of Cyclic Prefix (CP) is larger than the channel delay spread. However, the main drawbacks of OFDM is its Out-of-Band (OOB) emissions and high PAPR [19] which deteriorates the Energy Efficiency (EE) criterion.

According to the OFDM system model illustrated in Fig. 2.8, the expression of the received digital baseband signal is defined by

$$y[\tau] = x[\tau] \cdot e^{j\phi[\tau]} + n[\tau], \tag{2.20}$$

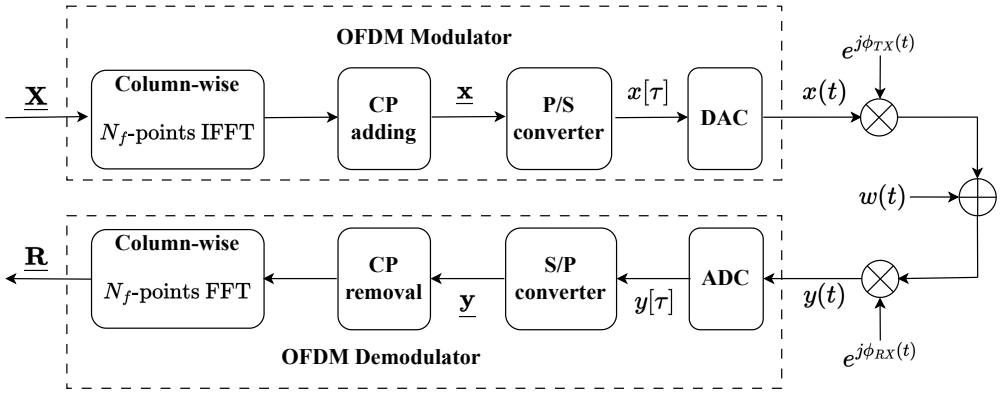


Figure 2.8: OFDM system model

where $\phi[\tau] = \phi_{TX}[\tau] + \phi_{RX}[\tau]$ represents the sum of the PN generated by the oscillators at the transmitter and receiver. The term $n[\tau] = w[\tau] \cdot e^{j\phi_{RX}[\tau]}$ with $w[\tau] \backsim \mathbb{CN}\left(0, \sigma_w^2\right)$ denotes the thermal noise. Furthermore, the expression of the frequency-domain received signal at the $k^{th}$ subcarrier on each symbol OFDM is defined by

$$R_k = X_k \underbrace{\frac{1}{N_f} \sum_{p=0}^{N_f-1} e^{j\phi_p}}_{\text{CPE}} + \underbrace{\frac{1}{N_f} \sum_{m=0, m\neq f}^{N_f-1} X_m \sum_{p=0}^{N_f-1} e^{j2\pi \frac{(m-f)}{N_f} p} e^{j\phi_p}}_{\text{ICI}} + \underbrace{\frac{1}{\sqrt{N_f}} \sum_{p=0}^{N_f-1} n_p e^{-j2\pi \frac{kp}{N_f}}}_{\text{Thermal noise}}, \tag{2.21}$$

where $X_k \in C$ is the frequency-domain transmitted signal. The term $\phi_p$ is the discrete-time PN and $n_p \backsim \mathbb{CN}\left(0, \sigma_n^2\right)$ represents the discrete-time thermal noise that we will assume circularly symmetric. One can notice the received signal is the sum of three terms:

- the first term is the product of the transmitted signal with the Common Phase Error (CPE) shared by all subcarriers
- the second term represents the ICI
- the last term is the FFT of the thermal noise.

Many contributions present the effects of PN in OFDM system [39–43]. In 5G-NR, PT-RS are introduced to allow the estimation and compensation of the PN effects at the receiver [42]. The ICI is the most binding effect in OFDM system (when the ICS is small). It requires sophisticated cancellation techniques [44] to enhance the OFDM system performance while the CPE effect can be easily compensated [45]. Regarding the considered channel model, the matrix form of the received OFDM symbol is given by

$$\begin{aligned} \underline{\mathbf{R}} &= \mathbf{F}_{N_f} \mathbf{\Phi}_E \mathbf{F}_{N_f}^H \underline{\mathbf{X}} + \mathbf{F}_{N_f} \underline{\mathbf{n}} \\ &= \mathbf{C}_{OFDM} \underline{\mathbf{X}} + \mathbf{F}_{N_f} \underline{\mathbf{n}}, \end{aligned} \tag{2.22}$$

where $\mathbf{C}_{OFDM} = \mathbf{F}_{N_f} \mathbf{\Phi}_E \mathbf{F}_{N_f}^H$ denotes the OFDM PN channel.

### 2.3.3 DFT-s-OFDM waveform

Due to the inefficiency of high-frequency PAs, achieving a low PAPR waveform becomes crucial. To preserve the benefits of OFDM, utilizing the DFT-s-OFDM appears to be a favorable

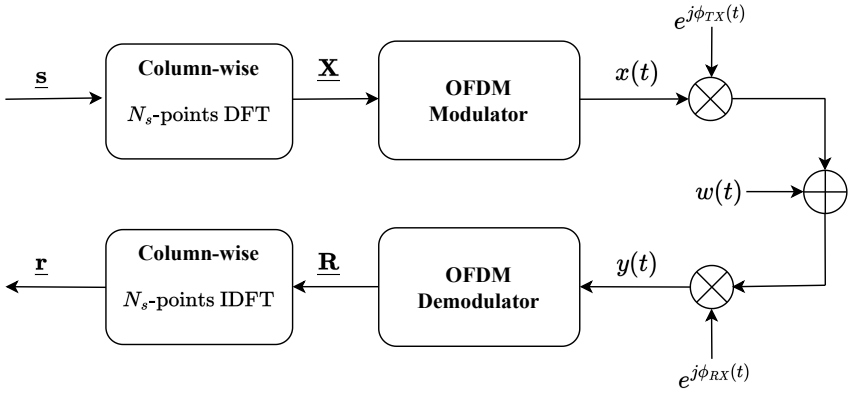


Figure 2.9: DFT-s-OFDM system model

compromise. Similar to OFDM, DFT-s-OFDM is standardized in 4G and 5G-NR especially in uplink transmissions [46] for energy consumption constraints at user level. The addition of an extra Discrete Fourier Transform (DFT) at the transmitter reduces fluctuations in the envelope of the transmitted signal, and hence its PAPR. At the receiver side, matched processing by adding an additional Inverse Discrete Fourier Transform (IDFT) is envisaged to enable reuse of OFDM baseband processing [21]. However, this comes at the cost of increased complexity. Based on the DFT-s-OFDM system model depicted in Fig. 2.9, the expression of the signal at the $m^{th}$ subcarrier after the DFT at the transmitter is:

$$X_m = \frac{1}{\sqrt{N_s}} \sum_{k=0}^{N_s-1} s_k e^{-j2\pi \frac{km}{N_s}}, \qquad \forall m = \{0, \cdots, N_s - 1\} \tag{2.23}$$

with $s_k \in C$ and $N_s$ is the DFT size block. Assuming $X_m = 0$ for $m > N_s$, the expression of the transmitted analog baseband signal is given by

$$x(t) = \frac{1}{\sqrt{N_f}} \sum_{f=0}^{N_f-1} X_f e^{j2\pi \frac{ft}{N}} = \frac{1}{\sqrt{N_s}} \frac{1}{\sqrt{N_f}} \sum_{f=0}^{N_s-1} \sum_{k=0}^{N_s-1} s_k e^{-j2\pi \frac{kf}{N_s}} e^{j2\pi \frac{ft}{N_f}}, \qquad \forall t = \{0, \cdots, N_f - 1\}. \tag{2.24}$$

The expression of the received signal before the OFDM demodulator is defined by

$$y(t) = x(t) \cdot e^{j\phi(t)} + n(t), \tag{2.25}$$

such that $n(t) = w(t) \cdot e^{j\phi_{RX}(t)}$ where $w(t) \backsim \mathbb{C}\mathcal{N}\left(0, \sigma_w^2\right)$ is the thermal noise. Finally, the expression of the received signal after IDFT at the $k^{th}$ subcarrier is expressed by

$$\begin{aligned} r_k = & \frac{1}{N_s} \frac{1}{N_f} \sum_{n=0}^{N_s-1} \sum_{f=0}^{N_s-1} \sum_{m=0}^{N_s-1} \sum_{p=0}^{N_f-1} s_n e^{j2\pi \frac{(m-f)}{N_f} p} e^{j2\pi \frac{kf-nm}{N_s}} e^{j\phi_p} \\ & + \frac{1}{\sqrt{N_s}} \frac{1}{\sqrt{N_f}} \sum_{f=0}^{N_s-1} \sum_{p=0}^{N_f-1} n_p e^{-j2\pi \frac{fp}{N_f}} e^{j2\pi \frac{kf}{N_s}}. \end{aligned} \tag{2.26}$$

We can rewrite (2.26) as follows

$$r_k = s_k \underbrace{\beta(k, N_s, N_f, \phi)}_{\text{SPE}} + \underbrace{\gamma(k, N_s, N_f, \phi)}_{\text{ICI}} + \underbrace{\eta(k, N_s, N_f)}_{\text{Thermal noise}}, \tag{2.27}$$

$$\begin{aligned}
\beta(k,N_s,N_f,\phi) &= \frac{1}{N_s}\frac{1}{N_f}\sum_{f=0}^{N_s-1}\sum_{m=0}^{N_s-1}\sum_{p=0}^{N_f-1} e^{j2\pi\frac{(m-f)}{N_f}p} e^{-j2\pi\frac{(m-f)}{N_s}k} e^{j\phi_p} \\
\gamma(k,N_s,N_f,\phi) &= \frac{1}{N_s}\frac{1}{N_f}\sum_{n=0,n\neq k}^{N_s-1} s_n \sum_{f=0}^{N_s-1}\sum_{m=0}^{N_s-1}\sum_{p=0}^{N_f-1} e^{j2\pi\frac{(m-f)}{N_f}p} e^{j2\pi\frac{kf-nm}{N_s}} e^{j\phi_p} \\
\eta(k,N_s,N_f) &= \frac{1}{\sqrt{N_s}}\frac{1}{\sqrt{N_f}}\sum_{f=0}^{N_s-1}\sum_{p=0}^{N_f-1} n_p e^{-j2\pi\frac{fp}{N_f}} e^{j2\pi\frac{kf}{N_s}}.
\end{aligned} \tag{2.29}$$

where the terms $\beta(k,N_s,N_f,\phi)$, $\gamma(k,N_s,N_f,\phi)$ and $\eta(k,N_s,N_f)$ are defined in (2.29). The term $\beta(k,N_s,N_f,\phi)$ is the term responsible of the transmitted symbols rotation denoted as the Subcarrier Phase Error (SPE). The term $\gamma(k,N_s,N_f,\phi)$ represents the ICI. The term $\eta(k,N_s,N_f)$ is the thermal noise after DFT-s-OFDM demodulator.

Extensive studies have been conducted on OFDM to highlight the improvement of the system performance using ICI mitigation techniques [44, 45, 47]. However, they are not directly applicable to the DFT-s-OFDM waveform. In [21], authors show that increasing the ICS up to 3840 kHz for DFT-s-OFDM systems, leads to the adaptation of 5G-NR waveform using sub-THz bands. Additionally, works were carried to enhance the channel estimation in the context of DFT-s-OFDM by proposing new PT-RS scheme. PN mitigation in DFT-s-OFDM is discussed in [43, 48, 49].

Regarding the considered channel model, the matrix form of the received DFT-s-OFDM symbol is given by

$$\begin{aligned}
\underline{\mathbf{r}} &= \mathbf{F}_{N_s}^H \mathbf{D}_{RX} \mathbf{F}_{N_f} \mathbf{\Phi}_E \mathbf{F}_{N_f}^H \mathbf{M}_{TX} \mathbf{F}_{N_s} \underline{\mathbf{s}} + \mathbf{F}_{N_s}^H \mathbf{D}_{RX} \mathbf{F}_{N_f} \underline{\mathbf{n}} \\
&= \mathbf{F}_{N_s}^H \mathbf{D}_{RX} \mathbf{C}_{OFDM} \mathbf{M}_{TX} \mathbf{F}_{N_s} \underline{\mathbf{s}} + \mathbf{F}_{N_s}^H \mathbf{D}_{RX} \mathbf{F}_{N_f} \underline{\mathbf{n}},
\end{aligned} \tag{2.28}$$

where $\mathbf{M}_{TX}$ is the $N_s$-to-$N_f$ mapping matrix and $\mathbf{D}_{RX}$ the $N_f$-to-$N_s$ demapping matrix.

**Remark 1.** *From (2.28) one can notice the expression of the DFT-s-OFDM PN channel as function of the OFDM one. This suggests that the PN effects in DFT-s-OFDM are different from those in OFDM.*

**Remark 2.** *We may find ourselves in the case of a SC with shaping filters* $\mathbf{G}_T = \mathbf{F}_{N_s}^H \mathbf{M}_{TX} \mathbf{F}_{N_f}$ *and* $\mathbf{G}_R = \mathbf{F}_{N_s}^H \mathbf{D}_{RX} \mathbf{F}_{N_f}$.

### 2.3.4 OTFS waveform

OTFS is a recent waveform representing the signal in a distinct domain known as the Delay-Doppler (DD) domain [50]. The uniqueness of OTFS lies in its resilience to high Doppler channels, in contrast to OFDM, where high Doppler effects disrupt the orthogonality between subcarriers. Moreover, the DD representation of the signal enables a clear depiction of all distortions induced by the channel, facilitating easier channel estimation for equalization purposes [51]. However, OTFS suffers of fractional Doppler equalization [52] and an increase of complexity compared to OFDM.

Let $\mathbf{X}_{DD} \in \mathbb{C}^{N\times M}$ represents a singular OTFS frame comprising symbols in the DD domain. According to the OTFS system model illustrated in Fig. 2.10, the OTFS frame in the Delay-

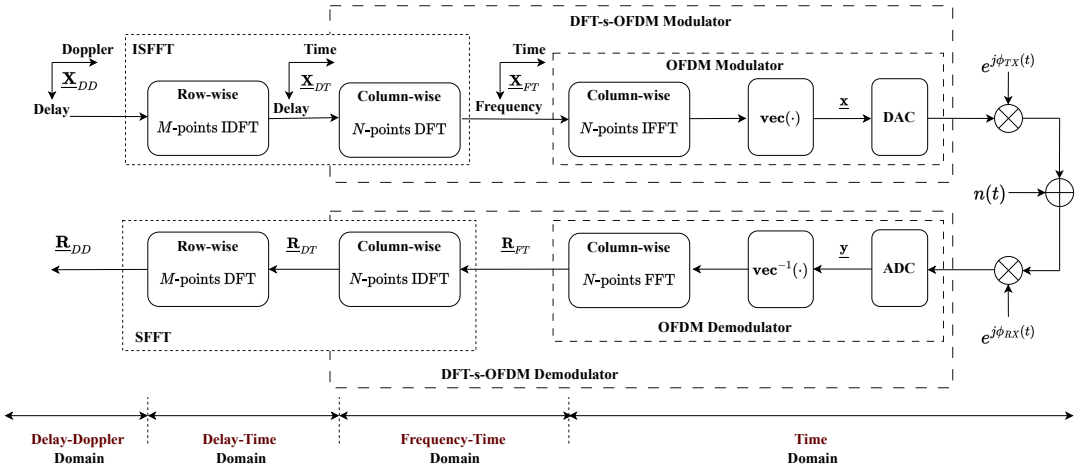


Figure 2.10: OTFS system model

Time (DT) domain is obtained by doing an IFFT along the Doppler axis by

$$\mathbf{X}_{DT} = \mathbf{X}_{DD}\mathbf{F}_M^H. \tag{2.30}$$

The expression of the signal in the Frequency-Time (FT) is obtained by compution the FFT of the signal in the DT through the Delay axis by

$$\begin{aligned} \mathbf{X}_{FT} &= \mathbf{F}_N\mathbf{X}_{DT} \\ &= \mathbf{F}_N\mathbf{X}_{DD}\mathbf{F}_M^H. \end{aligned} \tag{2.31}$$

The mapping from the DD-domain to the FT-domain is also called the Inverse Symplectic Finite Fourier Transform (ISFFT). Finally, the time-domain transmitted signal is obtained by doing the Heisenberg transformation of $\mathbf{X}_{FT}$ and given by

$$\begin{aligned} \underline{\mathbf{x}} &= \mathbf{vec}\left(\mathbf{F}_N^H\mathbf{X}_{FT}\right) \in \mathbb{C}^{NM\times 1} \\ &= \mathbf{vec}\left(\mathbf{X}_{DD}\mathbf{F}_M^H\right). \end{aligned} \tag{2.32}$$

Before transmitting the OTFS frame through the channel, one can add multiple CPs before the matrix-to-vector transformation, *i.e.* one CP in every "Delay symbol" and then we compute the **vec** operator. Otherwise, one CP after computing $\underline{\mathbf{x}}$. The expression of the time-domain received signal impaired by the generated oscillator PN is expressed as follows

$$\underline{\mathbf{y}} = \mathbf{\Phi}_E\underline{\mathbf{x}} + \underline{\mathbf{n}}, \tag{2.33}$$

where $\mathbf{\Phi}_E$ is the diagonal matrix which contains the sum of the applied PN by the oscillator at the transmitter and receiver. The term $\underline{\mathbf{n}}$ is the added thermal noise such that $n_k \backsim \mathbb{CN}\left(0, \sigma_n^2\right)$. After CP suppression (if it is added), the received OTFS frame in the FT-domain is recovered by performing the Wigner transform (which is FFT) as follows

$$\begin{aligned} \mathbf{R}_{FT} &= \mathbf{F}_N\mathbf{vec}^{-1}\left(\underline{\mathbf{y}}\right) \\ &= \mathbf{F}_N\mathbf{vec}^{-1}\left(\mathbf{\Phi}_E\underline{\mathbf{x}}\right) + \mathbf{F}_N\mathbf{vec}^{-1}\left(\underline{\mathbf{n}}\right). \end{aligned} \tag{2.34}$$

The expression of the received OTFS frame in the DD-domain is obtained by computing the

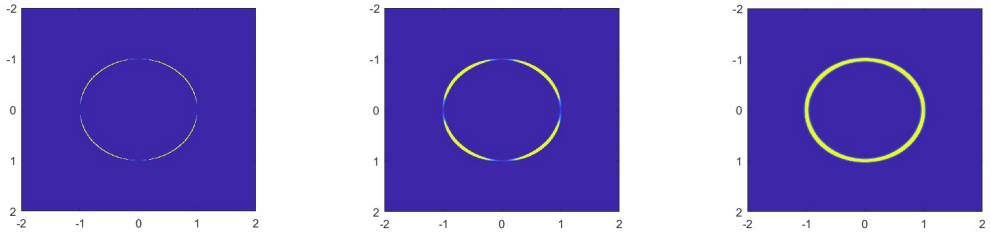

(a) No pulse shaping - 140 GHz (b) Pulse shaping - 140 GHz (c) Pulse shaping - 300 GHz

Figure 2.11: PN distortion upon SC received signal.

Table 2.3: Parameters

| Pulse shape | Root Raised Cosine Filter |
|---|---|
| Roll-off factor | 0.25 |
| Samples per symbol | 8 |
| Filter length in symbols | 10 |
| Modulation | 4-QAM |
| PN model | 3GPP Model 2 |
| Carrier frequency | {140, 300} GHz |
| Channel model | AWGN |
| SNR | 50 dB |

Symplectic Finite Fourier Transform (SFFT) transform as bellow

$$\begin{aligned}\mathbf{R}_{DD} &= \mathbf{F}_N^H \mathbf{R}_{FT} \mathbf{F}_M \\ &= \mathbf{vec}^{-1}\left(\mathbf{\Phi}_E \underline{\mathbf{x}}\right) \mathbf{F}_M + \mathbf{vec}^{-1}\left(\underline{\mathbf{n}}\right) \mathbf{F}_M \\ &= \mathbf{vec}^{-1}\left(\mathbf{\Phi}_E \underline{\mathbf{x}}\right) \mathbf{F}_M + \underline{\mathbf{w}},\end{aligned} \tag{2.35}$$

with $\underline{\mathbf{w}}$ the new thermal noise in the DD-domain. Obviously, the expression of the signal in the DT-domain is defined by

$$\begin{aligned}\mathbf{R}_{DT} &= \mathbf{F}_N^H \mathbf{R}_{FT} \\ &= \mathbf{vec}^{-1}\left(\mathbf{\Phi}_E \underline{\mathbf{x}}\right) + \mathbf{vec}^{-1}\left(\underline{\mathbf{n}}\right).\end{aligned} \tag{2.36}$$

OTFS corrupted by PN are considered in [53, 54] but, authors do not propose PN compensation techniques. Furthermore, from the best of our knowledge, PN compensation algorithms for OTFS are not yet well detailed and fair comparisons are missing. Consequently, the relation between the OTFS waveform with the traditional 5G-NR MC waveforms (OFDM & DFT-s-OFDM) as illustrated in Fig. 2.10 inspires us to propose a PN compensation in the DT domain rather than in the DD domain. Interested readers can refer to our contribution [55] entitled "*OTFS Waveform with Phase Noise in sub-THz*" (also in Appendix C) for more explanations. It is important to mention that this paper is a bonus contribution to this thesis.

Table 2.4: Simulation parameters

| | |
|---|---|
| Modulation | 16-QAM |
| Phase noise model | 3GPP Model 2 |
| Carrier frequency | 140 GHz |
| Sampling frequency $F_s$ | 1966.08 MHz |
| FFT size $N_f$ | 4096 |
| ICS $\Delta_f$ | 480 kHz |
| Allocated bandwidth $N_s$ | 512 subcarriers |
| DFT size $N_s$ | 512 |
| Doppler size $M$ | 512 |
| Delay size $N$ | 512 |
| Channel model | AWGN |
| SNR | 50 dB |

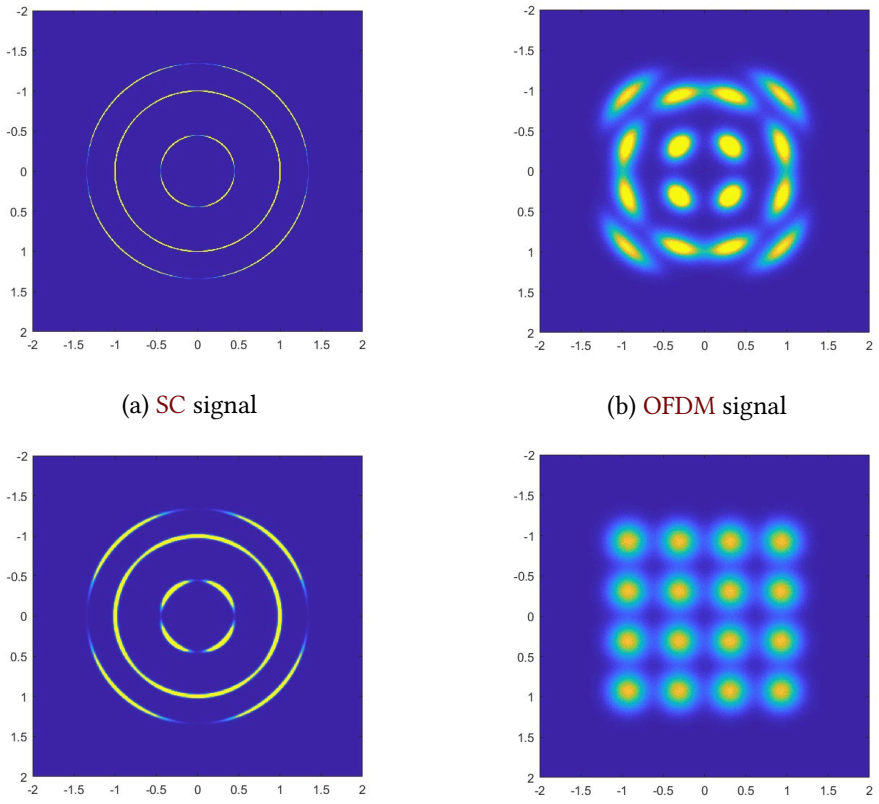

(a) SC signal

(b) OFDM signal

(c) DFT-s-OFDM signal

(d) OTFS signal

Figure 2.12: PN distortion upon different received signal without pulse shaping.

### 2.3.5 Received signal constellations

We present the PN effects on SC systems and MC waveform systems. Fig. 2.11 and Fig. 2.12 show the probability of a point appearing in In-phase and Quadrature (IQ) space. The more yellow the color, the higher the probability. The color blue represents an almost null probability of appearance.

Fig. 2.11 reveals the PN impairments when pulse shaping filter is considered for SC systems. The simulation parametres in Tables 2.3 are used. One can notice a noisy constellation in Fig. 2.11c compared to Fig. 2.11a. This is explained by the ISI caused by PN as highlighted in (2.19). Indeed, the generated PN prevents proper matching between receive and transmit pulse shaping filter. Moreover, Fig. 2.11c demonstrates the increase of ISI effect with the PN power (obviously, increasing the carrier frequency increases the PN power).

Fig. 2.12 illustrates the induced-PN effects on received constellations. The simulation parameters in Table 2.3 are considered. Fig. 2.12a shows the rotation of the transmitted signal when SC systems are impaired by PN. Additionally to symbol rotation by the CPE factor, Fig. 2.12b presents an additive noise representing the ICI for OFDM systems. In contrast for DFT-s-OFDM, Fig. 2.12c mostly notices a rotation of transmitted symbol as in SC system and a low ICI. Regarding the OTFS systems, Fig. 2.12d highlights a noisy constellation representing the ICI which seems to follow an uncorrelated Gaussian random process.

## 2.4 Phase Noise Effects considering a multi-path channel

So far, we have considered a frequency-flat channel. Now, we will consider the case where the propagation channel is frequency-selective on MC waveforms. Before that, if we neglect the presence of PN, the baseband discrete-time received signal before the OFDM demodulator is written as follows

$$\begin{aligned} \underline{\mathbf{y}} &= \mathbf{D}_{cp}\mathbf{H}\mathbf{M}_{cp}\underline{\mathbf{x}}, \\ &= \mathbf{H}_c\underline{\mathbf{x}}, \end{aligned} \tag{2.37}$$

with $\underline{\mathbf{x}} = \mathbf{F}^H\underline{\mathbf{X}}$. The term $\mathbf{H}$ is the channel matrix of size $N' \times N'$ representing the $L_{ds}$ resolvable multi-path components. The terms $\mathbf{M}_{cp}$ and $\mathbf{D}_{cp}$ respectively denote the CP adding and withdrawal matrix. In this case, adding and removing the CP produce a circulating channel matrix $\mathbf{H}_c$ of size $N_f \times N_f$ [1]. It is this circularity that allows "1-tap" Channel Equalization (CEQ) per subcarrier in the frequency-domain. Now when the PN generated by the oscillators are not negligible, the relation (2.37) becomes

$$\underline{\mathbf{y}} = \mathbf{D}_{cp}\mathbf{\Phi}_E^{RX}\mathbf{H}\mathbf{\Phi}_E^{TX}\mathbf{M}_{cp}\underline{\mathbf{x}}, \tag{2.38}$$

where $\mathbf{\Phi}_E^{TX}$ and $\mathbf{\Phi}_E^{RX}$ are respectively the PN adding matrices at transmitter and receiver. Because the generated PN at transmitter and receiver are independent, they prevent the simplification of the term $\mathbf{D}_{cp}\mathbf{\Phi}_E^{RX}\mathbf{H}\mathbf{\Phi}_E^{TX}\mathbf{M}_{cp}$ into a circulating matrix as in (2.37). Consequently, further analyis have to be done to propose some techniques in order to deal with channel and PN. This sccenario will be treated in this thesis.

## 2.5 Conclusion

In this chapter, we exhibit different PN models considered in this study:

- an uncorrelated GPN treated in few contributions

[1] we assume the delay spread of channel is lower than the duration of the CP

- the 3GPP PN models mostly used in the literature
- a realistic PN model based on real measurements upon a D-Band CMOS transceiver designed at CEA-Leti.

Before proposing PN compensation algorithms, the PN effects need to be well characterized. Consequently, we have also shown the impact of PN on MC waveforms. We highlighted the necessity to compensate the PN effects in the sub-THz and THz bands. Otherwise, it will deteriorate the system performance.

The 3GPP is studying how to adapt 5G-NR MC waveforms such as OFDM and DFT-s-OFDM to the specificities of the sub-THz bands, especially concerning PN impairments, for the future 6G. Employing a single OFDM waveform across all frequency bands encompassed by cellular systems has prompted a reevaluation of various phase compensation algorithms for MC systems. Of notable concern is the handling of ICI, which represents the primary factor restricting system performance. This critical aspect will be thoroughly examined in the next chapters.

# Part III

# Optimization of Receivers based on 5G-NR Multicarrier waveforms: Correlated PN

CHAPTER 3

# Post-FFT Wiener phase noise compensation

## Contents

## 3.1 Introduction

In the previous chapter, we presented the different PN models considered in this study. We also presented the impact of PN on different waveforms. We highlighted the need of advanced PN estimation and compensation techniques to improve the performance of RF communication systems. Fortunately, when the PN follows a Wiener process, its correlated nature as shown in Fig. 3.1, enables its estimation and therefore, its compensation (reduction of its effects) to improve the system performance. Thankfully, in DFT-s-OFDM systems, the PN retains its correlated nature after the IDFT transformation at the receiver. Thus, we can try to use this correlation behavior to compensate its effects. Thereby, PT-RS symbols introduced in 5G-NR, can be inserted for the PN tracking [42]. Several PN estimation and correction techniques are presented in the state-of-the-art. Most of them are designed for OFDM systems especially for ICI cancellation [41, 44]. Regarding the DFT-s-OFDM systems, low and high complexity algorithms are described in [43] such as CPEE, LI, DCT and Kalman Filter at mmWave frequencies. The DCT algorithm is firstly introduced in [56] in SC systems where the authors show the performance improvement as a function of the number of DCT coefficients used. A detailed comparison of these algorithms is provided in this chapter.

### 3.1.1 Motivations and contributions

Exploiting the PN correlated nature is a promising approach adressed in a recent literature. [57] presents a novel technique for OFDM systems based on the channel coherence bandwidth. However, there is no study presenting a PN estimation algorithm based on PN stochastic properties in DFT-s-OFDM systems. The contributions of this chapter are as follows

- We propose a PN estimation and compensation algorithm called WIF for DFT-s-OFDM systems. It is based on an *a-priori* knowlegde of the PN stochastic properties, *i.e.* its PSD.
- We present the flexibility of the WIF to the 3GPP contiguous PT-RS pattern.
- We provide performance analysis in terms of BER and TBLER considering high order modulation, 5G-NR LDPC code and 3GPP PN model 2 presented in Section 2.2.2.

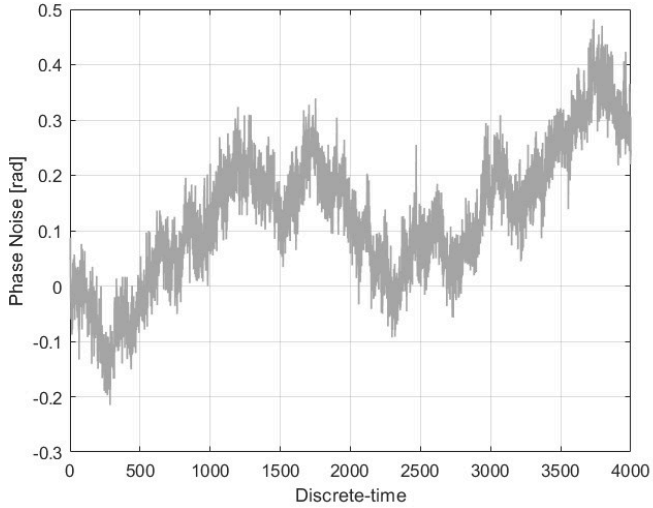


Figure 3.1: Discrete-time PN

- We highlight the possibility of implementing the WIF for different communication systems.
- We assess the performance of OFDM based waveform under realistic PN model shown in Section 2.2.3.

## 3.2 System model

### 3.2.1 Channel and PN models

As explained in the previous chapter, we assume a LoS propagation channel considered as frequency flat. We assume once again a coherent communication system impaired by PN with a receiver synchronised in time and frequency in order to avoid CFO effects. Concerning the PN characteristics, the 3GPP PN model 2 in Section 2.2.2 and the realistic one following the PSD given by the "Channel 1" in Section 2.2.3 are considered.

### 3.2.2 PT-RS Pattern

PT-RS are assumed to be distributed among the time/frequency grid as shown in Fig. 3.2 for MC systems. Regarding the DFT-s-OFDM, they are inserted before the DFT spreading block to avoid the increase of the PAPR. We define $\chi_p = \{p_0, p_1, \cdots, p_{K-1}\}$ the set which contains all the subcarrier indexes where PT-RS are inserted. We consider two PT-RS patterns:

- **Distributed PT-RS:** In this case, we assume the PT-RS symbols are inserted every $L$ subcarriers on each DFT-s-OFDM and OFDM symbol. The total number of inserted PT-RS symbols is given by:

$$\begin{cases} K_d = \frac{N_s}{L} & \text{for DFT-s-OFDM systems} \\ K_d = \frac{N_a}{L} & \text{for OFDM systems}\cdot \end{cases} \tag{3.1}$$

- **Contiguous PT-RS:** Regarding the contiguous pattern, we assume $N_p$ contiguous PT-RS symbols are inserted in $N_G$ groups with $N_s/N_G$ subcarriers per group in DFT-s-OFDM (resp. $N_a/N_G$ for OFDM). The total number of inserted PT-RS symbols is defined by $K_d = N_G \cdot N_p$ for both DFT-s-OFDM and OFDM systems.

### 3.2.3 5G-NR MC with PN

#### 3.2.3.1 DFT-s-OFDM waveform

We derived the expression of the received signal at the $k^{th}$ subcarrier in (2.27) as follows

$$r_k = s_k \beta(k, N_s, N_f, \phi) \; + \; \gamma(k, N_s, N_f, \phi) + \; \eta(k, N_s, N_f), \tag{3.2}$$

where the different terms are presented in (2.29). Let us denote $\beta_k = \beta(k, N_s, N_f, \phi)$, $\gamma_k = \gamma(k, N_s, N_f, \phi)$ and $\eta_k = \eta(k, N_s, N_f)$.

**Important note 1.** *According to the observation made in Fig. 2.12c, we take the following hypothesis*

$$\begin{aligned} \beta_k &= \beta_{k_\rho} e^{j\beta_{k_\phi}} \\ &\simeq e^{j\beta_{k_\phi}}. \end{aligned} \tag{3.3}$$

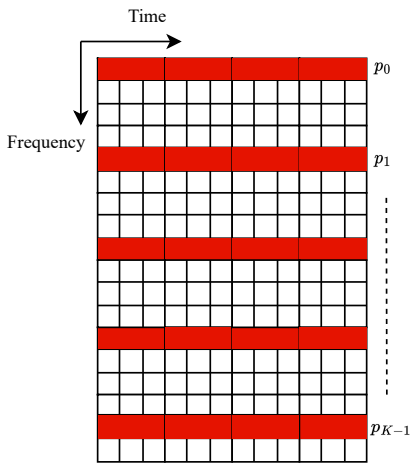


(a) Distributed PT-RS every $L = 4$.

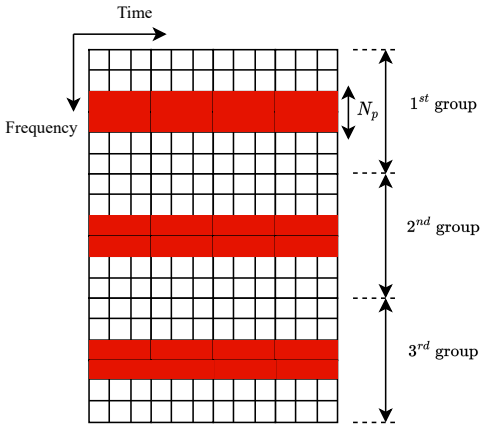


(b) Contiguous PT-RS Considering $N_G = 3$ groups with $N_p = 2$ PT-RS symbols per group.

Figure 3.2: PT-RS Pattern

Let us define $\phi_k^{'} = \beta_{k_\phi}$ as the PN-induced error after Fourier transformations. The expression (3.2) becomes

$$r_k \simeq s_k e^{j\phi_k^{'}} + \gamma_k + \eta_k, \tag{3.4}$$

with $\eta_k \backsim \mathbb{C}\mathcal{N}\left(0, \sigma_n^2\right)$ where $\sigma_n^2$ represents the thermal noise variance.

#### 3.2.3.2 OFDM waveform

As already presented in (2.21), we rewrite the expression of the received signal at the $k^{th}$ subcarrrier as bellow

$$R_k = X_k \mathcal{M} + \mathcal{V}_k + \mathcal{W}_k, \tag{3.5}$$

where $\mathcal{M}$ denotes the CPE, $\mathcal{V}_k$ the ICI and $\mathcal{W}_k$ the thermal noise. We rewrite the relation (3.5) as follows

$$R_k \simeq X_k e^{j\phi_M} + \mathcal{V}_k + \mathcal{W}_k, \tag{3.6}$$

where $\phi_M$ is the argument of the CPE *i.e.* $\phi_M = \arg(\mathcal{M})$.

## 3.3 State-of-the-art PN compensation methods

As presented in Section 2.2.1, the generated PN can be defined by

$$\phi[\tau] = \phi_W[\tau] + \phi_G[\tau] \tag{3.7}$$

where $\phi_W$ is the correlated component and $\phi_G$ the uncorrelated one. When $\phi_W \gg \phi_G$, the PN is considered as correlated and then, it is possible to estimate $\hat{\phi}_W \simeq \phi_W$ and compensate its effect. Therefore, in this section we present four estimation techniques: CPEE, LI and DCT are parts of the literature. A simple and low complexity algorithm called CI is also presented. The distributed PT-RS pattern in Fig. 3.2a is considered.

### 3.3.1 CPEE algorithm

This algorithm introduced in [43] consists in estimating the average phase error from PT-RS observations.

- **DFT-s-OFDM systems:** The estimated phase error is defined by

$$\hat{\phi} = \arg\left(\sum_{i\in\chi_p} \frac{\underline{\mathbf{r}}[i]\underline{\mathbf{s}}^*[i]}{\left|\underline{\mathbf{s}}[i]\right|^2}\right), \tag{3.8}$$

where $\underline{\mathbf{r}}$ represents the received DFT-s-OFDM symbol after the IDFT and $\underline{\mathbf{s}}$ is the transmitted DFT-s-OFDM symbol before the DFT. The expression of the received signal after PN compensation is given by

$$\hat{\underline{\mathbf{r}}} = \underline{\mathbf{r}} \odot e^{-j\hat{\phi}}. \tag{3.9}$$

- **OFDM systems:** It is given by

$$\hat{\phi} = \arg\left(\sum_{i\in\chi_p} \frac{\underline{\mathbf{R}}[i]\underline{\mathbf{X}}^*[i]}{\left|\underline{\mathbf{X}}[i]\right|^2}\right), \tag{3.10}$$

where $\underline{\mathbf{R}}$ and $\underline{\mathbf{X}}$ denote respectively the received and transmited OFDM symbols in frequency-domain. The expression of the received OFDM symbol after PN compensation is given by

$$\hat{\underline{\mathbf{R}}} = \underline{\mathbf{R}} \odot e^{-j\hat{\phi}}. \tag{3.11}$$

### 3.3.2 CI algorithm

This algorithm considers the PN as contant between two consecutive PT-RS. The expression of the estimated $\hat{\phi}_i$ at the $i^{th}$ PT-RS index is given by

$$\hat{\phi}_i = \underset{i\in\chi_p}{\arg}\left(\hat{\underline{\mathbf{r}}}[i]\underline{\mathbf{s}}^*[i]\right) \cdot \tag{3.12}$$

In DFT-s-OFDM systems, the estimated phase error is obtained as follows

$$\underline{\hat{\phi}}[k] = \begin{cases} \hat{\phi}_{p_0} & \text{if} \quad 0 \le k \le p_1 - 1 \\ \hat{\phi}_{p_1} & \text{if} \quad p_1 \le k \le p_2 - 1 \\ \hat{\phi}_{p_2} & \text{if} \quad p_2 \le k \le p_3 - 1 \\ \vdots & \\ \hat{\phi}_{p_{K-1}} & \text{if} \quad p_{K-1} \le k \le N_s - 1 \end{cases} \tag{3.13}$$

### 3.3.3 LI algorithm

This technique is based on making a linear interpolation upon estimation made on received PT-RS signal. We denote $\underset{A}{\mathcal{LI}}$ as the linear interpolation operation of size $A$. It is derived by

$$\underline{\hat{\phi}} = \underset{N_s}{\mathcal{LI}}\left(\underline{\hat{\phi}}_{\chi_p}\right), \tag{3.14}$$

with $N_s$ the DFT spreading size. The vector $\underline{\hat{\phi}}_{\chi_p}$ contains all the $\{\hat{\phi}_i\}_{i\in\chi_p}$ values defined by

$$\hat{\phi}_i = \arg\left(\frac{\underline{\mathbf{r}}[i]\underline{\mathbf{s}}^*[i]}{\left|\underline{\mathbf{s}}[i]\right|^2}\right) \cdot \tag{3.15}$$

The PN compensation of the received signal for both CI and LI algorithms is obtained by computing the following expression

$$\hat{\underline{\mathbf{r}}} = \underline{\mathbf{r}} \odot e^{-j\underline{\hat{\phi}}}. \tag{3.16}$$

### 3.3.4 DCT algorithm

This estimation technique relies on the approximation of PN by using DCT basis functions which are a set of cosine functions oscillating at different frequencies [56]. This is possible by determining the number of DCT coefficients which will be sufficient to estimate the PN properly. For DFT-s-OFDM systems, the orthonormal DCT basis functions are given by

$$\psi_n[u] = \begin{cases} \sqrt{\frac{1}{N_s}} & \text{if} \quad n = 0 \\ \sqrt{\frac{2}{N_s}} \cos\left(\frac{\pi n}{N_s}\left(u + \frac{1}{2}\right)\right) & \text{if} \quad n > 0 \end{cases} \qquad n = \{0, \cdots, N_D - 1\} \tag{3.17}$$

where $N_D$ represents the number of required DCT coefficients for PN estimation. The estimated phase error is obtained as follows

$$\underline{\hat{\phi}} = \phi_{avg}\underline{\mathbf{1}}_{N_s} + \mathbf{\Psi}_{N_s}\underline{\mathbf{v}}, \tag{3.18}$$

where $\mathbf{\Psi}_{N_s}$ is a $N_s \times N_D$ matrix containing all the $\psi_n[u]$ values with $u = \{0, \cdots, N_s - 1\}$. The terms $\phi_{avg}$ and $\underline{\mathbf{v}}$ are expressed as follows

$$\phi_{avg} = \arg\left(\sum_{i \in \chi_p} \frac{\underline{\mathbf{r}}[i]\underline{\mathbf{s}}^*[i]}{|\underline{\mathbf{s}}[i]|^2}\right) \quad \text{and} \quad \underline{\mathbf{v}} = \left(\mathbf{\Psi}_K^T \mathbf{\Psi}_K\right)^{-1} \mathbf{\Psi}_K^T \underline{\mathbf{r}}_P. \tag{3.19}$$

The matrix $\mathbf{\Psi}_K$ is a $K_d \times N_D$ matrix of coefficients $\psi_n[p]$ related to PT-RS length such that we have $p = \{0, \cdots, K_d - 1\}$. The vector $\underline{\mathbf{r}}_P$ contains all the $\underline{\mathbf{r}}_P[i]$ values defined by

$$\underline{\mathbf{r}}_P[i] = \arg\left(\underline{\mathbf{r}}[i]\underline{\mathbf{s}}^*[i]e^{-j\phi_{avg}}\right), \qquad \forall i \in \chi_p. \tag{3.20}$$

**Remark 3.** *This method is considered as more itensive computationnally than the three aforementioned algorithms due to the inverse operation in (3.19). This inversion operation is possible as long as the number of DCT coefficient is lower or equal than the number of inserted PT-RS symbols, i.e.*

$$N_D \leq K_d. \tag{3.21}$$

## 3.4 Proposed PN Compensation Technique: WIF algorithm

### 3.4.1 DFT-s-OFDM waveform

This algorithm relies on the stochastic properties of PN-induced effects. According to the received signal expression in (3.4), the goal is to determine the phase error from pilot observations by applying a Wiener filter on received data. Thereby, we look for a matrix $\mathbf{Z}$ satisfying the following condition

$$\underset{\mathbf{Z}}{\text{argmin}}\ \mathbb{E}\left[\left\|\mathbf{Z}\,\underline{\mathbf{a}}_P - e^{j\underline{\boldsymbol{\phi}}'}\right\|^2\right], \tag{3.22}$$

with $\mathbf{Z}$ denoting the Wiener interpolation filter of size $N_s \times K_d$ and $e^{j\underline{\boldsymbol{\phi}}'} = [e^{j\phi'_0}, \cdots, e^{j\phi'_{N_s-1}}]^T$ is the vector to be estimated. The vector $\underline{\mathbf{a}}_P = [a_{p_0}, \cdots, a_{p_{K-1}}]^T$ contains the tracking informations $\{a_i\}_{i \in \chi_p}$ obtained from received and inserted PT-RS. From (3.4), the terms $\{a_i\}_{i \in \chi_p}$ are given by

$$a_i = \frac{r_i s_i^*}{|s_i|^2} = e^{j\phi'_i} + \frac{\gamma_i s_i^*}{|s_i|^2} + \frac{\eta_i s_i^*}{|s_i|^2}, \quad \forall i \in \chi_p. \tag{3.23}$$

Hence, the PT-RS vector $\underline{\mathbf{a}}_P = [a_{p_0}, \cdots, a_{p_{K-1}}]^T$ is defined by

$$\underline{\mathbf{a}}_P = e^{j\underline{\boldsymbol{\phi}}'_P} + \underline{\boldsymbol{\gamma}}_P \odot \underline{\mathbf{s}}_P + \underline{\boldsymbol{\eta}}_P \odot \underline{\mathbf{s}}_P, \tag{3.24}$$

where the different terms are defined in (3.25) as follows

$$\begin{aligned} e^{j\underline{\boldsymbol{\phi}}'_P} &= \left[e^{j\phi'_{p_0}}, \cdots, e^{j\phi'_{p_{K-1}}}\right]^T, \ \underline{\boldsymbol{\gamma}}_P = \left[\underline{\gamma}_{p_0}, \cdots, \underline{\gamma}_{p_{K-1}}\right]^T, \ \underline{\boldsymbol{\eta}}_P = \left[\underline{\boldsymbol{\eta}}_{p_0}, \cdots, \underline{\boldsymbol{\eta}}_{p_{K-1}}\right]^T, \\ \underline{\mathbf{s}}_P &= \left[\frac{s^*_{p_0}}{|s_{p_0}|^2}, \cdots, \frac{s^*_{p_{K-1}}}{|s_{p_{K-1}}|^2}\right]^T. \end{aligned} \tag{3.25}$$

Finding the matrix $\mathbf{Z}$ that fills (3.22) means to solve the equation bellow

$$\frac{\partial}{\partial \mathbf{Z}} \mathbb{E}\left[\left\| \mathbf{Z}\, \underline{\mathbf{a}}_P - e^{j\underline{\boldsymbol{\phi}}'} \right\|^2\right] = 0, \tag{3.26}$$

where $\frac{\partial}{\partial \mathbf{Z}}$ is the derivative operation with respect to $\mathbf{Z}$. From (3.26), we have

$$\begin{aligned} \mathbb{E}\left[\|\mathbf{Z}\, \underline{\mathbf{a}}_P - e^{j\underline{\boldsymbol{\phi}}'}\|^2\right] &= \mathbb{E}\left[\mathcal{T}_r\left\{\left(\mathbf{Z}\, \underline{\mathbf{a}}_P - e^{j\underline{\boldsymbol{\phi}}'}\right)\left(\mathbf{Z}\, \underline{\mathbf{a}}_P - e^{j\underline{\boldsymbol{\phi}}'}\right)^H\right\}\right] \\ &= \mathbb{E}\left[\mathcal{T}_r\left\{\mathbf{Z}\, \underline{\mathbf{a}}_P \underline{\mathbf{a}}_P^H \mathbf{Z}^H - \mathbf{Z}\underline{\mathbf{a}}_P \left(e^{j\underline{\boldsymbol{\phi}}'}\right)^H - e^{j\underline{\boldsymbol{\phi}}'}\, \underline{\mathbf{a}}_P^H \mathbf{Z}^H + e^{j\underline{\boldsymbol{\phi}}'}\left(e^{j\underline{\boldsymbol{\phi}}'}\right)^H\right\}\right], \end{aligned} \tag{3.27}$$

where $\mathcal{T}_r\{\cdot\}$ denotes the trace operator. Assuming the development in (3.27), the expression (3.26) gives the relation bellow

$$\begin{aligned} \frac{\partial}{\partial \mathbf{Z}} \mathbb{E}\left[\left\| \mathbf{Z}\, \underline{\mathbf{a}}_P - e^{j\underline{\boldsymbol{\phi}}'} \right\|^2\right] = 0 &\Longleftrightarrow \mathbb{E}\left[\underline{\mathbf{a}}_P \underline{\mathbf{a}}_P^H \mathbf{Z}^H - \underline{\mathbf{a}}_P \left(e^{j\underline{\boldsymbol{\phi}}'}\right)^H\right] = 0 \\ &\Longleftrightarrow \mathbb{E}\left[\underline{\mathbf{a}}_P \underline{\mathbf{a}}_P^H \mathbf{Z}^H\right] = \mathbb{E}\left[\underline{\mathbf{a}}_P \left(e^{j\underline{\boldsymbol{\phi}}'}\right)^H\right]. \end{aligned} \tag{3.28}$$

**Remark 4.** *Let $\underline{\mathbf{b}}$, $\underline{\mathbf{d}}$, $\underline{\mathbf{f}}$ and $\underline{\mathbf{g}}$ be four vectors. The Hadamard product $\odot$ has the following properties*

$$\begin{cases} \left(\underline{\mathbf{b}} \odot \underline{\mathbf{d}}\right)\left(\underline{\mathbf{f}} \odot \underline{\mathbf{g}}\right) = \underline{\mathbf{b}}\, \underline{\mathbf{f}} \odot \underline{\mathbf{d}}\, \underline{\mathbf{g}} \\ \left(\underline{\mathbf{b}} \odot \underline{\mathbf{d}}\right)^H = \underline{\mathbf{b}}^H \odot \underline{\mathbf{d}}^H. \end{cases} \tag{3.29}$$

We denote by the symbol $\underline{\mathbf{a}}$, the vector containing $a_k$ values with $k = \{0, \cdots, N_s - 1\}$. we derive the expression bellow

$$\underline{\mathbf{a}}_P = \mathbf{M}_P \underline{\mathbf{a}}, \tag{3.30}$$

because $\chi_p \subset \{0, \cdots N_s - 1\}$, where $\mathbf{M}_P$ is the sampling PT-RS matrix (*i.e.* the matrix allowing to recover all the $\{a_i\}_{i \in \chi_p}$). From (3.30), the expression (3.24) becomes

$$\underline{\mathbf{a}}_P = \mathbf{M}_P e^{j\underline{\boldsymbol{\phi}}'} + \mathbf{M}_P \underline{\boldsymbol{\gamma}} \odot \underline{\mathbf{s}}_P + \mathbf{M}_P \underline{\boldsymbol{\eta}} \odot \underline{\mathbf{s}}_P, \tag{3.31}$$

with $\underline{\boldsymbol{\gamma}} = [\gamma_0, \cdots, \gamma_{N_s-1}]^T$ and $\underline{\boldsymbol{\eta}} = [\eta_0, \cdots, \eta_{N_s-1}]^T$. From (3.31), the expression (3.28) becomes

$$\begin{aligned} &\left(\mathbf{M}_P \mathbb{E}\left[e^{j\underline{\boldsymbol{\phi}}'}\left(e^{j\underline{\boldsymbol{\phi}}'}\right)^H\right] \mathbf{M}_P^H + \mathbf{M}_P \mathbb{E}\left[\underline{\boldsymbol{\gamma}}\, \underline{\boldsymbol{\gamma}}^H\right] \mathbf{M}_P^H \odot \mathbb{E}\left[\underline{\mathbf{s}}_P \underline{\mathbf{s}}_P^H\right] \mathbf{M}_P \mathbb{E}\left[\underline{\boldsymbol{\eta}}\, \underline{\boldsymbol{\eta}}^H\right] \mathbf{M}_P^H \odot \mathbb{E}\left[\underline{\mathbf{s}}_P \underline{\mathbf{s}}_P^H\right]\right) \mathbf{Z}^H \\ &= \mathbf{M}_P \mathbb{E}\left[e^{j\underline{\boldsymbol{\phi}}'}\left(e^{j\underline{\boldsymbol{\phi}}'}\right)^H\right]. \end{aligned} \tag{3.32}$$

**Important note 2.** *The relation (3.32) is obtained using (3.29) and considering* $\mathbb{E}\left[\underline{\boldsymbol{\eta}}\right] = \underline{\mathbf{0}}_{N_s}$ *because* $\eta_k \backsim \mathbb{CN}\left(0, \sigma_n^2\right)$. *Additionally, we suppose* $\mathbb{E}\left[\underline{\boldsymbol{\gamma}}\right] = \underline{\mathbf{0}}_{N_s}$.

Finally, if we assume $\{s_i\}_{i\in\chi_p}$ are uncorrelated, the expression of the interpolation matrix $\mathbf{Z}$ is given by

$$\mathbf{Z} = \mathbf{R}^H_{e^{j\underline{\boldsymbol{\phi}}'}} \mathbf{M}_P^H \left( \mathbf{M}_P \mathbf{R}^H_{e^{j\underline{\boldsymbol{\phi}}'}} \mathbf{M}_P^H + \mathbf{M}_P \left( \mathbf{R}^H_{\underline{\boldsymbol{\gamma}}} + \mathbf{R}^H_{\underline{\boldsymbol{\eta}}} \right) \mathbf{M}_P^H \odot \mathbf{I}_{K_d} \right)^{\dagger}, \tag{3.33}$$

where $\mathbf{I}_{K_d}$ is the identity matrix of size $K_d \times K_d$. The terms $\mathbf{R}_{e^{j\underline{\boldsymbol{\phi}}'}}$, $\mathbf{R}_{\underline{\boldsymbol{\gamma}}}$ and $\mathbf{R}_{\underline{\boldsymbol{\eta}}}$ denote respectively the correlation matrix of $e^{j\underline{\boldsymbol{\phi}}'}$, $\underline{\boldsymbol{\gamma}}$ and $\underline{\boldsymbol{\eta}}$. The matrix $\mathbf{Z}$ is the WIF of size $N_s \times K_d$.

**Remark 5.** *As one can notice in (3.33), the knowledge of the correlation matrices is necessary to compute the WIF.*

The phase error vector $\underline{\boldsymbol{\phi}}'$ can be estimated as follows

$$\underline{\hat{\boldsymbol{\phi}}}' = \arg\left(\mathbf{Z}\, \underline{\mathbf{a}}_P\right) \tag{3.34}$$

and then, we compensate the PN effect by using the following expression

$$\underline{\hat{\mathbf{r}}} = \underline{\mathbf{r}} \odot e^{-j\underline{\hat{\boldsymbol{\phi}}}'}. \tag{3.35}$$

**Remark 6.** *It is also possible to adapt the condition (3.33) to recover the phase error by using directly the received PT-RS vector* $\underline{\mathbf{r}}_P = [r_{p_0}, \cdots, r_{p_{K-1}}]^T$. *It becomes*

$$\min_{\mathbf{Z}} \mathbb{E}\left[ \left\| \mathbf{Z}\, \underline{\mathbf{r}}_P - e^{j\underline{\boldsymbol{\phi}}'} \right\|^2 \right]. \tag{3.36}$$

*By following the same steps as above, the filter expression associated to (3.36) is given by*

$$\mathbf{Z} = \left( \left( \mathbf{R}^H_{e^{j\underline{\boldsymbol{\phi}}'}} \mathbf{M}_{\mathrm{p}}^H \right) \odot \left( \underline{\mathbf{1}}_{N_s} \cdot \underline{\mathbf{s}}_{\mathrm{p}}^H \right) \right) \left( \mathbf{M}_P \mathbf{R}^H_{e^{j\underline{\boldsymbol{\phi}}'}} \mathbf{M}_P^H \odot \mathbf{I}_{K_d} + \mathbf{M}_P \left( \mathbf{R}^H_{\underline{\boldsymbol{\gamma}}} + \mathbf{R}^H_{\underline{\boldsymbol{\eta}}} \right) \mathbf{M}_P^H \right)^{\dagger}, \tag{3.37}$$

*where* $\underline{\mathbf{s}}_P = \left[ s_{p_0}, \cdots, s_{p_{K-1}} \right]^T$ *and* $\mathbf{I}_{K_d}$ *is the identity matrix of size* $K_d \times K_d$.

**Remark 7.** *The derived expression of the WIF in (3.33) does not depend on the inserted PT-RS symbols while the expression (3.37) does. Consequently, it is better suited to use the first WIF expression to avoid a PN estimation depending on the inserted PT-RS signature.*

**Remark 8.** *This Least Squared (LS) approach is suitable to SC systems. For SC system, we will have* $\mathbf{R}_{\underline{\boldsymbol{\gamma}}} = \underline{\mathbf{0}}_{N_s}$ *(because ICI does not exist) and* $\mathbf{R}_{e^{j\underline{\boldsymbol{\phi}}'}} = \mathbf{R}_{e^{j\underline{\phi}}}$ *with* $e^{j\underline{\phi}} = [e^{j\phi_0}, \cdots, e^{j\phi_{N_s-1}}]^T$. *The vector* $\underline{\phi}$ *is the sum of the applied PN at transmitter and receiver. Moreover, one can find a Wiener filter which estimates directly the vector* $\underline{\phi}$ *instead of* $e^{j\underline{\phi}}$ *as presented above by using the high SNR approximation. The entire details are mentioned in the Appendix Section B.*

Table 3.1: Simulation parameters

| Parameters | sections 3.5.1 and 3.5.2 | section 3.7 |
|---|---|---|
| Modulation $M_s$ | 16-QAM | {4-QAM; 16-QAM; 64-QAM} |
| Sampling Frequency $F_s$ | 1966.08 MHz | 3932.16 MHz |
| Numerology $\mu$ | 5 | 5 to 10 |
| System bandwidth $B_W$ | 983.04 MHz | 1884.32 MHz |
| FFT size $N_f$ | 4096 | $4096 \times 2^{-\mu+6}$ |
| Active subcarriers $N_a$ | 2048 | $12\left\lfloor \frac{B_W}{12 \cdot F_s} N_f \right\rfloor$ |
| DFT size $N_s$ | | |
| PN model | 3GPP PN Model 2 | Measured PN |
| Carrier frequency $F_c$ | 140 GHz | |
| Channel model | AWGN | |
| LDPC coding rate | 0.7 | {0.3; 0.5; 0.7; 0.9} |
| LDPC decoder | Layered Min-Sum | |

### 3.4.2 OFDM waveform

In the case of OFDM system, applying the WIF will give the following expression

$$\underset{\mathbf{Z}}{\operatorname{argmin}}\ \mathbb{E}\left[\left\|\mathbf{Z}\,\underline{\mathbf{R}}_P - e^{j\underline{\boldsymbol{\phi}}_M}\right\|^2\right], \tag{3.38}$$

where $\underline{\boldsymbol{\phi}}_M = \phi_M \cdot \underline{\mathbf{1}}_{N_a}$ represents the CPE vector and $N_a$ is the number of active subcarriers among the $N_f$. The term $\underline{\mathbf{R}}_P$ is the received PT-RS vector in frequency-domain. Inspired by the DFT-s-OFDM model, the solution of (3.38) will be defined by

$$\mathbf{Z} = \left(\left(\mathbf{R}^H_{e^{j\underline{\boldsymbol{\phi}}_M}} \mathbf{M}_P^H\right) \odot \left(\underline{\mathbf{1}}_{N_a} \cdot \underline{\mathbf{S}}_P^H\right)\right) \left(\mathbf{M}_P \mathbf{R}^H_{e^{j\underline{\boldsymbol{\phi}}_M}} \mathbf{M}_P^H \odot \mathbf{I}_{K_d} + \mathbf{M}_P \left(\mathbf{R}^H_{\underline{\boldsymbol{\gamma}}} + \mathbf{R}^H_{\underline{\boldsymbol{\eta}}}\right) \mathbf{M}_P^H\right)^{\dagger}, \tag{3.39}$$

where $\underline{\mathbf{S}}_P = \left[S_{p_0}, \cdots, S_{p_{K-1}}\right]^T$ represents the inserted PT-RS in each OFDM symbol in the frequency-domain. The term $\mathbf{I}_{K_d}$ is the identity matrix of size $K_d \times K_d$. Similarly, the phase error vector $\underline{\boldsymbol{\phi}}_M$ can be estimated as follows

$$\hat{\underline{\boldsymbol{\phi}}}_M = \arg\left(\mathbf{Z}\,\underline{\mathbf{a}}_P\right), \tag{3.40}$$

then we compensate the PN effect by using the following expression

$$\hat{\underline{\mathbf{R}}} = \underline{\mathbf{R}} \odot e^{-j\hat{\underline{\boldsymbol{\phi}}}_M}. \tag{3.41}$$

where the vector $\underline{\mathbf{R}} = \left[R_0, \cdots, R_{N_a-1}\right]^T$ is the received OFDM symbol.

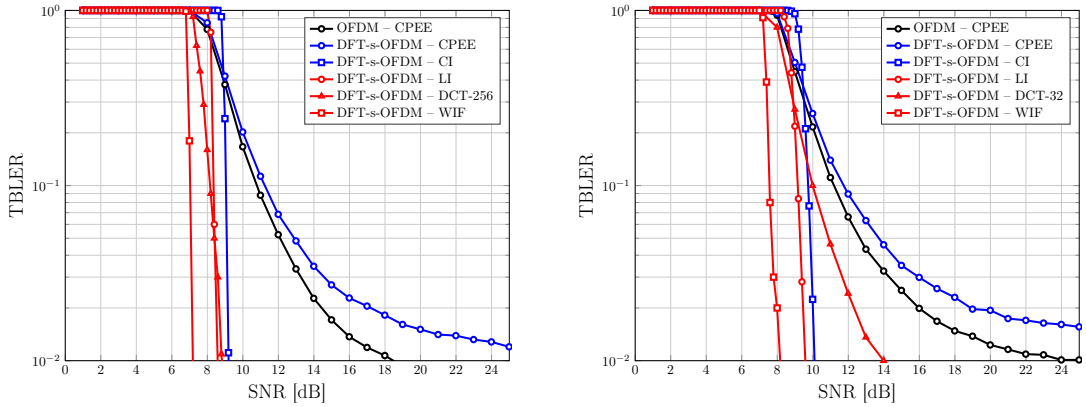


(a) Inserted PT-RS every $L = 8$ ($\mathcal{D} = 12.5\%$)

(b) Inserted PT-RS every $L = 64$ ($\mathcal{D} = 1.56\%$)

Figure 3.3: Performance comparison between OFDM and DFT-s-OFDM assuming distributed PT-RS pattern. The 3GPP PN model 2 in Section 2.2.2 is considered.

**Remark 9.** *From (3.38), one can notice that computing the WIF in frequency-domain comes down to only perform a CPE estimation. Therefore, performing the derived WIF in OFDM systems will be useless when the ICI effect is not negligible.*

## 3.5 Performance Assessment

In this section, we assess the accuracy of PN estimation algorithms described previously. The parameters used for numerical results are recorded in column "sections 3.5.1 and 3.5.2" of Table 3.1. The 3GPP PN model 2 presented in Section 2.2.2 is considered. For the WIF algorithm, we assume an *a-priori* knowledge of the correlation matrices $\mathbf{R}_{e^{j\underline{\phi}'}}$, $\mathbf{R}_{\underline{\gamma}}$ and $\mathbf{R}_{\underline{\eta}}$.

### 3.5.1 Distributed PT-RS

Fig. 3.3 presents a performance comparison between OFDM and DFT-s-OFDM systems in terms of TBLER as a function of SNR. The PN compensation algorithm considered for OFDM is the CPEE. Regarding the DFT-s-OFDM, five PN compensation algorithms are considered: the CPEE, the CI, the LI, the DCT and the proposed WIF. For the DCT algorithm, we arbitrarily choose three values of $N_D = \{K_d/4, K_d/2, K_d\}$. The $N_D$ value which allows the best performance is the only one depicted in Fig. 3.3. LDPC codes are considered for the channel coding. The distributed PT-RS pattern is considered with pilots inserted every $L = 8$ subcarriers in Fig. 3.3a and every $L = 64$ subcarriers in Fig. 3.3b. For all our simulations, received pilots are noisy. The pilot density is given for each OFDM and DFT-s-OFDM symbol by

$$\mathcal{D} = \frac{1}{L} \times 100 \ [\%]. \tag{3.42}$$

In Fig. 3.3a, one can notice the OFDM with CPEE is more efficient than DFT-s-OFDM with the CPEE. However, it performs worse than the DFT-s-OFDM with CI, LI, DCT-256 and WIF algorithms. A possible explanation for this could be the ICS is not wide enough to neglect the ICI effect. Regarding the DFT-s-OFDM, the proposed WIF is better than all the considered algorithms with a minimum SNR gain of 1.4 dB.

In Fig. 3.3b, one can remark the OFDM with the CPEE still outperforms the DFT-s-OFDM with the CPEE. Concerning the DFT-s-OFDM, the SNR gain of computing the LI algorithm

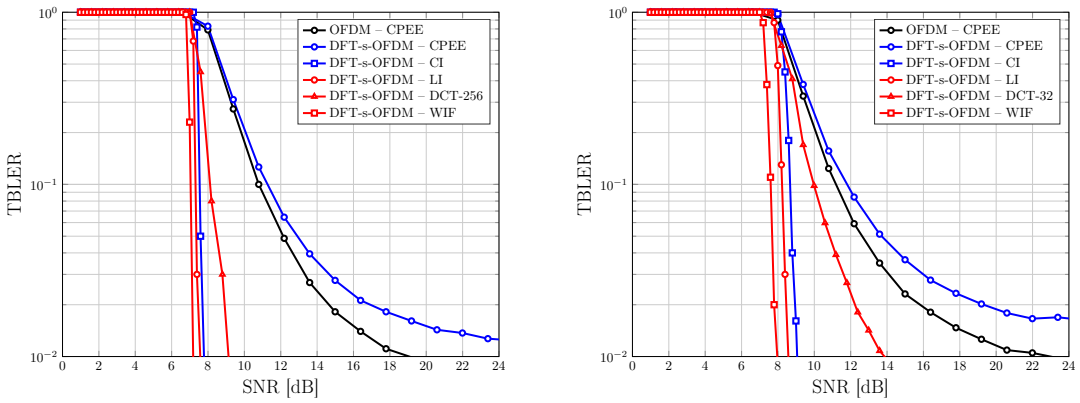


(a) $\{N_G, N_p\} = \{64, 4\}$ ($\mathcal{D} = 12.5\%$) (b) $\{N_G, N_p\} = \{16, 2\}$ ($\mathcal{D} = 1.56\%$)

Figure 3.4: Performance comparison between OFDM and DFT-s-OFDM assuming contiguous PT-RS pattern. The 3GPP PN model 2 in Section 2.2.2 is considered.

instead of the DCT-32 is more than 4 dB. Same observation is made for the CI compared to the DCT-32. When it comes to the WIF algorithm, the knowledge of the correlation information allows it to better predict the PN variation from PT-RS symbols whereas other algorithms cannot. Definitely, the DFT-s-OFDM with the proposed WIF outperforms all the implemented algorithms with low pilot density.

### 3.5.2 Contiguous PT-RS

Here, we assume contiguous PT-RS as represented in Fig. 3.2b. For both WIF and DCT algorithms, we consider all the PT-RS symbols for each group. For CI, CPEE and LI algorithms, we consider only one estimated PN value per group. This value is obtained by averaging all the $N_p$ PT-RS per group and is given by

$$\hat{\theta}^{(j)} = \arg\left( \sum_{m \in \xi^{(j)}} \frac{r[m]s^*[m]}{|s[m]|^2} \right), \tag{3.43}$$

where $\xi^{(j)}$ is the set of PT-RS index of the $j^{th}$ group with $j = \{0, \cdots, N_G - 1\}$. For CI, we assume the PN has a constant variation within a group and the estimated PN is given by

$$\hat{\phi}_n^{(j)} = \hat{\theta}^{(j)}, \quad \forall n \in j^{th} \text{ group with } n = \{0, \cdots N_s - 1\}\cdot \tag{3.44}$$

Regarding the CPEE algorithm, we average all the $\hat{\theta}^{(j)}$ computed for each group. The estimated PN is then expressed as follows

$$\hat{\phi} = \frac{1}{N_G} \sum_{j=0}^{N_G-1} \hat{\theta}^{(j)}. \tag{3.45}$$

Finally, the estimated PN using the LI algorithm is expressed as follows

$$\underline{\hat{\phi}}_{LI} = \underset{N_s}{\mathcal{LI}} \left( \underline{\hat{\theta}} \right), \quad \text{with} \quad \underline{\hat{\theta}} = \left[ \hat{\theta}^{(0)}, \cdots, \hat{\theta}^{(N_G-1)} \right]^T. \tag{3.46}$$

Fig. 3.4 presents a performance comparison between OFDM and DFT-s-OFDM systems in terms of TBLER as a function of the SNR. The results presented in Fig. 3.4a and Fig. 3.4b are obtained considering a pilot density respectively of 12.5% and 1.56% in order to have the same pilot density as for the results shown in Fig. 3.3. We compute the same performance comparison as

in Section 3.5.1. For all our simulations, received pilots are noisy. LDPC codes are considered for the channel coding.

In Fig. 3.4a, we observe the OFDM with the CPEE exceeds the DFT-s-OFDM with the CPEE. In contrast to the results presented in Fig. 3.3a, the CI now surpasses the DCT-256 with a SNR gain of 1.2 dB. Same observation for LI compared to DCT-256. In addition, the WIF outshines all the other algorithms but, the SNR gain between the WIF and CI or LI decreases compared to Fig. 3.3a.

Regarding Fig. 3.4b, we made the same remarks as in Fig. 3.3b for LI and CI compared to the DCT-32. As a consequence, the contiguous PT-RS pattern enables the LI and CI algorithms to enhance their PN estimation and compensation accuracy. However, they still less efficient than the WIF. As a consequence, the WIF offers higher performance regardless of the PT-RS pattern.

## 3.6 Derivation of the cross-correlation matrices

We show the effectiveness of the WIF in the previous section. The challenge in applying this algorithm relies in estimating the correlation matrices in realistic transmission scenarios. In this section, we will derive a theoretical expression of the correlation matrices.

### 3.6.1 General expressions

In DFT-s-OFDM systems, the vector $e^{j\underline{\boldsymbol{\phi}}'}$ can be expressed as follows

$$e^{j\underline{\boldsymbol{\phi}}'} = \mathbf{diag}\left\{\mathbf{F}_{N_s}^H \mathbf{D}_{RX} \mathbf{F}_{N_f} \boldsymbol{\Phi}_E \mathbf{F}_{N_f}^H \mathbf{M}_{TX} \mathbf{F}_{N_s}\right\}, \tag{3.47}$$

where $\boldsymbol{\Phi}_E$ is a diagonal matrix containing the PN shift vector $e^{j\underline{\boldsymbol{\phi}}}$ on its diagonal. The vector $\underline{\boldsymbol{\phi}}$ is the sum of the PN generated at transmitter and receiver. By posing

$$\begin{cases} \mathbf{A}_{TX} = \mathbf{F}_{N_f}^H \mathbf{M}_{TX} \mathbf{F}_{N_s} \\ \mathbf{A}_{RX} = \mathbf{F}_{N_s}^H \mathbf{D}_{RX} \mathbf{F}_{N_f}, \end{cases} \tag{3.48}$$

the relation (3.47) becomes

$$e^{j\underline{\boldsymbol{\phi}}'} = \mathbf{B} e^{j\underline{\boldsymbol{\phi}}}, \tag{3.49}$$

such that

$$\mathbf{B}^{(i,k)} = \mathbf{A}_{RX}^{(i,k)} \mathbf{A}_{TX}^{(k,i)}, \tag{3.50}$$

with $i \in \{0, \cdots, N_s - 1\}$ and $k \in \{0, \cdots, N_f - 1\}$. Therefore, the correlation matrix $\mathbf{R}_{e^{j\underline{\boldsymbol{\phi}}'}}$ is given by

$$\begin{aligned} \mathbf{R}_{e^{j\underline{\boldsymbol{\phi}}'}} &= \mathbb{E}\left[e^{j\underline{\boldsymbol{\phi}}'} \left(e^{j\underline{\boldsymbol{\phi}}'}\right)^H\right] \\ &= \mathbb{E}\left[\mathbf{B}\, e^{j\underline{\boldsymbol{\phi}}} \left(e^{j\underline{\boldsymbol{\phi}}}\right)^H \mathbf{B}^H\right] \\ &= \mathbf{B}\, \mathbb{E}\left[e^{j\underline{\boldsymbol{\phi}}} \left(e^{j\underline{\boldsymbol{\phi}}}\right)^H\right] \mathbf{B}^H \\ &= \mathbf{B} \mathbf{R}_{e^{j\underline{\boldsymbol{\phi}}}} \mathbf{B}^H. \end{aligned} \tag{3.51}$$

To express the correlation matrix of the vector $e^{j\underline{\boldsymbol{\phi}}}$, we use the following small-angle approximation

$$e^{j\underline{\boldsymbol{\phi}}} \simeq \underline{\mathbf{1}}_{N_f} + j\underline{\boldsymbol{\phi}}. \tag{3.52}$$

From (3.52), the correlation matrix $\mathbf{R}_{e^{j\underline{\phi}}}$ is defined by

$$\begin{aligned}\mathbf{R}_{e^{j\underline{\phi}}} &= \mathbb{E}\left[e^{j\underline{\phi}}\left(e^{j\underline{\phi}}\right)^H\right] \\ &\simeq \mathbb{E}\left[\left(\underline{1}_{N_f} + j\underline{\phi}\right)\left(\underline{1}_{N_f} + j\underline{\phi}\right)^H\right] \\ &\simeq \mathbf{1}_{N_f} + \mathbf{R}_{\underline{\phi}}.\end{aligned} \tag{3.53}$$

**Important note 3.** *The expression (3.53) is obtained assuming the PN vector $\underline{\phi}$ is a zero-mean process.*

According to (3.53), the relation (3.51) becomes

$$\mathbf{R}_{e^{j\underline{\phi}'}} \simeq \mathbf{B}\left(\mathbf{1}_{N_f} + \mathbf{R}_{\underline{\phi}}\right)\mathbf{B}^H. \tag{3.54}$$

As shown in (3.54), it is possible to obtain the correlation matrix $\mathbf{R}_{e^{j\underline{\phi}'}}$ by having the knowledge of the PN correlation matrix $\mathbf{R}_{\underline{\phi}}$. According to the PN generation method presented in Section 2.2.4, a theoretical expression of the generated PN at transmitter is given by

$$\begin{aligned}\underline{\phi}_{TX} &= \mathfrak{R}_{\mathfrak{e}}\left\{\sqrt{F_s}\mathbf{F}^H\sqrt{\mathbf{P}_{TX}}\,\underline{\mathbf{w}}\right\} \\ &= \sqrt{F_s}\mathfrak{R}_{\mathfrak{e}}\left\{\left(\mathbf{F}^R + j\mathbf{F}^I\right)^H\sqrt{\mathbf{P}_{TX}}\left(\underline{\mathbf{w}}^R + j\underline{\mathbf{w}}^I\right)\right\} \\ &= \sqrt{F_s}\left(\mathbf{F}^R\sqrt{\mathbf{P}_{TX}}\,\underline{\mathbf{w}}^R - \mathbf{F}^I\sqrt{\mathbf{P}_{TX}}\,\underline{\mathbf{w}}^I\right),\end{aligned} \tag{3.55}$$

where $\mathbf{P}_{TX}$ is a diagonal matrix of size $N_f \times N_f$ with the PSD of the generated PN (at the transmitter) on its diagonal. The matrix $\underline{\mathbf{w}}$ is a Gaussian random vector of size $N_f \times 1$ defined by

$$\underline{\mathbf{w}} \backsim \mathbb{CN}\left(\underline{\mathbf{m}}_{\mathbf{w}}, \mathbf{R}_{\underline{\mathbf{w}}}\right) = \begin{cases} \underline{\mathbf{m}}_{\mathbf{w}} = [0, \cdots, 0]^T \\ \mathbf{R}_{\underline{\mathbf{w}}} = \mathbf{I}_{N_f}. \end{cases} \tag{3.56}$$

Therefore, the correlation matrix of $\underline{\phi}_{TX}$ is given by

$$\begin{aligned}\mathbf{R}_{\underline{\phi}_{TX}} &= \mathbb{E}\left[\underline{\phi}_{TX}\underline{\phi}_{TX}^H\right] \\ &= \frac{F_s}{2}\left(\mathbf{F}^R\mathbf{P}_{TX}\mathbf{F}^{R^T} + \mathbf{F}^I\mathbf{P}_{TX}\mathbf{F}^{I^T}\right).\end{aligned} \tag{3.57}$$

Similarly, the correlation matrix of PN generated at receiver $\underline{\phi}_{RX}$ will be defined by

$$\begin{aligned}\mathbf{R}_{\underline{\phi}_{RX}} &= \mathbb{E}\left[\underline{\phi}_{RX}\underline{\phi}_{RX}^H\right] \\ &= \frac{F_s}{2}\left(\mathbf{F}^R\mathbf{P}_{RX}\mathbf{F}^{R^T} + \mathbf{F}^I\mathbf{P}_{RX}\mathbf{F}^{I^T}\right),\end{aligned} \tag{3.58}$$

where $\mathbf{P}_{RX}$ denotes the diagonal matrix of size $N_f \times N_f$ with the PSD of the generated PN (at the receiver) on its diagonal.

**Remark 10.** *By assuming the generated PN at the transmitter and receiver are zero-mean*

*and independent, the correlation matrix* $\mathbf{R}_{\underline{\phi}}$ *is obtained by*

$$\begin{aligned}\mathbf{R}_{\underline{\phi}} &= \mathbb{E}\left[\underline{\phi}\,\underline{\phi}^H\right] \\ \mathbf{R}_{\underline{\phi}} &= \mathbb{E}\left[\left(\underline{\phi}_{TX}+\underline{\phi}_{RX}\right)\left(\underline{\phi}_{TX}+\underline{\phi}_{RX}\right)^H\right] \\ &= \mathbb{E}\left[\underline{\phi}_{TX}\underline{\phi}_{TX}^H+\underline{\phi}_{TX}\underline{\phi}_{RX}^H+\underline{\phi}_{RX}\underline{\phi}_{TX}^H+\underline{\phi}_{RX}\underline{\phi}_{RX}^H\right] \\ &= \mathbf{R}_{\underline{\phi}_{TX}}+\mathbf{R}_{\underline{\phi}_{RX}}.\end{aligned} \tag{3.59}$$

Because $\eta_k \backsim \mathbb{CN}\left(0,\sigma_n^2\right)$, the vector $\underline{\boldsymbol{\eta}}$ can be considered as a Gaussian vector defined as follows

$$\underline{\boldsymbol{\eta}} \backsim \mathbb{CN}\left(\underline{\mathbf{m}}_{\eta},\mathbf{R}_{\underline{\eta}}\right) = \begin{cases}\underline{\mathbf{m}}_{\eta} = [0,\cdots,0]^T \\ \mathbf{R}_{\underline{\eta}} = \sigma_n^2\mathbf{I}_{N_s}.\end{cases} \tag{3.60}$$

**Important note 4.** *Consequently, it is possible to compute the correlation matrix* $\mathbf{R}_{e^{j\underline{\phi}'}}$ *by using relations (3.54) and (3.59). However, the knowlegde of the PSD of the applied PN is necessary. Additionally, a knowledge of the thermal noise power* $\sigma_n^2$ [a] *is sufficient to derive the correlation matrix* $\mathbf{R}_{\underline{\eta}}$*. Regarding the ICI correlation matrix* $\mathbf{R}_{\underline{\gamma}}$*, it is complex to estimate it.*

[a] The thermal noise is evaluated using the Johnson-Nyquist formula by $\sigma_n^2 = k_B T_0 B_W N_n$, where $k_B$ denotes the Boltzmann's constant and $B_W$ the system bandwidth. $N_n$ is the noise figure of the Low Noise Amplifier (LNA) and $T_0$ is the absolute temperature. So, a temperature measurement of the circuit can be considered.

### 3.6.2 Particular case: the D-Band CMOS Transceiver architecture

In this section, we show a practical case where it is possible to estimate the correlation matrix $\mathbf{R}_{e^{j\underline{\phi}'}}$. As a reminder, the D-Band CMOS transceiver in Fig. 2.3 generates a PN at high frequency whose PSD can be expressed as in (2.12) by

$$\mathrm{PSD} = \mathrm{PSD}_{in} + 20\log_{10}\left(\frac{f_{LO}}{f_{in}}\right), \tag{3.61}$$

where $\mathrm{PSD}_{in}$ represents the PSD of the PN generated by the first low frequency oscillator at carrier frequency $f_{in}$. The term $f_{LO}$ is the high frequency at the second oscillator to generate a PN such that the sum of the PN generated by the two oscillators is aligned with the real PN applied to transmitted signal. From (3.61) and assuming the PN generation method presented in Section 2.2.4, the correlation matrix of the global generated PN is given by

$$\mathbf{R}_{\underline{\phi}_{RX}} = \mathbf{R}_{\underline{\phi}_{TX}} = \left(\frac{f_{LO}}{f_{in}}\right)^2 \mathbf{R}_{\underline{\phi}^{in}}, \tag{3.62}$$

where $\mathbf{R}_{\underline{\phi}^{in}}$ denotes the correlation matrix of the PN generated at the low frequency $f_{in}$. Then, the correlation matrix of the global PN generated from relation (3.59) is expressed by

$$\mathbf{R}_{\underline{\phi}} = 2\left(\frac{f_{LO}}{f_{in}}\right)^2 \mathbf{R}_{\underline{\phi}^{in}}. \tag{3.63}$$

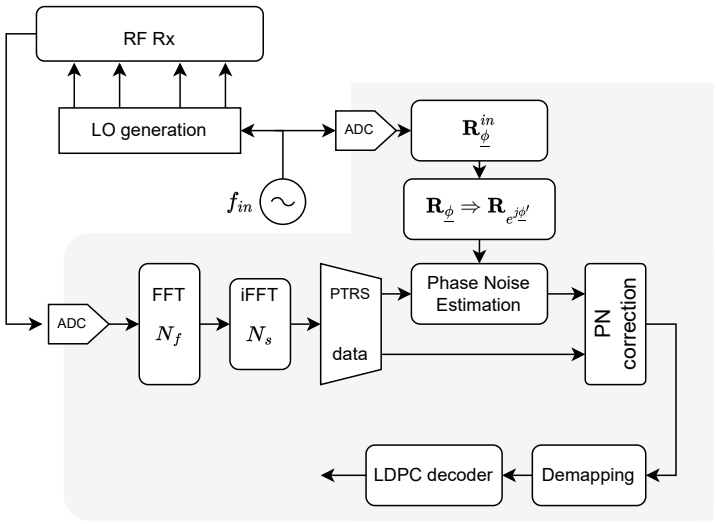


Figure 3.5: Block diagram of the proposed digital baseband receiver for DFT-s-OFDM.

As shown in (3.63), we need to estimate the correlation matrix $\mathbf{R}_{\underline{\phi}^{in}}$. To do that, we will take advantage of the two-stage high-frequency ramp-up of the transceiver. We directly sample the output of low-frequency oscillator as depicted in Fig. 3.5 to obtain $\mathbf{R}_{\underline{\phi}^{in}}$ and then, we compute the relations (3.63) and (3.54) to obtain the correlation matrix $\mathbf{R}_{e^{j\underline{\phi}'}}$. Afterwards, the received IQ samples once synchronized in time and frequency, are processed by a DFT-s-OFDM receiver. In this way, PT-RS are extracted and feed the PN estimation block.

**Remark 11.** *The transceiver architecture in Fig. 2.3 allows the computation of the PN correlation matrix in (3.62) without the knowledge of PN PSD as presented in Section 3.6.1.*

**Remark 12.** *The proposed digital receiver is derived assuming the transmitter and receiver have the same architecture.*

**Important note 5.** *If the transmitter architecture is different from the receiver one, it will be necessary to estimate the correlation matrix of the applied PN at both transmitter and receiver.*

## 3.7 Performance Comparison using the realistic measured PN

In this case, we consider the PN obtained from measurements upon the D-Band CMOS transceiver whose PSD is presented in 2.2.3. The simulation parameters in column "section 3.7" of Table 3.1 are considered. The generated PN is following the PSD of the “Channel 1" in Fig 2.5. The distributed PT-RS pattern is considered with pilots inserted every $L = 8$ subcarriers. For all our simulations, received pilots are noisy. LDPC codes are considered for the channel coding.

### 3.7.1 OFDM performance with CPEE

Fig 3.6 presents the performance of an OFDM system for different modulation orders and numerologies. We evaluate the SNR value that achieves the TBLER of $10^{-2}$. We consider three levels:

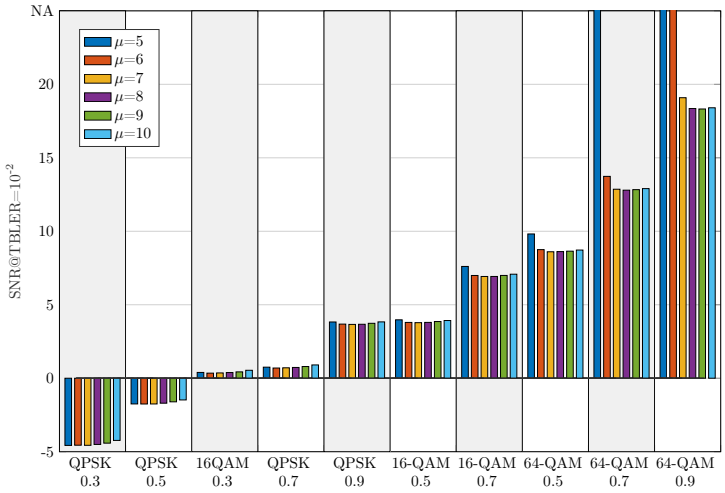


Figure 3.6: SNR [dB] values to achieve a TBLER of $10^{-2}$ in OFDM system. We consider the measured PN in Section 2.2.3, several numerologies and a pilot density of 6%. "NA" stands for "Non achievable".

- low SE with QPSK and CR of $\{0.3, 0.5, 0.7\}$ and (16-QAM,0.3),
- medium SE with (QPSK,0.9) and 16-QAM with CR=$\{0.5, 0.7\}$,
- high SE which includes 64-QAM with CR=$\{0.5, 0.7, 0.9\}$.

One can observe that for the low and medium SE, all the numerologies provide approximately the same SNR value, except in the case of (16-QAM,0.7) where we observe a SNR gap of 0.5 dB for the numerology 5 compared to the others. For the high SE, one can observe that for the numerologies 5 and 6, the SNR values increase until the target TBLER cannot be achieved. Indeed, when we increase the SE, the ICS is no longer sufficient and the ICI then starts to be disturbing. Therefore, if we plan to use 5G-NR numerologies in high SE, in addition to the CPE correction, ICI cancellation techniques are needed. Alternatively, the numerology can be increased (*i.e.* increase the ICS) following "Option 2" presented in Table. 1.1.

### 3.7.2 Performance comparison of 5G-NR MC systems

Concerning the DFT-s-OFDM systems, two algorithms are evaluated: first, the LI and the proposed WIF algorithm. In a first embodiment, we consider a perfect statistical knowledge of the PN statistic $\mathbf{R}_{e^{j\underline{\Phi}'}}$: "WIF genie-aided".

Fig. 3.7 depicts the TBLER versus SNR. Regarding DFT-s-OFDM systems with numerologies $\mu = \{5, 6, 7\}$, the proposed WIF algorithm outshines the LI algorithm. The LI does not allow efficient phase denoising because it is noise sensitive and the PN considered here is two times higher than the one considered in Section 3.5. Furthermore, one can notice the DFT-s-OFDM with WIF algorithm outperforms the OFDM with CPE correction for the numerology $\mu = 5$. For $\mu = 6$, one can observe the DFT-s-OFDM with WIF algorithm outperforms once again OFDM with CPE correction considering the 64-QAM modulation order and a CR=$\{0.7, 0.9\}$. But for $\mu = 7$, both DFT-s-OFDM with WIF algorithm and OFDM with CPEE correction provide the same performance. This is because increasing the numerology increases the ICS and therefore, the ICI effect is reducing. Thereby, the OFDM with CPEE challenges the DFT-s-OFDM with the WIF for $\mu \geq 7$. Otherwise, the DFT-s-OFDM systems with WIF algorithm could be a solution for sub-THz transmission.

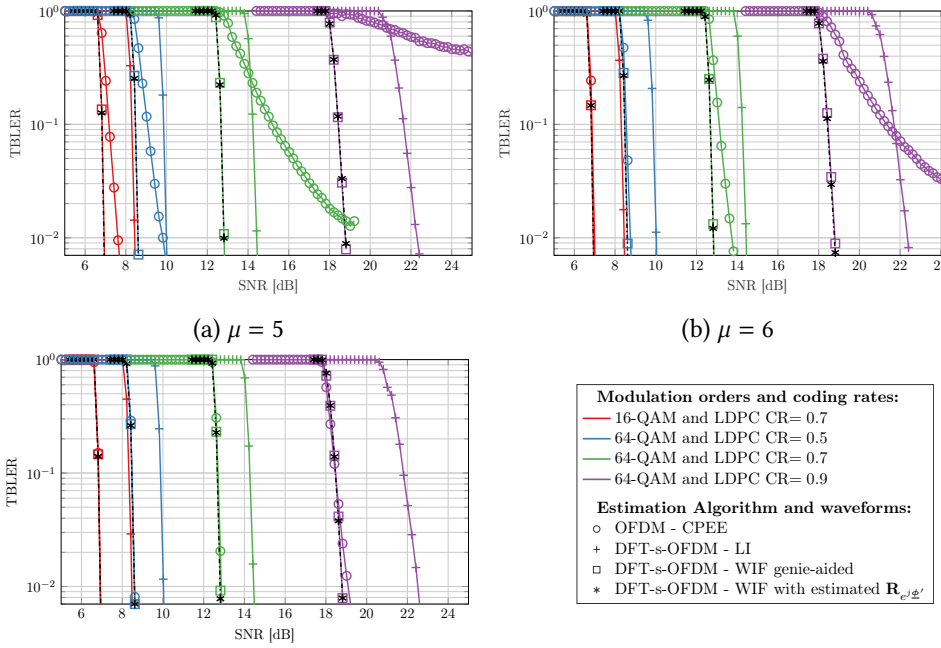


(a) $\mu = 5$ (b) $\mu = 6$

(c) $\mu = 7$

Figure 3.7: Performance of DFT-s-OFDM and OFDM systems in terms of TBLER as a function of SNR. The numerologies $\mu = \{5, 6, 7\}$ and the measured PN in Section 2.2.3 are considered.

We also perform the WIF algorithm by estimating the PN statistics. We first estimate the cross-correlation matrix $\mathbf{R}^{in}_{\underline{\phi}}$ of the low frequency oscillator and then, we derive the cross-correlation matrix $\mathbf{R}_{e^{j\underline{\phi}'}}$ by using the relations (3.63) and (3.54).

**Important note 6.** *Due to the complex derivation of the ICI correlation matrix $\mathbf{R}_{\underline{\gamma}}$, we will neglect it (i.e. $\mathbf{R}_{\underline{\gamma}} = \mathbf{0}_{N_s}$) and observe the impact of this assumption on system performance.*

As highlighted in Fig.3.7, the WIF algorithm with the estimated correlation matrix $\mathbf{R}_{e^{j\underline{\phi}'}}$ gives the same performance as the one with its perfect knowledge. This means for the PN model and system parameters considered, neglecting the ICI correlation matrix has no influence on the DFT-s-OFDM system performance. These results validate the possibility to implement the WIF algorithm for realistic RF transmission assuming a two-stage high-frequency ramp-up method as proposed by the presented transceiver in Fig. 2.3.

## 3.8 Complexity reduction of the proposed WIF

### 3.8.1 Complexity evaluation

In this section, we now evaluate the complexity of the WIF algorithm. The criterion for assessing this complexity will be the number of real multiplications and additions respectively denoting by MUL and AD required to compute the WIF. We assume a complex multiplication involves four individual real multiplications and two additions [1]. We also assume the filter calculation can be performed offline. In fact, this operation must be repeated at a period greater than the duration of a symbol, since the physical parameters governing the variability of PN vary according

[1] it is normally one addition and one subtraction but we consider the subtraction as an addition. It is also possible to perform the product of two complex values with three real multiplications but we do not consider this case

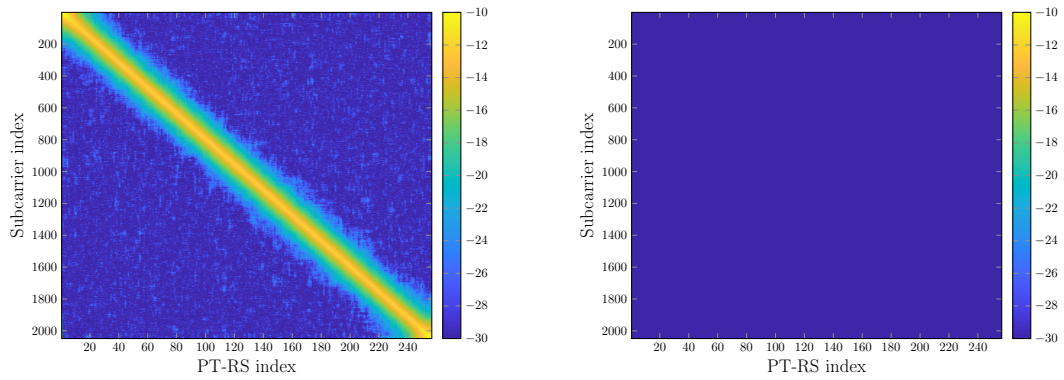


(a) Real part of the WIF

(b) Imaginary part of the WIF

Figure 3.8: Illustration of the power of WIF coefficients in [dB] considering parameters in column "sections 3.5.1 and 3.5.2" of Table. 3.1 and SNR = 15 dB.

to the duration of several symbols (e.g the temperature). Thus, the PN compensation will require $N_{OP} = N_s\,(4K_d \cdot \text{MUL} + 2\,(K_d + 2)\,\text{AD})$. For instance, if we consider a DFT spreading size $N_s = 2048$ and $K_d = 256$ inserted PT-RS symbols, computing the PN estimation with the WIF algorithm will need $N_{OP} = 2^{21}\text{MUL} + 2\,(2^8 + 2)$ AD which represents millions of operations. Consequently, implementing a filter with a large set of complex coefficients may be very costly from a practical approach. The question is whether this complexity can be reduced.

Let us first analyze the structure of the WIF filter. First of all, we plot in Fig. 3.8 the magnitude value (in dB) of the real and imaginary parts of the optimal WIF (*i.e.* with complex coefficients) for parameters in column "sections 3.5.1 and 3.5.2." of Table. 3.1. One can notice the imaginary part of the WIF is negligible. Hence, the WIF can be approximated by its real filter and therefore, the complexity can be reduced to $N_{OP} = N_s\,(2K_d \cdot \text{MUL} + 2\,(K_d - 1)\,\text{AD})$. In addition, we can also notice the WIF is block multi-diagonal matrix. Moreover, if we neglect the low-power coefficients, the matrix can be defined as a sparse matrix. The question is whether this property can be used to reduce the computational complexity of PN compensation.

Recall that the estimation problem can be considered as an interpolation problem. If we neglect the effects on the carrier edges, there is a regular structure that can be implemented with a symmetrical Finite Impulse Response (FIR) filter. Reusing the approach of [58], we can reduce the number of coefficients per row by searching for a matrix distributed as given by (3.64). We

$$\mathbf{Z} = \begin{bmatrix} \mathbf{Z}_L & \mathbf{0} & & & & \\ \mathbf{Z}_M & \mathbf{0} & & \mathbf{0} & & \\ \mathbf{0} & \mathbf{Z}_M & \mathbf{0} & & & \\ & \ddots & \ddots & \ddots & & \\ & & \mathbf{0} & \mathbf{Z}_M & \mathbf{0} & \\ & & & \mathbf{0} & \mathbf{Z}_M & \mathbf{0} \\ & \mathbf{0} & & & \mathbf{0} & \mathbf{Z}_M \\ & & & & \mathbf{0} & \mathbf{Z}_R \end{bmatrix} \tag{3.64}$$

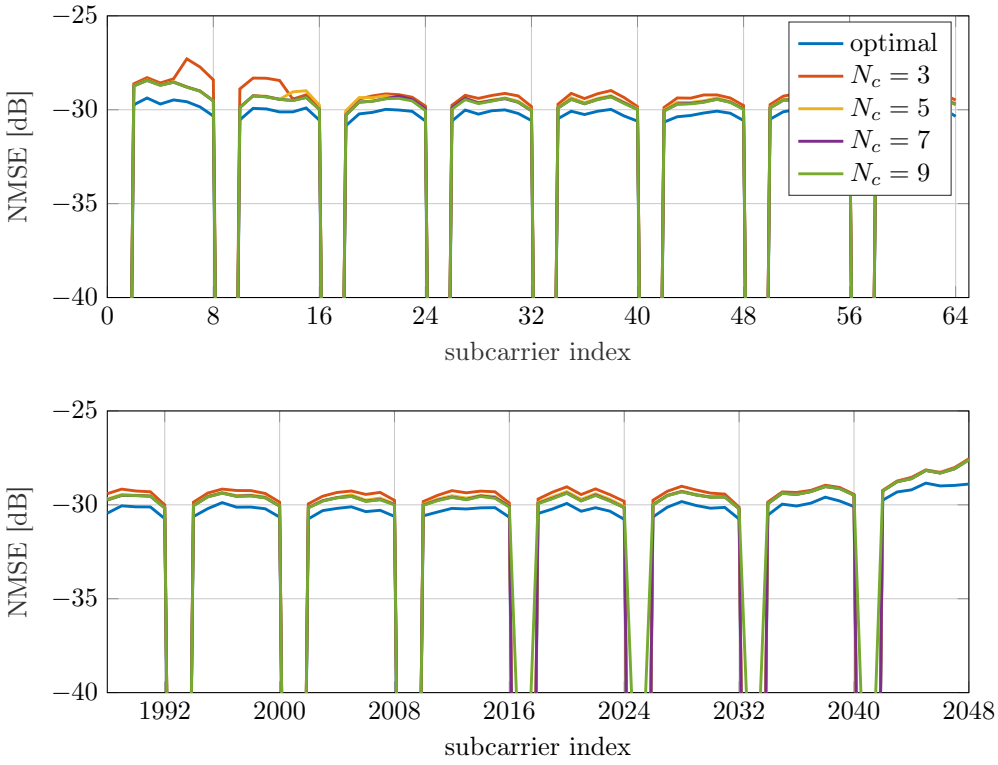


Figure 3.9: NMSE between the low complexity WIF and the optimal WIF.

divide the matrix in three sub-matrices: $\mathbf{Z}_L$ regrouping the coefficients for the left part of the subcarriers, $\mathbf{Z}_M$ for the middle and $\mathbf{Z}_R$ at the right.

We can thus write three optimisation problems, where we seek to minimise the MSE by limiting the number of coefficients in the proposed structure. This problem can be solved with the usual optimization routines. The number of operation can be deduced based on the number of coefficient $N_c$ used. The number of MUL becomes $2N_s \cdot N_c$ and the number of AD is $2N_s\,(N_c - 1)$.

### 3.8.2 Numerical results

Here we present the NMSE per carrier between the low complexity WIF and the optimal one. We consider arbitrarily $N_c = \{3; 5; 7; 9\}$ coefficients for optimization function. The results are depited in Fig. 3.9 considering parameters in column "sections 3.5.1 and 3.5.2." of Table. 3.1 without the thermal noise. One can notice the NMSE is around −30 dB. This validates the possibility to set to zero some coefficients whose contribution to the PN estimation is practically negligible. In addition, Fig. 3.10 presents the computational gain of computing the low complexity WIF instead of the optimal one. One can notice that computing the low complexity with $N_c = 5$ will require one hundred times fewer MUL and AD operations than using the optimal WIF. As a consequence, for a known SNR value, it may be possible to reduce the complexity of the proposed WIF in offline and used it for PN estimation and compensation.

As noted, optimizing the WIF for low computation is done for each SNR. This means an estimation of the SNR before performing the computational optimization in offline. Alternatively, we can imagine doing the WIF once that are valid for a given SNR range.

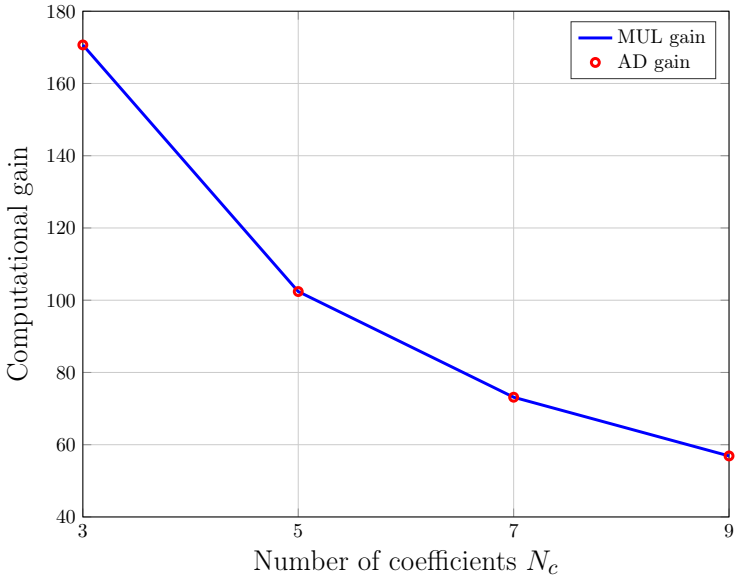


Figure 3.10: Computational gain of the low complexity WIF.

## 3.9 Conclusion

In this chapter, we proposed a PN estimator called WIF. This algorithm relies on the use of the correlation matrix of PN-induced effects. We compared several PN estimation algorithms in the literature with the proposed algorithm which is a new approach w.r.t existing algorithms. We observed that WIF provides a significant performance gain with respect to contenders using low pilot density and does not depend on the PT-RS pattern. For a possible implementation of the WIF algorithm in realistic RF transmission, we derived theoretical expressions of the correlation matrices. Moreover, we showed that it is possible to envisage the implementation of the WIF in realistic RF transmission if the transceiver architecture uses a two-stage high-frequency ramp-up for the baseband-passband transition and conversely. Furthermore, we proposed a special block diagram of a digital baseband DFT-s-OFDM receiver of the D-Band CMOS transceiver designed by CEA. Finally, we proposed a low complexity WIF approach which allows us to envisage an uncomplicated implementation of this latter.

The technical content of this chapter has been approved by the following patent and journal paper:

[C2] **Y. Bello**, J-B. Doré and D. Demmer, *"DFT-s-OFDM for sub-THz Transmission – Tracking and Compensation of Phase Noise,"* In Proc. IEEE Consumer Communications & Networking Conference (CCNC), Nevada, United States of America, pages 297–300, 2023.

[C3] **Y. Bello**, D. Demmer, A. Hamani, A. Siligaris, C. Dehos, N. Cassiau, J-B. Doré and J.L. González-Jiménez, *"Performance Assessment of a 5GNR D-Band Transceiver with Phase Noise Impairments,"* In Proc. Joint European Conference on Networks and Communications & 6G SUMMIT (EuCNC/6G SUMMIT), Goteborg, Sweden, pages 246-251, 2023.

[C4] **Y. Bello**, J-B. Doré and D. Demmer, *"Wiener Interpolation Filter for Phase Noise Estimation in sub-THz Transmission,"* In Proc. IEEE Vehicular Technology Conference

(VTC2023-Spring), Florence, Italy, pages 1-5, 2023.

We showed the OFDM with CPEE algorithm offers the same performance as the DFT-s-OFDM with the WIF for numerlogies higher than seven ($\mu \geq 7$). Nevertheless, OFDM with CPEE is useless considering 5G-NR numerologies while the DFT-s-OFDM with the WIF is more efficient. The WIF allows a performance enhancement of DFT-s-OFDM systems but not for OFDM systems. This is because computing the WIF in OFDM comes back to perform the CPE compensation. The possible reason behind this is the ICI effect is not negligible. To overcome the ICI effect, a first solution considered in this chapter is the increase of the ICS by increasing the numerologies. However, a second solution is to use ICI cancellation techniques while considering the use of today numerologies. Thus, *is the OFDM with ICI cancellation techniques better than the DFT-s-OFDM with the WIF?* We showed the use of PN statistics enhances its estimation and compensation for DFT-s-OFDM systems. Consequently, *is it possible to reduce the ICI effect by using PN statistics in OFDM systems?* These issues will be addressed in the next chapter.

CHAPTER 4

# Pre-FFT Wiener phase noise compensation

## Contents

## 4.1 Introduction

In the previous chapter, we proposed a WIF algorithm for PN mitigation in the frequency-domain. We showed the performance improvement of DFT-s-OFDM systems by considering this proposed technique. Nevertheless, we notice that extending this method to OFDM systems comes back to perform a simply CPE compensation. As well as the CPE, the PN induces ICI [40] which is the main term responsible of the performance degradation of OFDM systems. The increase of ICS by rising the numerology was proposed by the 3GPP to reduce its effects. However, doing that while keeping the 4096 FFT size as defined in 5G-NR, leads to the increase of the sampling frequency [21]. This increase of the sampling frequency will require fast conversion systems that are far beyond the current limits [17]. To avoid that, many contributions propose ICI cancellation techniques to enhance the system performance while keeping 5G-NR numerologies.

Moreover, the hypothesis of flat channels in frequency can be discussed. RF components (such as filter) can bring distortion, and there can be multi-path (ground bounce), especially if the antenna has a large aperture. This means that CEQ as well as PN compensation has to be performed before the detection of received symbols at the receiver. On the one hand, most of the papers in the state-of-the-art only take into account the PN tracking by considering the Channel State Information (CSI) as well known in advance or perfectly estimated [44, 47]. On the other hand, few papers consider that the PN tracking and the CEQ cannot be performed independently because of a poor tracking of the PN due to the channel effects and conversely. So, they propose a joint estimation approach of the two impairments [59]. In [45], the authors propose a pilot pattern associated to an algorithm which allows this joint compensation (PN and then channel). However, this method is efficient for the cases where the channel coherence bandwidth is significantly greater than the number of pilots per group based on the proposed pilot distribution.

### 4.1.1 Motivations and related work

Cancelling the PN in the time-domain has been introduced in [60] and takes up in [61]. [61] demonstrates that considering either the columns of the DFT matrix or those of the DCT matrix as basis vectors as presented in [60], leads to simply mitigate the CPE. To eliminate also the ICI effects, the authors in [61] suggest to build basis vectors with the eigenvectors of the covariance matrix of the PN (assuming a Karhunen-Loève representation of the latter). Unfortunately, imperfect CSI is not considered.

### 4.1.2 Contributions

This chapter highlights the following contributions:

- We propose a new ICI mitigation algorithm called TDF which is based on the stochastic properties of the PN and time signature of the inserted pilots. In contrast to [61], imperfect CSI is considered. PN compensation and CEQ are done independently by considering a simple pilot pattern.
- We consider a Rician fading channel to efficiently emulate a sub-THz channel. Furthermore, we also consider the standard PN model given by the 3GPP [30] (mostly considered in the literature).
- We assess the performance of a 5G-NR OFDM system with LDPC channel coding. We compare our proposed algorithm with classical PN estimation algorithms assuming a realistic channel estimation.

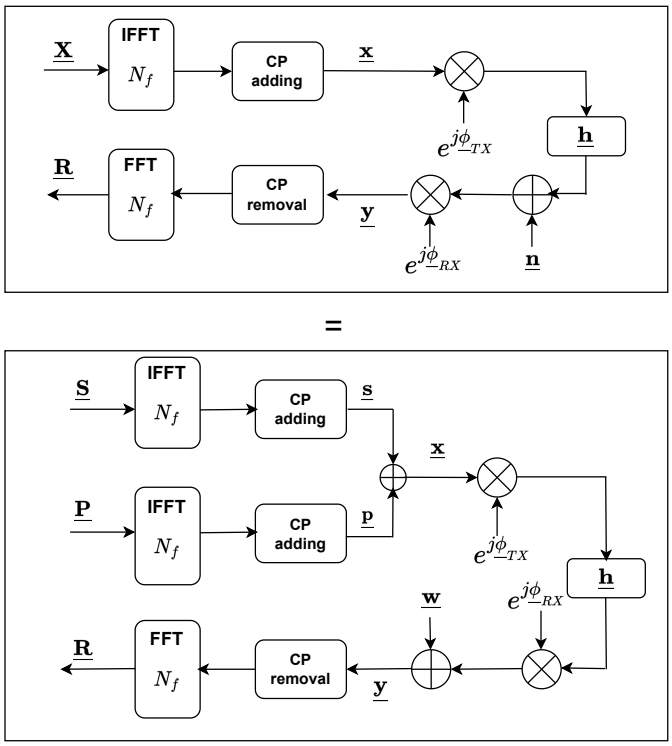


Figure 4.1: OFDM system model

## 4.2 Channel model: Rician model

We consider an OFDM system with the presence of the PN at the transmitter and receiver. We also consider a Rician fading channel with a strong LoS component to model the propagation environment. The choice of this channel model is motivated by the contributions [62, 63]. [62] shows that the use of high gain and directional antennas for RF transmission ensure the most energy contribution of the LoS path. Hence, the channel vector $\underline{\mathbf{h}}$ as follows:

$$\underline{\mathbf{h}} : \begin{cases} \underline{\mathbf{h}}[0] = h_{lp} = 1, \\ \underline{\mathbf{h}}[i] = h_i \backsim \mathbb{C}\mathcal{N}(0, 2\sigma^2), \quad 1 \leq i \leq L_{ds} - 1 \end{cases} \tag{4.1}$$

where $L_{ds}$ denotes the delay spread of the channel. The term $h_{lp}$ is the LoS path component and the $h_i$ are the Non Line-of-Sight (NLoS) paths which follow a Rayleigh distribution. The relation between the power of the LoS path with the power of scattered paths is defined by a factor $K$ defined as follows [64]:

$$K_{[\text{dB}]} = 10\log_{10}\left(\frac{1}{2\sigma^2}\right) = -10\log_{10}\left(2\sigma^2\right) \cdot \tag{4.2}$$

Regarding the PN model, we consider the 3GPP PN model 2 presented in Section 2.2.2 for simulations.

## 4.3 OFDM waveform

### 4.3.1 System model

The expression of the transmitted OFDM symbol $\underline{\mathbf{x}}$ after IFFT and CP insertion is

$$\underline{\mathbf{x}} = \mathbf{M}_{cp}\mathbf{F}_N^H\underline{\mathbf{X}}, \tag{4.3}$$

where $\mathbf{M}_{cp}$ is the CP adding matrix and $\underline{\mathbf{X}}$ is the vector which contains the information symbols $\underline{\mathbf{X}}[k] \in C$, with $C$ representing the set of the selected modulation scheme. Regarding the considered channel model, the expression of the received samples before the CP suppression and FFT is given by:

$$\underline{\mathbf{y}} = e^{j\underline{\phi}_{RX}} \odot \left(\underline{\mathbf{h}} \otimes \left(\underline{\mathbf{x}} \odot e^{j\underline{\phi}_{TX}}\right)\right) + \underline{\mathbf{w}}, \tag{4.4}$$

The terms $\underline{\phi}_{TX}$ and $\underline{\phi}_{RX}$ respectively are the vectors which contain the PN generated by the oscillator at the transmitter and receiver. The vector $\underline{\mathbf{w}} = \underline{\mathbf{n}} \odot e^{j\underline{\phi}_{RX}}$ *s.t.* $\underline{\mathbf{n}}[\tau] \backsim \mathbb{CN}\left(0, \sigma_n^2\right)$ denotes the thermal noise of variance $\sigma_n^2$. We develop the expression (4.4) as bellow

$$\underline{\mathbf{y}}[\tau] = e^{j\underline{\phi}_{RX}[\tau]} \sum_{j=0}^{L_{ds}-1} \underline{\mathbf{h}}[j]\underline{\mathbf{x}}[\tau - j]e^{j\underline{\phi}_{TX}[\tau-j]} + \underline{\mathbf{w}}[\tau], \tag{4.5}$$

and then, we put it in a matrix form as follows:

$$\underline{\mathbf{y}} = \mathbf{\Phi}_R \left(\sum_{j=0}^{L_{ds}-1} h_j \mathbf{U}^{(j)} \mathbf{\Phi}_T \underline{\mathbf{x}}\right) + \underline{\mathbf{w}}, \tag{4.6}$$

where $\mathbf{\Phi}_T$ and $\mathbf{\Phi}_R$ respectively are diagonal matrices which respectively contain the PN shifts $e^{j\underline{\phi}_{TX}}$ and $e^{j\underline{\phi}_{RX}}$ on their diagonal. The term $h_j$ corresponds to the $j^{th}$ channel tap coefficient $\underline{\mathbf{h}}[j]$ and $\mathbf{U}^{(j)}$ is the convolution matrix associated to the $j^{th}$ path. A representation of the system model is depicted in Fig. 4.1.

### 4.3.2 State-of-the-art ICI cancellation technique: the De_ICI algorithm

In [44], the authors propose an ICI cancellation method called De_ICI. It consists in applying an ICI filter to the received signal in the frequency-domain so that it becomes approximately free of ICI. To do so, we firstly compute a sub-sampled convolutional matrix $\mathbf{R}_{L_f}$ of size $T \times L_f$, where $L_f$ is the length of the ICI filter. This matrix contains on each row the received signals on subcarriers above and below the subcarrier where the PT-RS were inserted. Secondly, we define a vector $\underline{\mathbf{V}}$ which contains the product of the channel coefficients in frequency-domain with the inserted PT-RS symbols. Then, we obtain the ICI filter as follows

$$\underline{\mathbf{F}}_{\text{ICI}} = \left(\mathbf{R}_{L_f}^H \mathbf{R}_{L_f}\right)^{-1} \mathbf{R}_{L_f}^H \underline{\mathbf{V}}. \tag{4.7}$$

The received signal after ICI filtering is obtained as follows

$$\underline{\mathbf{R}}' = \underline{\mathbf{R}} \otimes \underline{\mathbf{F}}_{\text{ICI}}. \tag{4.8}$$

**Important note 7.** *The knowledge of the channel frequency response coefficients is necessary to perform the "De_ICI" algorithm.*

### 4.3.3 Proposed PN compensation algorithm

The presence of PN deteriorates the system performance. Indeed, in the case of OFDM systems, its presence induces a CPE and ICI. These CPE and ICI need to be cancelled in order to enhance the system performance. For the CPE compensation, a low complexity algorithm called CPEE can be performed [45]. It consists in averaging the observations made on PT-RS for CPE estimation. This technique can be sufficient to improve the system performance if the ICS is

large enough to avoid ICI effects. Otherwise, ICI cancellation techniques are required: that is the case if we envisage reusing 5G-NR numerologies for sub-THz frequencies as highlighted in the previous chapter. Some algorithms are presented in the literature where the ICI is compensated in the frequency-domain (*i.e.* after the FFT at the reception) [43, 44, 47].

We present in this section a new ICI mitigation technique based on the correlation nature of the PN. In the previous chapter, we propose a Wiener filter estimator in frequency-domain to compensate the PN effects in OFDM systems. Unfortunately, this estimator may prove useless when the ICI-induced degradation becomes non negligible. We now propose to extend the latter to the time-domain (*i.e.* before the FFT at the reception) by using the superposition property of the time-domain signal generated from inserted pilots and the one generated by data. By doing this, our aim is to reduce the effects of the PN on the received signal and therefore the impact of CPE and ICI as well. To do so, we look for a linear filter such that

$$\underset{\mathbf{Z}}{\operatorname{argmin}}\ \mathbb{E}\left[\left\|\mathbf{Z}\,\underline{\mathbf{y}} - e^{j\underline{\boldsymbol{\phi}}}\right\|^2\right], \tag{4.9}$$

where $\underline{\boldsymbol{\phi}} = \underline{\boldsymbol{\phi}}_{TX} + \underline{\boldsymbol{\phi}}_{RX}$. Regarding PT-RS insertion, let us denote $\chi_p$ (resp. $\chi_s$) as the set which contains subcarrier indexes where PT-RS symbols (resp. information symbols) are inserted. So, we can write the transmitted vector in (4.3)

$$\underline{\mathbf{X}} = \underline{\mathbf{S}} + \underline{\mathbf{P}}, \tag{4.10}$$

such that

$$\underline{\mathbf{S}} = \begin{cases} \underline{\mathbf{S}}[k] & \forall k \in \chi_s \\ 0 & \text{otherwise} \end{cases} \quad \text{and} \quad \underline{\mathbf{P}} = \begin{cases} \underline{\mathbf{P}}[k] & \forall k \in \chi_p \\ 0 & \text{otherwise} \end{cases} \tag{4.11}$$

where $\underline{\mathbf{S}}$ and $\underline{\mathbf{P}}$ respectively represent the transmitted signal vector and the PT-RS vector. From (4.1), the expression (4.6) can be written as:

$$\begin{aligned} \underline{\mathbf{y}} &= h_{lp}\boldsymbol{\Phi}_R\boldsymbol{\Phi}_T\underline{\mathbf{x}} + \boldsymbol{\Phi}_R\left(\sum_{i=1}^{L_{ds}-1} h_i\mathbf{U}^{(i)}\boldsymbol{\Phi}_T\underline{\mathbf{x}}\right) + \underline{\mathbf{w}} \\ &= \boldsymbol{\Phi}\underline{\mathbf{x}} + \boldsymbol{\Phi}_R\left(\sum_{i=1}^{L_{ds}-1} h_i\mathbf{U}^{(i)}\boldsymbol{\Phi}_T\underline{\mathbf{x}}\right) + \underline{\mathbf{w}}, \end{aligned} \tag{4.12}$$

where $\boldsymbol{\Phi} = \boldsymbol{\Phi}_R\boldsymbol{\Phi}_T$ and $h_{lp} = 1$ [1]. The first term represents the LoS path. According to the simplified system model in Fig. 4.1 and by replacing (4.10) in (4.3), the expression (4.12) becomes:

$$\underline{\mathbf{y}} = \boldsymbol{\Phi}\underline{\mathbf{s}} + \boldsymbol{\Phi}\underline{\mathbf{p}} + \boldsymbol{\Phi}_R\left(\sum_{i=1}^{L_{ds}-1} h_i\mathbf{U}^{(i)}\boldsymbol{\Phi}_T\left(\underline{\mathbf{s}} + \underline{\mathbf{p}}\right)\right) + \underline{\mathbf{w}}. \tag{4.13}$$

**Important note 8.** *By assuming that (i) the channel taps $h_i, \forall i \in \{1, \cdots, L_{ds}-1\}$ are known, (ii) the vectors $\underline{\mathbf{s}}$ and $\underline{\mathbf{w}}$ are zero-mean processes, (iii) the channel taps are not correlated and (iv) the transmitted signal and the PN are independent, the expression of the*

[1] It is obvious that there is an amplitude and phase term for the LoS. The phase term will be corrected by the channel estimation.

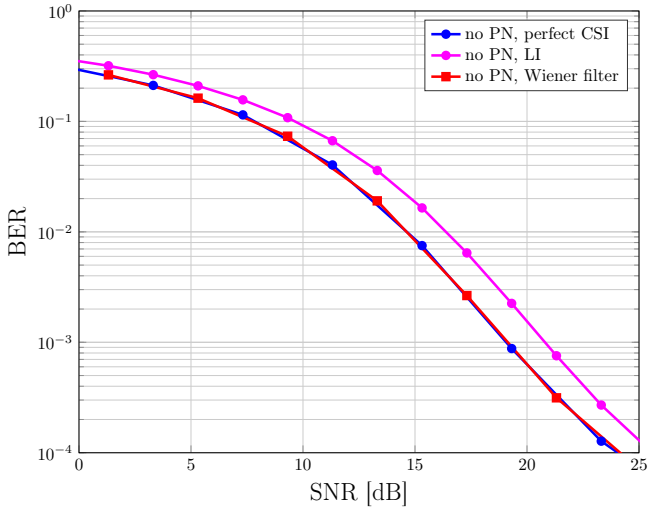


Figure 4.2: Uncoded BER as a function of SNR. Rician channel with $K = 15$ dB and 16-QAM are considered. The other simulation parameters are depicted in Table 4.1

*TDF, solution of (4.9) is defined as follows:*

$$\mathbf{Z} = \left(\mathbf{A}_{LoS}^H + \sum_{i=1}^{L_{ds}-1} h_i^* \mathbf{B}_i^H\right) \mathbf{C}^\dagger, \tag{4.14}$$

*where* $\mathbf{C} = \mathbf{E}^H + \mathbf{G}^H + \mathbf{R}_{\underline{\mathbf{w}}}^H$. *The matrices* $\mathbf{A}_{LoS}$, $\mathbf{B}_i$, $\mathbf{E}$ *and* $\mathbf{G}$ *are defined in (4.15) by*

$$\begin{aligned}
\mathbf{A}_{LoS} &= \mathbf{R}_{e^{j\underline{\phi}}} \odot \left(\underline{\mathbf{p}} \cdot \underline{\mathbf{1}}_N^H\right), \quad \mathbf{B}_i = \mathbf{R}_{e^{j\underline{\phi}_{RX}}} \odot \left(\mathbf{U}^{(i)} \mathbf{R}_{e^{j\underline{\phi}_{TX}}}\right) \odot \left(\mathbf{U}^{(i)} \underline{\mathbf{p}} \cdot \underline{\mathbf{1}}_N^H\right), \quad \mathbf{E} = \mathbf{R}_{e^{j\underline{\phi}}} \odot \left(\mathbf{R}_{\underline{\mathbf{s}}} + \underline{\mathbf{p}} \cdot \underline{\mathbf{p}}^H\right) \\
\mathbf{G} &= \sum_{i=1}^{L_{ds}-1} |h_i|^2 \mathbf{R}_{e^{j\underline{\phi}_{RX}}} \odot \left(\mathbf{U}^{(i)} \mathbf{R}_{e^{j\underline{\phi}_{TX}}} \mathbf{U}^{(i)H}\right) \odot \left(\mathbf{U}^{(i)} \left(\mathbf{R}_{\underline{\mathbf{s}}} + \underline{\mathbf{p}} \cdot \underline{\mathbf{p}}^H\right) \mathbf{U}^{(i)H}\right).
\end{aligned} \tag{4.15}$$

The terms $\mathbf{R}_{e^{j\underline{\phi}}}$, $\mathbf{R}_{e^{j\underline{\phi}_{RX}}}$ and $\mathbf{R}_{e^{j\underline{\phi}_{TX}}}$ respectively are the correlation matrices of $e^{j\underline{\phi}}$, $e^{j\underline{\phi}_{RX}}$ and $e^{j\underline{\phi}_{TX}}$. $\mathbf{R}_{\underline{\mathbf{s}}}$ and $\mathbf{R}_{\underline{\mathbf{w}}}$ for their part, respectively represent the auto-correlation matrices of $\underline{\mathbf{s}}$ and $\underline{\mathbf{w}}$.

#### 4.3.3.1 Assumption

As observed in (4.14), the knowledge of the channel taps in the time-domain (*i.e.* $h_i$) is required to compute the TDF. Assuming that, we have two options:

- **we can assume the channel is perfectly known:** this case is mostly taken in the literature [44, 47] but can be considered as a non realistic approach.
- **we can estimate these channel taps:** by estimating the channel coefficients in the frequency-domain and compute the IFFT operation to recover the channel tap in the time-domain. However, this estimation will be noisy due to the presence of the PN (and inevitable thermal noise) and will increase the complexity.

In order to simplify this channel estimation step, we will consider the scattered paths contribution is negligible in front of the LoS path contribution (despite the presence of NLoS paths), *i.e.* a

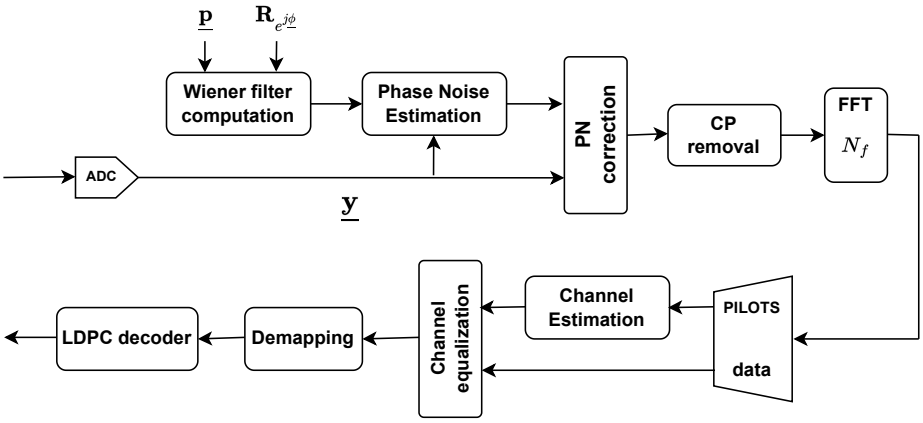


Figure 4.3: Block diagram of the receiver

large $K$ factor. In that case, the expression (4.14) of the TDF does not depend on the channel information at all and will be obtained by doing:

$$\mathbf{Z} = \mathbf{A}_{LoS}^{H}\mathbf{C}^{\dagger}, \tag{4.16}$$

where $\mathbf{C} = \mathbf{E}^{H} + \mathbf{R}_{\underline{\mathbf{w}}}^{H}$. Finally, we estimate the PN vector as follows:

$$\underline{\hat{\phi}} = \arg\left(\mathbf{Z} \cdot \underline{\mathbf{y}}\right) \cdot \tag{4.17}$$

Therefore, the expression of the received OFDM symbol in the time-domain after PN compensation is:

$$\underline{\hat{\mathbf{y}}} = \underline{\mathbf{y}} \odot e^{-j\underline{\hat{\boldsymbol{\phi}}}}. \tag{4.18}$$

### 4.3.4 Channel estimation and equalization method

After the PN compensation, we remove the CP and we perform the FFT. The received OFDM signal in the frequency-domain is obtained as follows:

$$\underline{\mathbf{R}} = \mathbf{F}_{N_f}\mathbf{D}_{cp}\underline{\hat{\mathbf{y}}}, \tag{4.19}$$

where $\mathbf{D}_{cp}$ is the CP withdrawal matrix. Then, we compute the channel estimation on pilot observations. In Fig 4.2, we present the uncoded BER of an OFDM system without PN and transmitting through a Rician channel (cf. Sec. Section 4.2) with $K$=15 dB. We compare two channel estimation approaches: (i) the Wiener filter [58] and (ii) the LI. We compare them with the case without PN and assuming a perfect knowledge of the channel ("no PN, perfect CSI"). Since the Wiener filter outperforms the LI in Fig 4.2, we choose to carry out the channel estimation by using a Wiener filter as presented in [58] after the PN mitigation with the TDF. We equalize the channel effects with a Zero Forcing (ZF) equalizer as follows

$$\underline{\hat{\mathbf{R}}}[k] = \underline{\mathbf{R}}[k]\frac{\underline{\hat{\mathbf{H}}}^{*}[k]}{\left|\underline{\hat{\mathbf{H}}}[k]\right|^{2}}, \tag{4.20}$$

The term $\underline{\hat{\mathbf{H}}}$ represents the estimated channel vector in the frequency-domain. The block diagram of the proposed digital receiver is illustrated in Fig. 4.3.

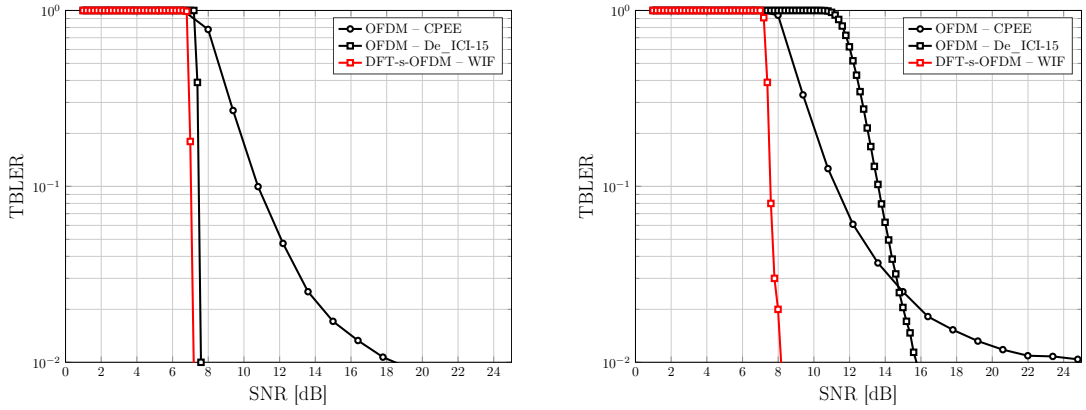


(a) Inserted PT-RS every $L = 8$ ($\mathcal{D} = 12.5\%$) (b) Inserted PT-RS every $L = 64$ ($\mathcal{D} = 1.56\%$)

Figure 4.4: Performance comparison between OFDM and DFT-s-OFDM.

## 4.4 Performance assessment

### 4.4.1 Comparison of DFT-s-OFDM with WIF vs. OFDM with De_ICI

For the performance assessment, we consider the simulation parameters listed in column "sections 3.5.1 and 3.5.2" of Table. 3.1. Fig. 4.4 presents a performance comparison between OFDM and DFT-s-OFDM systems in terms of TBLER as a function of the SNR. The PN estimation algorithms considered for OFDM are the CPEE and the De_ICI. For the De_ICI algorithm, we choose an ICI filter of size $L_f = 15$. LDPC codes are also considered for the channel coding. The distributed PT-RS pattern in Section 3.2.2 is considered with pilots inserted every $L = 8$ subcarriers in Fig. 4.4a and every $L = 64$ subcarriers in Fig. 4.4b, where $L$ is the spacing between two PT-RS symbols. The estimation is done on noisy received pilots and the pilot density is given for each OFDM symbol by

$$\mathcal{D} = \frac{1}{L} \times 100 \ [\%]\cdot \tag{4.21}$$

In Fig. 4.4a, one can notice the OFDM with the De_ICI algorithm outperforms the one with CPEE only. This means the ICI effect is not negligible. Regarding the DFT-s-OFDM, the proposed WIF is 0.4 dB more efficient than OFDM with De_ICI.

In Fig. 4.4b, one can remark the OFDM with the De_ICI algorithm still outperforms the one with the CPEE. Additionally, the DFT-s-OFDM with the WIF is now 7.5 dB more efficient than OFDM with the De_ICI at a TBLER of $10^{-2}$. Indeed, decreasing the pilot density increases the space between inserted PT-RS symbols. So, the ICI filter cannot catch a sufficient information from subcarriers adjacent to compute a good ICI filtering and therefore, a good ICI cancellation.

**Important note 9.** *DFT-s-OFDM may therefore be a more effective solution than OFDM in very low pilot density with the proposed WIF algorithm.*

### 4.4.2 OFDM Performance Comparison: TDF vs. De_ICI

In this section, we now present the performance of an OFDM system considering the Rician channel presented in Section 4.2. We consider our proposed TDF algorithm and the following state-of-the-art algorithms: the CPEE and the De_ICI algorithms. For the numerical results, we denote "De_ICI-9" (resp. "De_ICI-17") as the use of the "De_ICI" algorithm with an ICI filter size $L_f$=9 (resp. $L_f$=17).

Table 4.1: Simulation parameters

| | |
|---|---|
| Modulation | 16-QAM, 64-QAM |
| Phase noise model | 3GPP Model 2 |
| Carrier frequency | $F_c$ = 140 GHz |
| $N_f$ | 4096 |
| $\Delta_f$ | 120 kHz |
| $N_a$ | 3072 subcarriers |
| Pilot density | 25% |
| Coding scheme | 3GPP LDPC |
| Coding rate | $\{0.3; 0.5; 0.7; 0.9\}$ |
| Channel model | Rician (4.2) |
| $K$ [dB] | $\{10; 15; 20; 25\}$ |
| Delay spread | 10.17 ns |
| Cyclic prefix | 64 samples (0.13 $\mu$s) |

**Important note 10.** *Regarding the De_ICI algorithm which requires an a-priori knowledge of frequency-domain channel coefficients, we assume the channel estimation is done upon noisy received pilots in the frequency-domain before the ICI filtering. After computing the ICI mitigation algorithm, we do the CEQ before the symbol detection.*

The system performance are evaluated in terms of TBLER, more precisely the SNR which allows to achieve a TBLER of $10^{-2}$. The SNR is plotted as a function of the SE which is defined by the following product

$$\text{SE} = \log_2(M_s) \cdot \text{CR}, \tag{4.22}$$

where $M_s$ and CR respectively are the modulation order and the LDPC CR. We consider an OFDM system with simulation parameters depicted in Table 4.1. The presented algorithms are compared to the case without the presence of PN and considering a channel estimation using the Wiener filter [58] ("no PN, estimated CSI"). We also compared them with the case where we only compute the channel estimation (*i.e.* without PN compensation) denoted by "CEQ only" in numerical results. Regarding the TDF algorithm, an *a-priori* knowledge of correlation matrices $\mathbf{R}_{e^{j\underline{\phi}}}$, $\mathbf{R}_{\underline{\mathbf{s}}}$ and $\mathbf{R}_{\underline{\mathbf{w}}}$ is considered for the linear filter computation.

Fig 4.5 presents the system performance at the carrier frequency of 140 GHz considering different values of $K$ defined in (4.2). One can notice for $K$=10 dB, our proposed algorithm outperforms the others in low SE. Nevertheless, no algorithms can reach the targeted TBLER in high SE. On the other hand, our proposed algorithm is the only one that achieves the targeted TBLER at high SE for $K$=15 dB. We make the same observation for $K$=$\{20, 25\}$ dB (the Rician channel tends towards an AWGN channel). One can remark that doing the CPE compensation before the CEQ is not necessary because the "CEQ only" and CPEE give the same results. Additionally, one can observe in low SE, the "CEQ only" outperforms the "De_ICI" algorithm. This is because the "De_ICI" algorithm estimates a noisy ICI filter due to the bad

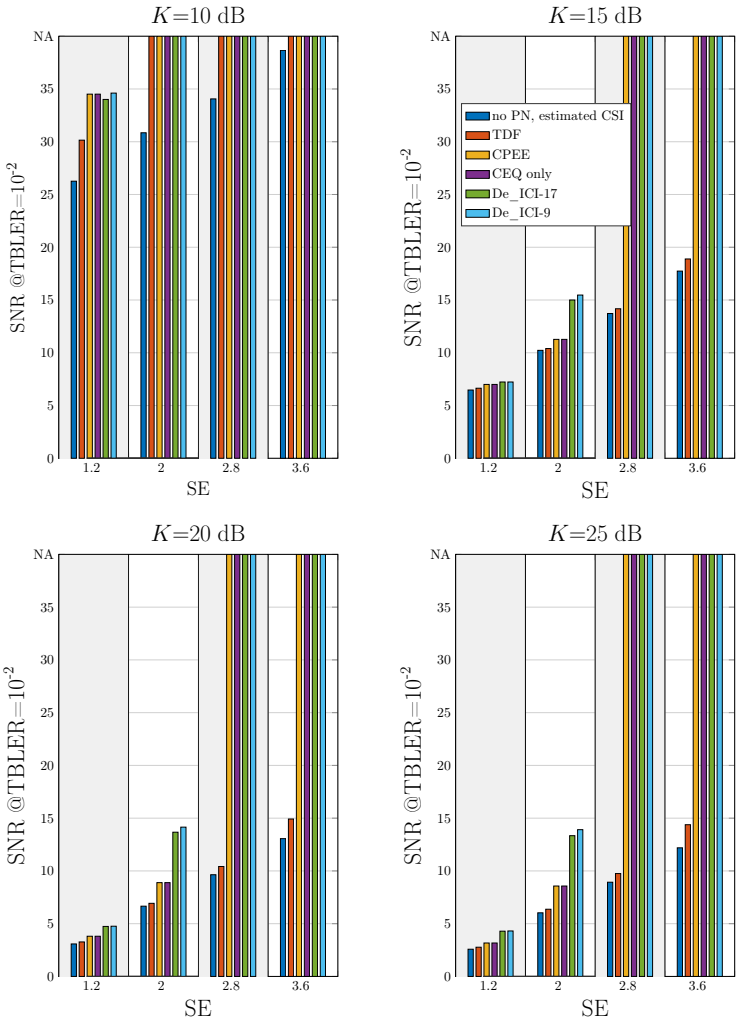


Figure 4.5: SNR [dB] values to achieve a TBLER of $10^{-2}$ as a function of the SE for $F_c$=140 GHz. 16-QAM modulation scheme is considered and different values of $K$ are considered. "NA" stands for "Non Achievable".

estimation of channel coefficients (because of the presence of the PN). Although the increase of the $K$ value, the "De_ICI" cannot reach the target TBLER. This shows that without a perfect knowledge of CSI, the "De_ICI" is not appropriate to cancel the ICI properly.

## 4.5 Performance and optimization of the proposed algorithm

### 4.5.1 Optimization of the pilot signature envelope

For the work presented above, we considered QPSK symbols as PT-RS symbols. When we observe the time-domain envelope of the pilots in Fig. 4.6, one can notice a significant fluctuations with values very close to zero at given instants for QPSK PT-RS symbols. This is not ideal for our PN estimator because it relies on this pilot time signature, as evident in (4.14) and (4.15). Thus, we propose to optimize the time-domain signature of the pilots. The idea is to find a frequency-domain pilot sequence that minimizes the fluctuation of the temporal signal generated by them. To do so, we first define the vector $\underline{\mathbf{P}}$ in (4.10) by

$$\underline{\mathbf{P}} = \mathbf{G}_P \check{\underline{\mathbf{P}}}, \tag{4.23}$$

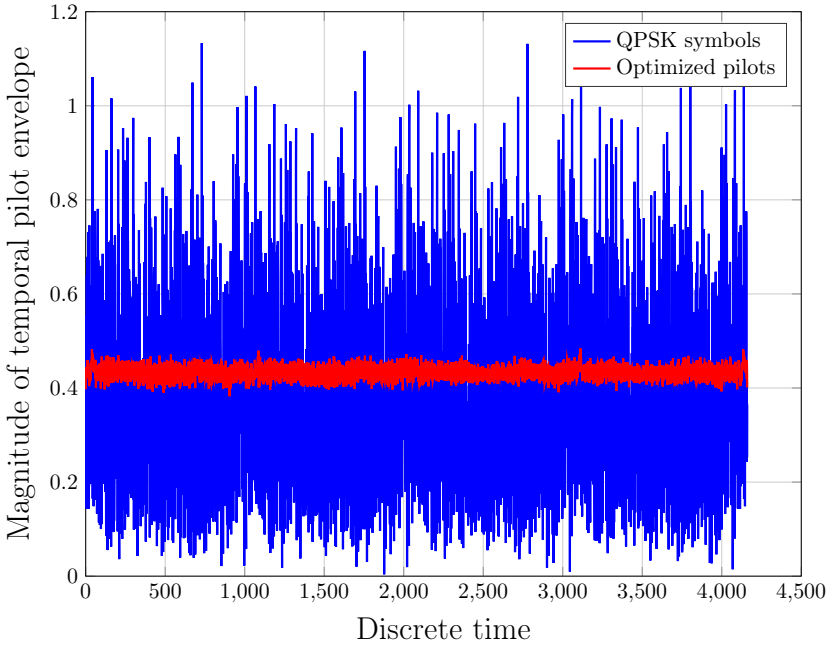


Figure 4.6: QPSK vs. optimized PT-RS symbols

where $\mathbf{G}_P$ is a $K_d$-to-$N_f$ mapping matrix of size $N_f \times K_d$ and $\underline{\check{\mathbf{P}}}$ is the PT-RS vector of size $K_d \times 1$. Let define $\underline{\check{\mathbf{P}}}[m] = e^{j\xi_m}$ as the new form of inserted PT-RS symbols. The objective is to find the $\xi_m$ such that

$$\underset{\xi_m}{\operatorname{argmin}} \left( \max \left( |\underline{\mathbf{p}}|^2 \right) - \min \left( |\underline{\mathbf{p}}|^2 \right) \right), \quad \forall m \in \chi_p. \tag{4.24}$$

The time-domain signature of the optimized PT-RS symbols is depicted in Fig. 4.6. One can notice the small fluctuations of the optimized temporal envelope compared to the QPSK one. Additionally, we don't have anymore some values close to zero.

### 4.5.2 New expression of the time-domain filter

We propose to determine a new TDF expression independent of the pilot signature. To do so, we divide the received signal $\underline{\mathbf{y}}$ by the pilot as follows

$$\underline{\check{\mathbf{y}}}[i] = \frac{\underline{\mathbf{y}}[i]\underline{\mathbf{p}}^*[i]}{\left|\underline{\mathbf{p}}[i]\right|^2}, \quad \forall i \in \{0, \cdots, N' - 1\}. \tag{4.25}$$

**Important note 11.** *It should be noticed that dividing the received signal by the time signature of pilots $|\underline{\mathbf{p}}[i]|^2$ could lead to a "noise amplification". Consequently, the use of a low time envelope variation of pilot will limit this phenomenon.*

Then, we look for an estimator $\check{\mathbf{Z}}$ such that

$$\check{\mathbf{Z}} = \underset{\mathbf{Z}}{\operatorname{argmin}}\ \mathbb{E}\left[ \left\| \mathbf{Z}\, \underline{\check{\mathbf{y}}} - e^{j\underline{\boldsymbol{\phi}}} \right\|^2 \right]. \tag{4.26}$$

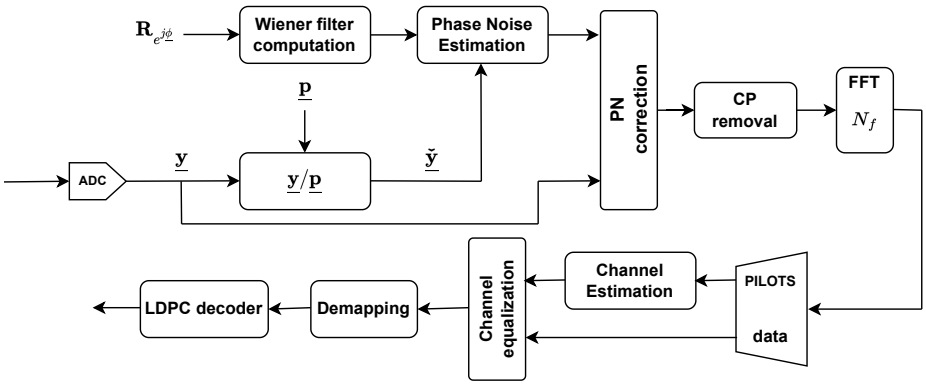


Figure 4.7: New block diagram of the receiver

By keeping the assumption made in Section 4.3.3.1, the new TDF expression is given by

$$\check{\mathbf{Z}} = \mathbf{A}_{LoS}^{H}\mathbf{C}^{\dagger}, \quad s.t \begin{cases} \mathbf{A}_{LoS} = \mathbf{R}_{e^{j\underline{\phi}}}, \\ \mathbf{C} = \mathbf{E}^{H} + \mathbf{R}_{\underline{\mathbf{w}}}^{H}, \\ \mathbf{E} = \mathbf{R}_{e^{j\underline{\phi}}} \odot \left(\mathbf{R}_{\underline{\mathbf{s}}} \odot \mathbf{I}_{N'} + \mathbf{1}_{N'}\right) \cdot \end{cases} \tag{4.27}$$

Obviously, we estimate the PN vector as follows

$$\hat{\underline{\phi}} = \arg\left(\check{\mathbf{Z}} \cdot \check{\underline{\mathbf{y}}}\right) \cdot \tag{4.28}$$

Therefore, the expression of the received OFDM symbol in the time-domain after PN compensation is

$$\hat{\underline{\mathbf{y}}} = \underline{\mathbf{y}} \odot e^{-j\hat{\underline{\phi}}}. \tag{4.29}$$

The new block diagram of the digital receiver is shown in Fig. 4.7.

### 4.5.3 Numerical results

In this section, we present the performance of the OFDM system considering QPSK symbols and optimized vector $\check{\underline{\mathbf{P}}}$ as PT-RS. The Rician channel presented in Section 4.2 is taken with $K = \{20; 30\}$ dB. Hence, we perform a Wiener filter and a ZF for channel estimation and equalization. The 3GPP PN model 2 in Section 2.2.2 is considered and the following system parameters: $F_c = 140$ GHz, $F_s = 491.52$ MHz, $N_f = 4096$, $N_a = 3072$, $M_s = 16$-QAM, delay spread of 10.17 ns and a $N_{CP} = 64$ samples ($0.13\mu s$). The distributed PT-RS pattern in Fig. 3.2a is chosen. We denote "TDF + CEQ" the computation of the TDF expression (4.16) in time-domain with CEQ in frequency-domain. Similarly, "new TDF + CEQ" means the computation of the new TDF expression (4.27) in time-domain with CEQ in the frequency-domain.

Fig. 4.8a shows the performance comparison when QPSK symbols and optimized vector $\check{\underline{\mathbf{P}}}$ are used as PT-RS considering $K = 20$dB. Concerning the TDF expression, one can notice that using QPSK symbols outperforms the use of the optimized PT-RS symbols. This is due to the more power (represents by the term $\underline{\mathbf{p}} \cdot \underline{\mathbf{p}}^{H}$ in (4.15)) of the time signature of QPSK compared to the optimized PT-RS, infront of the scattered channel taps $|h_i|^2$. So, the hypothesis of neglecting the scattered channel taps made in Section 4.3.3.1 is acceptable when QPSK symbols are considered but not for the optimized PT-RS.

When it comes to the new TDF expression, one can notice that computing the new TDF with the optimized pilots vector $\check{\underline{\mathbf{P}}}$ provides better performance than computing the new TDF with QPSK symbols. Indeed, the time-domain signature of QPSK pilots fluctuates enormously

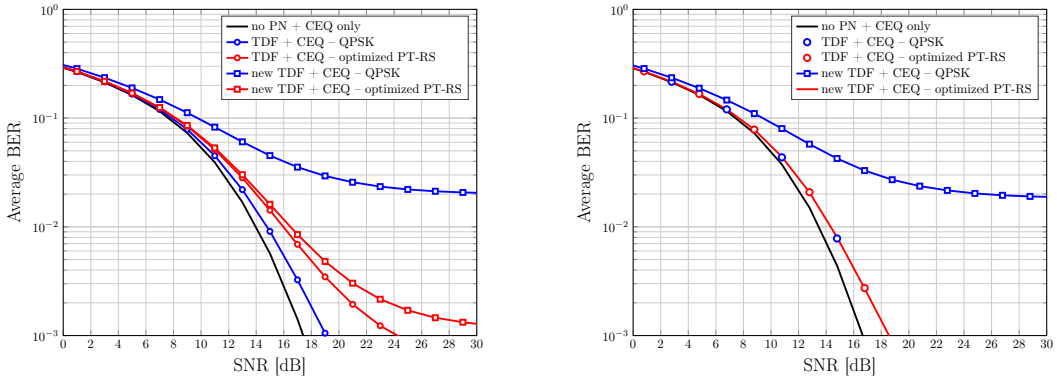


(a) $K = 20$ dB (b) $K = 30$ dB

Figure 4.8: OFDM system performance with $\mathcal{D} = 25\%$.

(cf. Fig. 4.6) with values $\left|\underline{\mathbf{p}}\right|$ very close to zero at given instants. Thus, dividing the received signal by the time envelope of pilots will amplify the channel tap coefficients $h_i$. Consequently, the assumption of neglecting the channel taps becomes no more acceptable and therefore, the PN estimation is noisier. In contrast, the time sequence of the optimized pilots $\underline{\check{\mathbf{P}}}$ shows very low fluctuations with practically constant values. Hence, the channel coefficients $h_i$ will be less amplified and therefore, the PN estimation will be better.

Fig. 4.8b shows the performance comparison when QPSK symbols and optimized vector $\underline{\check{\mathbf{P}}}$ are used as PT-RS considering $K = 30$dB. One can remark that using the optimized PT-RS symbols with either the TDF or the new TDF returns the same performance. Moreover, it gives the same performance as the TDF with QPSK symbols. This is because for $K = 30$ dB, the channel taps $h_i$ are sufficiently negligible. Nevertheless, the new TDF with QPSK symbols is always the worst compared to the new TDF with the optimized PT-RS symbols.

Fig. 4.9 highlights the impact of the pilot density defined in (4.21) on the system performance. We notice that reducing the pilot density deteriorates the system performance. This observation comes from the data-to-noise pilot. The expression of the new TDF in (4.27) depends on the correlation matrix of the time sequence of data $\mathbf{R}_{\underline{\mathbf{s}}}$. This matrix gives the power of the time sequence of data within the time-domain received signal and represents the power of the noise

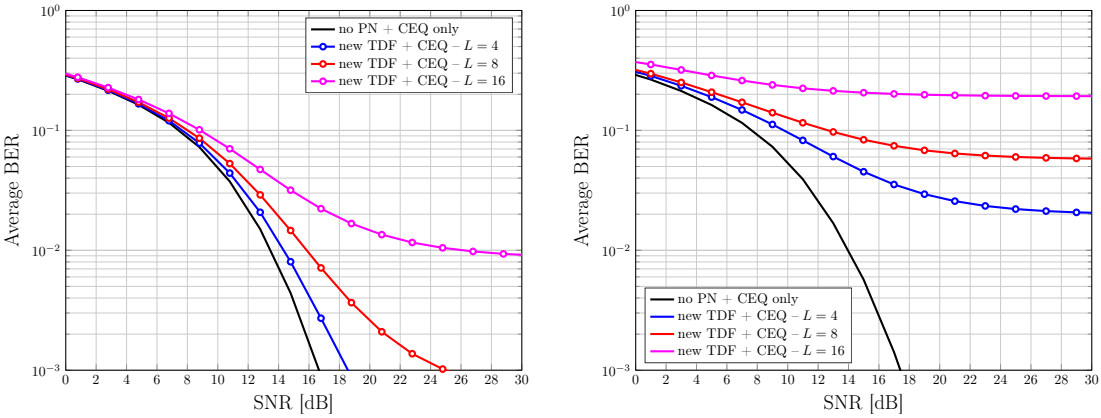


(a) New TDF considering optimized PT-RS vector. (b) New TDF considering QPSK symbols as PT-RS.

Figure 4.9: OFDM system performance with new TDF in (4.27) for different pilot density and a $K$-factor of 30 dB

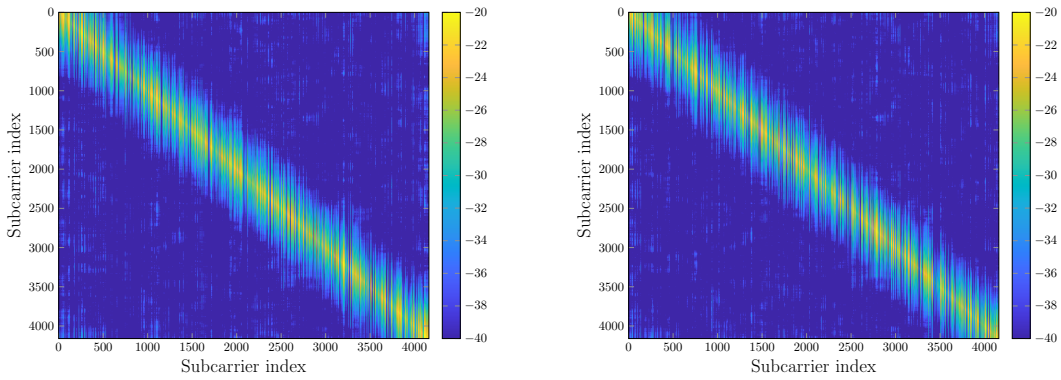


(a) Real part of the TDF

(b) Imaginary part of the TDF

Figure 4.10: Illustration of the power of TDF coefficients in [dB].

upon the time sequence of pilots. Thus, decreasing the pilot density in the frequency-domain increases the power of the time sequence of data. Thankfully, Fig. 4.9a highlights that decreasing the pilot density up to $\mathcal{D} = 12.5\%$ achieves an average BER of $10^{-3}$ with the optimzed PT-RS vector while the QPSK PT-RS symbols cannot as depicted in Fig. 4.9b.

### 4.5.4 Complexity evaluation

Here, we discuss about the computational complexity of the TDF in (4.16) and new TDF in (4.27). We plot in Fig. 4.10 the magnitude (in dB) of the real and imaginary parts of the TDF derived in (4.16). we notice that both real and imaginary part of the TDF are practically identical. Additionally, we remark that the TDF is a hollow matrix. As a consequence, it could be possible to reduce the computational complexity of the TDF by reducing the number of coefficients per row as presented in Section 3.8. Furthermore, we also highlight the magnitude (in dB) of the real part and the imaginary part of the new TDF in Fig. 4.11. In contrast to the TDF form in Fig. 4.10, we remark that the new TDF can be reduced to its real part. Also, its real part is a hollow matrix. So, we can envisage to reduce its computational complexity as demonstrated in Section 3.8 with less coefficients than the complex TDF. The performance evaluation of low computational TDF is left as study perspective.

In conclusion to the results presented in this section, for $K = 20$ dB, performing the TDF

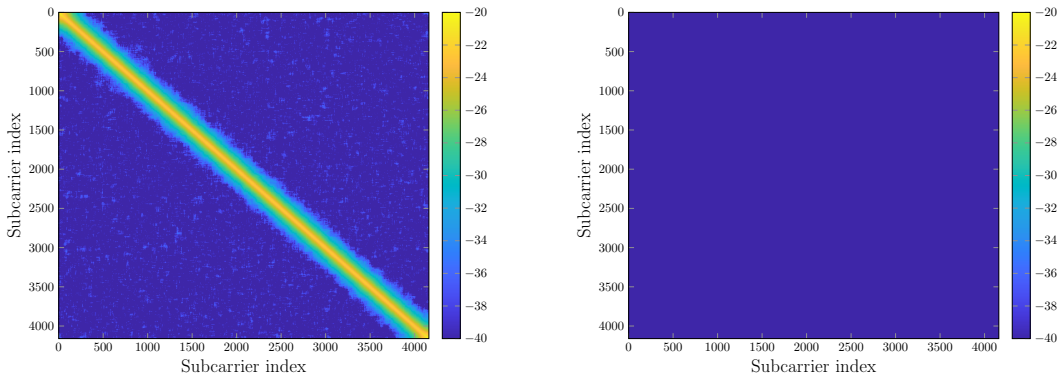


(a) Real part of the new TDF

(b) Imaginary part of the new TDF

Figure 4.11: Illustration of the power of new TDF coefficients in [dB].

in (4.16) with QPSK symbols as PT-RS is better than computing the new TDF in (4.27) with the optimized PT-RS. But, it will require two times more operations (real multiplications and additions) compared to the computation of the new TDF with the optimized PT-RS.

Otherwise for $K = 30$ dB (*i.e* the Rician channel tends towards a LoS channel), computing the new TDF with the optimized PT-RS will be the choice to provide good results and low computational complexity.

## 4.6 Conclusion

In this chapter, we proposed a PN estimation and compensation algorithm in the time-domain named TDF. This algorithm relies on the use of PN statistics and helps mitigate the CPE and ICI effects in the frequency-domain. We highlighted that the proposed TDF algorithm can be applied in OFDM systems when the time-domain signature of PT-RS symbols is known. Obviously, this algorithm can be also used in DFT-s-OFDM systems. We assessed the OFDM system performance by challenging the proposed TDF with PN estimation and compensation algorithms derived in the literature. We demonstrated the effectiveness of TDF compared with these algorithms under a Rician channel propagation which can be considered as a realistic channel model for sub-THz and THz transmission. We outlined the impact of the pilot density in computing the TDF, and the possibility of reducing the complexity by applying the approach presented in Section 3.8.

The technical contributions of this chapter have been approved by the following conference paper.

[C5] **Y. Bello**, J-B. Doré and D. Demmer, *"Time Domain Phase Noise Mitigation in OFDM Systems for Sub-THz Bands,"* In Proc. IEEE Global Communications Conference (GLOBECOM), Kuala Lumpur, MY, 2023.

[J2] **Y. Bello**, J-B. Doré and David Demmer, *"Low Complexity Time Domain Filtering of Phase Noise in OFDM Systems,"* **submitted**, 2023.

As demonstrated so far, it is possible to track and estimate the PN effects when this latter has a correlated nature. However, [24] demontrates that for large bandwidths usage as expected for 6G, the PN will be mostly represented by its uncorrelated part. Thereby, *What happens when the PN has an uncorrelated nature?* To answer this question, we will study the case where the PN follows a Gaussian process in the next chapter. We will present a new approach for the PN estimation and compensation.

# Part IV

# Optimization of Receivers based on 5G-NR Multicarrier waveforms : Uncorrelated PN

CHAPTER 5

# 5G-NR MC waveforms with Gaussian phase noise

## Contents

## 5.1 Introduction

Transmitting in the sub-THz bands presents some limitations among them, the PN generated by oscillators. The PN is caused by random fluctuations of the oscillator's components. The severity of this PN amplifies as the carrier frequency increases, posing a significant deterioration of system performance, particularly when transmitting in sub-THz frequencies. In chapter 2, we showed that PN consists of two parts: one correlated (the Wiener part) and one uncorrelated (the flat part). Up to now, we have considered that the correlated part of the PN is the most dominant (as in most of the literature). This has enabled us to propose algorithms for estimating and compensating the latter. However, the contributions [24,65] show that if we consider increasing the system bandwidth as envisaged in 6G for achieving higher data rates, the uncorrelated part of the PN will be as dominant as the correlated part, or even more so. Moreover, current PN compensation techniques will at best only be able to compensate the correlated part, since the uncorrelated part cannot be estimated. This is why [24] considers that for broadband transmissions in the sub-THz and THz frequencies, the adequate PN model would be the GPN model.

Several PN models are used in the state-of-the-art. The most frequently encountered are the Wiener PN [49] and the 3GPP PN models [30] which are correlated models used for instance in [39,41] and [44–46]. In [24], the authors discuss the selection of PN model when large bandwidths are considered. They use a state-of-the-art 200 GHz oscillator [25] and approximations in [23] for PN modeling. They show that the contribution of the Wiener nature of the PN is negligible compared to the white PN one in two cases: i) when the oscillator corner frequency remains small compared to the system bandwidth and ii) when the length of the sequence is short enough to fulfill the criterion presented in (2.6).

### 5.1.1 Motivations

GPN model has already been exploited in [15,16] to optimize constellations for PN channels, in [26] for optimal demodulation, and in [27] to compare performance of digital modulations. For all these contributions, a SC system is considered. They authors in [66] present the effects of GPN upon OFDM and DFT-s-OFDM systems, considering MIMO systems. They present performance evaluation of the PAPR, OOB emission, BER in function of ICS and SNR. Despite the contributions in [66], the GPN effects are not well studied and understood in case of DFT-s-OFDM.

### 5.1.2 Contributions

The main technical contributions of this chapter are as follows:

- We study the stochastic properties of the interference terms induced by the GPN in DFT-s-OFDM systems.
- We propose a novel detection criterion adapted to DFT-s-OFDM systems in the presence of strong GPN.
- We study the feasibility of implementing the proposed detector in practical RF transmission.
- We present the performance of a DFT-s-OFDM systems in terms of TBLER for different GPN regimes.

Table 5.1: Spectral density $K_0$ (dBc/Hz) of the GPN

| | | Bandwidth $B_W$ | | |
|---|---|---|---|---|
| GPN regime | Power $\sigma^2_\phi$ | 3.686 GHz | 7.372 GHz | 14.744 GHz |
| Strong GPN | $10^{-1}$ | −108.67 | −111.69 | −114.70 |
| Medium GPN | $5 \cdot 10^{-2}$ | −111.67 | −114.70 | −117.71 |
| Low GPN | $10^{-2}$ | −118.68 | −121.69 | −124.70 |

- In contrast to [44] where the PN has a correlated nature, we present the performance of an OFDM systems considering different GPN regimes. We use the ICI mitigation algorithm presented in [44].

## 5.2 System Model

### 5.2.1 Channel Model

The radio propagation channels in sub-THz frequencies are expected to be sparse [62]. It has been demonstrated that the LoS provides most of the energy contribution for the RF transmission assuming sub-THz parameters [62,63]. It is ensured by the use of high gain directional antennas which spatially filter the channel. We assume a LoS propagation channel with high gain antenna in this chapter. We also assume a coherent communication system impaired by PN with a receiver synchronized in time and frequency.

### 5.2.2 PN Model

Regarding the PN model, we consider in this chapter an uncorrelated GPN generated at the transmitter and receiver. The GPN applied to the signal is defined as in Section 2.2.1 by

$$\phi[\tau] \backsim \mathcal{N}(0, \sigma^2_\phi), \tag{5.1}$$

where $\phi$ is the sum of the PN generated at the transmitter and receiver. The PN variance $\sigma^2_\phi = \sigma^2_{\phi_{TX}} + \sigma^2_{\phi_{RX}}$ where

$$\sigma^2_{\phi_{TX}} = \sigma^2_{\phi_{RX}} = K_0 B_W \cdot \tag{5.2}$$

The term $K_0$ represents the PSD of the generated GPN at both transmitter and receiver. The term $B_W = N_s \Delta_f$ denotes the useful system bandwidth with $N_s$ denoting the DFT size block and $\Delta_f$ the ICS. Three levels of GPN are considered as depicted in Table 5.1: strong GPN, medium GPN and low GPN.

### 5.2.3 DFT-s-OFDM waveform with presence of PN

As a reminder, the expression of the baseband discrete-time received signal impaired by the PN at the $k^{th}$ subcarrier is expressed as follows

$$r_k = s_k \beta(k, N_s, N_f, \phi) \; + \; \gamma(k, N_s, N_f, \phi) + \; \eta(k, N_s, N_f), \tag{5.3}$$

where the terms $\beta(k, N_s, N_f, \phi)$, $\gamma(k, N_s, N_f, \phi)$ and $\eta(k, N_s, N_f)$ are defined in (2.29). The term $\beta(k, N_s, N_f, \phi)$ is responsible of the rotation of transmitted symbols. The second term $\gamma(k, N_s, N_f, \phi)$ represents the ICI and the last term $\eta(k, N_s, N_f)$ is the thermal noise after Fourier transformations.

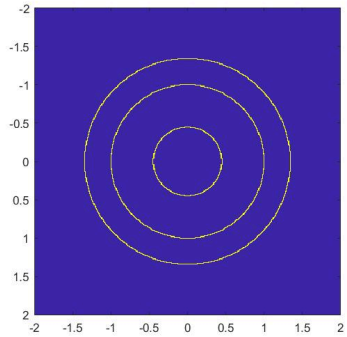

(a) SC signal

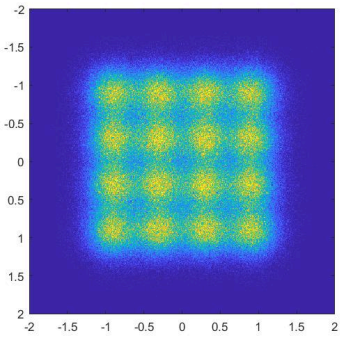

(b) OFDM signal

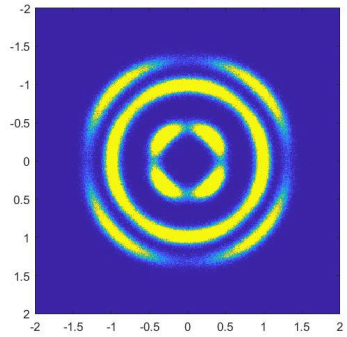

(c) DFT-s-OFDM signal at subcarrier $k = 1$

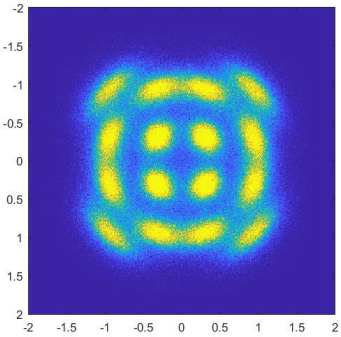

(d) DFT-s-OFDM signal at subcarrier $k = 10$

Figure 5.1: GPN distortion on 16-QAM modulated signal with SNR = 50 dB

#### 5.2.3.1 Received signal constellations

In order to observe the impact of GPN on 5G-NR MC waveforms, we display the probability of a point appearing in IQ space for different received signals in Fig. 5.1 and assuming a strong GPN regime. The more yellow the color, the higher the probability. The color blue represents an almost null probability of appearance.

In Fig. 5.1a, one can observe that in SC systems without pulse shaping filter, the presence of GPN only causes the rotation of the transmitted symbols. Regarding OFDM systems in Fig. 5.1b, we do not have the rotation as in SC. However, one can notice a noisy constellation, where the noise comes from the ICI induced by the GPN.

Concerning the DFT-s-OFDM system, one can notice a dependent behavior on the DFT spread subcarrier index. For a subcarrier index $k = 1$ as depicted in Fig. 5.1c, one can observe more rotation of received symbols and less ICI effect. In contrast for a subcarrier index $k = 10$ in Fig. 5.1d, one can observe less rotation and more ICI compared to Fig. 5.1c. From these observations, we will focus on the analysis of the terms $\beta(k, N_s, N_f, \phi)$ and $\gamma(k, N_s, N_f, \phi)$ in the next section.

## 5.3 Interference Analysis

In this section, we study the stochastic properties of interference terms $\beta(k, N_s, N_f, \phi)$ and $\gamma(k, N_s, N_f, \phi)$. Thereafter, we denote $\beta_k = \beta(k, N_s, N_f, \phi)$, $\gamma_k = \gamma(k, N_s, N_f, \phi)$ and $\eta_k = \eta(k, N_s, N_f)$. We write the terms $\beta_k$ and $\gamma_k$ in function of the one order Dirichlet kernel $K$ and

Table 5.2: Size of FFT and DFT blocks

| | First configuration | | | | Second configuration | | | |
|---|---|---|---|---|---|---|---|---|
| $N_s$ | 120 | 240 | 360 | 480 | 480 | 960 | 1920 | 3840 |
| $N_f$ | 512 | | | | 512 | 1024 | 2048 | 4096 |
| $\zeta = N_s/N_f$ | 0.2344 | 0.4688 | 0.7031 | 0.9375 | 0.9375 | | | |
| $\mu$ | 9 | | | | 9 | 8 | 7 | 6 |
| $\Delta_f$ [kHz] | 7680 | | | | 7680 | 3840 | 1920 | 960 |
| $B_W$ [GHz] | 0.922 | 1.843 | 2.765 | 3.686 | 3.686 | | | |

$G$ as follows

$$\begin{aligned}\beta(k,N_s,N_f,\phi) &= \sum_{p=0}^{N_f-1} e^{j\phi_p} K_{N_s}^{N_s}\left(\frac{p}{N_f}-\frac{k}{N_s}\right) G_{N_f}^{N_s}\left(\frac{k}{N_s}-\frac{p}{N_f}\right)\\ \gamma(k,N_s,N_f,\phi) &= \sum_{n=0,n\neq k}^{N_s-1} s_n \sum_{p=0}^{N_f-1} e^{j\phi_p} K_{N_s}^{N_s}\left(\frac{p}{N_f}-\frac{n}{N_s}\right) G_{N_f}^{N_s}\left(\frac{k}{N_s}-\frac{p}{N_f}\right),\end{aligned} \tag{5.4}$$

where

$$K_X^P(y) = \frac{1}{X}\sum_{m=0}^{P-1} e^{j2\pi m y} \quad \text{and} \quad G_X^P(z) = \frac{1}{X}\sum_{f=0}^{P-1} e^{j2\pi f z}. \tag{5.5}$$

According to these expressions, one can notice the dependence on the subcarrier index $k$, DFT spreading size $N_s$ and FFT size $N_f$. Hence, we decide to study the stochastic properties of $\beta_k$ and $\gamma_k$ by considering two configurations as depicted in Table 5.2.

### 5.3.1 First configuration

With this configuration, we want to highlight the impact of the system bandwidth $B_W$ under GPN impairments. To do so, we consider four DFT-s-OFDM systems with different values of $N_s$ (also representing the allocated RB). These systems use the same oscillator that introduces GPN with a PSD $K_0 = -108.67$ dBc/Hz. We consider a sampling frequency of $F_s = 3932.16$ MHz and a numerology $\mu = 9$.

### 5.3.2 Second configuration

Regarding the second configuration, we want to show the impact of the GPN when the numerology is varied. For that, we vary $N_s$ and $N_f$ while maintaining the system bandwidth $B_w$ (*i.e.* the ratio $\zeta = \frac{N_s}{N_f}$ is constant) as presented by the "Option 2" in Table 1.1. We consider $F_s = 3932.16$ MHz and $K_0 = -108.67$ dBc/Hz.

### 5.3.3 Stochastic properties of the subcarrier phase error

Let us express the term $\beta_k$ in the following form

$$\beta_k = \rho_k e^{j\Phi_k}, \tag{5.6}$$

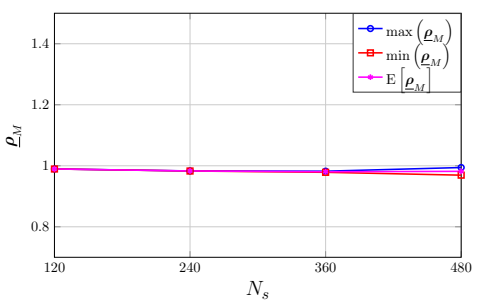


(a) Statistical analysis of $\underline{\rho}_M$.

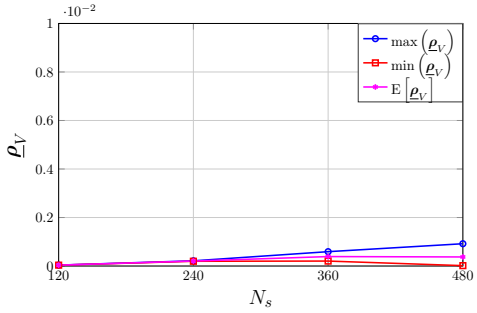


(b) Statistical analysis of $\underline{\rho}_V$

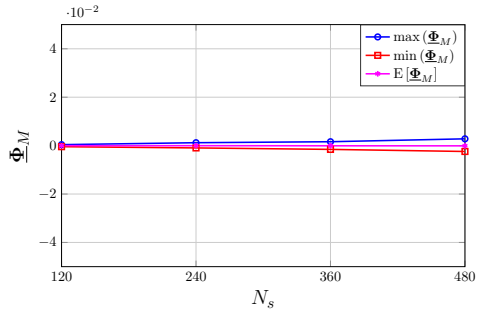


(c) Statistical analysis of $\underline{\Phi}_M$

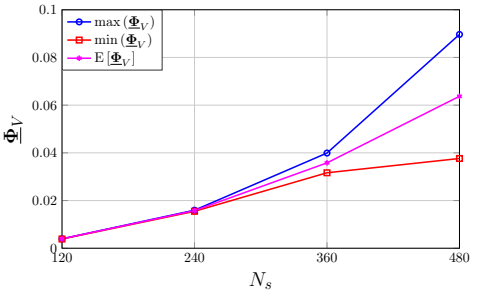


(d) Statistical analysis of $\underline{\Phi}_V$

Figure 5.2: Statistical analysis of $\rho_k$ and $\Phi_k$ using the **First configuration**

where $\rho_k$ and $\Phi_k$ are respectively the magnitude and the phase of $\beta_k$. Given the complex expression of $\beta_k$, Monte-Carlo simulations have been performed to study its stochastic properties. To do so, we consider $N_{br} = 10^5$ samples and we define the following vectors, $\forall k \in \{1, \cdots, N_s\}$:

$$\begin{aligned} \underline{\boldsymbol{\rho}}_k &= [\rho_k^{(1)}, \cdots, \rho_k^{(N_{br})}]^T \\ \underline{\boldsymbol{\Phi}}_k &= [\Phi_k^{(1)}, \cdots, \Phi_k^{(N_{br})}]^T. \end{aligned} \tag{5.7}$$

Then, we define the following terms for further analysis.

$$\begin{aligned} \underline{\boldsymbol{\rho}}_M &= \left[\mathbb{E}\left[\underline{\boldsymbol{\rho}}_0\right], \cdots, \mathbb{E}\left[\underline{\boldsymbol{\rho}}_{N_s-1}\right]\right]^T, \quad \underline{\boldsymbol{\rho}}_V = \left[\text{var}\left[\underline{\boldsymbol{\rho}}_0\right], \cdots, \text{var}\left[\underline{\boldsymbol{\rho}}_{N_s-1}\right]\right]^T \\ \underline{\boldsymbol{\Phi}}_M &= \left[\mathbb{E}\left[\underline{\boldsymbol{\Phi}}_0\right], \cdots, \mathbb{E}\left[\underline{\boldsymbol{\Phi}}_{N_s-1}\right]\right]^T, \quad \underline{\boldsymbol{\Phi}}_V = \left[\text{var}\left[\underline{\boldsymbol{\Phi}}_0\right], \cdots, \text{var}\left[\underline{\boldsymbol{\Phi}}_{N_s-1}\right]\right]^T. \end{aligned} \tag{5.8}$$

**First configuration:** Fig. 5.2a and Fig. 5.2b present the impact of varying $N_s$ on the properties of $\rho_k$. From Fig. 5.2a, one can notice a subcarrier behavior at $N_s = 480$ but, it can be considered as negligible. Additionally, one can remark $\underline{\boldsymbol{\rho}}_M[k] \simeq 1$ for each $N_s$ values. Regarding $\underline{\boldsymbol{\rho}}_V$, one can observe a subcarrier variation when $N_s$ increases in Fig 5.2b. However, we can assume $\underline{\boldsymbol{\rho}}_V[k] \simeq 0$ for each $N_s$ values. Therefore, we can characterize $\rho_k$ as a variable which follows a process with a mean equal to 1 and a variance equals to zero. So thereafter, we will assume $\rho_k \simeq 1$.

Fig. 5.2c and Fig. 5.2d show the effects of varying $N_s$ on the properties of $\Phi_k$. Fig. 5.2c presents a negligible subcarrier variation when $N_s$ increases and one can remark that $\underline{\boldsymbol{\Phi}}_M[k] \simeq 0$. Moreover in Fig. 5.2d, the three curves are merged for $N_s = \{120, 240\}$ while for $N_s = \{360, 480\}$, they are no longer merged together. Therefore a subcarrier behavior appears for $\underline{\boldsymbol{\Phi}}_V$ when $N_s$ tends towards $N_f$.

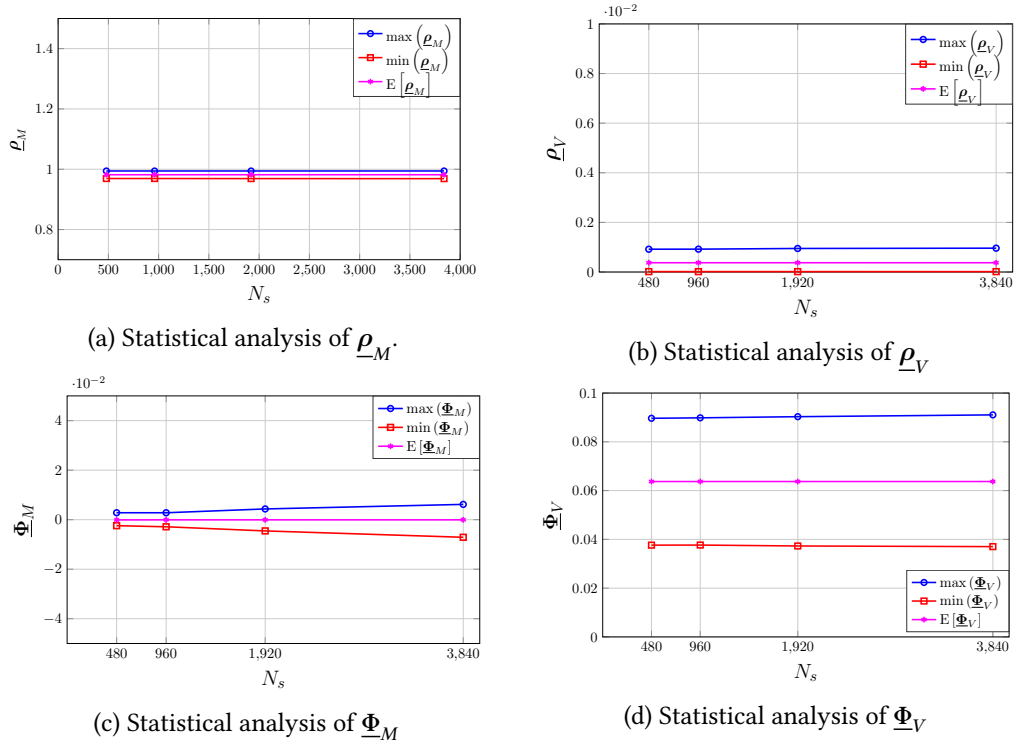


(a) Statistical analysis of $\underline{\rho}_M$.

(b) Statistical analysis of $\underline{\rho}_V$

(c) Statistical analysis of $\underline{\Phi}_M$

(d) Statistical analysis of $\underline{\Phi}_V$

Figure 5.3: Statistical analysis of $\rho_k$ and $\Phi_k$ using the **Second configuration**

**Second configuration:** Fig. 5.3 presents the stochastic analysis of $\rho_k$ and $\Phi_k$ considering the second configuration. By paying attention to the scales, one can notice that $\underline{\rho}_M$, $\underline{\rho}_V$, $\underline{\Phi}_M$ and $\underline{\Phi}_V$ do not vary when we keep the ratio $\zeta$ constant. Similarly, we draw the observations that $\underline{\rho}_M[k] \simeq 1$, $\underline{\rho}_V[k] \simeq 0$ and $\underline{\Phi}_M[k] \simeq 0$, $\forall k \in \{0, \cdots, N_s - 1\}$.

**Important note 12.** *These results show the term $\beta_k$ comes down to a phase shift term defined by*

$$\beta_k \backsimeq e^{j\Phi_k}, \tag{5.9}$$

*where $\Phi_k$ represents a zero-mean random process. Its variance depends on the DFT subcarrier index, the system bandwidth $B_W$ and PN power. Therefore, the term $\beta_k$ is different from the CPE in OFDM due to the DFT spreading operation. We rather have a SPE. The objective now is to determine whether this phase shift follows a known probability distribution. To do so, we perform a Gaussianity test.*

**Gaussianity test:** In order to properly define $\Phi_k$, we look at the particular case of a significant subcarrier variation, *i.e* $(N_s, N_f) = (480, 512)$. First, we simulate the CDF of $\underline{\Phi}_k$ and compared it with the CDF of a Gaussian random process with power $\sigma^2_{\Phi_k} = \mathbf{diag}_k\{\mathbf{R}_{\underline{\Phi}}\}$. The term $\mathbf{R}_{\underline{\Phi}} = \mathbb{E}\left[\underline{\Phi} \cdot \underline{\Phi}^H\right]$ represents the correlation matrix of the vector $\underline{\Phi} = \left[\Phi_0, \cdots, \Phi_{N_s-1}\right]^T$. The results are illustrated in Fig. 5.4a for two distincts subcarriers $k = \{1, 8\}$, chosen arbitrarily. One can notice the good matching between the CDFs of $\underline{\Phi}_k$ and the equivalent Gaussian random distribution. Second, we perform a Kolmogorov-Smirnov test [67], to evaluate the Gaussianity property of simulated $\underline{\Phi}_k$ with significance factor [1] $\alpha = 0.1$. This test validates the observations highlighted with the CDF comparison.

[1] It represents the validity factor of the Gaussianity test. By default on MATLAB, it is 0.05 and the max is 0.1 as considered in this paper.

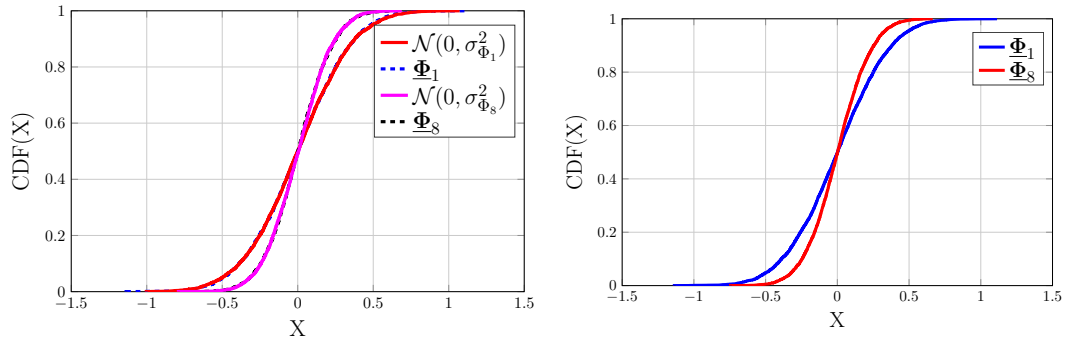


(a) CDF comparison

(b) CDF of X = $\underline{\Phi}_k$ for $k = \{1, 8\}$.

Figure 5.4: CDF of $\underline{\Phi}_k$

**Important note 13.** *From all these simulation results, we can assume that $\Phi_k$ follows an uncorrelated Gaussian random process.*

According to that, we define it $\forall k$ by

$$\Phi_k \backsim \mathcal{N}(m_{\Phi_k}, \sigma^2_{\Phi_k}) = \begin{cases} m_{\Phi_k} = E[\underline{\Phi}_k] \simeq 0 \\ \sigma^2_{\Phi_k} = \mathbf{diag}_k\{\mathbf{R}_{\underline{\Phi}}\} \end{cases} \tag{5.10}$$

where $m_{\Phi_k}$ and $\sigma^2_{\Phi_k}$ are respectively the mean and the variance of $\underline{\Phi}_k$. The statement in (5.10) is true for every $(N_s, N_f)$ configurations.

### 5.3.4 Stochastic properties of the intercarrier interference

As for stochastic properties of SPE, we make the same analysis for the ICI by defining $\underline{\gamma}_k = [\gamma_k^{(1)}, \cdots, \gamma_k^{(N_{br})}]^T$. Then we decide to study $\mathfrak{Re}\{\gamma_k\}$ and $\mathfrak{Im}\{\gamma_k\}$ by posing

$$\begin{aligned} \underline{\gamma}^R_M &= \left[\mathbb{E}\left[\mathfrak{Re}\{\underline{\gamma}_0\}\right], \cdots, \mathbb{E}\left[\mathfrak{Re}\{\underline{\gamma}_{N_s-1}\}\right]\right]^T, \quad \underline{\gamma}^R_V = \left[\mathrm{var}\left[\mathfrak{Re}\{\underline{\gamma}_0\}\right], \cdots, \mathrm{var}\left[\mathfrak{Re}\{\underline{\gamma}_{N_s-1}\}\right]\right]^T \\ \underline{\gamma}^I_M &= \left[\mathbb{E}\left[\mathfrak{Im}\{\underline{\gamma}_0\}\right], \cdots, \mathbb{E}\left[\mathfrak{Im}\{\underline{\gamma}_{N_s-1}\}\right]\right]^T, \quad \underline{\gamma}^I_V = \left[\mathrm{var}\left[\mathfrak{Im}\{\underline{\gamma}_0\}\right], \cdots, \mathrm{var}\left[\mathfrak{Im}\{\underline{\gamma}_{N_s-1}\}\right]\right]^T \end{aligned} \tag{5.11}$$

**First configuration:** Fig. 5.5a and Fig. 5.5b show the effects of varying $N_s$ on the properties of $\mathfrak{Re}\{\gamma_k\}$ [2]. Fig. 5.5a presents a negligible subcarrier variation when $N_s$ increases and one can remark that $\underline{\gamma}^R_M[k] \simeq 0$ (same $\underline{\gamma}^I_M[k] \simeq 0$). Moreover, Fig. 5.5b highlights a subcarrier behavior which appears from $N_s = 360$ and increases for $\underline{\gamma}^R_V$ (same for $\underline{\gamma}^I_V$).

**Second configuration:** Fig. 5.6a and Fig. 5.6b highlight an almost invariance of $\underline{\gamma}^R_M$ and $\underline{\gamma}^R_V$ when we keep the ratio $\zeta$ constant. The same observation is made for $\underline{\gamma}^I_M$ and $\underline{\gamma}^I_V$.

**Important note 14.** *These results highlight the term $\gamma_k$ represents a zero-mean complex random process. Its variance depends on the DFT subcarrier index, the system bandwidth*

[2] we only present the analysis of $\mathfrak{Re}\{\gamma_k\}$ because the results obtained are similar to $\mathfrak{Im}\{\gamma_k\}$

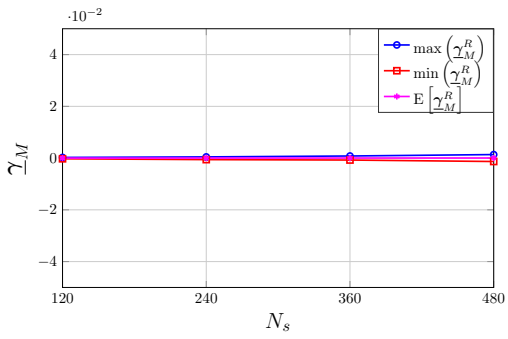


(a) Statistical analysis of $\underline{\gamma}_M^R$.

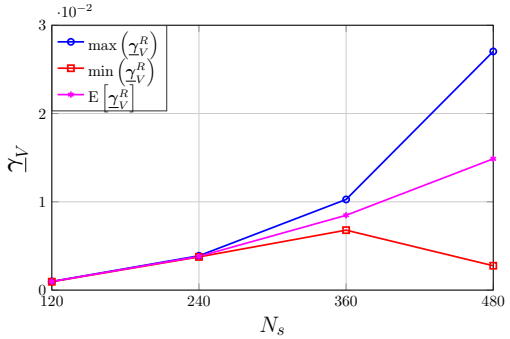


(b) Statistical analysis of $\underline{\gamma}_V^R$.

Figure 5.5: Statistical analysis of $\gamma_k$ using **First configuration**

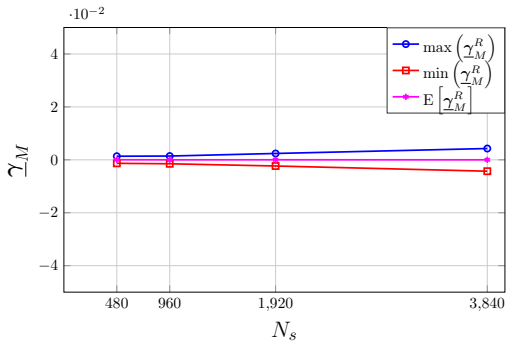


(a) Statistical analysis of $\underline{\gamma}_M^R$.

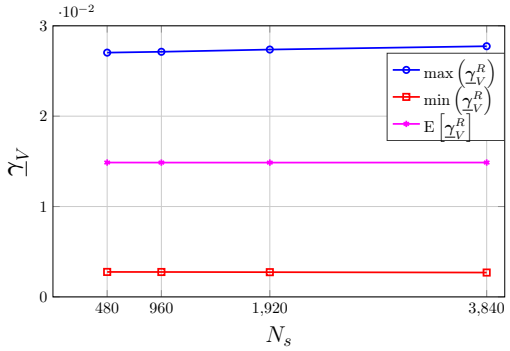


(b) Statistical analysis of $\underline{\gamma}_V^R$.

Figure 5.6: Statistical analysis of $\gamma_k$ using **Second configuration**

*$B_W$ and PN power. The objective now is to determine whether this ICI follows a known probability distribution. As for the SPE, we compute a Gaussianity test.*

**Gaussianity test:** To correctly characterize $\gamma_k$, we look at the particular case of a significant subcarrier variation, *i.e.* $(N_s, N_f) = (480, 512)$. We only present the analysis of $\mathfrak{Re}\{\underline{\gamma}_k\}$ [3]. First, we simulate the CDF of $\mathfrak{Re}\{\underline{\gamma}_k\}$ and compared it with the CDF of a Gaussian random process with variance $\sigma_\gamma^{'2} = \sigma_\gamma^2/2$ where $\sigma_\gamma^2 = \mathbf{diag}_k\{\mathbf{R}_{\underline{\gamma}}\}$. The term $\mathbf{R}_{\underline{\gamma}} = \mathbb{E}\left[\underline{\gamma} \cdot \underline{\gamma}^H\right]$ represents the correlation matrix of the ICI vector $\underline{\gamma} = \left[\gamma_0, \cdots, \gamma_{N_s-1}\right]^T$. This CDF comparison is depicted in Fig. 5.7a for subcarrier indexes $k = \{1, 8\}$. One can notice that CDFs of $\mathfrak{Re}\{\underline{\gamma}_1\}$ and $\mathfrak{Re}\{\underline{\gamma}_8\}$ seem to be following those of the Gaussian random distributions but, the curves are not so closely intertwined.

In order to be sure, we perform a Kolmogorov-Smirnov test [67], to test simulated $\underline{\gamma}_k$ for Gaussianity with a significance factor $\alpha = 0.1$. Despite the observations made from CDF comparison, the Kolmogorov-Smirnov test does not validate the complex Gaussian property of the ICI.

### 5.3.5 Conclusion

In this section, we characterize the SPE term $\beta_k$ and the ICI term $\gamma_k$. We show that the SPE can be defined as a phase shift where the phase follows a zero-mean Gaussian random process

[3] because they are similar to those obtained for $\mathfrak{Im}\{\underline{\gamma}_k\}$

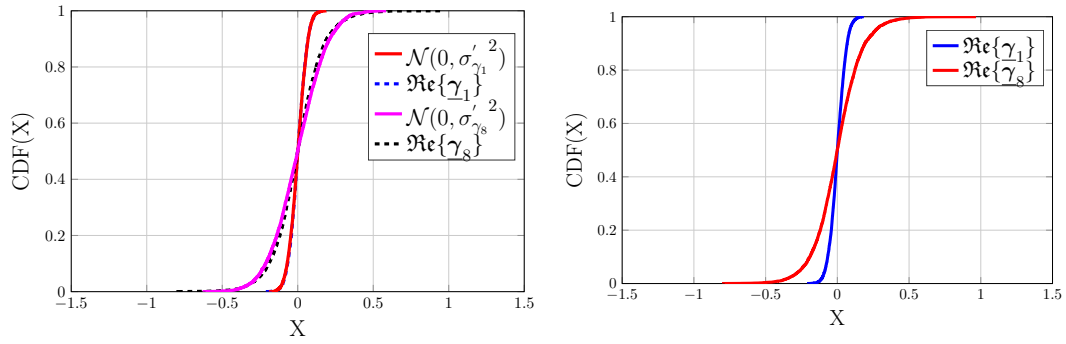


(a) CDF comparison

(b) CDF of X = $\mathfrak{Re}\{\underline{\gamma}_k\}$ for $k = \{1, 8\}$.

Figure 5.7: CDF of $\mathfrak{Re}\{\underline{\gamma}_k\}$

with a power depending on the DFT spread subcarrier index, system bandwidth and the power of the oscillator PN $\sigma^2_\phi$. According to the Gaussianity test, the ICI cannot be considered as a complex Gaussian random process. Nevertheless, some Gaussian properties will be taken in the next section for performance improvement proposals. The expression (5.3) can be simplified as follows:

$$r_k \backsimeq s_k e^{j\Phi_k} + \gamma_k + \eta_k. \tag{5.12}$$

### 5.3.6 Numerical results

In this section, we assess the DFT-s-OFDM system performance with GPN impairments. For the detection, we use the Euclidean detector denoted by *EUC-D* whose Maximum Likelihood (ML) expression is defined as follows:

$$\hat{s}_k = \underset{s_i \in C}{\operatorname{argmin}} \parallel r_k - s_i \parallel_2^2, \tag{5.13}$$

where symbols $s_i \in C$, with $C$ the set of the selected modulation scheme. Fig. 5.8a and Fig. 5.8b present the TBLER performance as a function of the SNR considering a 16-QAM modulation and CR=0.7. **First configuration** parameters in Table 5.2 are used in Fig. 5.8a and **Second configuration** parameters in Fig. 5.8b.

From Fig. 5.8a, one can notice that reducing the DFT spreading size $N_s$ allows to reach the targeted TBLER with a low SNR. This result can be explained by the fact that varying $N_s$ means varying the useful bandwidth $B_W$, which is proportional to the PN power. Thus, reducing $N_s$ reduces the impact of PN on the system, resulting in decoding with low SNR. Conversely, increasing $N_s$ means increasing the PN power, which will require a high SNR to decode properly, or an inability to decode if the PN power is too high. Fig. 5.8b highlights that varying $N_s$ and $N_f$ while keeping the ratio $\zeta$ constant do not vary the GPN effects on the system performance. Consequently, varying the numerology while holding the system bandwidth constant has no effect on DFT-s-OFDM systems with presence of GPN.

The results presented above demonstrate the inefficiency of the Euclidean detector when the PN power is high (larger $\zeta$). Thankfully, the stochastic study presented above shows a subcarrier behavior for large $\zeta$. Additionally, we demonstrate that the expression of the received signal at the DFT subcarrier $k$ slightly approaches the one of a SC system. According to that, two detection criteria are derived in the next section in order to make the DFT-s-OFDM systems robust to the presence of strong GPN.

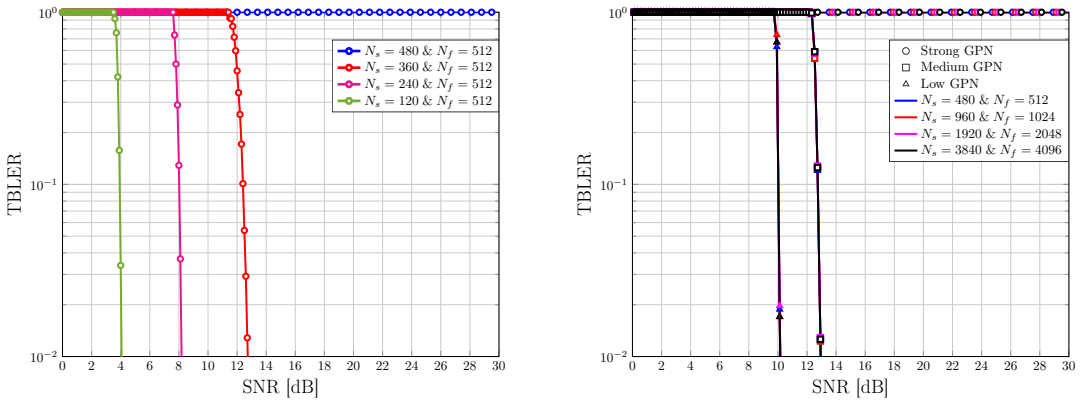


(a) **First configuration** (b) **Second configuration**

Figure 5.8: DFT-s-OFDM system performance

## 5.4 Optimum demodulation in the presence of GPN

In this section, we derive an accurate detection criterion in order to enhance the system performance of DFT-s-OFDM in presence of PN. In that way, we find the expressions of an optimal detection and a sub-optimal detection. For that, we rewrite the expression (5.12) in a vector form as follows

$$\underline{\mathbf{r}} \simeq \underline{\mathbf{s}} \odot e^{j\underline{\mathbf{\Phi}}} + \underline{\mathbf{w}}, \tag{5.14}$$

with $\underline{\mathbf{r}} = [r_0, \cdots, r_{N_s-1}]^T$, $\underline{\mathbf{s}} = [s_0, \cdots, s_{N_s-1}]^T$, $\underline{\boldsymbol{\eta}} = [\eta_0, \cdots, \eta_{N_s-1}]^T$. The term $\underline{\mathbf{w}} = \underline{\boldsymbol{\eta}} + \underline{\gamma}$ denotes the additive noise after DFT-s-OFDM demodulator. The expression (5.14) brings us back to SC a system in the presence of the PN $\underline{\mathbf{\Phi}}$ and a noise $\underline{\mathbf{w}}$ [16]. The authors in [15] propose an accurate detector for a SC system impaired by PN, based on the use of PN and thermal noise statistics. Based on this work, we need to determine the stochastic properties of both $\underline{\mathbf{\Phi}}$ and $\underline{\mathbf{w}}$.

### 5.4.1 Stochastic properties of the noise

According to the results presented in Section 5.3, we define the PN vector $\underline{\mathbf{\Phi}}$ as a real Gaussian vector with a mean $\underline{\mathbf{m}}_\Phi$ and a correlation matrix $\mathbf{\Gamma}_\Phi$ as follows:

$$\underline{\mathbf{\Phi}} \backsim \mathcal{N}(\underline{\mathbf{m}}_\Phi, \mathbf{\Gamma}_\Phi) = \begin{cases} \underline{\mathbf{m}}_\Phi = \underline{\mathbf{0}}_{N_s} \\ \mathbf{\Gamma}_\Phi = \sigma^2_{\Phi_k} \mathbf{I}_{N_s}, \end{cases} \tag{5.15}$$

where $\sigma^2_{\Phi_k}$ is defined in (5.10) and $\mathbf{I}_{N_s}$ is the identity matrix with size $N_s \times N_s$. The noise vector $\underline{\mathbf{w}}$ is the sum of the thermal noise vector $\underline{\boldsymbol{\eta}}$ and the ICI vector $\underline{\gamma}$. The thermal noise vector $\underline{\boldsymbol{\eta}}$ is defined as a complex Gaussian vector (independent and identically distributed) given by:

$$\underline{\boldsymbol{\eta}} \backsim \mathbb{C}\mathcal{N}(\underline{\mathbf{m}}_\eta, \mathbf{\Gamma}_\eta) = \begin{cases} \underline{\mathbf{m}}_\eta = \underline{\mathbf{0}}_{N_s} \\ \mathbf{\Gamma}_\eta = \sigma^2_n \mathbf{I}_{N_s}, \end{cases} \tag{5.16}$$

where $\underline{\mathbf{m}}_\eta$ denotes the mean vector and $\mathbf{\Gamma}_\eta$ is the correlation matrix.

**Important note 15.** *To simplify the analysis, we consider the ICI vector $\underline{\gamma}$ follows a correlated complex Gaussian vector (also independent and identically distributed).*

According to that, we define it by

$$\underline{\gamma} \backsim \mathbb{CN}(\underline{\mathbf{m}}_\gamma, \mathbf{\Gamma}_\gamma) = \begin{cases} \underline{\mathbf{m}}_\gamma = \underline{\mathbf{0}}_{N_s} \\ \mathbf{\Gamma}_\gamma = \mathbf{R}_{\underline{\gamma}}, \end{cases} \tag{5.17}$$

where $\underline{\mathbf{m}}_\gamma$ is the mean vector and $\mathbf{\Gamma}_\gamma$ the correlation matrix.

Considering (5.16) and (5.17), the noise vector $\underline{\mathbf{w}}$ can be defined as a Gaussian vector with a mean vector $\underline{\mathbf{m}}_w$ and a correlation matrix $\mathbf{\Gamma}_w$. It is defined as:

$$\underline{\mathbf{w}} \backsim \mathbb{CN}(\underline{\mathbf{m}}_w, \mathbf{\Gamma}_w) = \begin{cases} \underline{\mathbf{m}}_w = \underline{\mathbf{m}}_\eta \ + \ \underline{\mathbf{m}}_\gamma = \underline{\mathbf{0}}_{N_s} \\ \mathbf{\Gamma}_w = \mathbf{\Gamma}_\eta \ + \ \mathbf{\Gamma}_\gamma. \end{cases} \tag{5.18}$$

### 5.4.2 Optimal detection criterion

The Symbol Error Probability (SEP) is minimized by the ML decision criterion for equiprobable and independent symbols. The channel likelihood function can be written as follows [15]:

$$p(\underline{\mathbf{r}}|\underline{\mathbf{s}}) = p(\underline{\mathbf{r}}_\rho, \underline{\mathbf{r}}_\theta \mid \underline{\mathbf{s}}_\rho, \underline{\mathbf{s}}_\theta). \tag{5.19}$$

Thus, we have to express more clearly the ML decision criterion. Before studying the amplitude and phase of the received signal vector $\underline{\mathbf{r}}$, we denote $\underline{\mathbf{w}} \odot e^{-j(\underline{\mathbf{\Phi}}+\underline{\mathbf{s}}_\theta)}$ by $\underline{\mathbf{w}}'$. The term $\underline{\mathbf{w}}'$ has the same stochastic properties as $\underline{\mathbf{w}}$ [4]. The amplitude of the received DFT-s-OFDM symbol is given by

$$\begin{aligned} \underline{\mathbf{r}}_\rho &= \left| \ (\underline{\mathbf{s}}_\rho + \underline{\mathbf{w}}') \odot e^{j(\underline{\mathbf{\Phi}}+\underline{\mathbf{s}}_\theta)} \ \right| \\ &= \sqrt{(\underline{\mathbf{s}}_\rho + \mathfrak{Re}\{\underline{\mathbf{w}}'\})^2 + \mathfrak{Im}\{\underline{\mathbf{w}}'\}^2}, \end{aligned} \tag{5.20}$$

and the phase by

$$\begin{aligned} \underline{\mathbf{r}}_\theta &= \arg\left( \ (\underline{\mathbf{s}}_\rho + \underline{\mathbf{w}}') \odot e^{j(\underline{\mathbf{\Phi}}+\underline{\mathbf{s}}_\theta)} \ \right) \\ &= \underline{\mathbf{s}}_\theta + \underline{\mathbf{\Phi}} + \arctan\left( \frac{\mathfrak{Im}\{\underline{\mathbf{w}}'\}}{\underline{\mathbf{s}}_\rho + \mathfrak{Re}\{\underline{\mathbf{w}}'\}} \right). \end{aligned} \tag{5.21}$$

Assuming the high SNR approximation [24], we obtain:

$$\begin{cases} \underline{\mathbf{r}}_\rho - \underline{\mathbf{s}}_\rho \backsimeq \mathfrak{Re}\{\underline{\mathbf{w}}'\} \\ \underline{\mathbf{r}}_\theta - \underline{\mathbf{s}}_\theta \backsimeq \underline{\mathbf{\Phi}} + \mathfrak{Im}\{\underline{\mathbf{w}}'\} \odot \underline{\mathbf{s}}_\rho^{-1}. \end{cases} \tag{5.22}$$

The symbol $\underline{\mathbf{s}}_\rho^{-1}$ is the vector containing the inverse of elements of $\underline{\mathbf{s}}_\rho$. The following terms $\mathfrak{Re}\{\underline{\mathbf{w}}'\}$ and $\underline{\mathbf{\Phi}} + \mathfrak{Im}\{\underline{\mathbf{w}}'\} \odot \underline{\mathbf{s}}_\rho^{-1}$ are respectively the additive noise in the amplitude channel and the additive Gaussian noise in the phase channel [15]. In order to express the ML decision criterion in (5.19), we have to derive the Probability Density Function (PDF) of the expressions in (5.22). The PDF of the first expression can be expressed as follows:

$$p(\underline{\mathbf{r}}_\rho \mid \underline{\mathbf{s}}_\rho) = \frac{1}{\sqrt{(2\pi)^{N_s} |\det(\mathbf{\Gamma}_{w_R})|}} \cdot e^{-\frac{1}{2}z}, \tag{5.23}$$

[4] by assuming that the complex Gaussian noise vector is circularly symmetric

where $\mathbf{\Gamma}_{w_R} = \mathbf{\Gamma}_w/2$ and $z = (\underline{\mathbf{r}}_\rho - \underline{\mathbf{s}}_\rho)^T \mathbf{\Gamma}_{w_R}^{-1} (\underline{\mathbf{r}}_\rho - \underline{\mathbf{s}}_\rho)$. When it comes to the phase domain, the term $\underline{\mathbf{\Phi}} + \Im\mathfrak{m}\{\underline{\mathbf{w}}'\} \odot \underline{\mathbf{s}}_\rho^{-1}$ is expressed as follows

$$\underline{\mathbf{\Phi}} + \Im\mathfrak{m}\{\underline{\mathbf{w}}'\} \odot \underline{\mathbf{s}}_\rho^{-1} \backsim \mathcal{N}(\underline{\mathbf{m}}, \mathbf{\Gamma}) = \begin{cases} \underline{\mathbf{m}} = \underline{\mathbf{0}}_{N_s} \\ \mathbf{\Gamma} = \mathbf{\Gamma}_\Phi + \mathbf{\Gamma}_{w_I} \odot \underline{\mathbf{s}}_\rho^{-2}, \end{cases} \tag{5.24}$$

where $\mathbf{\Gamma}_{w_I} = \mathbf{\Gamma}_w/2$. Then, we can express the PDF of the second expression in (5.22) by

$$p(\underline{\mathbf{r}}_\theta \mid \underline{\mathbf{s}}_\theta) = \frac{1}{\sqrt{(2\pi)^{N_s} |\det(\mathbf{\Gamma})|}} \cdot e^{-\frac{1}{2} l}, \tag{5.25}$$

where $l = (\underline{\mathbf{r}}_\theta - \underline{\mathbf{s}}_\theta)^T \mathbf{\Gamma}^{-1} (\underline{\mathbf{r}}_\theta - \underline{\mathbf{s}}_\theta)$. From (5.23) and (5.25), the conditional PDF is written as

$$p(\underline{\mathbf{r}} \mid \underline{\mathbf{s}}) = \frac{e^{\left(-\frac{1}{2}(z+l)\right)}}{(2\pi)^{N_s} \sqrt{|\det(\mathbf{\Gamma}_{w_R})| \cdot |\det(\mathbf{\Gamma})|}}, \tag{5.26}$$

where $z$ and $l$ are expressed above. The correlation matrices $\mathbf{\Gamma}_w$ and $\mathbf{\Gamma}$ are considered known by the detector. Based on the joint observation of phase and amplitude of the received signal vector, the ML decision rule can be expressed as

$$\begin{aligned} \hat{\underline{\mathbf{s}}} &= \underset{\underline{\mathbf{s}} \in C'}{\text{argmax}} \quad P\left(\underline{\mathbf{r}} \mid \underline{\mathbf{s}}\right) \\ &= \underset{\underline{\mathbf{s}} \in C'}{\text{argmax}} \quad \log\left(p\left(\underline{\mathbf{r}} \mid \underline{\mathbf{s}}\right)\right) \\ &= \underset{\underline{\mathbf{s}} \in C'}{\text{argmin}} \; (\underline{\mathbf{r}}_\rho - \underline{\mathbf{s}}_\rho)^T \mathbf{\Gamma}_{w_R}^{-1} (\underline{\mathbf{r}}_\rho - \underline{\mathbf{s}}_\rho) + (\underline{\mathbf{r}}_\theta - \underline{\mathbf{s}}_\theta)^T \mathbf{\Gamma}^{-1} (\underline{\mathbf{r}}_\theta - \underline{\mathbf{s}}_\theta) + \log\left(|\det(\mathbf{\Gamma})|\right) \cdot \end{aligned} \tag{5.27}$$

where the estimated vector $\hat{\underline{\mathbf{s}}}$ is supposed to be the transmitted symbols sequence.

**Remark 13.** *In the case of SC systems in presence of GPN [16], the ML decision rule is based on a symbol-by-symbol detector. In the expression (5.27), the ML decision rule holds a sequence of symbols. It means that for DFT-s-OFDM systems in presence of a GPN, we have to find the transmitted symbol sequence which satisfy the ML decision rule. The set $C'$ contains all the possible transmitted symbol sequences with a size of $(N_s)^{M_s}$, where $M_s$ is the modulation order.*

**Remark 14.** *For $N_s$ and $M_s$ values used in 5G-NR, it is complex to implement this optimal detector. For instance, if we assume $N_s = 1024$ and $M_s = 64$, the set $C'$ will require $1024^{64}$ reference vectors to perform the ML expression in (5.27). This detection of sequence of symbols comes from the ICI which does not follow an uncorrelated complex Gaussian random process.*

### 5.4.3 Sub-optimal detection criterion

**Important note 16.** *For the sub-optimal detection, let us suppose that the ICI follows an uncorrelated complex Gaussian random process.*

This means that its correlation matrix is a diagonal matrix and we can defined it as follows:

$$\gamma_k \backsim \mathbb{CN}(m_{\gamma_k}, \sigma^2_{\gamma_k}) = \begin{cases} m_{\gamma_k} = E[\underline{\gamma}_k] \ \backsimeq 0 \\ \sigma^2_{\gamma_k} = \mathbf{diag}_k\{\mathbf{R}_{\underline{\gamma}}\}. \end{cases} \tag{5.28}$$

where $m_{\gamma_k}$ and $\sigma^2_{\gamma_k}$ are respectively the mean and the power of $\underline{\gamma}_k$.

The expression (5.12) becomes:

$$r_k \backsimeq s_k \cdot e^{j\Phi_k} \ + \ w_k, \tag{5.29}$$

where $\Phi_k \backsim \mathcal{N}(0, \sigma^2_{\Phi_k})$ and $w_k = \eta_k + \gamma_k$ is defined as follows

$$w_k \backsim \mathbb{CN}(m_{w_k}, \sigma^2_{w_k}) = \begin{cases} m_{w_k} = m_{\eta_k} + m_{\gamma_k} \ \backsimeq 0 \\ \sigma^2_{w_k} = \sigma^2_n + \sigma^2_{\gamma_k}. \end{cases} \tag{5.30}$$

Considering a high SNR approximation, the expressions (5.20) and (5.21) become

$$\begin{aligned} r_{k_\rho} &= \left| \ (s_{k_\rho} + w'_k) \cdot e^{j(\Phi_k + s_{k_\theta})} \ \right| \\ &\backsimeq s_{k_\rho} + \mathfrak{Re}\{w'_k\} \end{aligned} \tag{5.31}$$

$$\begin{aligned} r_{k_\theta} &= \arg\left( \ (s_{k_\rho} + w'_k) \cdot e^{j(\Phi_k + s_{k_\rho})} \ \right) \\ &\backsimeq s_{k_\theta} + \Phi_k + \frac{\mathfrak{Im}\{w'_k\}}{s_{k_\rho}} \end{aligned} \tag{5.32}$$

where $w'_k = w_k \cdot e^{-j(\Phi_k + s_{k_\theta})} \backsim \mathbb{CN}(0, \sigma^2_{w_k})$. So, expressions in (5.22) become:

$$\begin{cases} r_{k_\rho} - s_{k_\rho} \backsim \mathcal{N}(0, \sigma^2_{w_k}/2) \\ r_{k_\theta} - s_{k_\theta} \backsim \mathcal{N}(0, \sigma^2_{\Phi_k} + \frac{\sigma^2_{w_k}}{2s^2_{k_\rho}}). \end{cases} \tag{5.33}$$

The join PDF of expressions in (5.33) is expressed as follows:

$$p(r_k \mid s_k) = \frac{\exp\left(-\frac{1}{2}\left(\frac{(r_{k_\rho} - s_{k_\rho})^2}{\sigma^2_{w_k}/2} + \frac{(r_{k_\theta} - s_{k_\theta})^2}{\sigma^2_{\Phi_k} + \sigma^2_{w_k}/2s^2_{k_\rho}}\right)\right)}{2\pi\sqrt{\frac{\sigma^2_{w_k}}{2}(\sigma^2_{\Phi_k} + \sigma^2_{w_k}/2s^2_{k_\rho})}}. \tag{5.34}$$

When we observe the expression (5.34), we remark that the expression has the same form as the conditional PDF derived in [15] and taken up in [16]. Hence, the ML decision rule using the channel likelihood expression (5.34) can be expressed as:

$$\begin{aligned} \hat{s}_k &= \underset{s_i \in C}{\text{argmax}} \ P(r \mid s_i) \\ &= \underset{s_i \in C}{\text{argmin}} \ \frac{(r_{k_\rho} - s_{i_\rho})^2}{\sigma^2_{w_k}/2} + \frac{(r_{k_\theta} - s_{i_\theta})^2}{\sigma^2_{\Phi_k} + \frac{\sigma^2_{w_k}}{2s^2_{i_\rho}}} \ + \ \log\left(\sigma^2_{\Phi_k} + \frac{\sigma^2_{w_k}}{2s^2_{i_\rho}}\right). \end{aligned} \tag{5.35}$$

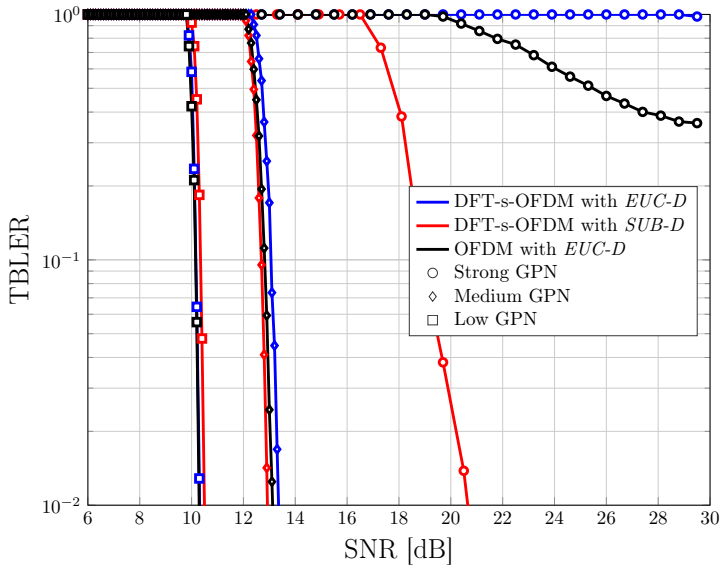


Figure 5.9: OFDM vs DFT-s-OFDM performance: TBLER in function of the SNR for a 16-QAM modulation with $N_s = 480$, $N_f = 512$ and CR=0.7.

**Remark 15.** *Contrary to what was presented earlier, the ML decision rule is given for different received symbols $r_k$ (i.e. for each DFT subcarrier $k$) and not for received signal vectors $\underline{\mathbf{r}}$ as in (5.27). The detector based on the ML metric (5.35) will be denoted by SUB-D from now.*

## 5.5 Performance assessment

In this section, we highlight the performance of a DFT-s-OFDM system under the presence of a GPN. We compare our proposed detector *SUB-D* with the Euclidean detector denoted by *EUC-D* defined in (5.13). We present the TBLER performance as a function of the SNR for a DFT-s-OFDM and OFDM systems assuming different GPN regimes. We consider a LDPC code frame format respecting the 5G-NR specifications [68] assuming different CR.

Fig. 5.9 shows the system performance assuming a 16-QAM modulation scheme and a CR=0.7. Regarding the DFT-s-OFDM, one can notice that our proposed detector *SUB-D* outperforms the *EUC-D* in strong GPN regime. In medium GPN regime, our proposed detector still outperforms the *EUC-D* but with a small SNR gain compared to the strong GPN case. In the low GPN regime, the two detectors provide the same performance. Additionally, one can observe that OFDM and DFT-s-OFDM provide the same performance in medium and low GPN regimes. In contrast, the OFDM is penalized in the strong GPN regime while the DFT-s-OFDM achieves a TBLER of $10^{-2}$ with the proposed *SUB-D*.

We have demonstrated the gain of the *SUB-D* detector over the *EUC-D* detector in a strong GPN regime using perfect knowledge of SPE and ICI stochastic properties.

**Important note 17.** *DFT-s-OFDM waveform may therefore be a more effective solution than OFDM in high GPN channels with the proposed SUB-D detector.*

**Remark 16.** *For the scenarios considered, the assumption of ICI independence is sufficiently valid not to result in a drop in performance.*

## 5.6 Estimation of the SPE and ICI

We show the effectiveness of the *SUB-D* detector in the previous section. The challenge in applying this detector relies in estimating $\sigma^2_{\Phi_k}$ and $\sigma^2_{\gamma_k}$ in realistic transmission scenarios. In this section, we focus on the estimation of the latter in order to compute the *SUB-D* detector in a realistic RF transmission scenario. For that, let us define the SPE vector $\underline{\beta}$ as follows:

$$\begin{aligned}\underline{\beta} &= \left[\beta_0, \cdots, \beta_{N_s-1}\right]^T \\ &\simeq \left[e^{j\Phi_0}, \cdots, e^{j\Phi_{N_s-1}}\right]^T \\ &\simeq e^{j\underline{\Phi}}\end{aligned} \tag{5.36}$$

where $\underline{\Phi} = \left[\Phi_0, \cdots, \Phi_{N_s-1}\right]^T$ is the new PN vector after DFT-s-OFDM demodulator. The expression (5.36) is obtained from (5.9). We also define the PN vector generated by the oscillators as $\underline{\phi} = \left[\phi_0, \cdots, \phi_{N_f-1}\right]^T$. The relation between $\underline{\Phi}$ and $\underline{\phi}$ is

$$e^{j\underline{\Phi}} = \mathbf{B}e^{j\underline{\phi}} \quad \text{with} \quad \mathbf{B}^{(i,k)} = \mathbf{A}_{RX}^{(i,k)}\mathbf{A}_{TX}^{(k,i)} \tag{5.37}$$

for $i \in \{0, \cdots, N_s - 1\}$ and $k \in \{0, \cdots, N_f - 1\}$. The matrices $\mathbf{A}_{TX}$ and $\mathbf{A}_{RX}$ are defined as follows:

$$\mathbf{A}_{TX} = \mathbf{F}_{N_f}^H \mathbf{M}_{TX}\mathbf{F}_{N_s} \quad \text{and} \quad \mathbf{A}_{RX} = \mathbf{F}_{N_s}^H \mathbf{D}_{RX}\mathbf{F}_{N_f}, \tag{5.38}$$

where $\mathbf{M}_{TX}$ and $\mathbf{D}_{RX}$ respectively represent the $N_s$-to-$N_f$ mapping matrix and the $N_f$-to-$N_s$ demapping matrix. By using the small angle approximation, the expression (5.37) gives:

$$\underline{\mathbf{1}}_{N_s} + j\underline{\Phi} = \mathbf{B}\left(\underline{\mathbf{1}}_{N_f} + j\underline{\phi}\right) \Longleftrightarrow \underline{\Phi} = \mathbf{B}\underline{\phi} \tag{5.39}$$

because $\mathbf{B} \in \mathbb{R}^{N_s \times N_f}$. Then, the correlation of $\underline{\Phi}$ is obtained as follows:

$$\mathbf{R}_{\underline{\Phi}} = \mathbb{E}\left[\underline{\Phi} \cdot \underline{\Phi}^H\right] \simeq \mathbf{B}\mathbf{R}_{\underline{\phi}}\mathbf{B}^H, \tag{5.40}$$

where $\mathbf{R}_{\underline{\phi}} = \mathbb{E}\left[\underline{\phi} \cdot \underline{\phi}^H\right]$ represents the correlation matrix of the PN vector generated by the oscillators. Finally, we compute the expression (5.10) upon (5.40) to obtain the different $\sigma^2_{\Phi_k}$ for each DFT subcarrier $k$ as follows:

$$\sigma^2_{\Phi_k} = \mathbf{diag}_k\{\mathbf{B}\mathbf{R}_{\underline{\phi}}\mathbf{B}^H\}. \tag{5.41}$$

For the ICI power, we propose the easiest way to estimate it. It is defined for $k \in \{0, \cdots, N_s - 1\}$ by the relation bellow:

$$\sigma^2_{\gamma_k} = \sigma^2_{\phi} - \sigma^2_{\Phi_k}. \tag{5.42}$$

In this section, we show that if we know the correlation matrix of the PN generated by the oscillator, one can be able to estimate $\sigma^2_{\Phi_k}$ and $\sigma^2_{\gamma_k}$. Thankfully, it is possible to have it if its PSD $K_0$ and the system bandwidth $B_W$ are known. Since the PN generated by the oscillator follows an uncorrelated Gaussian random process, its correlation matrix is given by

$$\mathbf{R}_{\underline{\phi}} = \sigma^2_{\phi}\mathbf{I}_{N_f}, \tag{5.43}$$

where $\mathbf{I}_{N_f}$ is the identity matrix with size $N_f \times N_f$. Fig. 5.10 presents the performance comparison by using the estimated and the genie-aided *SUB-D*. The estimated *SUB-D* means the implementation of the *SUB-D* detector with estimated $\sigma^2_{\Phi_k}$ and $\sigma^2_{\gamma_k}$. In contrast, genie-aided *SUB-D* denotes the implementation of the *SUB-D* detector with perfect knowlegde of $\sigma^2_{\Phi_k}$ and $\sigma^2_{\gamma_k}$. One can notice the estimated *SUB-D* yields the same results as the genie-aided one. These results validate the presented estimation approach.

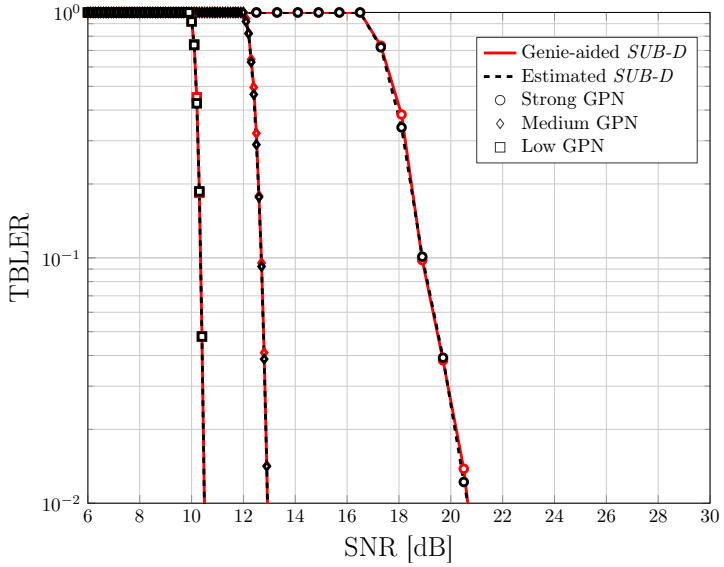


Figure 5.10: DFT-s-OFDM performance: estimated *SUB-D* vs. genie-aided *SUB-D* assuming a 16-QAM modulation, $N_s = 480$, $N_f = 512$ and CR=0.7.

## 5.7 Further analysis of GPN effect on MC waveform

### 5.7.1 OFDM system case

Many contributions in the state-of-the-art propose ICI cancellation techniques [44, 47] to improve the performance of OFDM systems. In all these contributions, the considered PN is a superposition of a mostly correlated PN and a low white PN [30]. Therefore, we decide to evaluate the OFDM system performance under GPN effects. To do so, we implement two PN estimation algorithms: (i) the CPEE algorithm [43] and (ii) the De_ICI algorithm [44]. The CPEE algorithm involves taking an average of pilot observations to estimate the CPE. The De_ICI algorithm consists in applying an ICI filter to the received signal in order to become nearly devoid of ICI. In what follows, the term "De_ICI-$L_f$" denotes the use of the De_ICI algorithm with an ICI filter of length $L_f$. In [44], the authors show that the increase of $L_f$ enhances the mitigation of the ICI. Additionally, they demonstrate that computing the De_ICI-1 comes back to do the CPEE algorithm.

Fig. 5.11 highlights the performance of an OFDM system in terms of uncoded BER as a function of the SNR. One can notice that for all the GPN regimes, performing the CPEE algorithm is not necessary because it gives the same results as the case where we do not compensate the PN. When it comes to the De_ICI algorithm, one can observe that De_ICI-1 provides the same performance as the CPEE. Unfortunately, in contrast to the results presented in [44], the De_ICI algorithm fails for all the GPN regimes when we increase the ICI filter length. The reason behind this observation is the uncorrelated nature of the applied PN induces an ICI having an almost uncorrelated nature (due to the Fourier transform linearity property). Consequently, the ICI filter will not be able to remove the random ICI induced. Finally, we draw the conclusion that state-of-the-art compensation techniques are useless in OFDM when the PN has an uncorrelated nature.

### 5.7.2 Case of GPN considering multi-path channel

All the work presented above is based on the assumption that the channel is dominated by its LoS contribution (the NLoS paths are negligible). This assumption is made on the contributions

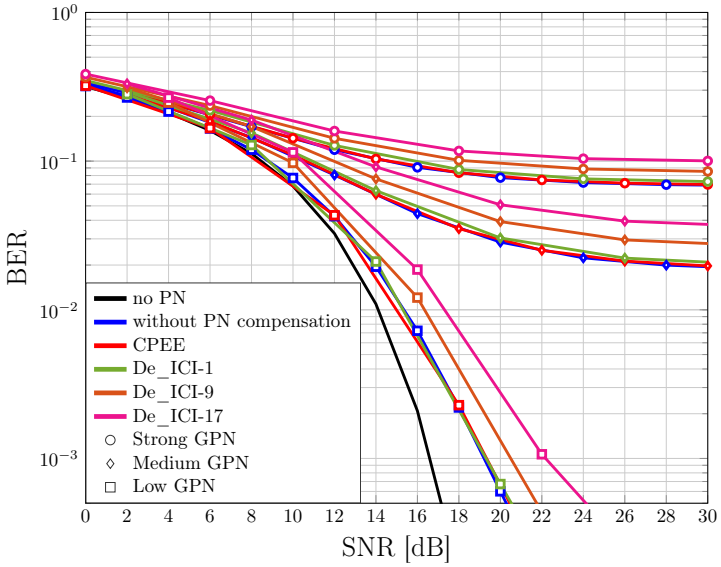


Figure 5.11: OFDM performance: BER in function of the SNR for a 16-QAM, $N_s$=480 and $N_f$=512.

about sub-THz and THz channel characteristics in the state-of-the-art. However, the NLoS paths may not always be negligible (indoor reflections for instance). Therefore, CEQ is required before using the proposed *SUB-D* detector. Unfortunately, the uncorrelated nature of the GPN will not allow its good tracking and estimation in real time. Thus, the channel statement has to be perfectly known when the GPN power becomes important.

## 5.8 Conclusion

In this chapter, we addressed the effects of GPN on 5G-NR MC waveforms. In DFT-s-OFDM systems, we noticed the presence of GPN causes two distortions namely SPE and ICI. To better characterize these two terms, we performed a statistical study. It revealed that the SPE term can be reduced to a simple phase shift where the phase follows an uncorrelated Gaussian random process while the ICI term cannot be considered as following a complex Gaussian random process. Moreover, both SPE and ICI depend on the DFT subcarrier index as a function of the $\zeta = N_s/N_f$. We also showed that the system performance depends on the power of the GPN. We highlighted that the performance of DFT-s-OFDM systems by using the traditional detector based on the minimization of the Euclidean distance does not work out in strong GPN regime. To address this concern, we proposed a detector which relies on considering the ICI follows a complex Gaussian random process. It requires the knowledge of the PN power of the SPE and the ICI on each subcarrier. We showed a performance comparison of the proposed detector with the Euclidean detector. We demonstrated that our proposed detector outperforms the Euclidean one in strong GPN regime. Additionally, the DFT-s-OFDM is more effective than OFDM in strong GPN channels with the proposed receiver. Otherwise, both DFT-s-OFDM and OFDM achieve the same performance.

Furthermore, we study the feasibility of implementing our proposed detector in practical RF transmission scenario. We presented how to estimate the subcarrier PN power of the SPE and the ICI. We showed that our proposed detector by using estimated subcarrier PN powers provides the same performance as the case where they are perfectly known. We also present the impacts of GPN upon OFDM system performance by using two PN compensation algorithms of the literature. We highlighted the CPE and ICI cancellation techniques mostly presented in the literature are useless due to the uncorrelated nature of the GPN. Consequently, our proposed

detector could be implemented to satisfy high SE and therefore high throughput goal of future 6G systems in strong GPN regime.

The technical content of this chapter has been disseminated by the following conference papers and journal paper in part:

[C7] **Y. Bello**, D. Demmer and J-B. Doré, *"Analyse des effets du bruit de phase Gaussien sur un signal DFT-s-OFDM,"* Colloque Gretsi, Grenoble, France, 2023.

[J1] **Y. Bello**, J-B. Doré and David Demmer, *"Analysis of Gaussian Phase Noise Effects in DFT-s-OFDM systems for sub-THz Transmissions,"* **submitted**, 2023.

# Part V

# Conclusion and Perspectives

CHAPTER 6

# Conclusion and Perspectives

## Contents

## 6.1 Overall conclusion

In this thesis, we carried out research into reducing the PN effects generated by high-frequency oscillators for RF transmission in the sub-THz spectrum. More specifically, the reduction of PN effects on MC communication systems such as OFDM and DFT-s-OFDM systems. To propose effective solutions, we first describe various PN models highlighted in chapter 2. In particular, we present the 3GPP standard PN model, widely used in the literature; the GPN model, little discussed in the state-of-the-art, but consistent with the characteristics of the sub-THz and THz spectrum. In addition to these two models, we considered a realistic PN model obtained from measurements carried out on a real CMOS-based oscillator mounted on a transceiver designed at the CEA and operating in D-band. Knowing the PN nature is crucial to adapt a proper PN mitigation technique to consider. In this way, these different PN models can be classified into two groups: those of a correlated nature, such as the 3GPP standard PN and the one obtained from measurements; and those of an uncorrelated nature, such as the GPN model. Then, we have presented the PN effects by deriving received signal expressions for each of the MC systems. It was shown that the PN causes a CPE common to all subcarriers of an OFDM symbol and an ICI in OFDM systems. On the other hand, it causes an SPE specific to each subcarrier and an ICI in DFT-s-OFDM systems.

We then moved onto the design of algorithms for estimating and compensating the various effects induced by PN. When the PN has a correlated nature, 3GPP pilots named PT-RS can be inserted to track and estimate it. Thus, in Chapter 3, we proposed an estimation and compensation algorithm based on LS estimation. This algorithm requires the knowledge of the correlation level of the PN-induced effects in DFT-s-OFDM systems (after the IDFT at receiver). To assess the efficiency of this algorithm, we compared it to several algorithms presented in the state-of-the-art. The results showed that the proposed algorithm enables the considered DFT-s-OFDM systems to achieve better performance than the algorithms presented in the literature by reaching a SE of 5.4 bits/s/Hz with a SNR gain of 3 dB considering a 5G-NR numerology $\mu = 5$. Moreover, the proposed algorithm for DFT-s-OFDM systems gives better performance at low pilot density. Furthermore, it appears that the proposed solution is rather complex to implement. Therefore, we investigated how to limit the implementation complexity by reducing the number of FIR coefficients, enabling DFT-s-OFDM systems to operate at low complexity and high SE in the sub-THz bands.

The presence of ICI limits the performance of OFDM systems with the proposed WIF. Given the performance gain offered by the WIF algorithm in DFT-s-OFDM systems, we proposed an algorithm in Chapter 4 using the same approach as that proposed in Chapter 3, but extended in the time-domain (before the FFT at the receiver) and considering a frequency-selective channel. Regarding the proposed algorithm for OFDM systems, the PN compensation is done in the time-domain and therefore, it reduces the effects of induced CPE and ICI. Better performance are obtained compared to the algorithms presented in the state-of-the-art when the receiver has no knowledge of the CSI. Typically, the proposed algorithm enables a SE of 3.6 bits/s/Hz with a SNR gain of more than 5 dB considering a 5G-NR numerology $\mu = 3$ and a Rician channel with a $K$-factor of 15 dB. Additionally, the implementation complexity of this algorithm was outlined and the computational reduction method described in Chapter 3 can be implemented, allowing OFDM systems to also operate at low complexity and high SE in the sub-THz bands.

When the PN has an uncorrelated nature, it is impossible to estimate it from the pilots as for the case of correlated PN. Thus, for the GPN model, we have proposed an optimal detector specific to DFT-s-OFDM systems and based on the stochastic properties of PN-induced effects. To validate the effectiveness of this detector, we compared it to the detector based on Euclidean distance minimization. The results show that the proposed detector presented in Chapter 5 performs better in the strong GPN regime. We then compared the DFT-s-OFDM and OFDM

systems under strong GPN. This comparison revealed that DFT-s-OFDM is a solution to be considered over OFDM in high GPN regime by providing a TBLER of $10^{-2}$ with a SNR gain more than 5 dB. We considered the implementation of this detector for realistic RF transmissions by presenting an approach for estimating the needed parameters. Furthermore, we presented the performance of an OFDM system by implementing an ICI compensation algorithm presented in the literature. We found that this ICI compensation algorithm is useless when the PN has an uncorrelated nature. Moreover, we also found that if the propagation channel is frequency-selective, it is necessary to have perfect knowledge of it. Otherwise, channel estimation would not be possible due to the uncorrelated nature of the PN, especially in a strong GPN regime.

> To summarize, when the PN has a correlated nature and the channel is frequency flat, OFDM with CPE algorithm can be sufficient to enhance the system performance considering numerologies above seven ($\mu \geq 7$ *i.e.* the ICS $\Delta_f \geq 1920$ kHz), a carrier frequency $F_c = 140$ GHz and a pilot density $\mathcal{D} = 12.5\%$ on each OFDM and DFT-s-OFDM symbol. In the case of 5G-NR numerologies, ICI cancellation techniques will be necessary to improve the performance of OFDM systems. However, DFT-s-OFDM with the proposed WIF algorithm may be a better solution compared to OFDM in low pilot density. When the PN has a correlated nature and the channel is frequency selective (and the receiver has no knowlegde on it), OFDM with the proposed TDF algorithm may be a better solution compared to OFDM with ICI cancellation techniques of the literature. Finally, when the PN has an uncorrelated nature and the channel is frequency flat, DFT-s-OFDM with the proposed detector *SUB-D* may be a solution compared to OFDM in strong GPN regime. In medium and low GPN regime, OFDM and DFT-s-OFDM provides the same performance with the detector based on the Euclidean distance.

## 6.2 Which waveform for 6G in sub-THz spectrum?

A final question to close this report is: **which waveform is best suited for 6G in sub-THz spectrum**. Considering the realistic PN model at 140 GHz carrier frequency obtained from measurements carried out at CEA[1], we can say the following considering a LoS channel[2]:

> if we want to minimize the PAPR and maximize the system performance (in terms of TBLER), the SC waveform (without pulse shaping) with the WIF algorithm is best suited to achieve a SE of 4.2 bits/s/Hz. Now, if we wish to use MC waveforms, then the DFT-s-OFDM waveform with the WIF algorithm is best suited to achieve a SE of 4.2 bits/s/Hz considering $\mu = 6$.
> However, to reach data rates in the Tbits/s range, MIMO technology will have its part to play. So, if we consider MIMO systems using the DFT-s-OFDM waveform, then the PAPR gain of the latter compared to OFDM will become negligible (depending on the number of antennas). In this case, we can consider using the OFDM waveform with the De_ICI[a] or TDF[b] algorithms to achieve a SE of 4.2 bits/s/Hz with $\mu = \{5, 6\}$.
> The higher the numerology ($\mu \geq 8$), the more the implementation of OFDM and DFT-s-OFDM waveforms with the CPEE algorithm is sufficient to achieve a SE of 4.2 bits/s/Hz.
>
> [a] by considering a pilot density of 12.5%
> [b] by considering a pilot density of 1.56%

[1] This PN has a dominant correlated nature
[2] We consider a sampling frequency of 3932.16 GHz and allocated signal bandwidth of 1.966 GHz

**Remark 17.** *Increasing the numerology means increasing the ICS. This may imply other constraints such as increasing the sampling frequency which is critical as presented in chapter 1. Further, it implies the reduce of the CP size which results in lowered robustness against delay spread in the case of multipath channel [69].*

**Remark 18.** *In the case of SC waveform, the signal is filtered with a Root Raise Cosine (RRC) pusle shaping filter to limit its spectral response. In [69], the authors show how the roll-off factor of the RRC filter can increase the PAPR of the SC systems with pulse shaping.*

**Important note 18.** *Furthermore, when the PN has an uncorrelated nature, the SC waveform may be a better solution to reach higher SE [16].*

Finally, it is worth mentioning that the choice of a waveform for a standard is not only based on technical considerations. In particular, the use of OFDM could allow the reuse of all 3GPP concepts on framing, definition of physical signals, channel estimation, beamforming, and enable a single modem technology to address the whole spectrum (5G-NR spectrum and future 6G).

## 6.3 Perspectives

### 6.3.1 Towards a realistic implementation

Various PN compensation algorithms for multi-carrier systems are presented in this report. Estimation methods for a possible low-complexity implementation of these are also discussed. A short-term task is to implement these algorithms in real transmission tests. An implementation will enable us to measure the effectiveness of these algorithms by comparing the performance obtained with those presented in this report, and thus validate or not these algorithms for practical sub-THz transmission.

### 6.3.2 PN Mitigation in MC systems using AI

In recent years, AI has been increasingly considered in a number of fields, in view of the progress it has made. These advances in AI have prompted researchers to consider its use in communication systems for tasks such as channel estimation and equalization, resource optimization, etc. [70–72]. As a result, AI has an important role to play in the future communication technology called 6G [73]. Regarding PN impairments, we can see works proposing how to manage it in the literature with Deep Learning (DL) tools. [74–76] propose constellation optimization with autoencoders to minimize detection errors in SC systems. In contrast, [77] proposes to compensate the PN effects in OFDM at the carrier frequency of 30 GHz. It would therefore be interesting to study the use of AI tools to improve the performance of MC systems affected by PN for sub-THz transmission. Subsequently, a performance comparison with the processing algorithms presented in this report could be envisaged.

### 6.3.3 PN Cancellation in distributed MIMO systems

Reaching a 1 Tbit/s data rate using only a single communication link is an immensely challenging task, even when employing advanced modulation techniques. To overcome this challenge, multi-antenna systems such as MIMO configurations become essential. MIMO enables us to enhance data rates by concurrently transmitting multiple communication streams through space. To

address the substantial signal losses encountered in sub-THz channels, high-gain and directional antennas are indispensable. Thus, beamforming and beam alignment are also employed to focus the signal toward the direction of interest. However, the PN generated by high-frequency oscillator in sub-THz will make difficult to use these techniques efficiently. Consequently, it can be interesting to investigate how these techniques can be managed with the presence of PN especially in distributed massive MIMO, where we have several independent oscillators.

### 6.3.4 PN Compensation in joint communication and sensing in sub-THz bands

For 6G, we would like to do the sensing and communication jointly. The exploration of incorporating sensing capabilities into a communication network is an area of great promise under examination in the early stages of 6G research. Leveraging the sub-THz spectrum allows the integration of large antenna arrays, offering benefits such as improved MIMO capabilities, as well as the potential for enhanced range and angular resolution [78]. However, the idea of high-frequency detection inevitably involves hardware imperfections, notably PN. The impact of PN in radar systems is not a new subject [79]. The waveform commonly used in radar is the Frequency Modulated Continuous Wave (FMCW). In [80], the authors highlight the problem of reflected transmitter PN from large targets. [81] treats about PN problem when the propagation time is greater than the coherence time of the oscillator. Moreover, doing detection and communication at the same time means that we are in a bistatic scenario, *i.e.* the LO at transmitter is different from that at receiver and therefore, the PN generated at transmitter and receiver are uncorrelated. Some solutions have been proposed in the literature to overcome the PN problem in this case. In [82], the authors propose to mitigate the PN by transmitting the carrier frequency. Nevertheless, there is a consensus in the literature in favor of using techniques to reduce the PN power [81] or using high-quality oscillators with low PN generation [83], to enhance the sensing performance. This would also be beneficial for communication. However, this is not an easy task, despite advances in semiconductor technologies. According to the correlated PN models and compensation algorithms proposed in this report, we could imagine to extend the principle of the proposed algorithms to manage the correlated part of the PN and improve the detection.

# Appendices

Appendix A

# Résumé étendu de thèse

Ce rapport de thèse présente des travaux qui sont axés sur l'amélioration des futures systèmes de communication sans fil pour des transmissions dans des spectres de fréquence au-délà de 100 GHz appélées *sub-THz bands*. Plus précisément, nous nous sommes intéressés à l'amélioration des performances de ces systèmes en vue d'atteindre des débits de données de l'ordre du Tbit/s. Les composants électroniques permettant cette montée en fréquence présentent certaines limites qui doivent être prises en compte. Ce qui est le cas de l'oscillateur, composant intervenant dans la conversion du signal en bande de base (basse fréquence) en signal haute fréquence et inversement. Ce dernier introduit du bruit qui dans les bandes *sub-THz*, dégrade les performances des systèmes. Ainsi, nous proposons des algorithmes de traitement du signal pour pallier ce bruit afin d'améliorer les performances de ces systèmes. Nous allons présenter les éléments qui ont motivé cette thèse et un résumé des travaux qui y ont été menés.

## A.1 Chapitre 1 : Introduction

Comme toute nouvelle technologie de communication, on s'attend à ce que la 6G soit supérieure à la 5G notamment en terme de performance comme mentionné sur la figure A.1. Ainsi, la 6G devra permettre d'atteindre des débits de données de l'ordre du Tbits/s, proposer une latence plus courte comparée à celle de la 5G, augmenter l'efficacité énergétique, la fiabilité de transmission, etc. Pour mes travaux, nous nous sommes penchés sur le volet portant sur l'augmentation du débit de données. Conformément au théorème de Shannon-Hartley, la capacité du canal est caractérisée par le taux de transmission d'informations le plus élevé pouvant être atteint tout en maintenant un taux d'erreur extrêmement faible. Le théorème de Shannon-Hartley [4] considérant un canal altéré par un bruit Gaussien est donné par

$$R < C = B_w \log\left(1 + \frac{P_r}{P_n}\right) = B_W \log\left(1 + \mathrm{SNR}\right), \tag{A.1}$$

où $R$ est le débit d'information en bit/s, $C$ la capacité du canal en bit/s, $B_W$ la largeur de bande du système en Hz et $P_r$ la puissance du signal reçu. La puissance du bruit est représentée par $P_n = N_0 B$, $N_0$ représentant la densité spectrale de puissance (PSD) du bruit thermique. On peut remarquer que la capacité du canal augmente linéairement avec la largeur de bande $B_W$ et avec le logarithme du SNR. Si on se réfère à l'équation de la capacité du canal selon Shannon dans (A.1), une solution possible pour augmenter le débit de données serait d'augmenter la largeur

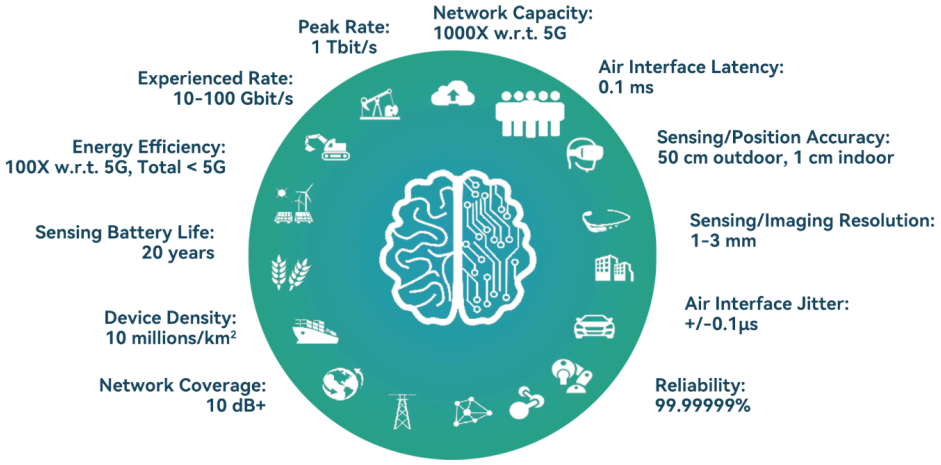


Figure A.1: Les indicateurs clés de performance pour la future 6G technology [1].

de la bande du signal. Sauf que, augmenter la largeur de la bande du signal rendrait difficile la réutilisation des spectres de fréquence considérés dans les technologies actuelles. Une solution est donc présentée à la communauté des Télécommunications : transmettre dans le spectre sub-THz et THz plus précisément à des fréquences au-delà de 100 GHz. Malheureusement, plusieurs facteurs empêchent la transposition des technologies actuelles à cette gamme de fréquences parmi lesquels : la forte atténuation de l'onde électromagnétique par le canal de propagation, l'échantillonnage très rapide voire critique requis par les DAC/ADC, le bruit de phase généré par les oscillateurs et la faible efficacité des amplificateurs de puissance. Dans le cadre de ma thèse, nous nous sommes intéressés aux effets du bruit de phase généré par les oscillateurs.

#### A.1.0.1 Le bruit de phase (en anglais PN)

L'un des principaux défis à relever lorsqu'il s'agit de mettre en place une communication dans les bandes sub-THz est de traiter avec un composant appelé oscillateur. Ceux-ci sont très importants dans le processus de communication, car ils sont responsables de la transposition en haute fréquence du signal en bande de base. Le bémol est que ces oscillateurs radio-fréquence, qui sont cruciaux, ont des imperfections qui introduisent des problèmes, en particulier quelque chose appelée le bruit de phase (PN) comme mis en évidence dans la figure A.2 par la réponse réelle de l'oscillateur. Plus la fréquence porteuse est élevée, plus ce problème de PN s'aggrave. La sortie complexe $v$ d'un oscillateur avec une fréquence porteuse $F_c$ est définie par

$$v(t) = (1 + \varepsilon(t))\, e^{j2\pi(F_c+\varsigma)t+j\phi(t)}, \tag{A.2}$$

où $\varepsilon$, $\varsigma$ et $\phi$ désignent respectivement le bruit d'amplitude, le CFO et le PN. Pour les communications dans les bandes sub-6GHz, le PN n'est pas vraiment un problème car les oscillateurs sont assez fiables, et d'autres problèmes matériels sont généralement plus importants. Par contre pour des systèmes de communication numériques pour les bandes sub-THz, le PN devient l'un des principaux problèmes [12, 13], et il peut sérieusement limiter la qualité du fonctionnement du système et la rapidité avec laquelle les données peuvent être transférées avec un niveau élevé de fiabilité [14].

Comme on peut le constater dans (A.2), le PN n'est pas la seule altération de phase générée par l'oscillateur. Nous avons également ce que l'on appelle le CFO. Elle est causée par la désynchronisation entre l'oscillateur de l'émetteur et celui du récepteur. En général, des signaux de référence sont insérés pour suivre et compenser le CFO afin d'en réduire ses effets.

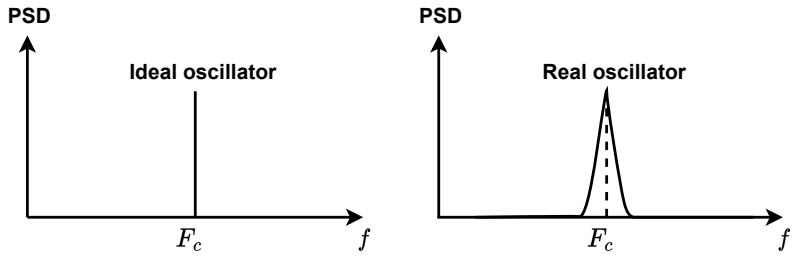


Figure A.2: Densité spectrale de puissance (PSD) de la réponse fréquentielle d'un oscillateur idéal (ideal) vs. oscillateur réel (real)

## A.2 Chapitre 2 : Modélisation de notre système de communication

### A.2.1 Modèle de PN

Le PN provient d'une variation aléatoire, brève et rapide des composants de l'oscillateur qui est un composant électronique. Dans cette thèse, trois modèles de PN ont été considérés : un PN non corrélé (dit Gaussien) et deux bruits de phase corrélés ou partiellement corrélés puisqu'ils contiennent également une partie non corrélée. Le PN corrélé peut être défini comme suit

$$\phi[\tau] = \phi_W[\tau] + \phi_G[\tau] \tag{A.3}$$

où $\phi_W[\tau]$ représente la partie corrélée du PN et $\phi_G[\tau]$ la partie non corrélée. Les deux modèles corrélés qui sont représentés sur la figure A.3b sont :

- Le modèle du standard 3GPP dont la particularité est qu'il présente une densité spectrale (PSD) du PN à la station de base (BS) différente de celle du côté de l'utilisateur (UE). Cette différence de PSD provient des contraintes énergétiques de chacun.
- Le modèle de PSD de PN obtenu à partir de mesures effectuées sur un émetteur-récepteur opérant à bande D (c'est-à-dire à 140 GHz) à base de CMOS fabriqué au CEA.

Des travaux dans la littérature [24] ont montré que si la largeur de la bande du signal est très grande devant la fréquence de coupure de l'oscillateur, alors le PN peut être caractérisé par sa partie non corrélé $\phi_G[\tau]$ telle que

$$\phi[\tau] \backsim \mathcal{N}(0, \sigma_\phi^2), \tag{A.4}$$

où $\sigma_\phi^2 = K_0 B_W$ avec $K_0$ qui représente la PSD du PN non corrélé et $B_W$ la bande du signal allouée.

### A.2.2 Effets du PN sur les systèmes de communication

Après avoir selectionné les différents modèles de PN pour nos travaux, nous passons à la présentation des effets du PN sur les différents systèmes de communication multi-porteuses que nous allons étudier notamment les systèmes OFDM et DFT-s-OFDM.

L'OFDM est une forme d'onde standardisée en 4G et 5G pour des communications descendantes (de la BS vers l'UE). Sa particularité est qu'elle permet de transmettre les données sur plusieurs sous-porteuses orthogonales entre elles. Elle a l'avantage de simplifier l'égalisation du canal dans le domaine fréquentiel lorsque la taille du préfixe cyclique est supérieure ou égale à l'étalement du canal. Néanmoins, l'OFDM présente des inconvénients parmi lesquels : sa forte

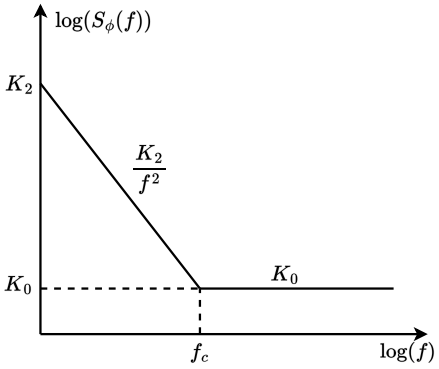


(a) PSD du PN.

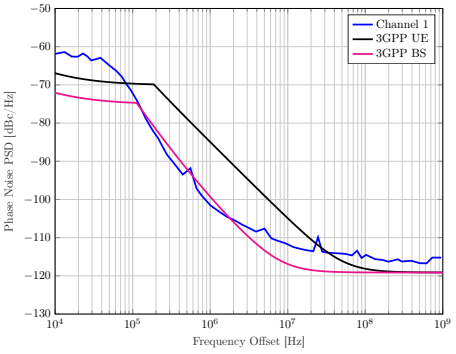


(b) Représensation de la PSD du PN : (noire) standard 3GPP au niveau de l'UE; (rose) standard 3GPP au niveau de la BS; (bleue) : Mesurée au CEA.

Figure A.3: PSD du PN

émission hors bande qui peut causer de l'interférence entre utilisateurs ; et son PAPR élevé qui est facteur critique pour un bon fonctionnement des amplificateurs de puissance (en anglais PA).

La DFT-s-OFDM quant à elle est une forme d'onde standardisée en 4G et 5G pour des transmissions montantes (de l'UE vers la BS). En plus des avantages de l'OFDM, elle permet d'avoir un PAPR faible comparé à l'OFDM. En contrepartie, la DFT-s-OFDM est plus complexe que l'OFDM et peut perdre son gain de PAPR lorsqu'il faut insérer des pilotes pour l'égalisation du canal. Nous avons considéré ces deux formes d'onde pour mes travaux parce que le 3GPP étudie la possibilité de les réutiliser pour les communications sub-THz d'autant plus que l'Institute of Electrical and Electronics Engineers (IEEE) a fait une première standardisation pour les fréquences sub-THz avec la forme d'onde mono-porteuse.

Il en ressort que la présence du PN dans les systèmes OFDM induit la présence de deux effets qui sont:

- l'erreur de phase commune notée CPE, propre à toutes les sous-porteuses
- l'interférence entre porteuse notée ICI

Les expressions de ces deux bruits induits par le PN sont présentées par l'équation suivante [1]:

$$R_k = X_k \underbrace{\frac{1}{N_f}\sum_{p=0}^{N_f-1} e^{j\phi_p}}_{\text{CPE}} + \underbrace{\frac{1}{N_f}\sum_{m=0,m\neq f}^{N_f-1} X_m \sum_{p=0}^{N_f-1} e^{j2\pi\frac{(m-f)}{N_f}p} e^{j\phi_p}}_{\text{ICI}}, \tag{A.5}$$

où $X_k$ et $R_k$ representent le signal transmis et reçu sur la sous-porteuse $k$. Le terme $N_f$ fait reférence à la taille du bloc effectuant la transformée de Fourier et $\phi_p$ le PN.

En ce qui concerne les systèmes DFT-s-OFDM, la présence du PN génère également deux bruits qui sont :

- l'erreur de phase par porteuse notée SPE, propre à chaque sous-porteuse contrairement au CPE en OFDM

[1] le terme représentant le bruit thermique est négligé ici pour mieux mettre en évidence les effets induits par le PN uniquement

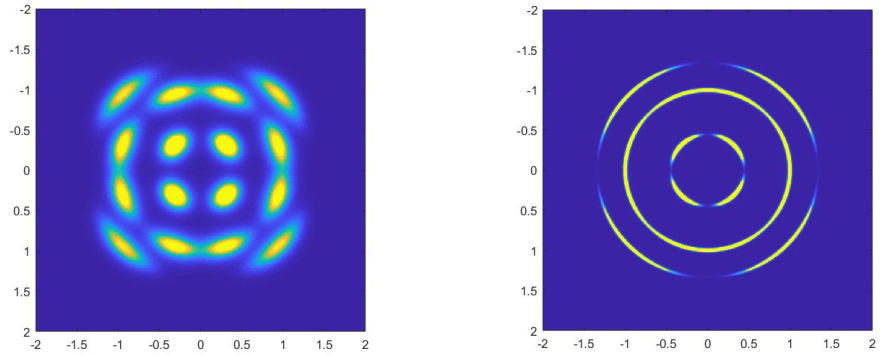

(a) OFDM signal (b) DFT-s-OFDM signal

Figure A.4: Effets du PN sur les différents signaux reçus en considérant les paramètres dans le tableau 2.4 .

- l'interférence entre porteuse notée ICI

Les expressions de ces deux bruits induits par le PN sont présentées par l'équation suivante [2]:

$$r_k = \underbrace{s_k \frac{1}{N_s}\frac{1}{N_f}\sum_{f=0}^{N_s-1}\sum_{m=0}^{N_s-1}\sum_{p=0}^{N_f-1} e^{j2\pi\frac{(m-f)}{N_f}p} e^{-j2\pi\frac{(m-f)}{N_s}k} e^{j\phi_p}}_{\text{SPE}} + \underbrace{\frac{1}{N_s}\frac{1}{N_f}\sum_{n=0,n\neq k}^{N_s-1} s_n \sum_{f=0}^{N_s-1}\sum_{m=0}^{N_s-1}\sum_{p=0}^{N_f-1} e^{j2\pi\frac{(m-f)}{N_f}p} e^{j2\pi\frac{kf-nm}{N_s}} e^{j\phi_p}}_{\text{ICI}}, \tag{A.6}$$

où $s_k$ et $r_k$ representent le signal transmis et reçu sur la sous-porteuse $k$. Le terme $N_s$ et $N_f$ font reférence à la taille des blocs effectuant la transformée de Fourier et $\phi_p$ le PN. les schemas de modèle de transmission de ces deux systèmes sont représentés sur les figures 2.8 et 2.9.

De plus nous avons mis en évidence les différentes constellations indiquant la probabilité d'apparition d'un point dans l'espace IQ sur la figure A.4. Plus la couleur est jaune, plus la probabilité d'apparition est élevée. La couleur bleue représente une probabilité d'apparition quasi nulle. On remarque donc que s'il faut utiliser les formes d'onde OFDM et DFT-s-OFDM pour les communications sub-THz, il faudra compenser les effets induits par le PN afin de permettre une bonne détection à la réception des symboles de données transmis. Par conséquent, l'objectif principal de ma thèse est de **proposer des techniques de compensation de PN qui permettront aux formes d'onde OFDM et DFT-s-OFDM d'être robustes aux effets du PN**.

## A.3 Chapitre 3 : Compensation de PN dans le domaine après les transformées de Fourier

Dans ce chapitre, nous considerons le modèle de PN du standard 3GPP et celui obtenu à partir des mesures effectuées au CEA. Comme mentionné dans A.2, ces deux modèles etant des modèles

[2] le terme représentant le bruit thermique est négligé ici pour mieux mettre en évidence les effets induits par le PN uniquement

majoritairement corrélés, alors il est possible de les traquer. Pour ce faire, le 3GPP propose d'inserer des pilotes nommés PT-RS pour traquer le PN afin de l'estimer et de le compenser à la réception.

En OFDM, les pilotes sont extraits après la FFT à la réception tandis qu'en DFT-s-OFDM, ils sont extraits dans le domaine après la IDFT. Après extraction, un algorithme d'estimation est alors utilisé pour estimer le PN pour ensuite le compenser sur les données avant l'étape de décodage et détection.

Dans le cas d'un système DFT-s-OFDM, l'expression du signal reçu s'écrit comme suit :

$$\begin{aligned} r_k &= s_k\beta(k,N_s,N_f,\phi) \;+\; \gamma(k,N_s,N_f,\phi) \;+\; \underbrace{\frac{1}{\sqrt{N_s}}\frac{1}{\sqrt{N_f}}\sum_{f=0}^{N_s-1}\sum_{p=0}^{N_f-1} n_p e^{-j2\pi\frac{fp}{N_f}} e^{j2\pi\frac{kf}{N_s}}}_{\text{bruit thermique}} \\ &= s_k\beta(k,N_s,N_f,\phi) \;+\; \gamma(k,N_s,N_f,\phi) + \;\eta(k,N_s,N_f), \end{aligned} \tag{A.7}$$

où $\beta(k,N_s,N_f,\phi)$ et $\gamma(k,N_s,N_f,\phi)$ représentent respectivement le SPE et l'ICI définis dans (A.6). Le terme $\eta(k,N_s,N_f)$ represente le bruit thermique après les deux blocs de transformée de Fourier à la réception. Au vue de la constellation présentée par la figure A.4, nous allons simplifié l'expression (A.7) par la suivante :

$$r_k \simeq s_k e^{j\phi_k^{'}} \;+\; \gamma_k + \;\eta_k, \tag{A.8}$$

avec $\phi_k^{'}$ qui représente l'argument (ou la phase) du SPE sur la porteuse $k$ et le nouveau PN à compenser. Dans ma thèse, nous avons proposé de trouver un filtre de Wiener $\mathbf{Z}$ qui minimise l'erreur quadratique moyenne (MSE) ci-dessous :

$$\underset{\mathbf{Z}}{\operatorname{argmin}}\; E\left[\left\|\mathbf{Z}\,\underline{\mathbf{a}}_P - e^{j\underline{\boldsymbol{\phi}}^{'}}\right\|^2\right]. \tag{A.9}$$

Le filtre $\mathbf{Z}$ est une matrice de taille $N_s \times K_d$ avec $K_d$ le nombre de pilotes insérés pour le tracking du PN. Le terme $e^{j\underline{\boldsymbol{\phi}}^{'}}$ est le vecteur que nous voulons estimer. Le terme $\underline{\mathbf{a}}_P = [a_{p_0},\cdots,a_{p_{K-1}}]^T$ est le vecteur contenant le PN estimé à partir des pilotes $\{a_i\}_{i\in\chi_p}$, avec $\chi_p$ l'ensemble contenant les indices des sous-porteuses où les pilotes sont insérés. A partir de l'expression (A.8), on deduit les termes $\{a_i\}_{i\in\chi_p}$ comme suit :

$$a_i = \frac{r_i s_i^*}{|s_i|^2} \simeq e^{j\phi_i'} + \frac{\gamma_i s_i^*}{|s_i|^2} + \frac{\eta_i s_i^*}{|s_i|^2}, \quad \forall i \in \chi_p. \tag{A.10}$$

Ainsi, le vecteur $\underline{\mathbf{a}}_P = [a_{p_0},\cdots,a_{p_{K-1}}]^T$ s'exprime comme suit

$$\begin{aligned} \underline{\mathbf{a}}_P &\simeq e^{j\underline{\boldsymbol{\phi}}_P^{'}} + \underline{\boldsymbol{\gamma}}_P \odot \underline{\mathbf{s}}_P + \underline{\boldsymbol{\eta}}_P \odot \underline{\mathbf{s}}_P \\ &\simeq \mathbf{M}_P e^{j\underline{\boldsymbol{\phi}}^{'}} + \mathbf{M}_P\underline{\boldsymbol{\gamma}} \odot \underline{\mathbf{s}}_P + \mathbf{M}_P\underline{\boldsymbol{\eta}} \odot \underline{\mathbf{s}}_P, \end{aligned} \tag{A.11}$$

tel que $\mathbf{M}_P$ est la matrice d'echantillonnage des pilotes de taille $K_d \times N_s$. Trouver le filtre $\mathbf{Z}$ solution de l'équation (A.9) revient à trouver la matrice qui annule la derivée par rapport à $\mathbf{Z}$ de l'expression (A.9). En considerant les hypothèses suivantes:

- $E\left[\underline{\boldsymbol{\eta}}\right] = \underline{\mathbf{0}}_{N_s}$ parce que $\eta_k \backsim \mathbb{C}\mathcal{N}\left(0,\sigma_n^2\right)$
- $E\left[\underline{\boldsymbol{\gamma}}\right] = \underline{\mathbf{0}}_{N_s}$ (*i.e.* l'ICI est de moyenne nulle)

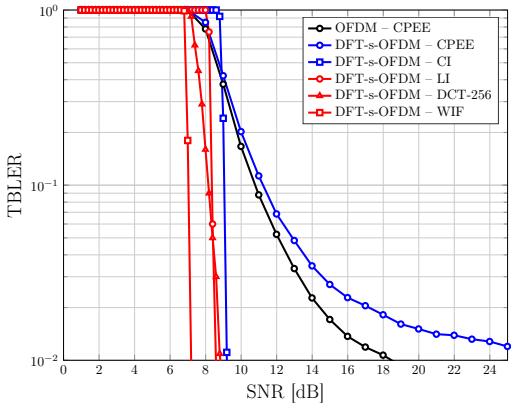


(a) PT-RS insérés tous les $L = 8$ ($\mathcal{D} = 12.5\%$)

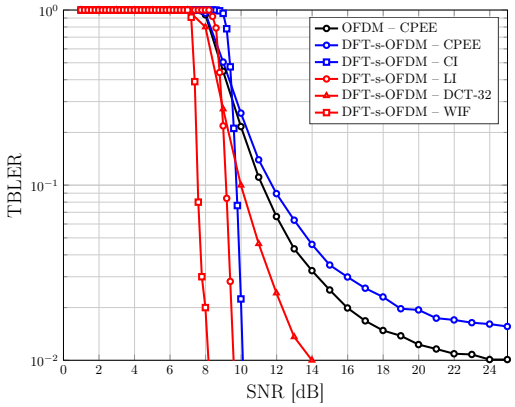


(b) PT-RS insérés tous les $L = 64$ ($\mathcal{D} = 1.56\%$)

Figure A.5: Comparaison des performances entre l'OFDM et la DFT-s-OFDM en considérant le schéma de PT-RS distribué. Le modèle de PN considéré est celui du 3GPP dans figure A.3b.

- les symboles pilotes insérés $\{s_i\}_{i \in \chi_p}$ sont décorrélés

alors, la matrice $\mathbf{Z}$ solution de (A.9) s'exprime comme suit :

$$\mathbf{Z} = \mathbf{R}^H_{e^{j\underline{\phi}'}} \mathbf{M}_P^H \left( \mathbf{M}_P \mathbf{R}^H_{e^{j\underline{\phi}'}} \mathbf{M}_P^H + \mathbf{M}_P \left( \mathbf{R}^H_{\underline{\gamma}} + \mathbf{R}^H_{\underline{\eta}} \right) \mathbf{M}_P^H \odot \mathbf{I}_{K_d} \right)^{\dagger}, \tag{A.12}$$

avec $\mathbf{I}_{K_d}$ la matrice "identité" de taille $K_d \times K_d$. Les termes $\mathbf{R}_{e^{j\underline{\phi}'}}$, $\mathbf{R}_{\underline{\gamma}}$ et $\mathbf{R}_{\underline{\eta}}$ représentent respectivement la matrice d'autocorrélation des vecteurs $e^{j\underline{\phi}'}$, $\underline{\gamma}$ et $\underline{\eta}$. L'algorithme WIF est l'algorithme utilisant l'expression (A.12) du filtre pour l'estimation du PN.

Lorsqu'on observe l'expression (A.12), on remarque que l'utilisation de l'algorithme WIF requiert la connaissance des matrices de correlation des différents termes intervenant dans l'expression du signal reçu. En supposant qu'on ait une connaissance de ces matrices de corrélation, nous pouvons estimer et compenser le PN à l'aide des expressions suivantes :

$$\hat{\underline{\phi}}' = \arg\left(\mathbf{Z}\, \underline{\mathbf{a}}_P\right) \quad \text{et} \quad \hat{\underline{\mathbf{r}}} = \underline{\mathbf{r}} \odot e^{-j\hat{\underline{\phi}}'}, \tag{A.13}$$

avec $\underline{\mathbf{r}} = \left[r_0, \cdots, r_{N_s-1}\right]^T$ le vecteur représentant le symbole DFT-s-OFDM reçu.

### A.3.1 Analyse des performances

Pour évaluer l'efficacité de l'algorithme WIF, nous nous sommes comparés à quelques algorithmes présentés dans l'état de l'art et nous avons obtenu les résultats mentionnés sur la figure A.5 en considérant les paramètres de simulation mentionnés dans la colonne "1" du tableau A.1. Ces différents algorithmes sont les suivantes :

- CPEE : il permet de compenser l'erreur de phase commune (CPE) induit par le PN en OFDM.
- De_ICI : il permet de filtrer l'ICI en OFDM
- CI : il consiste à faire une interpolation linéaire d'ordre 0.
- LI : il consiste à faire une interpolation linéaire d'ordre 1.

Table A.1: Paramètres de simulation

| Parameters | Colonne 1 | Colonne 2 |
|---|---|---|
| Modulation $M_s$ | 16-QAM | {4-QAM; 16-QAM; 64-QAM} |
| Fréquence d'echant $F_s$ | 1966.08 MHz | 3932.16 MHz |
| Numerologie $\mu$ | 5 | 5 to 10 |
| Bande du système $B_W$ | 983.04 MHz | 1884.32 MHz |
| Taille FFT $N_f$ | 4096 | $4096 \times 2^{-\mu+6}$ |
| Porteuses actives $N_a$ | 2048 | $12\left\lfloor \frac{B_W}{12 \cdot F_s} N_f \right\rfloor$ |
| Taille DFT $N_s$ | | |
| Modèle de PN | Modèle 3GPP | Modèle de PN mesuré |
| Fréquence porteuse $F_c$ | 140 GHz | |
| Modèle Canal | AWGN | |
| Rendement codage LDPC | 0.7 | $\{0.3; 0.5; 0.7; 0.9\}$ |
| Décodeur LDPC | Layered Min-Sum | |

- DCT : il consiste à faire une interpolation utilisant des bases de cosinus. Tous les algorithmes d'interpolation concernent la forme d'onde DFT-s-OFDM.

Comme illustré dans la figure A.5, on remarque que notre algorithme WIF améliore davantage les performances des systèmes DFT-s-OFDM comparé aux autres algorithmes de la littérature. Dans le cas de l'OFDM, l'algorithme WIF donne les mêmes performances que l'algorithme CPEE. Ce résultat s'explique par le fait qu'étant donné que l'erreur de phase en OFDM est commune à toutes les sous-porteuses, alors le filtre WIF en OFDM tend vers un filtre moyenneur. De plus, on remarque que pour les numérologies 5G-NR, compenser l'ICI améliore davantage les performances en OFDM comparé au cas où le CPE seul est compensé.

### A.3.2 Estimation des différentes matrices de corrélation

Après avoir montré l'efficacité de l'algorithme WIF, nous nous sommes tournés sur son implémentation pour des transmissions RF pratiques. Pour que cela soit possible, nous aurons besoin d'estimer les différentes matrices d'autocorrélation $\mathbf{R}_{e^{j\underline{\phi}'}}$, $\mathbf{R}_{\underline{\gamma}}$ et $\mathbf{R}_{\underline{\eta}}$.

- Etant donné que le bruit thermique suit une distribution Gaussienne, alors on peut estimer sa matrice d'autocorrélation en multipliant la matrice "identité" par sa variance.

- Vu l'expression complexe de l'ICI, nous allons négliger sa matrice d'autocorrélation et voir l'impact de cette hypothèse sur les performances de l'algorithme WIF.

Il nous reste donc à estimer la matrice d'autocorrélation du PN $\mathbf{R}_{e^{j\underline{\phi}'}}$. Pour cela, deux approches sont envisageables :

- Si la PSD du PN généré par les oscillateurs est connue alors, on peut estimer sa matrice d'autocorrélation comme suit :

$$\begin{aligned}\mathbf{R}_{\underline{\boldsymbol{\phi}}_X} &= \mathbb{E}\left[\underline{\boldsymbol{\phi}}_X \underline{\boldsymbol{\phi}}_X^H\right] \\ &= \frac{F_s}{2}\left(\mathbf{F}^R \mathbf{P}_X \mathbf{F}^{R^T} + \mathbf{F}^I \mathbf{P}_X \mathbf{F}^{I^T}\right), \quad X = \{TX, RX\}\end{aligned} \tag{A.14}$$

où $\mathbf{P}$ représente la matrice diagonale contenant la PSD du PN. Si les bruits de phase générés à l'émission et à la réception sont indépendants et de moyennes nulles, alors on obtient :

$$\mathbf{R}_{\underline{\boldsymbol{\phi}}} = \mathbf{R}_{\underline{\boldsymbol{\phi}}_{TX}} + \mathbf{R}_{\underline{\boldsymbol{\phi}}_{RX}}. \tag{A.15}$$

Ensuite à l'aide de l'approximation "faibles angles", on déduit l'expression de la matrice d'autocorrélation du PN qui nous intéresse à l'aide de l'expression suivante :

$$\mathbf{R}_{e^{j\underline{\boldsymbol{\phi}}'}} \simeq \mathbf{B}\left(\mathbf{1}_{N_f} + \mathbf{R}_{\underline{\boldsymbol{\phi}}}\right)\mathbf{B}^H, \tag{A.16}$$

tel que

$$\mathbf{B}^{(i,k)} = \mathbf{A}_{RX}^{(i,k)} \mathbf{A}_{TX}^{(k,i)} \quad \text{avec} \quad \begin{cases} \mathbf{A}_{TX} = \mathbf{F}_{N_f}^H \mathbf{M}_{TX} \mathbf{F}_{N_s} \\ \mathbf{A}_{RX} = \mathbf{F}_{N_s}^H \mathbf{D}_{RX} \mathbf{F}_{N_f}, \end{cases} \tag{A.17}$$

où $i \in \{0, \cdots, N_s - 1\}$ et $k \in \{0, \cdots, N_f - 1\}$.

- Si la PSD du PN généré par les oscillateurs n'est pas connue, alors nous allons tirer profit de l'architecture de l'émetteur-récepteur conçu au CEA. La particularité de ce dernier est que la montée en fréquence se fait en deux temps par une multiplication fréquentielle de la sortie de l'oscillateur à faible fréquence. Cette multiplication en fréquence permet d'approximer la PSD du PN appliqué au signal RF à partir de la PSD du PN généré par l'oscillateur à faible fréquence. Cette relation est la suivante :

$$\text{PSD} = \text{PSD}_{in} + 20\log_{10}\left(\frac{f_{LO}}{f_{in}}\right), \tag{A.18}$$

où $\text{PSD}_{in}$ est la PSD du PN généré par l'oscillateur à faible fréquence $f_{in}$. A partir de cette équation, on déduit l'expression de la matrice d'autocorrélation du PN qui nous intéresse à l'aide de l'expression suivante :

$$\mathbf{R}_{e^{j\underline{\boldsymbol{\phi}}'}} \simeq \mathbf{B}\left(\mathbf{1}_{N_f} + 2\left(\frac{f_{LO}}{f_{in}}\right)^2 \mathbf{R}_{\underline{\boldsymbol{\phi}}^{in}}\right)\mathbf{B}^H, \tag{A.19}$$

en prenant comme hypothèse que les bruits de phase à l'émission et à la réception suivent la même PSD.

Pour valider cette approche d'estimation des différentes matrices d'autocorrélation, nous avons présenté les performances d'un système DFT-s-OFDM avec l'algorithme WIF en comparaison avec l'algorithme LI sur la figure A.6 en considérant les paramètres de simulation mentionnés dans la colonne "2" du tableau A.1. Nous observons premièrement que le WIF surpasse une fois de plus l'algorithme LI quand on change de modèle de PN. De plus, on constate également que le WIF avec une estimation des matrices d'autocorrélation donne les mêmes performances que le WIF lorsqu'on a une connaissance parfaite de ces matrices. Ce résultat permet de valider les expressions théoriques dérivées plus haut. Sur la figure A.6, on remarque également qu'augmenter la numérologie permet d'améliorer les performances d'un système

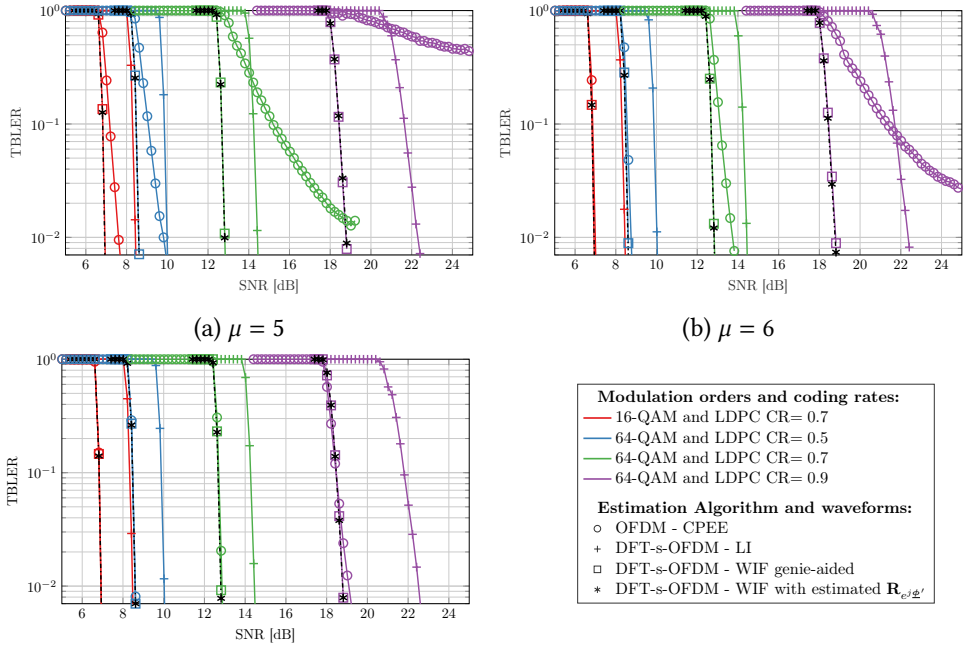


(a) $\mu = 5$ (b) $\mu = 6$

(c) $\mu = 7$

Figure A.6: Performances de la DFT-s-OFDM et de l'OFDM en terme de TBLER en fonction du SNR. Les numerologies $\mu = \{5, 6, 7\}$ et le modèle de PN proposé par le CEA sont considérés.

OFDM avec uniquement l'algorithme CPEE. Ce résultat s'explique par le fait qu'augmenter l'espacement entre porteuses permet de réduire l'ICI.

En conclusion, dans ce chapitre nous avons montré que l'algorithme WIF permet d'avoir de meilleures performances en DFT-s-OFDM comparé aux autres algorithmes de l'état de l'art présentés dans ce chapitre. Ces différents résultats nous ont également poussé à évaluer la complexité d'implémentation de l'algorithme WIF. Nous avons étudié cette complexité et nous avons proposé une approche de réduction de celle-ci qui permet de réduire d'un facteur 100 le nombre de multiplications réelles et additions requis pour le calcul du filtre WIF. Malgré cela, le WIF reste plus complexe que le CPEE en OFDM en octroyant les mêmes résultats de performances. Nous avons également montré qu'augmenter la numérologie permet d'améliorer les performances de l'OFDM en utilisant uniquement l'algorithme CPEE.

### A.3.3 Contributions

Ces travaux ont donné lieu aux contributions suivantes :

[C2] **Y. Bello**, J-B. Doré and D. Demmer, *"DFT-s-OFDM for sub-THz Transmission – Tracking and Compensation of Phase Noise,"* In Proc. IEEE Consumer Communications & Networking Conference (CCNC), NV, USA, pages 297–300, 2023.

[C3] **Y. Bello**, D. Demmer, A. Hamani, A. Siligaris, C. Dehos, N. Cassiau, J-B. Doré and J.L. González-Jiménez, *"Performance Assessment of a 5GNR D-Band Transceiver with Phase Noise Impairments,"* In Proc. Joint European Conference on Networks and Communications & 6G SUMMIT (EuCNC/6G SUMMIT), Goteborg, Sweden, pages 246-251, 2023.

[C4] **Y. Bello**, J-B. Doré and D. Demmer, *"Wiener Interpolation Filter for Phase Noise Estimation in sub-THz Transmission,"* In Proc. IEEE Vehicular Technology Conference

(VTC2023-Spring), Florence, IT, pages 1-5, 2023.

## A.4 Chapitre 4 : Compensation de PN dans le domaine temporel

Dans le chapitre précédent, nous avons montré l'efficacité de l'algorithme WIF comparé aux algorithmes de la littérature. Sauf que l'algorithme WIF ne permet pas de compenser l'ICI notamment en OFDM où son effet n'est pas négligeable pour des numérologies 5G-NR. Pour pallier ce problème, nous proposons de compenser le PN dans le domaine temporel de façon à conjointement réduire les effets du CPE et de l'ICI dans le domaine fréquentiel (pour le cas de l'OFDM). Cette approche est très rarement considérée dans la littérature [60, 61]. De plus, en compensant le PN dans le domaine temporel, on pourrait envisager réutiliser les PT-RS dans le domaine fréquentiel pour estimer les effets du canal pour ensuite l'égaliser en temps réel, ce qui est une approche réaliste. L'expression du signal discret avant le démodulateur OFDM pour un canal multi-trajets peut s'exprimer comme suit :

$$\underline{\mathbf{y}} = \mathbf{\Phi}_R \left( \sum_{j=0}^{L_{ds}-1} h_j \mathbf{U}^{(j)} \mathbf{\Phi}_T \underline{\mathbf{x}} \right) + \underline{\mathbf{w}}, \tag{A.20}$$

où $\mathbf{\Phi}_T$ et $\mathbf{\Phi}_R$ sont les matrices diagonales contenant respectivement les déphasages $e^{j\underline{\phi}_{TX}}$ and $e^{j\underline{\phi}_{RX}}$ sur leurs diagonales. Le terme $h_j$ correspond au coefficient du canal du $j^{ime}$ trajet $\underline{\mathbf{h}}[j]$ et $\mathbf{U}^{(j)}$ est la matrice de convolution associée à ce trajet. Le modèle du système est représenté sur la figure 4.1. On peut réecrire l'expression ci-dessus comme suit :

$$\begin{aligned} \underline{\mathbf{y}} &= \underbrace{h_{lp} \mathbf{\Phi}_R \mathbf{\Phi}_T \underline{\mathbf{x}}}_{\text{Trajet direct (LoS)}} + \underbrace{\mathbf{\Phi}_R \left( \sum_{i=1}^{L_{ds}-1} h_i \mathbf{U}^{(i)} \mathbf{\Phi}_T \underline{\mathbf{x}} \right)}_{\text{Trajets non directs (NLoS)}} + \underline{\mathbf{w}} \\ &= \mathbf{\Phi} \underline{\mathbf{x}} + \mathbf{\Phi}_R \left( \sum_{i=1}^{L_{ds}-1} h_i \mathbf{U}^{(i)} \mathbf{\Phi}_T \underline{\mathbf{x}} \right) + \underline{\mathbf{w}}, \end{aligned} \tag{A.21}$$

où $\mathbf{\Phi} = \mathbf{\Phi}_R \mathbf{\Phi}_T$ et $h_0 = h_{lp} = 1$ [3]. A partir de la propriété de la transformée de Fourier, on peut decomposer le signal transmis $\underline{\mathbf{x}}$ comme la somme du signal temporel des données $\underline{\mathbf{s}}$ avec celui des pilotes insérés $\underline{\mathbf{p}}$. Ainsi, l'expression du signal reçu devient :

$$\underline{\mathbf{y}} = \mathbf{\Phi} \underline{\mathbf{s}} + \mathbf{\Phi} \underline{\mathbf{p}} + \mathbf{\Phi}_R \left( \sum_{i=1}^{L_{ds}-1} h_i \mathbf{U}^{(i)} \mathbf{\Phi}_T \left( \underline{\mathbf{s}} + \underline{\mathbf{p}} \right) \right) + \underline{\mathbf{w}}. \tag{A.22}$$

On se propose une fois de plus de trouver un filtre de Wiener dans le domaine temporel appelé TDF qui satisfait le critère suivant :

$$\underset{\mathbf{Z}}{\operatorname{argmin}}\ \mathbb{E}\left[ \left\| \mathbf{Z}\, \underline{\mathbf{y}} - e^{j\underline{\boldsymbol{\phi}}} \right\|^2 \right] \quad \text{avec} \quad \underline{\boldsymbol{\phi}} = \underline{\boldsymbol{\phi}}_{TX} + \underline{\boldsymbol{\phi}}_{RX}. \tag{A.23}$$

[3] Naturellement le trajet direct (LoS) possède une amplitude et une phase. La phase sera corrigée par l'étape d'égalisation du canal.

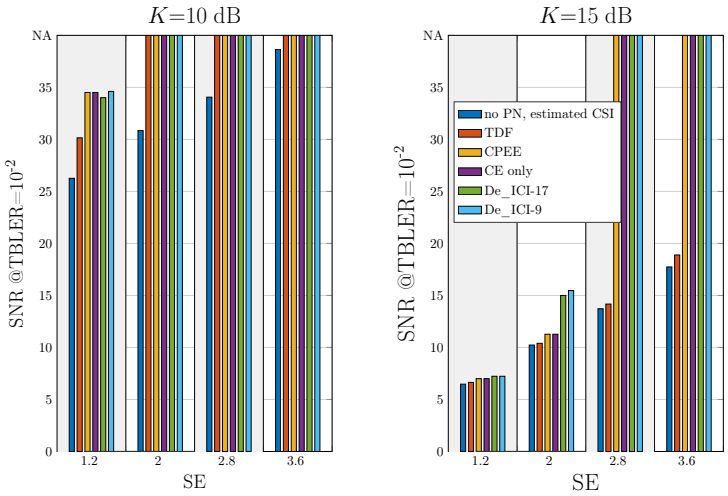


Figure A.7: Performance d'un système OFDM avec une densité de PT-RS par symbole OFDM égale à $\mathcal{D} = 25\%$.

**Important note 19.** *En considérant que (i) les coefficients de canal $h_i, \forall i \in \{1, \cdots, L_{ds}-1\}$ sont connus et non corrélés entre eux, (ii) les vecteurs $\underline{\mathbf{s}}$ et $\underline{\mathbf{w}}$ sont de moyennes nulles, (iii) le signal transmis et le PN sont indépendants, l'expression du filtre TDF s'écrit comme suit :*

$$\mathbf{Z} = \left(\mathbf{A}_{LoS}^{H} + \sum_{i=1}^{L_{ds}-1} h_i^{*}\mathbf{B}_i^{H}\right)\mathbf{C}^{\dagger}, \tag{A.24}$$

*où $\mathbf{C} = \mathbf{E}^{H} + \mathbf{G}^{H} + \mathbf{R}_{\underline{\mathbf{w}}}^{H}$. Les matrices $\mathbf{A}_{LoS}$, $\mathbf{B}_i$, $\mathbf{E}$ et $\mathbf{G}$ sont definies ci-dessous.*

$$\mathbf{A}_{LoS} = \mathbf{R}_{e^{j\underline{\phi}}} \odot \left(\underline{\mathbf{p}} \cdot \underline{\mathbf{1}}_N^{H}\right), \quad \mathbf{B}_i = \mathbf{R}_{e^{j\underline{\phi}_{RX}}} \odot \left(\mathbf{U}^{(i)}\mathbf{R}_{e^{j\underline{\phi}_{TX}}}\right) \odot \left(\mathbf{U}^{(i)}\underline{\mathbf{p}} \cdot \underline{\mathbf{1}}_N^{H}\right), \quad \mathbf{E} = \mathbf{R}_{e^{j\underline{\phi}}} \odot \left(\mathbf{R}_{\underline{\mathbf{s}}} + \underline{\mathbf{p}} \cdot \underline{\mathbf{p}}^{H}\right)$$
$$\mathbf{G} = \sum_{i=1}^{L_{ds}-1} |h_i|^2 \mathbf{R}_{e^{j\underline{\phi}_{RX}}} \odot \left(\mathbf{U}^{(i)}\mathbf{R}_{e^{j\underline{\phi}_{TX}}}\mathbf{U}^{(i)H}\right) \odot \left(\mathbf{U}^{(i)}\left(\mathbf{R}_{\underline{\mathbf{s}}} + \underline{\mathbf{p}} \cdot \underline{\mathbf{p}}^{H}\right)\mathbf{U}^{(i)H}\right). \tag{A.25}$$

On constate que le filtre dépend des coefficients du canal dans le domaine temporel. Pour envisager une implémentation de cet algorithme, on peut imaginer faire une estimation du canal dans le domaine fréquentiel et ensuite faire une opération d'IFFT pour retrouver les coefficients du canal dans le domaine temporel. Mais cette approche n'est pas adéquate car, n'ayant pas compensé les effets du PN, l'estimation du canal dans le domaine fréquentiel sera faussée et par la même occasion celle faite dans le domaine temporel. Afin de simplifier cette étape d'estimation et aussi l'expression du filtre, nous avons regardé du côté des campagnes de mesures et de caractérisation du canal au-dessus de 100 GHz. Il en ressort que le trajet direct est celui le plus dominant lorsque des antennes très directives à gains élevés sont considérées. Par conséquent, l'expression du filtre devient :

$$\mathbf{Z} = \mathbf{A}_{LoS}^{H}\mathbf{C}^{\dagger}, \tag{A.26}$$

avec $\mathbf{C} = \mathbf{E}^{H} + \mathbf{R}_{\underline{\mathbf{w}}}^{H}$. Ainsi, on peut estimer et compenser le PN dans le domaine temporel en utilisant les expressions suivantes :

$$\hat{\underline{\phi}} = \arg\left(\mathbf{Z} \cdot \underline{\mathbf{y}}\right) \quad \text{et} \quad \hat{\underline{\mathbf{y}}} = \underline{\mathbf{y}} \odot e^{-j\hat{\underline{\phi}}}. \tag{A.27}$$

Table A.2: Paramètres de simulation

| | |
|---|---|
| Modulation | 16-QAM |
| Modèle de PN | 3GPP |
| Frequence porteuse | $F_c$ = 140 GHz |
| $N_f$ | 4096 |
| $\Delta_f$ | 120 kHz |
| $N_a$ | 3072 porteuses |
| Densité de PT-RS | 25% |
| Schema de codage | 3GPP LDPC |
| Rendement de codage | $\{0.3; 0.5; 0.7; 0.9\}$ |
| Modèle de canal | Rice (4.2) |
| $K$ [dB] | $\{10; 15; 20; 25\}$ |
| Etalement du canal | 10.17 ns |
| Préfixe cyclique | 64 échantillons (0.13 $\mu$s) |

### A.4.1 Analyse des performances

Sur la figure A.7, on représente le rapport signal à bruit (SNR) nécessaire pour atteindre un TBLER de $10^{-2}$ en fonction de l'efficacité spectrale (SE). Nous avons considéré les paramètres de simulation mentionnés dans le tableau A.2. On constate que l'algorithme TDF que nous proposons permet d'avoir un TBLER de $10^{-2}$ avec un faible SNR comparé aux autres algorithmes de l'état de l'art pour une faible efficacité spectrale (1.2 bits/s/Hz). Par contre lorsqu'on augmente l'efficacité spectrale, on remarque tout de suite que tous les algorithmes ne fonctionnent pas. Ceci peut s'expliquer par le fait que pour une valeur de $K$ = 10 dB, où $K$ désigne le rapport entre la puissance du trajet direct et la puissance des trajets non directs, notre hypothèse de négligence des trajets non directs n'est pas remplie et par conséquent, notre expression du filtre TDF simplifiée n'est plus valide.

En revanche lorsque $K$ = 15 dB, on remarque que l'algorithme TDF que nous proposons permet d'atteindre un TBLER de $10^{-2}$ en haute efficacité spectrale (3.6 bits/s/Hz). Ce résultat vient de la valeur de $K$ qui, pour ce cas de figure, valide notre hypothèse de négligence des trajets non directs et ainsi permet une amélioration de performance avec l'algorithme TDF.

En conclusion, nous avons montré dans ce chapitre que si nous avons un canal sélectif en fréquence avec trajet direct dominant ($K$ supérieur ou égale à 15 dB), alors il est possible de compenser le PN dans le domaine temporel de façon à réduire conjointement les effets du CPE et de l'ICI. Ce qui rend possible une estimation et une égalisation du canal en temps réel. Néanmoins, les performances de l'algorithme TDF peuvent être dégradées si la densité de pilotes dans le domaine fréquentiel à l'émission (avant l'opération de IFFT) n'est pas suffisamment élevée (inférieure ou égale à 12.5 %). Ce qui représente un compromis en terme d'efficacité spectrale bien évidemment. Il faudrait aussi mentionner qu'une réduction de la complexité d'implémentation du TDF est possible en considérant la même approche présentée pour le WIF.

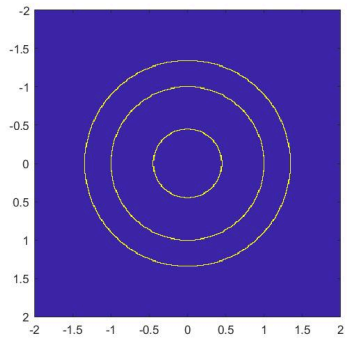

(a) signal SC

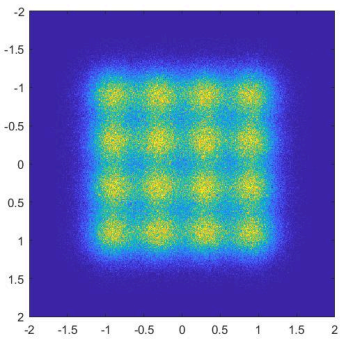

(b) signal OFDM

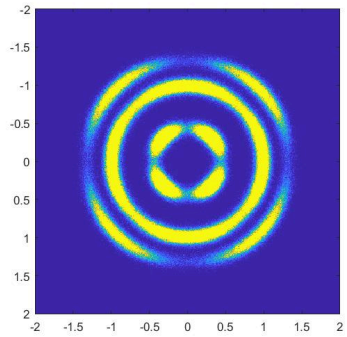

(c) signal DFT-s-OFDM à la porteuse $k = 1$

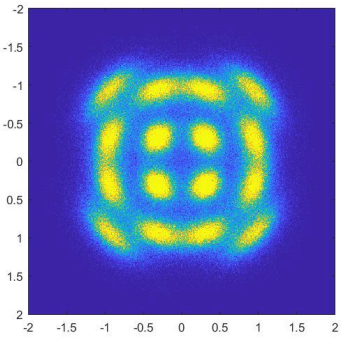

(d) signal DFT-s-OFDM à la porteuse $k = 10$

Figure A.8: Effets du PN Gaussien (GPN) sur divers signaux utilisant de la 16-QAM avec un SNR = 50 dB

### A.4.2 Contributions

Ces travaux ont donné lieu aux contributions suivantes :

[C5] **Y. Bello**, J-B. Doré and D. Demmer, *"Time Domain Phase Noise Mitigation in OFDM Systems for Sub-THz Bands,"* In Proc. IEEE Global Communications Conference (GLOBECOM), Kuala Lumpur, MY, 2023.

[J2] **Y. Bello**, J-B. Doré and David Demmer, *"Low Complexity Time Domain Filtering of Phase Noise in OFDM Systems,"* **submitted**, 2023.

## A.5 Chapitre 5 : PN de nature non corrélée (GPN)

Jusqu'ici dans les chapitres précédents, nous avons considéré que la partie corrélée de la PSD du PN était la plus dominante. Ce qui nous a permis de proposer des algorithmes de filtrage de Wiener pour estimer et compenser le PN ou les effets induits par le PN. Sauf qu'après compensation de ce dernier, le PN résiduel présente une nature non corrélée, ce qui rend impossible son estimation comme dans les chapitres précédents. Dans ce chapitre, nous nous intéressons au cas où le PN résiduel de nature non corrélé devient limitant. Des recherches ont déjà été faites concernant les effets de ce type de PN non corrélé notamment dans le cas de la forme d'onde mono-porteuse (en anglais Single-Carrier SC) où des contributions ont été apportées pour améliorer les performances des systèmes mono-porteuses lorsque le PN est fort

Table A.3: PSD $K_0$ (dBc/Hz) du GPN

| | | Bande du signal $B_W$ | | |
|---|---|---|---|---|
| régime de GPN | Puissance $\sigma_\phi^2$ | 3.686 GHz | 7.372 GHz | 14.744 GHz |
| Fort GPN | $10^{-1}$ | $-108.67$ | $-111.69$ | $-114.70$ |
| Moyen GPN | $5 \cdot 10^{-2}$ | $-111.67$ | $-114.70$ | $-117.71$ |
| Faible GPN | $10^{-2}$ | $-118.68$ | $-121.69$ | $-124.70$ |

(lorsque le PN suit une distribution Gaussienne de variance égale à $10^{-1}$) parmi lesquels un détecteur optimal et un schéma de modulation de constellation optimal.

Dans le cas des formes d'onde multi-porteuses OFDM et DFT-s-OFDM, des études sur les effets du PN de nature non corrélée ont été faites mais sans proposition de solutions [66], ce qui motivera notre étude dans ce chapitre. Nous représentons les effets du PN non corrélé dit Gaussien (avec une variance de $10^{-1}$) sur différentes formes d'onde sur la figure A.8. On remarque que dans le cas de la DFT-s-OFDM, nous avons des comportements différents par sous-porteuse et aussi un comportement qui tend parfois au cas de la mono-porteuse. Nous nous sommes donc inspirés des travaux et contributions présentés dans le cas mono-porteuse et nous avons essayé de transposer ceux-ci en DFT-s-OFDM. L'expression du signal à la sous-porteuse $k$ en considérant un canal AWGN peut s'exprimer de la manière suivante :

$$\begin{aligned} r_k &= s_k \beta(k, N_s, N_f, \phi) \; + \; \gamma(k, N_s, N_f, \phi) + \; \eta(k, N_s, N_f), \\ &= s_k \beta_k \; + \; \gamma_k + \; \eta_k \end{aligned} \tag{A.28}$$

tel que $\beta_k = \beta(k, N_s, N_f, \phi)$ et $\gamma_k = \gamma(k, N_s, N_f, \phi)$ sont définis dans l'équation (A.6) et $\eta_k = \eta(k, N_s, N_f)$ dans (A.7).

Ensuite, nous sommes passés à une étude stochastique des différents termes induits par la présence du PN qui sont l'erreur de phase par porteuse (SPE) et l'ICI. Cette étude nous a permis de caractériser le SPE comme un déphasage (car son amplitude ou module vaut 1 pour toutes les sous-porteuses). En effectuant un test de normalité sur la phase du SPE, nous pouvons davantage le caractériser comme une variable aléatoire qui suit une distribution Gaussienne non corrélée avec une variance propre à la sous-porteuse. Concernant l'ICI, nous avons effectué les mêmes tests cette fois-ci sur la partie réelle et imaginaire. Malgré une fonction de répartition (CDF) proche d'une distribution complexe Gaussienne, il en ressort que l'ICI ne peut pas être caractériser comme une variable aléatoire suivant une distribution Gaussienne complexe non corrélée. l'expression du signal reçu dans (A.28) devient :

$$r_k \simeq s_k e^{j\Phi_k} \; + \; \gamma_k + \; \eta_k. \tag{A.29}$$

Pour pouvoir pousser l'étude plus loin et proposer un éventuel détecteur, deux hypothèses ont été prises concernant la normalité de l'ICI :

- **L'ICI est un vecteur Gaussien complexe** : Cette hypothèse nous permet de dériver l'expression du détecteur de maximum de vraisemblance suivant :

$$\begin{aligned} \hat{\underline{\mathbf{s}}} &= \underset{\underline{\mathbf{s}} \in C'}{\text{argmax}} \quad P\left(\underline{\mathbf{r}} \mid \underline{\mathbf{s}}\right) \\ &= \underset{\underline{\mathbf{s}} \in C'}{\text{argmax}} \quad \log\left(p\left(\underline{\mathbf{r}} \mid \underline{\mathbf{s}}\right)\right) \\ &= \underset{\underline{\mathbf{s}} \in C'}{\text{argmin}} \; (\underline{\mathbf{r}}_\rho - \underline{\mathbf{s}}_\rho)^T \mathbf{\Gamma}_{w_R}^{-1} (\underline{\mathbf{r}}_\rho - \underline{\mathbf{s}}_\rho) + (\underline{\mathbf{r}}_\theta - \underline{\mathbf{s}}_\theta)^T \mathbf{\Gamma}^{-1} (\underline{\mathbf{r}}_\theta - \underline{\mathbf{s}}_\theta) + \log\left(|\det(\mathbf{\Gamma})|\right) \cdot \end{aligned} \tag{A.30}$$

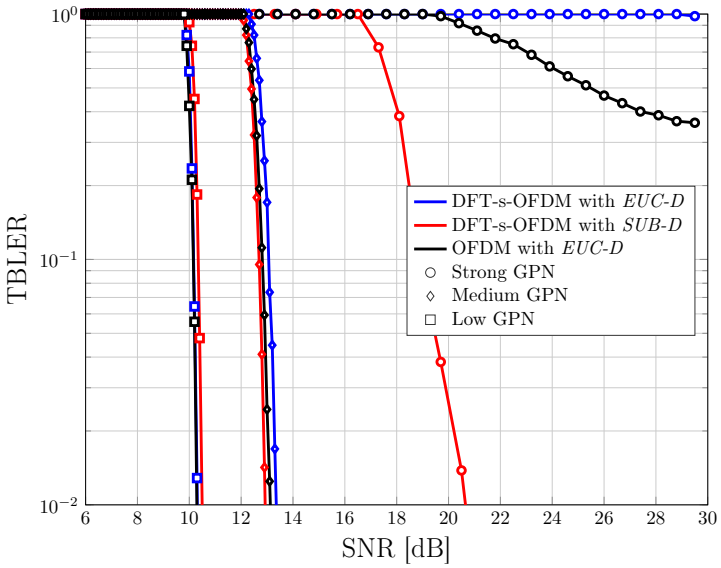


Figure A.9: Performance OFDM vs DFT-s-OFDM: TBLER en fonction du SNR pour une modulation 16-QAM avec $N_s = 480$, $N_f = 512$ et CR=0.7.

où $\mathbf{\Gamma}_{w_R}$ représente la partie réelle de la matrice d'autocorrélation de $\underline{\mathbf{w}} = \underline{\gamma} + \underline{\eta}$. Le terme $\mathbf{\Gamma} = \mathbf{\Gamma}_\Phi + \mathbf{\Gamma}_{w_I} \odot \underline{\mathbf{s}}_\rho^{-2}$ tel que $\mathbf{\Gamma}_\Phi$ représente la matrice d'autocorrélation de la phase du SPE et $\mathbf{\Gamma}_{w_I}$ la partie imaginaire de la matrice d'autocorrélation de $\underline{\mathbf{w}}$. On remarque que ce détecteur fait une détection par symbole DFT-s-OFDM ce qui le rend complexe car l'ensemble des séquences de symboles DFT-s-OFDM de référence est de taille $N_s^{M_s}$ (avec $N_s$ la taille du bloc DFT et $M_s$ l'ordre de modulation). Pour réduire cette complexité, nous avons pris comme deuxième hypothèse que l'ICI par porteuse est une variable aléatoire qui suit une distribution Gaussienne complexe non corrélée.

- **L'ICI suit une distribution Gaussienne complexe non corrélée** : Cette hypothèse nous permet de dériver l'expression du détecteur de maximum de vraisemblance suivant :

$$\begin{aligned}\hat{s}_k &= \underset{s_i \in C}{\operatorname{argmax}}\ P(r \mid s_i) \\ &= \underset{s_i \in C}{\operatorname{argmin}}\ \frac{(r_{k_\rho} - s_{i_\rho})^2}{\sigma^2_{w_k}/2} + \frac{(r_{k_\theta} - s_{i_\theta})^2}{\sigma^2_{\Phi_k} + \frac{\sigma^2_{w_k}}{2s^2_{i_\rho}}} + \log\left(\sigma^2_{\Phi_k} + \frac{\sigma^2_{w_k}}{2s^2_{i_\rho}}\right).\end{aligned} \tag{A.31}$$

Comme on peut l'observer, le détecteur obtenu permet de faire une détection symbole par symbole et pour une porteuse donnée. De plus l'ensemble des séquences de symboles de référence est de taille égale à l'ordre de modulation considéré. Ce qui réduit largement sa complexité d'implémentation. Par la suite, nous avons nommé ce détecteur le *SUB-D*.

### A.5.1 Analyse des performances

Nous avons évalué les performances d'un système utilisant la forme d'onde DFT-s-OFDM en comparant le détecteur Euclidien noté *EUC-D* (basé sur la minimisation de la distance Euclidienne entre le symbole reçu et le symbole de référence) au détecteur *SUB-D* sur la figure A.9. On peut observer le gain qu'apporte le détecteur *SUB-D* en régime de GPN fort (pour une valeur de $K_0 = -108.67$ dBc/Hz et une bande de signal $B_W = 3.686$ GHz) contrairement au détecteur

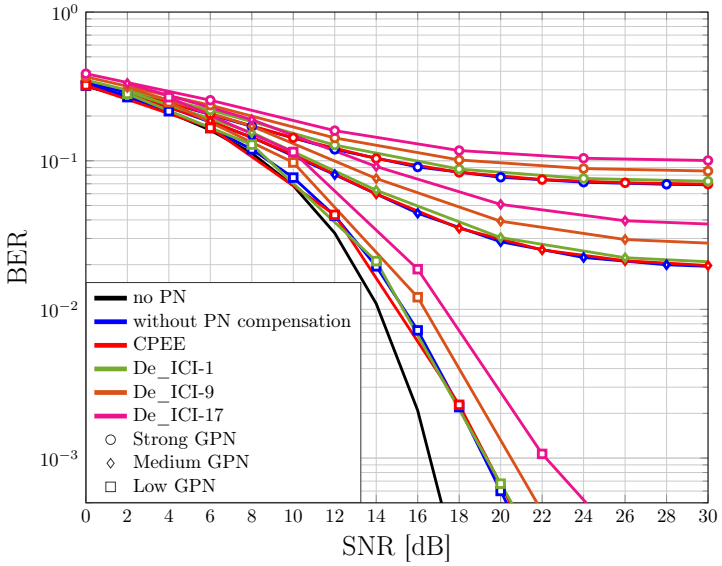


Figure A.10: Performance d'un système OFDM: le taux d'erreur binaire non codé (BER) en fonction du SNR pour une modulation 16-QAM, $N_s$=480 et $N_f$=512.

*EUC-D* qui ne s'en sort pas du tout. La même observation est faite lorsqu'on se compare à la forme d'onde OFDM avec le détecteur *EUC-D*.

Ensuite nous avons considéré l'implémentation des algorithmes de compensation de CPEE et d'ICI de la littérature en OFDM dans le cas où le PN suit une distribution Gaussienne sur la figure A.10. Il en résulte que ces algorithmes sont inefficaces lorsque le PN est non corrélé.

En conclusion, lorsque la partie corrélée du PN est traquée et compensée, la partie residuelle qui est non corrélée peut devenir très embêtant en fonction de la PSD de la partie Gaussienne du PN (qui dépend de la fréquence porteuse et de la qualité de l'oscillateur); et de la largeur de la bande de signal allouée. Dans le cas des formes d'onde multi-porteuses, la forme d'onde DFT-s-OFDM avec le détecteur *SUB-D* qu'on propose serait une meilleure solution comparée à l'OFDM pour des canaux à PN non corrélé fort.

### A.5.2 Contributions

Ces travaux ont donné lieu aux contributions suivantes :

[C7] **Y. Bello**, D. Demmer and J-B. Doré, *"Analyse des effets du PN Gaussien sur un signal DFT-s-OFDM,"* Colloque Gretsi, Grenoble, France, 2023.

[J1] **Y. Bello**, J-B. Doré and David Demmer, *"Analysis of Gaussian Phase Noise Effects in DFT-s-OFDM systems for sub-THz Transmissions,"* **submitted**, 2023.

## A.6 Chapitre 6: Conclusion

Pour conclure ces travaux de recherche, nous avons essayé de répondre à la question de savoir : **quelle forme d'onde pour les transmissions sub-THz?**

Pour un système de communication RF opérant en bande D (c'est-à-dire à 140 GHz), en considérant le modèle de bruit de phase obtenu à partir des mesures effectuées au CEA et en considérant un canal AWGN, si l'on souhaite atteindre une efficacité spectrale de 4.2 bits/s/Hz,

il en ressort que : si la partie corrélée de la PSD du PN est la plus dominante, alors on peut répondre comme suit :

- si on veut minimiser le PAPR et maximiser les performances, alors la forme d'onde mono-porteuse avec l'algorithme WIF est la solution la mieux adaptée (dépendamment du coefficient de roll-off pour le filtre de mise en forme) comparée aux formes d'onde multi-porteuses.
- si on veut utiliser les formes d'onde multi-porteuses, alors la DFT-s-OFDM avec l'algorithme WIF serait la solution la mieux adaptée comparée à l'OFDM avec une numérologie $\mu = 6$.
- l'utilisation du multiplexage spatiale avec le MIMO est inévitable pour atteindre des débits de l'ordre du Tbits/s. Par conséquent, le gain de PAPR du DFT-s-OFDM par rapport à l'OFDM pourrait devenir négligeable. Dans ce cas de figure, on pourrait donc utiliser l'OFDM avec l'algorithme TDF (pour des densités de pilote faibles) ou l'algorithme De_ICI en considérant les numérologies 5G-NR $\mu = \{5, 6\}$.
- maintenant, s'il y a une possibilité d'utiliser des numérologies plus grandes, c'est-à-dire $\mu \geq 8$ (ce qui correspond a un espacement entre porteuse $\Delta_f \geq 1920$ kHz), l'algorithme CPEE serait suffisant pour améliorer les performances des systèmes multi-porteuses.

Dans le cas où cette partie corrélée du bruit de phase est compensée et que le bruit de phase résiduel, qui est non corrélé, devient limitant, alors :

- la forme d'onde mono-porteuse serait une solution préférable comparée aux formes d'onde multi-porteuses [24].
- si on veut utiliser les formes d'onde multi-porteuses, alors la DFT-s-OFDM avec le détecteur *SUB-D* que nous proposons serait une meilleure solution comparée à l'OFDM.

APPENDIX B

# WIF for PN estimation in SC systems

### B.0.1 No approximation

As a reminder, the expression of the received signal in a SC system impaired by PN is defined in (2.13) as follows

$$r[\tau] = s[\tau]e^{j\phi[\tau]} + n[\tau]\cdot \tag{B.1}$$

To apply the WIF algorithm in SC systems, we filter the received signal per block (that can be overlap). Let suppose we transmit a frame of $N_b$ samples. We reshape the received signal in a $N_{sb} \times M_{sb}$ matrix form such that $N_b = N_{sb} \cdot M_{sb}$ as below

$$\underline{\mathbf{R}}^{(m)} = \underline{\mathbf{S}}^{(m)} \odot e^{j\underline{\boldsymbol{\phi}}^{(m)}} + \underline{\mathbf{N}}^{(m)}, \quad m \in \{0, \cdots, M_{sb}-1\} \tag{B.2}$$

where we assume PT-RS symbols are inserted in every column vector. Then, we search a Wiener filter such that

$$\underset{\mathbf{Z}}{\operatorname{argmin}}\, E\left[\left\|\mathbf{Z}\,\underline{\mathbf{a}}_P^{(m)} - e^{j\underline{\boldsymbol{\phi}}^{(m)}}\right\|^2\right]\cdot \tag{B.3}$$

The expression of the $i^{th}$ received PT-RS symbol is defined by

$$\underline{\mathbf{a}}_P^{(m)}[i] = e^{j\underline{\boldsymbol{\phi}}^{(m)}[i]} + \frac{\underline{\mathbf{N}}^{(m)}[i]\underline{\mathbf{S}}^{(m)^*}[i]}{\left|\underline{\mathbf{S}}^{(m)}[i]\right|^2}, \quad \begin{cases} m \in \{0, \cdots, M_{sb}-1\} \\ i \in \chi_p = \{p_0, \cdots, p_{K-1}\} \end{cases} \tag{B.4}$$

and therefore, we obtain the following vector $\underline{\mathbf{a}}_P^{(m)} = \left[\underline{\mathbf{a}}_P^{(m)}[p_0], \cdots, \underline{\mathbf{a}}_P^{(m)}[p_{K-1}]\right]^T$ defined by

$$\underline{\mathbf{a}}_P^{(m)} = e^{j\underline{\boldsymbol{\phi}}_P^{(m)}} + \underline{\mathbf{N}}_P^{(m)} \odot \underline{\mathbf{S}}_P^{(m)}, \quad m \in \{0, \cdots, M_{sb}-1\} \tag{B.5}$$

with

$$\begin{aligned} e^{j\underline{\boldsymbol{\phi}}_P^{(m)}} &= \left[e^{j\underline{\boldsymbol{\phi}}^{(m)}[p_0]}, \cdots, e^{j\underline{\boldsymbol{\phi}}^{(m)}[p_{K-1}]}\right]^T, \ \underline{\mathbf{N}}_P^{(m)} = \left[\underline{\mathbf{N}}^{(m)}[p_0], \cdots, \underline{\mathbf{N}}_P^{(m)}[p_{K-1}]\right]^T, \\ \underline{\mathbf{S}}_P^{(m)} &= \left[\frac{\underline{\mathbf{S}}^{(m)^*}[p_0]}{\left|\underline{\mathbf{S}}^{(m)}[p_0]\right|^2}, \cdots, \frac{\underline{\mathbf{S}}^{(m)^*}[p_{K-1}]}{\left|\underline{\mathbf{S}}^{(m)}[p_{K-1}]\right|^2}\right]^T. \end{aligned} \tag{B.6}$$

We can rewrite the relation (B.5) as follows

$$\underline{\mathbf{a}}_P^{(m)} = \mathbf{M}_P e^{j\underline{\boldsymbol{\phi}}^{(m)}} + \mathbf{M}_P \underline{\mathbf{N}}^{(m)} \odot \underline{\mathbf{S}}_P^{(m)}, \quad m \in \{0, \cdots, M_{sb}-1\} \tag{B.7}$$

with $e^{j\underline{\boldsymbol{\phi}}^{(m)}} = \left[e^{j\underline{\boldsymbol{\phi}}^{(m)}[0]}, \cdots, e^{j\underline{\boldsymbol{\phi}}^{(m)}[N_{sb}-1]}\right]^T$ and $\left[\underline{\mathbf{N}}^{(m)}[0], \cdots, \underline{\mathbf{N}}^{(m)}[N_{sb}-1]\right]^T$. The matrix $\mathbf{M}_P$ is the PT-RS sampling matrix. From (3.33), we derive the WIF expression as follows

$$\mathbf{Z} = \mathbf{R}_{e^{j\underline{\boldsymbol{\phi}}}}^H \mathbf{M}_P^H \left(\mathbf{M}_P \mathbf{R}_{e^{j\underline{\boldsymbol{\phi}}}}^H \mathbf{M}_P^H + \mathbf{M}_P \mathbf{R}_{\underline{\mathbf{N}}}^H \mathbf{M}_P^H \odot \mathbf{I}_{K_d}\right)^{\dagger}, \tag{B.8}$$

by assuming $E\left[\underline{\mathbf{N}}\right] = \underline{\mathbf{0}}_{N_{sb}}$ because $\underline{\mathbf{N}}[k] \backsim \mathbb{C}\mathcal{N}\left(0, \sigma_n^2\right)$. The term $\mathbf{I}_{K_d}$ denotes the identity matrix of size $K_d \times K_d$, where $K_d$ is number of inserted PT-RS per block. $\mathbf{R}_{e^{j\underline{\boldsymbol{\phi}}}}$ is the $N_{sb} \times N_{sb}$ correlation matrix of $e^{j\underline{\boldsymbol{\phi}}}$ where $\underline{\boldsymbol{\phi}}$ is the sum of the generated PN at transmitter and receiver. The phase error vector at the $m^{th}$ sub-frame $\underline{\boldsymbol{\phi}}^{(m)}$ is estimated as follows

$$\hat{\underline{\boldsymbol{\phi}}}^{(m)} = \arg\left(\mathbf{Z}\, \underline{\mathbf{a}}_P^{(m)}\right), \tag{B.9}$$

then we compensate the PN effect by using the following expression

$$\hat{\underline{\mathbf{R}}}^{(m)} = \underline{\mathbf{R}}^{(m)} \odot e^{-j\hat{\underline{\boldsymbol{\phi}}}^{(m)}}. \tag{B.10}$$

### B.0.2 High SNR approximation

A second approach consists in using the correlation matrix of the applied PN $\mathbf{R}_{\underline{\boldsymbol{\phi}}}$ instead of $\mathbf{R}_{e^{j\underline{\boldsymbol{\phi}}}}$ by considering the high SNR (HSNR) approximation. The equation (B.4) becomes

$$\underline{\mathbf{a}}_P^{(m)}[i] = e^{j\underline{\boldsymbol{\phi}}^{(m)}[i]}\left(1 + \frac{\underline{\mathbf{N}}^{'(m)}[i]\underline{\mathbf{S}}^{(m)*}[i]}{\left|\underline{\mathbf{S}}^{(m)}[i]\right|^2}\right), \quad \begin{cases} m \in \{0, \cdots, M_{sb}-1\} \\ i \in \chi_p = \{p_0, \cdots, p_{K-1}\} \end{cases} \tag{B.11}$$

where $\underline{\mathbf{N}}^{'(m)}[i] = \underline{\mathbf{N}}^{(m)}[i]e^{-j\underline{\boldsymbol{\phi}}^{(m)}[i]}$. From (B.11), we obtain the relation bellow

$$\arg\left(\underline{\mathbf{a}}_P^{(m)}[i]\right) = \underline{\boldsymbol{\phi}}^{(m)}[i] + \arctan\left(\frac{\mathfrak{Im}\left\{\underline{\mathbf{N}}^{'(m)}[i]\underline{\mathbf{S}}^{(m)*}[i]\right\}}{\left|\underline{\mathbf{S}}^{(m)}[i]\right|^2 + \mathfrak{Re}\left\{\underline{\mathbf{N}}^{'(m)}[i]\underline{\mathbf{S}}^{(m)*}[i]\right\}}\right), \quad \begin{cases} m \in \{0, \cdots, M_{sb}-1\} \\ i \in \chi_p = \{p_0, \cdots, p_{K-1}\} \end{cases} \tag{B.12}$$

Assuming the HSNR approximation, the relation (B.12) becomes

$$\begin{aligned} \arg\left(\underline{\mathbf{a}}_P^{(m)}[i]\right) &\simeq \underline{\boldsymbol{\phi}}^{(m)}[i] + \frac{\mathfrak{Im}\left\{\underline{\mathbf{N}}^{'(m)}[i]\underline{\mathbf{S}}^{(m)*}[i]\right\}}{\left|\underline{\mathbf{S}}^{(m)}[i]\right|^2}, \quad \begin{cases} m \in \{0, \cdots, M_{sb}-1\} \\ i \in \chi_p = \{p_0, \cdots, p_{K-1}\} \end{cases} \\ &\simeq \underline{\boldsymbol{\phi}}^{(m)}[i] + \frac{\mathfrak{Im}\left\{\underline{\mathbf{N}}^{''(m)}[i]\right\}}{\left|\underline{\mathbf{S}}^{(m)}[i]\right|} \end{aligned} \tag{B.13}$$

with $\underline{\mathbf{N}}^{''(m)}[i] = \underline{\mathbf{N}}^{'(m)}[i]e^{-j\underline{\mathbf{S}}_\theta^{(m)*}[i]}$. The expression (B.7) becomes

$$\underline{\mathbf{a}}_{P_\theta}^{(m)} = \mathbf{M}_P \underline{\boldsymbol{\phi}}^{(m)} + \mathbf{M}_P \underline{\mathbf{N}}^{''I(m)} \odot \underline{\mathbf{S}}_P^{(m)}, \quad m \in \{0, \cdots, M_{sb}-1\} \tag{B.14}$$

where $\underline{\mathbf{a}}_{P_\theta}^{(m)} = \left[\arg\left(\underline{\mathbf{a}}_P^{(m)}[p_0]\right), \cdots, \arg\left(\underline{\mathbf{a}}_P^{(m)}[p_{K-1}]\right)\right]^T$. The terms $\underline{\boldsymbol{\phi}}^{(m)}$, $\underline{\mathbf{N}}^{''I(m)}$ and $\underline{\mathbf{S}}_P^{(m)}$ are given in (B.15)

$$\begin{aligned}
&\underline{\boldsymbol{\phi}}^{(m)} = \left[\underline{\boldsymbol{\phi}}^{(m)}[0], \cdots, \underline{\boldsymbol{\phi}}^{(m)}[N_{sb}-1]\right], \ \underline{\mathbf{N}}^{''I(m)} = \left[\Im\mathfrak{m}\left\{\underline{\mathbf{N}}^{''(m)}[0]\right\}, \cdots, \Im\mathfrak{m}\left\{\underline{\mathbf{N}}^{''(m)}[N_{sb}-1]\right\}\right]^T, \\
&\underline{\mathbf{S}}_P^{(m)} = \left[\frac{1}{\left|\underline{\mathbf{S}}^{(m)}[p_0]\right|}, \cdots, \frac{1}{\left|\underline{\mathbf{S}}^{(m)}[p_{K-1}]\right|}\right]^T.
\end{aligned} \tag{B.15}$$

The LS estimation condition in (3.22) becomes

$$\min_{\mathbf{Z}} E\left[\left\|\mathbf{Z}\ \underline{\mathbf{a}}_{P_\theta}{}^{(m)} - \hat{\underline{\boldsymbol{\phi}}}^{(m)}\right\|^2\right]. \tag{B.16}$$

Similarly, we derive the expression of the WIF as follows

$$\mathbf{Z} = \mathbf{R}_{\underline{\boldsymbol{\phi}}}^H \mathbf{M}_P^H \left(\mathbf{M}_P \mathbf{R}_{\underline{\boldsymbol{\phi}}}^H \mathbf{M}_P^H + \mathbf{M}_P \mathbf{R}_{\underline{\mathbf{N}}^{''I}}^H \mathbf{M}_P^H \odot \mathbf{I}_{K_d}\right)^\dagger, \tag{B.17}$$

by assuming $E\left[\underline{\mathbf{N}}^{''I}\right] = \underline{\mathbf{0}}_{N_{sb}}$ because $\underline{\mathbf{N}}^{''I}[k] \backsim \mathcal{N}\left(0, \frac{\sigma_n^2}{2}\right)$. The phase error vector at the $m^{th}$ sub-frame $\underline{\boldsymbol{\phi}}^{(m)}$ is estimated as follows

$$\hat{\underline{\boldsymbol{\phi}}}^{(m)} = \mathbf{Z}\ \underline{\mathbf{a}}_{P_\theta}^{(m)}, \tag{B.18}$$

then we compensate the PN effect by using the following expression

$$\hat{\underline{\mathbf{R}}}^{(m)} = \underline{\mathbf{R}}^{(m)} \odot e^{-j\hat{\underline{\boldsymbol{\phi}}}^{(m)}}. \tag{B.19}$$

### B.0.3 Theoretical MSE expression

Here, we will derive the theoretical MSE expressions. From (B.3) we have

$$\begin{aligned}
\text{MSE} = \mathbb{E}\left[\|\mathbf{Z}\ \underline{\mathbf{a}}_P - e^{j\underline{\boldsymbol{\phi}}}\|^2\right] &= \mathbb{E}\left[\mathcal{T}_r\left\{\left(\mathbf{Z}\ \underline{\mathbf{a}}_P - e^{j\underline{\boldsymbol{\phi}}}\right)\left(\mathbf{Z}\ \underline{\mathbf{a}}_P - e^{j\underline{\boldsymbol{\phi}}}\right)^H\right\}\right] \\
&= \mathbb{E}\left[\mathcal{T}_r\left\{\mathbf{Z}\ \underline{\mathbf{a}}_P\underline{\mathbf{a}}_P^H\mathbf{Z}^H - \mathbf{Z}\underline{\mathbf{a}}_P\left(e^{j\underline{\boldsymbol{\phi}}}\right)^H - e^{j\underline{\boldsymbol{\phi}}}\ \underline{\mathbf{a}}_P^H\mathbf{Z}^H + e^{j\underline{\boldsymbol{\phi}}}\left(e^{j\underline{\boldsymbol{\phi}}}\right)^H\right\}\right],
\end{aligned} \tag{B.20}$$

where $\mathcal{T}_r\{\cdot\}$ denotes the trace operator. We can write the expression as follows

$$\begin{aligned}
\text{MSE} =&\mathbb{E}\left[\|\mathbf{Z}\ \underline{\mathbf{a}}_P - e^{j\underline{\boldsymbol{\phi}}}\|^2\right] = \mathbb{E}\left[\mathcal{T}_r\left\{\left(\mathbf{Z}\ \underline{\mathbf{a}}_P - e^{j\underline{\boldsymbol{\phi}}}\right)\left(\mathbf{Z}\ \underline{\mathbf{a}}_P - e^{j\underline{\boldsymbol{\phi}}}\right)^H\right\}\right] \\
&= \mathcal{T}_r\left\{\mathbb{E}\left[\mathbf{Z}\ \underline{\mathbf{a}}_P\underline{\mathbf{a}}_P^H\mathbf{Z}^H - \mathbf{Z}\underline{\mathbf{a}}_P\left(e^{j\underline{\boldsymbol{\phi}}}\right)^H - e^{j\underline{\boldsymbol{\phi}}}\ \underline{\mathbf{a}}_P^H\mathbf{Z}^H + e^{j\underline{\boldsymbol{\phi}}}\left(e^{j\underline{\boldsymbol{\phi}}}\right)^H\right]\right\}, \\
&= \mathcal{T}_r\left\{\begin{array}{l}\mathbf{Z}\ \mathbb{E}\left[\underline{\mathbf{a}}_P\underline{\mathbf{a}}_P^H\right]\mathbf{Z}^H - \mathbf{Z}\ \mathbb{E}\left[\underline{\mathbf{a}}_P\left(e^{j\underline{\boldsymbol{\phi}}}\right)^H\right] - \mathbb{E}\left[e^{j\underline{\boldsymbol{\phi}}}\ \underline{\mathbf{a}}_P^H\right]\mathbf{Z}^H \\ + \mathbb{E}\left[e^{j\underline{\boldsymbol{\phi}}}\left(e^{j\underline{\boldsymbol{\phi}}}\right)^H\right].\end{array}\right\}.
\end{aligned} \tag{B.21}$$

We will determine the mean expection of the different argument. For a chosen block, we replace the relation (B.7) in (B.21). Assuming $E\left[\underline{\mathbf{N}}\right] = \underline{\mathbf{0}}_{N_{sb}}$, we will have

$$\mathbb{E}\left[e^{j\underline{\boldsymbol{\phi}}}\left(e^{j\underline{\boldsymbol{\phi}}}\right)^H\right] = \mathbf{R}_{e^{j\underline{\boldsymbol{\phi}}}}, \tag{B.22}$$

Table B.1: Simulation parameters

| | |
|---|---|
| Carrier frequency | $F_c$ = 140 GHz |
| Sampling frequency | $F_s$ = 1966.08 MHz |
| PN model | 3GPP PN Model 2 |
| Modulation | 16-QAM |
| Channel model | AWGN |

$$\begin{aligned}
\mathbb{E}\left[\underline{\mathbf{a}}_P\underline{\mathbf{a}}_P^H\right] &= \mathbb{E}\left[\left(\mathbf{M}_P e^{j\underline{\boldsymbol{\phi}}} + \mathbf{M}_P\underline{\mathbf{N}} \odot \underline{\mathbf{S}}_P\right)\left(\mathbf{M}_P e^{j\underline{\boldsymbol{\phi}}} + \mathbf{M}_P\underline{\mathbf{N}} \odot \underline{\mathbf{S}}_P\right)^H\right] \\
&= \mathbb{E}\left[\mathbf{M}_P e^{j\underline{\boldsymbol{\phi}}}\left(e^{j\underline{\boldsymbol{\phi}}}\right)^H \mathbf{M}_P^H + \mathbf{M}_P\underline{\mathbf{N}}\,\underline{\mathbf{N}}^H\mathbf{M}_P^H \odot \underline{\mathbf{S}}_P\underline{\mathbf{S}}_P^H\right] \\
&= \mathbf{M}_P\mathbb{E}\left[e^{j\underline{\boldsymbol{\phi}}}\left(e^{j\underline{\boldsymbol{\phi}}}\right)^H\right]\mathbf{M}_P^H + \mathbf{M}_P\mathbb{E}\left[\underline{\mathbf{N}}\,\underline{\mathbf{N}}^H\right]\mathbf{M}_P^H \odot \mathbb{E}\left[\underline{\mathbf{S}}_P\underline{\mathbf{S}}_P^H\right] \\
&= \mathbf{M}_P\mathbf{R}_{e^{j\underline{\boldsymbol{\phi}}}}\mathbf{M}_P^H + \mathbf{M}_P\mathbf{R}_{\underline{\mathbf{N}}}\mathbf{M}_P^H \odot \mathbf{I}_{K_d}
\end{aligned} \tag{B.23}$$

$$\begin{aligned}
\mathbb{E}\left[\underline{\mathbf{a}}_P\left(e^{j\underline{\boldsymbol{\phi}}}\right)^H\right] &= \mathbb{E}\left[\left(\mathbf{M}_P e^{j\underline{\boldsymbol{\phi}}} + \mathbf{M}_P\underline{\mathbf{N}} \odot \underline{\mathbf{S}}_P\right)\left(e^{j\underline{\boldsymbol{\phi}}}\right)^H\right] \\
&= \mathbf{M}_P\mathbb{E}\left[e^{j\underline{\boldsymbol{\phi}}}\left(e^{j\underline{\boldsymbol{\phi}}}\right)^H\right] \\
&= \mathbf{M}_P\mathbf{R}_{e^{j\underline{\boldsymbol{\phi}}}}
\end{aligned} \tag{B.24}$$

$$\begin{aligned}
\mathbb{E}\left[e^{j\underline{\boldsymbol{\phi}}}\,\underline{\mathbf{a}}_P^H\right] &= \mathbb{E}\left[e^{j\underline{\boldsymbol{\phi}}}\left(\mathbf{M}_P e^{j\underline{\boldsymbol{\phi}}} + \mathbf{M}_P\underline{\mathbf{N}} \odot \underline{\mathbf{S}}_P\right)^H\right] \\
&= \mathbb{E}\left[e^{j\underline{\boldsymbol{\phi}}}\left(e^{j\underline{\boldsymbol{\phi}}}\right)^H\right]\mathbf{M}_P^H \\
&= \mathbf{R}_{e^{j\underline{\boldsymbol{\phi}}}}\mathbf{M}_P^H
\end{aligned} \tag{B.25}$$

Therefore, because the $\mathbf{R}_{\underline{\boldsymbol{N}}}$ is a diagonal matrix, the theoretical expression of the MSE is given by

$$\text{MSE} = \mathcal{T}_r\left\{\mathbf{Z}\mathbf{M}_P\mathbf{R}_{e^{j\underline{\boldsymbol{\phi}}}}\mathbf{M}_P^H\mathbf{Z}^H - \mathbf{Z}\mathbf{M}_P\mathbf{R}_{e^{j\underline{\boldsymbol{\phi}}}} + \mathbf{Z}\mathbf{M}_P\mathbf{R}_{\underline{\mathbf{N}}}\mathbf{M}_P^H\mathbf{Z}^H - \mathbf{R}_{e^{j\underline{\boldsymbol{\phi}}}}\mathbf{M}_P^H\mathbf{Z}^H + \mathbf{R}_{e^{j\underline{\boldsymbol{\phi}}}}\right\} \tag{B.26}$$

Identically, for the HSNR approximation, the MSE will be defined by

$$\text{MSE}_{HSNR} = \mathcal{T}_r\left\{\mathbf{Z}\mathbf{M}_P\mathbf{R}_{\underline{\boldsymbol{\phi}}}\mathbf{M}_P^H\mathbf{Z}^H - \mathbf{Z}\mathbf{M}_P\mathbf{R}_{\underline{\boldsymbol{\phi}}} + \mathbf{Z}\mathbf{M}_P\mathbf{R}_{\underline{\mathbf{N}}''I}\mathbf{M}_P^H\mathbf{Z}^H - \mathbf{R}_{\underline{\boldsymbol{\phi}}}\mathbf{M}_P^H\mathbf{Z}^H + \mathbf{R}_{\underline{\boldsymbol{\phi}}}\right\}. \tag{B.27}$$

### B.0.4 Numerical results

In this section, we assess the performance of a SC system with the presence of PN. To highlight the effectiveness of the WIF, we compare this latter with state-of-the-art PN estimation and compensation algorithms: the CPEE and the LI defined in Section 3.3. The simulation parameters are depicted in Table. B.1. The distributed PT-RS pattern in Fig. 3.2a is taken with inserted PT-RS every $L = 64$.

Fig. B.1a presents the system performance of a SC system in terms of uncoded BER. WIF, CPEE and LI algorithms are considered for PN estimation and compensation. Regarding the WIF algorithm, we consider two cases:

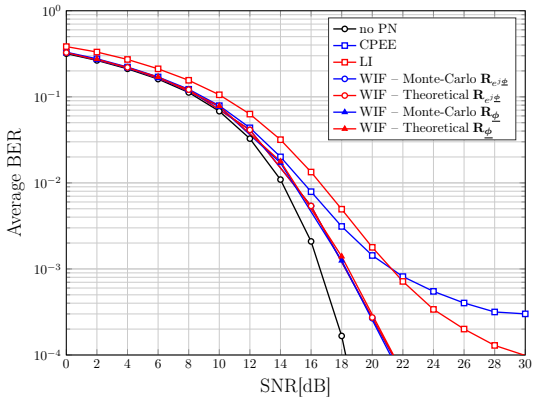


(a) Uncoded BER performance of a SC system. We use a 16-QAM modulation with the insertion of 16 pilots per block, considering blocks of size $N_{sb} = 1024$.

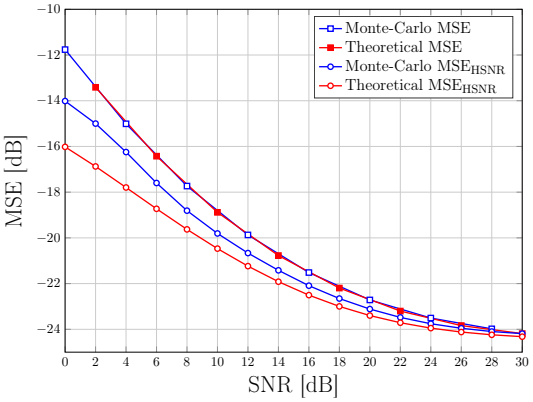


(b) Theoretical versus Monte-Carlo MSE performance. We consider a 16-QAM modulation with the insertion of 16 pilots per block, considering blocks of size $N_{sb} = 1024$.

Figure B.1: SC system performance

- for the case without HSNR approximation, we consider the theoretical correlation matrix $\mathbf{R}_{e^{j\underline{\phi}}}$ by using the small angle approximation $e^{j\underline{\phi}} = \underline{\mathbf{1}}_{N_{sb}} + \underline{\phi}$ is given by

$$\mathbf{R}_{e^{j\underline{\phi}}} \simeq \mathbf{1}_{N_{sb}} + \mathbf{R}_{\underline{\phi}} \tag{B.28}$$

  where $\mathbf{R}_{\underline{\phi}}$ is obtained considering the expression (3.59). In addition, we consider the $\mathbf{R}_{e^{j\underline{\phi}}}$ obtained by Monte-Carlo simulations.

- for the case with HSNR approximation, we consider the theoretical correlation matrix $\mathbf{R}_{\underline{\phi}}$ expressed in (3.59) and the one obtained by Monte-Carlo simulations.

We transmit a frame of $N_p = 65536$ samples. Before the symbols detection, we operate the PN estimation and compensation per blocks of 1024 samples. One can notice the system performance obtained by using theoretical correlation matrices match well with those obtained with the Monte-Carlo correlation matrices. Moreover, the WIF outperforms the CPEE and LI.

Fig. B.1b presents the comparison between the theoretical and the Monte-Carlo MSE. We consider the theoretical MSE expressions in (B.26) and (B.27). We show once again a good match between theoretical MSE expressed in (B.26) and the Monte-Carlo. For the MSE expression in (B.27), a performance gap is observed in low SNR because the HSNR approximation is no longer valid.

APPENDIX C

# OTFS Waveform with Phase Noise in sub-THz

# OTFS Waveform with Phase Noise in sub-THz

Yaya Bello, Samuel Barnola, David Demmer, Jean-Baptiste Doré
CEA-Leti, Univ. Grenoble Alpes, F-38000 Grenoble, France
{yaya.bello, samuel.barnola, david.demmer, jean-baptiste.dore}@cea.fr

***Abstract*—The availability of large bandwidths in the sub-THz bands appears to be a solution for increasing the capabilities of future wireless communication technologies. However, phase noise generated by oscillators in these bands generates significant signal distortion which needs to be addressed. In this paper, we study the impact of phase noise on OTFS. We propose phase noise compensation scheme and associated frame format. Two dedicated pilot schemes are studied for the phase noise tracking: the first one consists in adding pilots in the delay-Doppler (DD) domain while the other in the delay-Time (DT) domain. We highlight that compensating phase noise in DT domain gives better performance. A comparison between OFDM, DFT-s-OFDM and OTFS according to the 5G-NR numerology is presented. We show that the OTFS waveform is robust to phase noise and may even significantly outperform OFDM and DFT-s-OFDM.**

***Index Terms*—OFDM, DFT-s-OFDM, PTRS, Tracking, 6G, 5G-NR.**

## I. Introduction

As for previous mobile network generations, the deployment of cellular technologies in wider bandwidths at higher frequencies is an appealing solution to increase the capacity. The 5G-New Radio (5G-NR) standard is today limited to $52.6$ GHz. The 3GPP is forward looking the use of new spectrum for future releases. A potential candidate for 6G has been identified: the "sub-THz" spectrum ($[100 - 300]$ GHz) [1] where an aggregated bandwidth of 58.6 GHz was identified in [2]. A first standardization of the sub-THz band for communications has been done in [1] for single carrier transmission and now the 3GPP studies the possibility to implement multicarrier waveforms for sub-THz bands transmissions [3]. However transmitting in the sub-THz brings new challenges such as dealing with phase noise (PN) generated by the oscillators.

On the one hand, orthogonal frequency division multiplexing (OFDM) is a multicarrier waveform standardized in 4G and 5G-NR for downlink transmissions. It allows the signal to be sent simultaneously on several orthogonal subcarriers and is therefore, robust to frequency selective channels. The discrete Fourier transform-spread-OFDM (DFT-s-OFDM) appears to be a potential candidate for sub-THz transmssions. It is standardized in 4G and 5G-NR for uplink transmissions and has the advantage of a lower peak-to-average power ratio (PAPR) [4] than the OFDM. This advantage gives the possibility to amplify the signal at higher efficiencies. On the other hand, orthogonal time frequency space (OTFS) is a new waveform where the signal is represented in the so-called the delay-Doppler (DD) domain [5]. This waveform attracts the attention of the community for its ability to deal with high Doppler effects and the joint communication and sensing applications [6].

The analysis of PN effects on OFDM and DFT-s-OFDM has been studied in [7], [8], [9] and shows that the compensation of PN effects is necessary. The authors in [10] demonstrated that inscreasing the subcarrier spacing (SCS) can be a practical solution to reduce the inter-carrier interference (ICI) caused by PN. In addition, they proposed a new phase tracking reference signal (PTRS) scheme to enhance the channel estimation. Some estimation algorithms are presented in [8] and [9] respectively to compensate PN impairments in OFDM and DFT-s-OFDM systems. OTFS with presence of PN was studied in [11]-[12] but, authors did not propose PN estimation algorithm. However, from the best of our knowledge, PN compensation algorithms for OTFS are not yet detailed and fair comparisons are missing. The effects of PN is not well studied and understood in case of OTFS.

*Contributions:* (i) Contrary to the work done in [12], we propose two PTRS schemes for OTFS and associated compensation algorithms: the first in DD domain and the second in DT domain. (ii) We fairly compare OFDM, DFT-s-OFDM and OTFS assuming equivalent band under a common framework with 3GPP PN model and considering 5G-NR numerology extension as presented in [13].

*Notations:* In what follows, bold letters denote matrices and underlined bold one denote column vectors. Upper-case and lowercase letters denote frequency domain and time domain variables respectively. The symbols $E[\cdot]$, $(\cdot)^H$, $(\cdot)^*$, $|\cdot|$, $\arg(\cdot)$ denote respectively the expectation operator, the Hermitian transform, the conjugate, the magnitude and the phase value of the argument. Letters $M$ and $K$ are respectively size of Doppler and delay axis for OTFS and $N$ is the size of OFDM inverse fast Fourier transform (IFFT). $N_a$ is the number of allocated subcarriers among the $N$ possible subcarriers. $\mathbf{F_N}$ stands for the discrete Fourier transform (DFT) matrix of size $N$ defined as $\mathbf{F_N}^{(i,k)} = \frac{1}{\sqrt{N}} w_N^{ik}$, where $w_N = e^{-j\frac{2\pi}{N}}$ and $(i,k)$ represents the $i^{th}$ row and the $k^{th}$ column index.

## II. System model

In this section, we describe the system model, OFDM, DFT-s-OFDM and OTFS waveforms as well as the channel model considered.

### A. OFDM and DFT-s-OFDM

Assuming an OFDM transmission system, the transmitted vector $\underline{\mathbf{y}}$ after the IFFT can be expressed as follows:

$$\underline{\mathbf{y}} = \mathbf{F_N}^H \underline{\mathbf{X}}, \tag{1}$$

where $\underline{\mathbf{X}}$ is the transmitted symbols vector of size $N$, $\underline{\mathbf{X}}[n] \in \mathcal{C}$ where $\mathcal{C}$ is the set of the selected modulation. We assume an

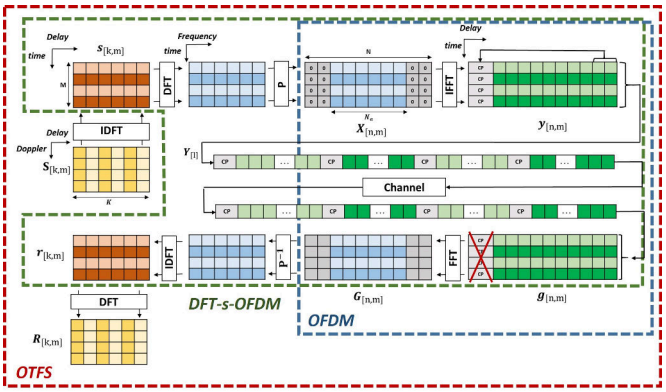


Fig. 1: System model matrix form with domain representation: DD (yellow), DT (red and green), Frequency-Time (Blue).

addition of a cyclic prefix (CP) at the transmitter to avoid the inter-symbol interference (ISI). The expression of the received signal, after CP removal, is:

$$\underline{\mathbf{G}} = \mathbf{F_N} \mathbf{h} \underline{\mathbf{y}} + \underline{\mathbf{z}} = \mathbf{F_N} \mathbf{h} \mathbf{F_N^H} \underline{\mathbf{X}} + \underline{\mathbf{z}}, \tag{2}$$

where $\mathbf{h}$ represents the time domain channel impulse response matrix and $\underline{\mathbf{z}}$ the thermal noise such that $\underline{\mathbf{z}}[n] \backsim \mathbb{CN}(0, \sigma_z^2)$ where $\sigma_z^2$ is the noise variance. It should be mentioned that in case of static channel (*i.e* without mobility) $\mathbf{h}$ is circulant if the delay spread of the channel is shorter than the duration of the CP. This common assumption is made in this study.

In the case of a DFT-s-OFDM transmission scheme, the expression of the signal after the DFT spreading is:

$$\underline{\mathbf{X}} = \mathbf{P} \mathbf{F_{N_a}} \underline{\mathbf{s}}. \tag{3}$$

$\mathbf{P}$ and $\mathbf{F_{N_a}}$ are respectively the $N_a$-to-$N$ mapping matrix (that models the subcarrier allocation) and the DFT matrix of size $N_a \times N_a$. The vector $\underline{\mathbf{s}}$ is the the symbol vector to be transmitted. The transmitted signal $\underline{\mathbf{y}}$ is expressed as follows:

$$\underline{\mathbf{y}} = \mathbf{F_N^H} \mathbf{P} \mathbf{F_{N_a}} \underline{\mathbf{s}}. \tag{4}$$

As in OFDM, we add a CP before the transmission to avoid ISI. The expression of the received symbols after removing the CP is:

$$\underline{\mathbf{r}} = \mathbf{F_{N_a}^H} \mathbf{P^{-1}} \mathbf{F_N} \mathbf{h} \mathbf{F_N^H} \mathbf{P} \mathbf{F_{N_a}} \underline{\mathbf{s}} + \underline{\mathbf{z}}', \tag{5}$$

with $\mathbf{P^{-1}}$ the $N$-to-$N_a$ mapping matrix. $\underline{\mathbf{z}}'$ represents the thermal noise after DFT operations at the receiver and $\underline{\mathbf{z}}'[n] \backsim \mathbb{CN}(0, \sigma_z^2)$. A synopsis of OFDM and DFT-s-OFDM tranceiver is given in Fig. 1.

### B. OTFS

Orthogonal time frequency space (OTFS) is a waveform where signal is represented in a particular domain called delay-Doppler (DD) domain. Its particularity is that it is robust to high Doppler channel as opposed to OFDM where high Doppler breaks the orthogonality between subcarriers. Additionally, this DD representation of the signal allows a clear representation of all impairments caused by the channel and therefore an easier channel estimation for equalization.

Let $\mathbf{S} \in \mathcal{C}^{K \times M}$ denotes one OTFS frame containing symbols in the DD domain (yellow matrix in Fig. 1 at the transmitter). The transmitted DT matrix is obtained through an inverse DFT (IDFT) along Doppler axis and is expressed as follows:

$$\mathbf{s} = \mathbf{S} \mathbf{F_M^H}. \tag{6}$$

The expression of the transmitted matrix $\mathbf{y}$ is:

$$\mathbf{y} = \mathbf{F_N^H} \mathbf{P} \mathbf{F_{N_a}} \mathbf{S} \mathbf{F_M^H}, \tag{7}$$

assuming that $K = N_a$. The transmitted signal, as depicted in Fig. 1 is expressed as follows:

$$\underline{\mathbf{y}} = \mathbf{vec}(\mathbf{y_{CP}}), \tag{8}$$

where **vec** represents the operation which transforms a matrix to a vector. $\mathbf{y_{CP}}$ is the time domain matrix including the CP. The expression of the received signal vector is:

$$\underline{\mathbf{g}} = \mathbf{h_o} \underline{\mathbf{y}} + \underline{\mathbf{z}}, \tag{9}$$

where $\mathbf{h_o}$ is the time domain channel matrix. After the suppression of the CP, the received signal in the DD domain is expressed as follows:

$$\mathbf{R} = \mathbf{F_{N_a}^H} \mathbf{P^{-1}} \mathbf{F_N} \mathbf{vec}^{-1}(\mathbf{h_o}' \underline{\mathbf{y}'}) \mathbf{F_M} + \mathbf{z}'', \tag{10}$$

where $\mathbf{h_o}'$ is the equivalent time domain channel matrix after CP removal. The vector $\underline{\mathbf{y}'}$ is the time domain signal without CP and $\mathbf{z}''$ represents the thermal noise in the DD domain. It is obvious that $\mathbf{z}''$ follows a normal distribution.

### C. Channel Model

The radio propagation channels in sub-THz frequencies are expected to be sparse. It has been demonstrated that the line-of-sight (LoS) provides most of the energy contribution. This effect is mainly due to the use of high gain antennas which spatially filter the channel. For this work we assume a LoS propagation channel with high gain antenna. The channel is considered frequency flat. We also assume a coherent communication system impaired by PN with a receiver synchronized in time and frequency. Therefore, $\mathbf{h}$ and $\mathbf{h_o}$ are diagonal matrices with $\mathbf{h}[k,k] = e^{j\Phi[k]}$ (resp. $\mathbf{h_o}[k',k'] = e^{j\Phi'[k']}$). The terms $\Phi[k]$ and $\Phi'[k']$ describe the oscillator PN after sampling at the reception. They result from the sum of the continuous time PN at transmitter and receiver. For this work the 3GPP PN model is assumed [14]. This model is based on power spectral density expression for both transmitter and receiver.

## III. Compensation of Phase Noise in OTFS

### A. Phase Noise Effect

The effect of PN is widely studied for OFDM [15]. In the case of OFDM, the wiener PN causes: (i) constellation rotation with the same phase shift called common phase error (CPE) and (ii) inter-carrier interference (ICI). The compensation algorithms are mainly concerned with the correction of the CPE [8] based on pilot carriers distributed in each OFDM symbol. Phase tracking reference signal (PTRS) is introduced in 5G-NR to mitigate the performance loss due to PN.

The case of DFT-s-OFDM is more complex to analyze. As in OFDM, the PN causes the rotation of transmitted symbols and ICI. On the one hand, when the spreading size $N_a$ is small

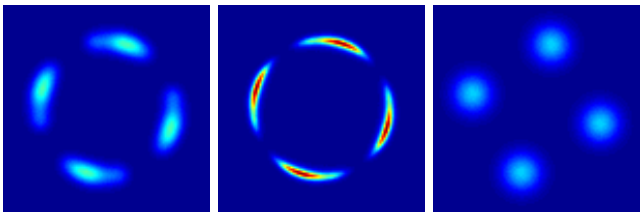

Fig. 2: Probability density function of a received QPSK modulation in case of OFDM (left), DFT-s-OFDM (middle) and OTFS (right) in a noiseless channel with PN, 3GPP model at 300 GHz. $N = 2048, K = N_a = 1024, M = 32$, $F_s = 3932.16$MHz.

compared to the size of the OFDM IFFT $N$, the behavior is similar to that of OFDM. On the other hand, when the size of the spreading moves toward $N$, we go toward the behavior of a single carrier waveform, *i.e* constellation rotation and limited interference. Depending on the size of the SCS, we increase or decrease the effects of ICI [13].

As far as OTFS is concerned, from the best of our knowledge, the behavior is not well documented. Starting from the OTFS model described previously, *i.e* a precoding of a signal on top of DFT-s-OFDM, it is obvious that the PN causes constellation rotation and interference in the Doppler domain. This particularly true when the size of the spreading $N_a$ is close to $N$. However, it is worth mentioning that the OTFS dimensioning can lead to different effects. Indeed, the transformation in the DT domain distributes and mixes symbols in time. The correlated nature of the PN can therefore be broken (depending on the coherence time of the wiener process). As a matter of illustration, we depict in Fig. 2 the probability density function of a received QPSK modulation considering OFDM, DFT-s-OFDM and OTFS waveforms under the 3GPP PN model at 300 GHz. This figure clearly illustrates the effect of PN for OTFS, *i.e* a CPE and interference across the Doppler grid.

While the effects on the DFT-s-OFDM clearly show a rotation with little ICI, we can notice that in the case of OTFS the impact of the interference is more important. This justifies the proposal of a frame format adapted and a PN compensation algorithm for OTFS. Two strategies using PTRS are investigated: the compensation of PN effects (i) in the DD domain and (ii) in the DT domain.

### B. PTRS in DD Domain

As state previously, we aim to compensate the CPE in the Doppler grid. A first solution consists in the insertion of PTRS pilot in DD domain with a dedicated pattern described in Fig. 3-(a). We insert one pilot every $L_{DD}$ subcarriers in the Doppler axis. Before the demodulation at the reception, we estimate and compensate the effects of PN using the CPE Estimation (CPEE) algorithm defined as follows [9]:

$$\underline{\hat{\phi}}^{DD}_{CPEE}[k] = \arg\left(\sum_{i\in\chi_p} \frac{\mathbf{R}_{[k,i]}\mathbf{S}^{*}_{[k,i]}}{|\mathbf{S}_{[k,i]}|^2}\right), \forall k \in [0, K-1]\cdot \quad (11)$$

The term $\chi_p$ is the set which contains all the $Q$ index where PTRS symbols are positioned. The estimated symbol $\hat{\mathbf{S}}_{[k,m]}$ is obtained by computing the expression:

$$\hat{\mathbf{S}}_{[k,m]} = \mathbf{R}_{[k,m]}.e^{-j\underline{\hat{\phi}}^{DD}_{CPEE}[k]}. \quad (12)$$

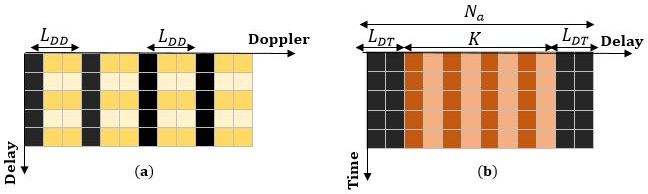


Fig. 3: PTRS Pattern : (a)-DD domain and (b)-DT domain. black grid : inserted PTRS.

### C. PTRS in DT Domain

OTFS can be interpreted as a precoding over the DFT-s-OFDM . If the precoding function of the DFT-s-OFDM cancels the IFFT of OFDM then, we will have more ICI in the DD domain than in the DT domain. Thus, compensating PN effects in the DT domain could minimize detection errors in the DD domain. Therefore, we propose to insert PTRS in the DT domain to estimate and compensate PN effects before the DT-to-DD transformation. A potential insertion of PTRS in DT domain can be the pattern distribution depicted in Fig. 3-(b). The transmitted signal is mapped between $L_{DT}$ contiguous pilots inserted in the delay grid for the tracking. We define $\mathbf{s}'$ as the matrix after the $K$-to-$N_a$ mapping where pilots are inserted. The matrix $\mathbf{r}'$ represents the received DT matrix before the $N_a$-to-$K$ demapping. The estimation of the CPE is expressed as follows:

$$\underline{\hat{\phi}}^{DT}_{CPEE}[m] = \arg\left(\sum_{i\in\chi_p} \frac{\mathbf{r}'_{[i,m]}\mathbf{s}'^{*}_{[i,m]}}{|\mathbf{s}'_{[i,m]}|^2}\right), \forall m \in [0, M-1]\cdot \quad (13)$$

The estimated DT matrix $\hat{\mathbf{s}}_{[k,m]}$ can be recovered as follows:

$$\hat{\mathbf{s}}_{[k,m]} = \mathbf{r}_{[k,m]}.e^{-j\hat{\phi}^{DT}_{CPEE}[m]}. \quad (14)$$

The estimated transmitted symbols in the DD domain can then be expressed as follows:

$$\hat{\mathbf{S}} = \hat{\mathbf{s}}.\mathbf{F_M}. \quad (15)$$

## IV. Simulation Results

In this section, we assess the performance of the two CPE compensation algorithms. Then, we compare OTFS to OFDM and DFT-s-OFDM on a common framework. For the performance evaluation, we assess the Transport Block Error Rate (TBLER) performance with the 3GPP 5G-NR LDPC code. The system parameters considered for performance evaluation are summarized in TABLE I. For all the simulations, the CPE is estimated with noisy pilots. The signal-to-noise ratio (SNR) is evaluated on the full signal bandwidth, *i.e* 3.93216 GHz. The signal of interest is 1GHz bandwidth. Different numerologies are assessed. For each numerology, the number of QAM symbol remains the same. A resource element (RE) is defined as one subcarrier by one symbol for OFDM, one DT element by one symbol for DFT-s-OFDM and one DD element by one symbol for OTFS. The discrete-time PN is generated by considering the method presented in [16].

TABLE I: Simulation parameters

| | | |
|---|---|---|
| Sampling Frequency | $F_s$ | 3932.16 MHz |
| Numerology | $\mu$ | 6 to 11 |
| Signal bandwidth | $B$ | 983.04 MHz |
| Carrier frequency | $F_c$ | 90, 140 and 300 GHz |
| Phase noise model | | 3GPP |
| Doppler grid | $M$ | $16 \times 2^{\mu-6}$ |
| Tx IFFT size (OFDM) | $N$ | $4096 \times 2^{-\mu+6}$ |
| Number of active carriers | $N_a$ | $1024 \times 2^{-\mu+6}$ |
| LDPC coding rate | $R$ | $0.3, 0.5, 0.7$ and $0.9$ |
| LDPC decoder iteration | $n_{it}$ | 15 |
| LDPC decoder | | Layered Min-Sum |
| Modulation | | QPSK, 16 and 64 QAM |
| Achievable rate | $\eta$ | from 0.6 to 5.4 bit/RE |

### A. CPE Estimation with OTFS

The Fig. 4 highlights the SNR values necessary to reach a TBLER of $10^{-2}$ in OTFS considering the two PTRS schemes and associated algorithms presented above. It should be mentioned that $L_{DD} = 8$. $L_{DT}$ is chosen in such way that the same spectral efficiency is reached. For compensation in DD domain, we consider that $K = N_a$ and in DT domain, we have $K = N_a - 2L_{DT}$. We show that the DT domain compensation gives performance which outperform those obtained assuming the DD domain compensation. Above 2 bit/RE, the DD domain PN correction is not able to fulfill the target TBLER. That is why there is no results for DD in this range. Indeed, The DFT-s-OFDM is a waveform which emulates the single carrier when the size of the spreading DFT is closed to the OFDM IFFT size $N$. Because OTFS can be viewed as a precoding over the DFT-s-OFDM, PN will add interference in DD domain. In addition to the observation made in Fig. 2-(right), the results in Fig. 4 once again confirm our assertion that there is less interference in the DT domain than in the DD domain. So basically, compensating PN in the DT domain allows to reduce PN effects in order to minimize the interference that the precoding inverse DFT (IDFT) could add in the DD domain.

### B. Comparison to OFDM and DFT-s-OFDM

We estimate the SNR gap between OTFS and OFDM, DFT-s-OFDM to reach $10^{-2}$ TBLER for various carrier frequency and numerology. For OFDM and DFT-s-OFDM, a CPE correction is made based on PTRS. All the waveforms have the same spectral efficiency. A synthesis is given in Fig. 5 and Fig. 6. For three carrier frequencies $(90, 140$ and $300$GHz), we give the SNR gap depending on the numerology for 11 couples of modulation and coding rate. Overall, we can still find a numerology where the performance difference between OTFS and OFDM is below $0.3$ dB. For some particular cases, *i.e* low numerology and high achievable rate, OTFS with CPE correction in the DT domain can give better performance than OFDM and DFT-s-OFDM. It is particularly true for the PN model at 300 GHz. In conclusion, OTFS with a correction in the DT domain does not suffer losses but does not give better results either if appropriate numerology is chosen for OFDM and DFT-s-OFDM.

It may also be interesting to analyze the PAPR of OTFS with the proposed configurations. Our numerical simulations have shown that OTFS modulation does not provide higher PAPR than OFDM; while DFT-s-OFDM brings significant gain (up to 3 dB for QPSK considering parameters of TABLE I) whatever the considered numerologies. In the case of OTFS, the first DFT block (IDFT) transforms the QAM symbols into a signal with Gaussian statistics making the PAPR high.

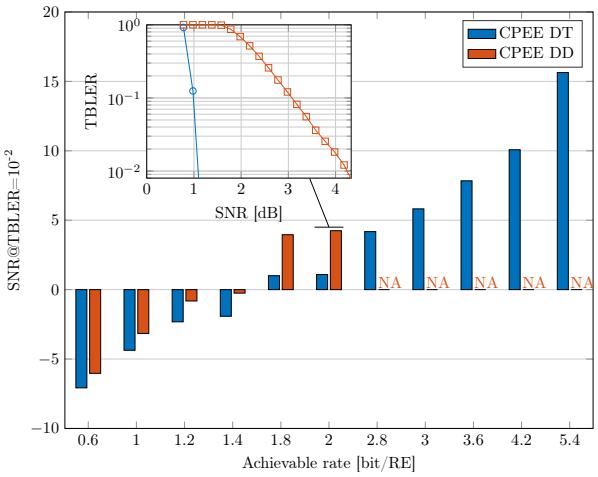


Fig. 4: Comparison of the two PN compensating strategies at 140 GHz for numerology $\mu = 8$. NA stands for Not Achievable.

### C. Discussions

We have shown that it is possible to make OTFS robust to PN in the same orders of magnitude as OFDM and DFT-s-OFDM. The latter is particularly interesting for sub-THz as DFT-s-OFDM combines low PAPR and robustness to PN with appropriated numerology. Nevertheless, our numerical evaluations do not take into account mobility. Indeed, in the case of high Doppler effect (combination of high carrier frequency and high mobility), DD domain properties provide a straightforward channel estimation for equalization purpose which makes OTFS particularly interesting. Moreover, unlike 5G-NR OFDM, OTFS frame can be sent with only one CP which permits to increase the spectral efficiency. With parameters of TABLE I, we can expect $6\%$ spectral efficiency gain. Last but not least, joint communication and sensing rise a particular interest in sub-THz. In this context, OTFS has a strong interest. Coming back to the PN challenge, this one becomes negligible for monostatic Radar as oscillator is shared for transmitter and receiver. However, for bistatic Radar, PN manifests itself as additionnal noise in the Doppler range and dedicated signal processing have to be done to cope with potential high level of PN.

## V. Conclusion

Sub-THz bands are seen as a solution to increase the capacities of future wireless communication technologies. But PN effects in these bands cause critical damages that have to be addressed. In this paper, we study the impact of PN on OTFS. We proposed two PTRS schemes for the PN tracking: (i) PTRS in DD domain and (ii) PTRS in DT domain. We used a low complexity algorithm to estimate and compensate PN effects in OTFS according the domain where PTRS are inserted. Our results demonstrated that performance with PN

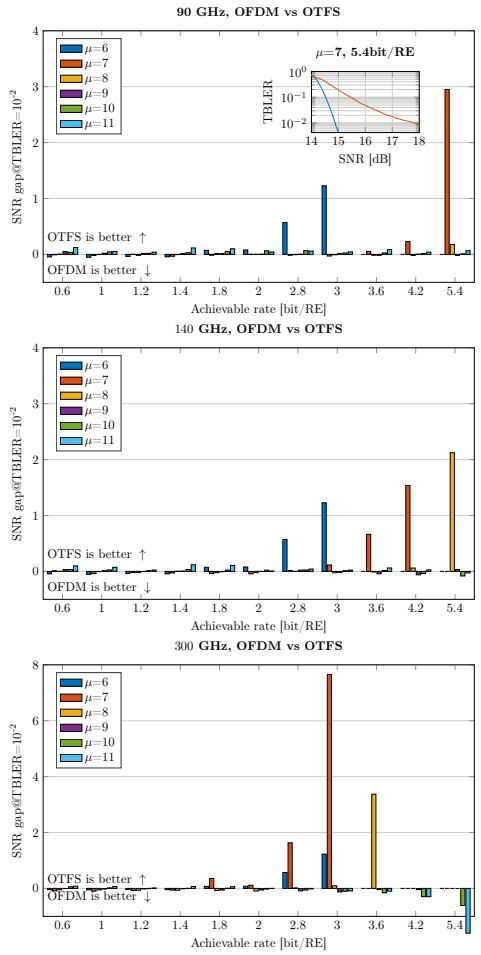


Fig. 5: Comparison of OFDM and OTFS. CPEE in the DT domain is considered for OTFS.

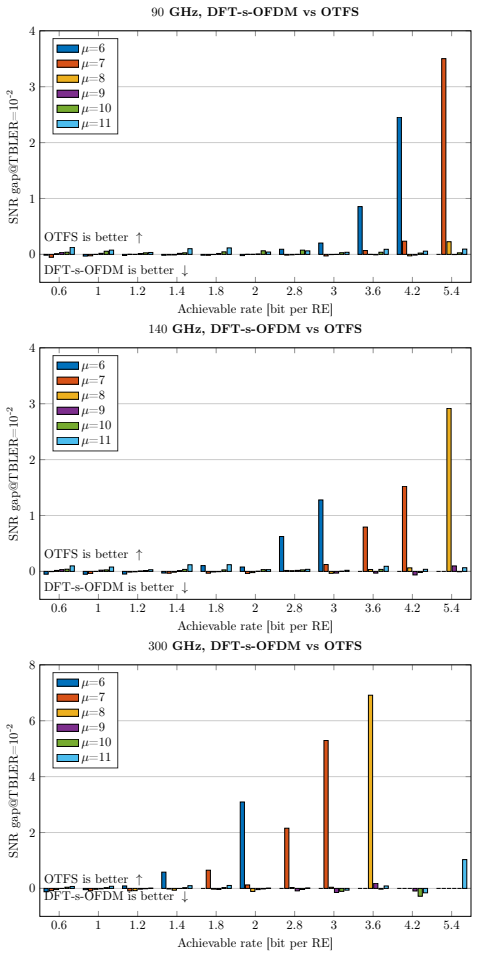


Fig. 6: Comparison of DFT-s-OFDM and OTFS. CPEE in the DT domain is considered for OTFS.

compensation in DT domain outperform those achieve with PN compensation in DD domain. This is because in the DD domain, the interference is greater than in the DT domain due to the last IDFT operation at the reception. So, compensating PN in DT domain allows to reduce the interference in the DD domain and minimize detection errors. Additionally, we compared OTFS performance with OFDM and DFT-s-OFDM. We have shown that depending on the 5G-NR numerology, OTFS can significantly outperfom OFDM and DFT-s-OFDM.

## REFERENCES


[1] V. Petrov, T. Kurner, and I. Hosako, "IEEE 802.15.3d: First Standardization Efforts for Sub-Terahertz Band Communications toward 6G," *IEEE Commun. Mag.*, pp. 28–33, 2020.

[2] J.-B. Doré *et al.*, "Above-90GHz Spectrum and Single-Carrier Waveform as Enablers for Efficient Tbit/s Wireless Communications," in *proc. Int. Conf. Telecommun. (ICT'2018)*, Saint-Malo, France, Jun. 2018.

[3] O. Tervo *et al.*, "5G New Radio Evolution Towards Sub-THz Communications," in *proc. 6G Wireless Summit (6G SUMMIT)*, 2020, pp. 1–6.

[4] G. Berardinelli *et al.*, "Generalized DFT-Spread-OFDM as 5G Waveform," *IEEE Commun. Mag.*, pp. 99–105, 2016.

[5] R. Hadani and A. Monk, "OTFS: A New Generation of Modulation Addressing the Challenges of 5G," *CoRR*, vol. abs/1802.02623, 2018. [Online]. Available: http://arxiv.org/abs/1802.02623

[6] Z. Wei *et al.*, "Orthogonal Time-Frequency Space Modulation: A Promising Next-Generation Waveform," *IEEE Wireless Commun.*, vol. 28, no. 4, pp. 136–144, 2021.

[7] D. Petrovic, W. Rave, and G. Fettweis, "Intercarrier interference due to phase noise in OFDM - estimation and suppression," in *proc. IEEE Vehicular Technology Conf. VTC-Fall*, vol. 3, 2004, pp. 2191–2195.

[8] M. Afshang *et al.*, "On Phase Noise Compensation for OFDM Operation in 5G and Beyond," in *proc. IEEE Wireless Commun. and Networking Conf. (WCNC)*, 2022, pp. 2166–2171.

[9] J.-C. Sibel, "Pilot-Based Phase Noise Tracking for Uplink DFT-s-OFDM in 5G," in *proc. Int. Conf. Telecommun. (ICT)*, 2018, pp. 52–56.

[10] T. Levanen *et al.*, "Mobile Communications Beyond 52.6 GHz: Waveforms, Numerology, and Phase Noise Challenge," *IEEE Wireless Commun.*, vol. 28, no. 1, pp. 128–135, 2021.

[11] R. Hadani *et al.*, "Orthogonal Time Frequency Space (OTFS) modulation for millimeter-wave communications systems," in *proc. IEEE MTT-S Int. Microwave Symp. (IMS)*, 2017, pp. 681–683.

[12] G. D. Surabhi, M. K. Ramachandran, and A. Chockalingam, "OTFS Modulation with Phase Noise in mmWave Communications," in *proc. IEEE Vehicular Technology Conf. (VTC2019-Spring)*, 2019, pp. 1–5.

[13] O. Tervo *et al.*, "On the potential of using sub-THz frequencies for beyond 5G," in *Proc. Accepted to the 2022 EuCNC-6G Summit*, 2022.

[14] 3GPP, "Study on new radio access technology: Radio Frequency (RF) and co-existence aspects," TS 38.803, 2017-09.

[15] T. Pollet, M. Van Bladel, and M. Moeneclaey, "BER sensitivity of OFDM systems to carrier frequency offset and Wiener phase noise," *IEEE Trans. Commun.*, vol. 43, no. 2/3/4, pp. 191–193, 1995.

[16] 3GPP, "RF Impairment models for 60GHz-band SYS/PHY Simulation," Project IEEE 802.15-06-0477-00-003c, November, 2006.

# Bibliography


[1] T. Wen and Z. Peiying, "6G The Next Generation: From Connected People and Things to Connected Intelligence," 2020. (Cited on pages xv, xvi, 4, 5, 6 and 106.)

[2] ITU-R, "IMT Vision - Framework and overall objectives of the future development of IMT for 2020 and beyond."," in *Recommendation ITU-R M.2083-0*, 2015. (Cited on page 4.)

[3] T. S. Rappaport, Y. Xing, O. Kanhere, S. Ju, A. Madanayake, S. Mandal, A. Alkhateeb, and G. C. Trichopoulos, "Wireless Communications and Applications Above 100 GHz: Opportunities and Challenges for 6G and Beyond," *IEEE Access*, vol. 7, pp. 78 729–78 757, 2019. (Cited on page 4.)

[4] J. Proakis, "Digital communications 5th Edition," no. ser. McGraw-Hill series in electrical and computer engineering: communication and signal processing, 2007. (Cited on pages 4 and 105.)

[5] A. de Régulation des communications Electroniques et des Postes, "5G : procédure d'attribution de la bande 3.4-3.8 GHz en métropole," June 2020. (Cited on page 5.)

[6] L. Pometcu and R. D'Errico, "Characterization of sub-THz and mmwave propagation channel for indoor scenarios," in *12th European Conference on Antennas and Propagation (EuCAP 2018)*, 2018, pp. 1–4. (Cited on pages 6 and 8.)

[7] L. Pometcu and R. D'Errico, "Channel Model Characteristics in D-Band for NLOS Indoor Scenarios," in *2019 13th European Conference on Antennas and Propagation (EuCAP)*, 2019, pp. 1–4. (Cited on page 6.)

[8] Y. Xing and T. S. Rappaport, "Propagation Measurement System and Approach at 140 GHz-Moving to 6G and Above 100 GHz," in *2018 IEEE Global Communications Conference (GLOBECOM)*, 2018, pp. 1–6. (Cited on page 6.)

[9] J. M. Eckhardt, T. Doeker, S. Rey, and T. Kürner, "Measurements in a Real Data Centre at 300 GHz and Recent Results," in *2019 13th European Conference on Antennas and Propagation (EuCAP)*, 2019, pp. 1–5. (Cited on page 6.)

[10] B. Murmann, "ADC Performance Survey 1997-2022," [Online]. Available: . (Cited on pages 6 and 9.)

[11] H. Halbauer and T. Wild, "Towards Power Efficient 6G Sub-THz Transmission," in *2021 Joint European Conference on Networks and Communications & 6G Summit (EuCNC/6G Summit)*, 2021, pp. 25–30. (Cited on page 6.)

[12] T. S. Rappaport, Y. Xing, O. Kanhere, S. Ju, A. Madanayake, S. Mandal, A. Alkhateeb, and G. C. Trichopoulos, "Wireless Communications and Applications Above 100 GHz: Opportunities and Challenges for 6G and Beyond," *IEEE Access*, vol. 7, pp. 78 729–78 757, 2019. (Cited on pages 7 and 106.)

[13] J.-B. Doré, Y. Corre, S. Bicais, J. Palicot, E. Faussurier, D. Kténas, and F. Bader, "Above-90GHz Spectrum and Single-Carrier Waveform as Enablers for Efficient Tbit/s Wireless Communications," in *Proc. 25th Int. Conf. on Telecommun. (ICT'2018)*, Saint-Malo, France, Jun 2018. (Cited on pages 7 and 106.)

[14] A. Ugolini, A. Piemontese, and T. Eriksson, "Spiral Constellations for Phase Noise Channels," *IEEE Transactions on Communications*, vol. 67, no. 11, pp. 7799–7810, 2019. (Cited on pages 7 and 106.)

[15] R. Krishnan, M. R. Khanzadi, T. Eriksson, and T. Svensson, "Soft Metrics and Their Performance Analysis for Optimal Data Detection in the Presence of Strong Oscillator Phase Noise," *IEEE Trans. on Commun.*, pp. 2385–2395, 2013. (Cited on pages 7, 17, 23, 76, 85, 86 and 88.)

[16] S. Bicaïs and J.-B. Doré, "Design of Digital Communications for Strong Phase Noise Channels," *IEEE Open J. of Veh. Technol.*, pp. 227–243, 2020. (Cited on pages 7, 17, 23, 76, 85, 87, 88 and 100.)

[17] 3GPP, "NR: Physical channels and modulation," Tech. Spec. Group Radio Access Netw. Rel. 17 TS 38.211 v. 17.1.0, 2022-April. (Cited on pages 7 and 58.)

[18] T. Levanen, O. Tervo, K. Pajukoski, M. Renfors, and M. Valkama, "Mobile Communications Beyond 52.6 GHz: Waveforms, Numerology, and Phase Noise Challenge," *IEEE Wireless Commun.*, vol. 28, 2021. (Cited on pages 7 and 8.)

[19] N. Dinur and D. Wulich, "Peak to average power ratio in amplitude clipped high order OFDM," in *Proc. IEEE Mil. Commun. Conf. (MILCOM) (Cat. No.98CH36201)*, vol. 2, 1998, pp. 684–687 vol.2. (Cited on pages 8 and 23.)

[20] G. Berardinelli, K. I. Pedersen, T. B. Sorensen, and P. Mogensen, "Generalized DFT-Spread-OFDM as 5G Waveform," *IEEE Commun. Mag.*, pp. 99–105, 2016. (Cited on page 8.)

[21] T. Oskari, N. Ilmari, N. I. Peruga, T. Esa, and H. Jari, "On the Potential of Using Sub-THz Frequencies for Beyond 5G," in *Proc. Joint Eur. Conf. on Netw. and Commun. & 6G Summit (EuCNC/6G Summit)*, 2022, pp. 37–42. (Cited on pages 9, 25, 26 and 58.)

[22] A. Demir, "Computing Timing Jitter From Phase Noise Spectra for Oscillators and Phase-Locked Loops With White and $1/f$ Noise," *IEEE Trans. on Circuits and Syst. I: Regular Papers*, pp. 1869–1884, 2006. (Cited on page 16.)

[23] M. R. Khanzadi, D. Kuylenstierna, A. Panahi, T. Eriksson, and H. Zirath, "Calculation of the Performance of Communication Systems From Measured Oscillator Phase Noise," *IEEE Trans. on Circuits and Syst. I: Regular Papers*, vol. 61, no. 5, pp. 1553–1565, 2014. (Cited on pages 16, 17, 21 and 76.)

[24] S. Bicais and J.-B. Doré, "Phase Noise Model Selection for Sub-THz Communications," in *Proc. IEEE Global Commun. Conf. (GLOBECOM)*, 2019, pp. 1–6. (Cited on pages 16, 17, 71, 76, 86, 107 and 122.)

[25] S. Li, D. Fritsche, C. Carta, and F. Ellinger, "A 200-GHz Sub-Harmonic Injection-Locked Oscillator with 0-dBm Output Power and 3.5% DC-to-RF-Efficiency," in *Proc. IEEE Radio Freq. Integr. Circuits Symp. (RFIC)*, 2018, pp. 212–215. (Cited on pages 16 and 76.)

[26] S. Bicaïs, J.-B. Doré, and J. L. Gonzalez Jimenez, "On the Optimum Demodulation in the Presence of Gaussian Phase Noise," in *Proc. 25th Int. Conf. on Telecommun. (ICT)*, 2018, pp. 269–273. (Cited on pages 17 and 76.)

[27] P. Desombre, H. Farès, and Y. Louët, "Performance Comparison of Digital Modulations in the Presence of Gaussian Phase Noise in the Sub-THz Context," in *Proc. 4th Int. Workshop on Mobile Terahertz Syst. (IWMTS)*, 2021, pp. 1–5. (Cited on pages 17 and 76.)

[28] C. Hager, A. Graell i Amat, A. Alvarado, and E. Agrell, "Design of APSK Constellations for Coherent Optical Channels with Nonlinear Phase Noise," *IEEE Trans. on Commun.*, vol. 61, no. 8, pp. 3362–3373, 2013. (Cited on page 17.)

[29] G. J. Foschini, R. D. Gitlin, and S. B. Weinstein, "On the selection of a two-dimensional signal constellation in the presence of phase jitter and Gaussian noise," *The Bell System Technical Journal*, vol. 52, no. 6, pp. 927–965, 1973. (Cited on page 17.)

[30] 3GPP, "Study on new radio access technology: Radio Frequency (RF) and co-existence aspects," TS 38.803, 2017-09. (Cited on pages 17, 20, 58, 76 and 91.)

[31] J. González-Jiménez, A. Siligaris, A. Hamani, C. Dehos, F. Foglia Manzillo, A. Clemente, and N. Cassiau, "Channel Bonding Transceivers for Efficient 100 Gb/s and Beyond Wireless and Plastic Waveguide Communications," in *Proc. IEEE Int. Conf. on Electron., Circuits and Syst. (ICECS)*, 2022, pp. 1–4. (Cited on page 21.)

[32] A. Hamani, F. F. Manzillo, A. Siligaris, N. Cassiau, F. Hameau, F. Chaix, C. Dehos, A. Clemente, and J. L. González-Jiménez, "A 56.32 Gb/s 16-QAM D-band Wireless Link using RX-TX Systems- in-Package with Integrated Multi-LO Generators in 45nm RFSOI," in *Proc. 2022 IEEE Radio Freq. Integrated Circuits Symp. (RFIC)*, 2022, pp. 75–78. (Cited on page 21.)

[33] A. Siligaris, P. Courouve, G. Waltener, A. Hamani, C. Dehos, and J. González-Jiménez, "A 42.24 Gb-s Channel Bonding Up-Converter withintegrated multi-LO generation in 45nm CMOS," in *Proc. IEEE 23rd Topical Meeting on Silicon Monolithic Integr. Circuits in RF Syst.*, 2023, pp. 4–7. (Cited on page 21.)

[34] A. Piemontese, G. Colavolpe, and T. Eriksson, "A New Analytical Model of Phase Noise in Communication Systems," in *2022 IEEE Wireless Commun. and Netw. Conf. (WCNC)*, 2022, pp. 926–931. (Cited on page 21.)

[35] 3GPP, "RF Impairment models for 60GHz-band SYS/PHY Simulation," Project IEEE 802.15-06-0477-00-003c, November, 2006. (Cited on page 21.)

[36] 3GPP TSG RAN WG1, "Discussion on phase noise modeling," Meeting R1-163984, May, 2016. (Cited on page 21.)

[37] T. Pollet and M. Moeneclaey, "Synchronizability of OFDM signals," in *Proc. of GLOBECOM*, vol. 3, 1995, pp. 2054–2058 vol.3. (Cited on page 23.)

[38] M. Clark, "Adaptive frequency-domain equalization and diversity combining for broadband wireless communications," *IEEE J. on Sel. Areas in Commun.*, vol. 16, no. 8, pp. 1385–1395, 1998. (Cited on page 23.)

[39] T. Pollet, M. Van Bladel, and M. Moeneclaey, "BER sensitivity of OFDM systems to carrier frequency offset and Wiener phase noise," *IEEE Trans. Commun.*, vol. 43, no. 2/3/4, pp. 191–193, 1995. (Cited on pages 24 and 76.)

[40] A. Garcia Armada, "Understanding the effects of phase noise in orthogonal frequency division multiplexing (OFDM)," *IEEE Trans. on Broadcast.*, vol. 47, no. 2, pp. 153–159, 2001. (Cited on pages 24 and 58.)

[41] D. Petrovic, W. Rave, and G. Fettweis, "Intercarrier interference due to phase noise in OFDM - estimation and suppression," in *Proc. IEEE 60th Veh. Technol. Conf. (VTC-Fall)*, vol. 3, 2004, pp. 2191–2195. (Cited on pages 24, 36 and 76.)

[42] Y. Qi, M. Hunukumbure, H. Nam, H. Yoo, and S. Amuru, "On the Phase Tracking Reference Signal (PT-RS) Design for 5G New Radio (NR)," in *Proc. IEEE Veh. Technol. Conf. (VTC-Fall)*, 2018. (Cited on pages 24 and 36.)

[43] J.-C. Sibel, "Pilot-Based Phase Noise Tracking for Uplink DFT-s-OFDM in 5G," in *Proc. Int. Conf. Telecommunications (ICT)*, 2018, pp. 52–56. (Cited on pages 24, 26, 36, 38, 61 and 91.)

[44] M. Afshang, D. Hui, J.-F. T. Cheng, and S. Grant, "On Phase Noise Compensation for OFDM Operation in 5G and Beyond," in *Proc. IEEE Wireless Commun. and Netw. Conf. (WCNC)*, 2022, pp. 2166–2171. (Cited on pages 24, 26, 36, 58, 60, 61, 62, 76, 77 and 91.)

[45] J.-C. Sibel, "Tracking the phase noise in sub-THz bands," in *Proc. IEEE Wireless Commun. and Netw. Conf. (WCNC)*, 2022, pp. 932–937. (Cited on pages 24, 26, 58, 60 and 76.)

[46] O. Tervo, T. Levanen, K. Pajukoski, J. Hulkkonen, P. Wainio, and M. Valkama, "5G New Radio Evolution Towards Sub-THz Communications," in *Proc. 2nd 6G Wireless Summit (6G SUMMIT)*, 2020, pp. 1–6. (Cited on pages 25 and 76.)

[47] J. L. Hernando, A. S. Tan, and A. Shojaeifard, "Mitigation of Phase Noise-induced ICI at THz bands using CP-OFDM PT-RS signals," in *Proc. IEEE Globecom Workshops (GC Wkshps)*, 2022, pp. 1766–1771. (Cited on pages 26, 58, 61, 62 and 91.)

[48] Yingshan Li, Heung-Gyoon Ryu, Li-jie Zhou, Dongyan Sun, Haiyuan Liu, and Junwen Li, "Frequency offset and phase noise influence and its compensation in the DFT-spread OFDM system," in *Proc. Int. Conf. on Commun., Circuits and Syst. (ICCCAS)*, 2008, pp. 52–56. (Cited on page 26.)

[49] V. Syrjälä, T. Levanen, and M. Valkama, "Methods for phase noise mitigation for DFT-S-OFDM waveforms," in *Proc. IEEE Global Conf. on Signal and Inf. Process. (GlobalSIP)*, 2016, pp. 660–664. (Cited on pages 26 and 76.)

[50] R. Hadani and A. Monk, "OTFS: A New Generation of Modulation Addressing the Challenges of 5G," *CoRR*, vol. abs/1802.02623, 2018. (Cited on page 26.)

[51] Z. Wei, W. Yuan, S. Li, J. Yuan, G. Bharatula, R. Hadani, and L. Hanzo, "Orthogonal Time-Frequency Space Modulation: A Promising Next-Generation Waveform," *IEEE Wireless Commun.*, vol. 28, no. 4, pp. 136–144, 2021. (Cited on page 26.)

[52] H.-T. Sheng and W.-R. Wu, "Time-Frequency Domain Channel Estimation for OTFS Systems," *IEEE Transactions on Wireless Communications*, pp. 1–1, 2023. (Cited on page 26.)

[53] R. Hadani, S. Rakib, A. F. Molisch, C. Ibars, A. Monk, M. Tsatsanis, J. Delfeld, A. Goldsmith, and R. Calderbank, "Orthogonal Time Frequency Space (OTFS) modulation for millimeter-wave communications systems," in *proc. IEEE MTT-S Int. Microwave Symp. (IMS)*, 2017, pp. 681–683. (Cited on page 28.)

[54] G. D. Surabhi, M. K. Ramachandran, and A. Chockalingam, "OTFS Modulation with Phase Noise in mmWave Communications," in *proc. IEEE Veh. Technol. Conf. (VTC2019-Spring)*, 2019, pp. 1–5. (Cited on page 28.)

[55] Y. Bello, S. Barnola, D. Demmer, and J.-B. Doré, "OTFS Waveform with Phase Noise in sub-THz," in *2022 IEEE 96th Veh. Technol. Conf. (VTC2022-Fall)*, 2022, pp. 1–5. (Cited on page 28.)

[56] J. Bhatti and M. Moeneclaey, "Pilot-Aided Carrier Synchronization Using an Approximate DCT-Based Phase Noise Model," in *IEEE Int. Symp. Signal Process. and Information Technol. (ISSPIT)*, 2007, pp. 1143–1148. (Cited on pages 36 and 40.)

[57] M. Chung, L. Liu, and O. Edfors, "Phase-Noise Compensation for OFDM Systems Exploiting Coherence Bandwidth: Modeling, Algorithms, and Analysis," *IEEE Trans. on Wireless Commun.*, vol. 21, 2022. (Cited on page 36.)

[58] J.-B. Doré, V. Berg, and D. Kténas, "Channel estimation techniques for 5G cellular networks: FBMC and multiuser asynchronous fragmented spectrum scenario," *Trans. on Emerging Telecommun. Technol.*, pp. 15–30, 2014. (Cited on pages 52, 63 and 65.)

[59] P. Rabiei, W. Namgoong, and N. Al-Dhahir, "A Non-Iterative Technique for Phase Noise ICI Mitigation in Packet-Based OFDM Systems," *IEEE Trans. on Signal Process.*, pp. 5945–5950, 2010. (Cited on page 58.)

[60] R. Casas, S. Biracree, and A. Youtz, "Time domain phase noise correction for OFDM signals," *IEEE Trans. on Broadcasting*, 2002. (Cited on pages 58 and 115.)

[61] A. Leshem and M. Yemini, "Phase Noise Compensation for OFDM Systems," *IEEE Trans. on Signal Process.*, 2017. (Cited on pages 58 and 115.)

[62] L. Pometcu and R. D'Errico, "An Indoor Channel Model for High Data-Rate Communications in D-Band," *IEEE Access*, vol. 8, pp. 9420–9433, 2020. (Cited on pages 59 and 77.)

[63] Y. Xing and T. S. Rappaport, "Propagation Measurements and Path Loss Models for sub-THz in Urban Microcells," in *ICC 2021 - IEEE International Conference on Communications*, 2021, pp. 1–6. (Cited on pages 59 and 77.)

[64] D. Bouras, P. Mathiopoulos, and D. Makrakis, "Optimal detection of coded differentially encoded QAM and PSK signals with diversity reception in correlated fast Rician fading channels," *IEEE Trans. on Veh. Technol.*, pp. 245–258, 1993. (Cited on page 59.)

[65] M. Sarajlić, N. Tervo, A. Pärssinen, L. H. Nguyen, H. Halbauer, K. Roth, V. Kumar, T. Svensson, A. Nimr, S. Zeitz, M. Dörpinghaus, and G. Fettweis, "Waveforms for sub-THz 6G: Design Guidelines," in *2023 Joint European Conf. on Networks and Commun. & 6G Summit (EuCNC/6G Summit)*, 2023, pp. 168–173. (Cited on page 76.)

[66] S. Tarboush, H. Sarieddeen, M.-S. Alouini, and T. Y. Al-Naffouri, "Single-Versus Multicarrier Terahertz-Band Communications: A Comparative Study," *IEEE Open J. of the Commun. Soc.*, vol. 3, pp. 1466–1486, 2022. (Cited on pages 76 and 119.)

[67] F. J. Massey, "The kolmogorov-smirnov test for goodness of fit," in *J. of the Amer. Statistical Assoc.*, 1951, pp. 68–78. (Cited on pages 81 and 83.)

[68] 3GPP, "Overall Description Stage 2," TS 38.300, 2017-12. (Cited on page 89.)

[69] L. H. Nguyen, V. Braun, H. Halbauer, and T. Wild, "Waveform Comparison under Hardware Limitations for 6G Sub-THz Communications," in *2022 IEEE 19th Annual Consumer Commun. & Netw. Conf. (CCNC)*, 2022, pp. 1–6. (Cited on page 100.)

[70] H. Ye, G. Y. Li, and B.-H. Juang, "Power of Deep Learning for Channel Estimation and Signal Detection in OFDM Systems," *IEEE Wireless Commun. Letters*, vol. 7, no. 1, pp. 114–117, 2018. (Cited on page 100.)

[71] M. Sana, A. De Domenico, and E. Calvanese Strinati, "Multi-Agent Deep Reinforcement Learning Based User Association for Dense mmWave Networks," in *2019 IEEE Global Commun. Conf. (GLOBECOM)*, 2019, pp. 1–6. (Cited on page 100.)

[72] S. Naoumi, R. Alami, H. Hacid, E. Almazrouei, M. Debbah, M. Bennis, and M. Chafii, "Emergent Communication in Multi-Agent Reinforcement Learning for Flying Base Stations," in *2023 IEEE Int. Mediterranean Conf. on Commun. and Netw. (MeditCom)*, 2023, pp. 133–138. (Cited on page 100.)

[73] M. Chafii, L. Bariah, S. Muhaidat, and M. Debbah, "Twelve Scientific Challenges for 6G: Rethinking the Foundations of Communications Theory," *IEEE Commun. Surveys and Tutorials*, vol. 25, no. 2, pp. 868–904, 2023. (Cited on page 100.)

[74] A. Omidi, M. Zeng, and L. A. Rusch, "Constellation Shaping for Phase Noise Channels with Deep Learning Approach," in *2022 IEEE Int. Black Sea Conf. on Commun. and Netw. (BlackSeaCom)*, 2022, pp. 118–122. (Cited on page 100.)

[75] A. Omidi, X. Guan, M. Zeng, and L. A. Rusch, "Optimizing Geometric Constellations for Phase Noise Channels Using Deep Learning," in *2022 IEEE Photonics Conf. (IPC)*, 2022, pp. 1–2. (Cited on page 100.)

[76] X. Guan, A. Omidi, M. Zeng, and L. A. Rusch, "Experimental Demonstration of a Constellation Shaped via Deep Learning and Robust to Residual-Phase-Noise," in *2022 Conf. on Lasers and Electro-Optics (CLEO)*, 2022, pp. 1–2. (Cited on page 100.)

[77] H. S. Park, E.-Y. Choi, Y. S. Song, S. Noh, and K. Seo, "DNN-based Phase Noise Compensation for Sub-THz Communications," in *2020 Int. Conf. on Information and Commun. Technol. Convergence (ICTC)*, 2020, pp. 866–868. (Cited on page 100.)

[78] T. Wild, V. Braun, and H. Viswanathan, "Joint Design of Communication and Sensing for Beyond 5G and 6G Systems," *IEEE Access*, vol. 9, pp. 30 845–30 857, 2021. (Cited on page 101.)

[79] Y. Songhua, W. Shicai, Y. Zijie, and W. Biyang, "The effect of phase noise on the remote sensing of ocean surface currents," in *2004 Asia-Pacific Radio Science Conference, 2004. Proceedings.*, 2004, pp. 299–302. (Cited on page 101.)

[80] P. D. L Beasley, "The Influence of Transmitter Phase Noise on FMCW Radar Performance," in *2006 European Radar Conference*, 2006, pp. 331–334. (Cited on page 101.)

[81] K. Siddiq, M. K. Hobden, S. R. Pennock, and R. J. Watson, "Phase Noise in FMCW Radar Systems," *IEEE Transactions on Aerospace and Electronic Systems*, vol. 55, no. 1, pp. 70–81, 2019. (Cited on page 101.)

[82] A. Dürr, B. Schweizer, J. Bechter, and C. Waldschmidt, "Phase Noise Mitigation for Multistatic FMCW Radar Sensor Networks Using Carrier Transmission," *IEEE Microwave and Wireless Components Letters*, vol. 28, no. 12, pp. 1143–1145, 2018. (Cited on page 101.)

[83] M. Dudek, I. Nasr, D. Kissinger, R. Weigel, and G. Fischer, "The impact of phase noise parameters on target signal detection in FMCW-radar system simulations for automotive applications," in *Proceedings of 2011 IEEE CIE International Conference on Radar*, vol. 1, 2011, pp. 494–497. (Cited on page 101.)

# Waveform optimization for 6G communication systems in sub-THz bands

**Yaya BELLO**

The deployment of cellular technologies with broader bandwidths at higher frequencies presents an attractive solution for augmenting the capacities of wireless communication systems, particularly in terms of enhancing throughput. Fortunately, the sub-THz spectrum, spanning from 100 to 300 GHz, has been recognized as a promising contender for the next generation of wireless technology, known as 6G. This is primarily due to the substantial bandwidth it offers. However, transmitting signals in the sub-THz frequencies introduces several challenges. These include the significant attenuation of electromagnetic waves by the propagation environment, the demand for high sampling rates for analog-to-digital conversion, and the adverse impact of phase noise mainly generated by oscillators. Consequently, the direct transposition of existing wireless technologies is not straighforward. On one hand, the IEEE 802.15.3d specification standardizes a single-carrier waveform with carrier aggregation. On the other hand, ongoing research aims to adapt 5G New Radio multi-carrier waveforms like Orthogonal Frequency Division Multiplexing (OFDM) and Discrete Fourier Transform-Spread-OFDM (DFT-s-OFDM) to suit the characteristics of sub-THz frequencies. In this thesis, our objective is to investigate the performance of multi-carrier waveform systems that are affected by the harmful effects of high-frequency oscillator phase noise.

The genesis of phase noise can be traced back to sudden, brief and random fluctuations in the phase of an oscillator's components. This issue becomes increasingly severe as the carrier frequency rises, posing a substantial challenge to system performance, especially when operating in sub-THz frequency bands. As a result, the primary focus of this thesis centers on the development of signal-processing algorithms aimed at mitigating phase noise. To achieve this goal, two core aspects are explored within this research: the formulation of efficient techniques for phase noise reduction and their practical implementation for realistic radio-frequency transmissions. To provide a fair performance evaluation, we consider statistical phase noise models such as: (i) correlated phase noise as proposed by the 3GPP and direct measurements obtained from a D-Band CMOS transceiver designed at CEA-Leti; as well as (ii) purely uncorrelated Gaussian phase noise. Leveraging these models, we have proposed a phase noise compensation algorithm characterized by a low pilot density, particularly effective when dealing with correlated phase noise in both OFDM and DFT-s-OFDM systems. This algorithm relies on the knowledge of stochastic properties of various noise sources induced by phase noise. We assess the performance for a-priori knowledge, *i.e* genie-aided, and estimated knowledge, *i.e.* practical scenario of these stochastic properties. In the case of uncorrelated phase noise where its tracking is no longer possible, we introduce an optimal detector particularly suited for DFT-s-OFDM systems, operating under strong uncorrelated phase noise conditions. The performance of this detector is contingent upon the statistical properties of the noises introduced by phase noise. Throughout these contributions, we maintain a focus on achieving low implementation complexity and high spectral efficiency, with an underlying assumption of coherent communication systems.

**Keywords** – *5G and beyond Networks, Wireless Networks, 5G-NR Multi-carrier waveforms, sub-THz bands, Phase Noise, CMOS transceivers, 3GPP, 6G.*

cea leti

UGA Université Grenoble Alpes